NASA CR-132724 c.89

*Final Report*

# A PRELIMINARY STUDY OF AIR-POLLUTION MEASUREMENT BY ACTIVE REMOTE-SENSING TECHNIQUES

By: M. L. WRIGHT    E. K. PROCTOR    L. S. GASIOREK    E. M. LISTON

*Prepared for:*

**STANFORD RESEARCH INSTITUTE**
**Menlo Park, California 94025 · U.S.A.**

**STANFORD RESEARCH INSTITUTE**

Menlo Park, California 94025 · U.S.A.

*Final Report*

*June 1975*

# A PRELIMINARY STUDY OF AIR-POLLUTION MEASUREMENT BY ACTIVE REMOTE-SENSING TECHNIQUES

*By:* M. L. WRIGHT     E. K. PROCTOR     L. S. GASIOREK     E. M. LISTON

*Prepared for:*

NATIONAL AERONAUTICS AND SPACE ADMINISTRATION
LANGLEY RESEARCH CENTER
HAMPTON, VIRGINIA 23365

CONTRACT NAS1-11657

SRI Project 1966

*Approved by:*

DAVID A. JOHNSON, *Director*
*Radio Physics Laboratory*

RAY L. LEADABRAND, *Executive Director*
*Electronics and Radio Sciences Division*

*Copy No.* 89

| 1. Report No. NASA CR-132724 | 2. Government Accession No. | 3. Recipient's Catalog No. |
|---|---|---|
| 4. Title and Subtitle A PRELIMINARY STUDY OF AIR-POLLUTION MEASUREMENT BY ACTIVE REMOTE-SENSING | | 5. Report Date June 1975 |
| | | 6. Performing Organization Code 1966 |
| 7. Author(s) M. L. Wright; E. K. Proctor; L. S. Gasiorek; and E. M. Liston | | 8. Performing Organization Report No. Final Report |
| 9. Performing Organization Name and Address Stanford Research Institute 333 Ravenswood Avenue Menlo Park, California 94025 | | 10. Work Unit No. 645-20-01-01 |
| | | 11. Contract or Grant No. NAS1-11657 |
| 12. Sponsoring Agency Name and Address National Aeronautics and Space Administration Washington, D.C. 20546 | | 13. Type of Report and Period Covered Contractor Report |
| | | 14. Sponsoring Agency Code |

15. Supplementary Notes

This contract was monitored by the Environmental and Space Sciences Division of Langley Research Center. For additional information, contact G. Burton Northam, Langley Research Center, Mail Stop 401A, Hampton, Virginia 23665.

16. Abstract

The important air pollutants (some of which are also natural constituents of the normal atmosphere) are identified, and the needs for their measurement from satellites and aircraft are discussed. An assessment is made of the properties of these pollutants and of the normal atmosphere, including interactions with light of various wavelengths and the resulting effects on transmission and scattering of optical signals. The possible methods (both double-ended and single-ended) for active remote measurement are described; the relative performance capabilities of double-ended and single-ended systems are compared qualitatively; and the capabilities of the several single-ended or backscattering techniques are compared quantitatively. The differential-absorption lidar (DIAL) technique is shown to be superior to the other backscattering techniques for the purposes under consideration. The lidar system parameters and their relationships to the environmental factors and the properties of pollutants are examined in detail. A computer program that models both the atmosphere (including pollutants) and the lidar system is described. The performance capabilities of present and future lidar components are assessed, and projections are made of prospective measurement capabilities for future lidar systems. Following a discussion of some important operational factors that affect both the design and measurement capabilities of airborne and satellite-based lidar systems, the extensive analytical results obtained through more than 1000 individual cases analyzed with the aid of the computer program are summarized and discussed at length. The conclusions that were reached are presented. Recommendations are also made for additional studies to investigate cases that could not be explored adequately during this study.

| 17. Key Words (Suggested by Author(s)) (STAR category underlined) Masers       Air Pollution Shuttle       Remote Sensing Laser Radar | 18. Distribution Statement |
|---|---|

| 19. Security Classif. (of this report) UNCLASSIFIED | 20. Security Classif. (of this page) UNCLASSIFIED | 21. No. of Pages 340 | 22. Price* |
|---|---|---|---|

## SUMMARY

This study contains four major tasks. The first task is to identify important air pollutants and needs for their measurement. Thirteen gases ($CO_2$, CO, $SO_2$, $H_2S$, $O_3$, NO, $NO_2$, $N_2O$, $NH_3$, $CH_4$, HCHO, $H_2O$, and HCl) and aerosols are examined. $CO_2$, CO, $O_3$, and $N_2O$ have relatively long atmospheric residence times and thus smaller maximum-to-minimum concentration variations. The remaining gases, with short atmospheric residence times, will have large concentration variations between polluted urban atmospheres and rural atmospheres. The second task in the study is to examine a variety of active remote-measurement methods for monitoring gases. Systems using differential-absorption, fluorescence, Raman scattering, resonant Raman scattering, elastic scattering, and double-ended absorption are examined. The differential-absorption lidar (DIAL) technique is found to be the most sensitive and generally applicable technique for the measurement of gases. The third task in the study is a detailed analysis of the performance of both range-resolved and column-content differential-absorption lidar (DIAL) systems. This task includes a detailed analysis of the error mechanisms that affect the accuracy of DIAL system measurements. In the fourth task, this detailed analysis is utilized in the SRI-developed Modular Atmospheric Propagation Program (MAPP) to provide detailed performance analyses for monitoring $O_3$, $SO_2$, $NO_2$, CO, and $N_2O$ from altitudes of 166 km, 12 km, and 3 km. Both range-resolved and column-content calculations are presented. In addition to the DIAL system predictions for gaseous monitoring performance, the performance of conventional lidar systems at 0.6943 and 1.06 μm are presented for monitoring both aerosols and clouds in the atmosphere.

The feasibility of realizing each of these monitoring systems is largely dependent on the availability of certain laser energies at the desired wavelengths. A detailed examination of present and future capabilities of tunable lasers is presented and the expected energies for present (0 to 1 year), near-future (1 to 2 years), and future (3 to 5 years) capabilities of these tunable lasers are given. These predictions for laser performance lead to the following conclusions:

(1) **From 166 km**

   (a) Column-content measurements of $O_3$, $SO_2$, $NO_2$, CO, and $N_2O$ will be feasible within five years.

   (b) Range-resolved measurements of $O_3$, $NO_2$, $N_2O$ and possibly CO will be technologically feasible within five years.

   (c) Cloud-top heights can be measured for cirrus clouds, stratus clouds, and cumulus clouds with present technology. Cloud thickness measurements can be measured for cirrus clouds. Optical depth can be determined for thin cirrus and medium cirrus, but not thick cirrus clouds, with presently available technology.

   (d) Present technology will permit measurement of stratospheric aerosols (scattering ratio) using multiple-pulse integration. Future technology may permit single-pulse measurements of stratospheric aerosol scattering ratios.

(2) **From 12 km**

   Range-resolved measurements of $O_3$, $SO_2$, $NO_2$, CO, and $N_2O$ should be feasible within five years.

(3) **From 3 km**

   Range-resolved measurements of $O_3$, $SO_2$, $NO_2$, CO, and $N_2O$ should be feasible within two years.

This is a preliminary study because certain alternative or advanced techniques (involving fixed-tuned lasers and/or heterodyne receivers, for example) were not considered in great detail and not all gases of interest in pollution and heat-balance problems were examined. It is

recommended that a more detailed analysis be made of these advanced laser techniques. Feasibility assessments should be made for additional pollution gases and for gases of interest in heat-balance problems, particularly $H_2O$, $CO_2$, and $O_3$.

# CONTENTS

# ILLUSTRATIONS

## TABLES

# ACKNOWLEDGMENTS

# I   INTRODUCTION

This report presents the results of a feasibility study for remote measurement of air pollutants from satellites and aircraft by active remote-sensing techniques at infrared, visible, and ultraviolet wavelengths. The principal objectives as contained in the Statement of Work are:

- Prepare a summary of pertinent information on global concentrations and distributions of the major pollutants, including at least CO, $SO_2$, $O_3$, $NH_3$, $NO_x$, PAN, hydrocarbons, and atmospheric aerosols.

- Prepare a detailed treatment of active measurement techniques including both single-ended laser radar (lidar) systems and double-ended systems in satellite-to-satellite, satellite-to-ground, and ground-to-satellite configurations.

- Consider pollutant measurement using resonant fluorescence, resonant Raman scattering, and absorption methods.

- Prepare a review of resonant Raman theory and identify resonant wavelengths of potential importance for pollutant molecules.

- Examine the possibilities of measuring the optical depth and height of cirrus clouds.

- Study the feasibility of measuring the properties of aerosols in the terrestrial mixing layer and the lower stratosphere, including concentration, size distribution, composition, and particle shape.

- Establish and assess the relationships among the important measurement-system parameters, environmental factors, information content, data rate, and the complexity, weight, volume, power consumption, and operational requirements for each technique.

Following the oral review in the fifth month of the project, additional instructions were received that provided clarification and guidance concerning areas for emphasis. The major items were:

- Define the satellite orbit as an altitude of 166 km with orbital inclination of 28 degrees to 55 degrees.

- For global distributions, consider grid spacings in the range of 5 to 20 km, modified as necessary by cloud-cover statistics.

- Assume that airborne applications are primarily for studying the dispersion of local and regional pollutants from fixed altitudes of 3 km and 12 km.

- Emphasize remote measurement of $SO_2$, $O_3$, $NO_2$, and aerosols using single-ended lidar techniques that provide range resolution, but evaluate the differential-absorption technique using terrestrial echoes that yield no range-resolved data.

- Evaluate the usefulness of the scattering ratio (total/molecular) for measuring global circulation of air masses and for providing useful data concerning the effects of aerosols on the thermal balance of the terrestrial system.

- Assume that the power available to a lidar system aboard a satellite is 1.5 to 2 kW.

The report begins with consideration of the needs for remote measurement of air pollutants, including a listing of the pollutants of interest and their residence times in the atmosphere, and a determination of which ones are important on a global scale and which ones are of only local or regional importance. Consideration of the physical and spectral properties of the species of interest is followed by a section on the properties of the atmosphere that affect remote-measurement capabilities. This is followed by an examination of the applicable remote-measurement techniques, including quantitative comparisons of sensitivities and other measures of capability. The various system performance parameters, constraints, and trade-offs are then examined in detail. A detailed theoretical analysis of the DIAL (Differential Absorption Lidar) systems is given.

Quantitative analyses of the system performance requirements for remote measurement of pollutants, aerosols, and cirrus clouds from both satellites and aircraft are presented. Also included is an assessment of

2

the current and prospective future capabilities of implementing these requirements with equipment capable of flight qualification, and a discussion of operational concepts, sizes, weights, and power consumption. The body of the report ends with a presentation of the conclusions reached as a result of the study, and recommendations for additional research tasks to achieve capabilities for remote measurement of air pollutants. A technical appendix provides additional details to support the body of the report.

## II ATMOSPHERIC CONSTITUENTS AND MEASUREMENT NEEDS

### A. General Review

Although the principal focus of the study reported here is toward remote measurement of pollutants in the atmosphere, it is not always possible to distinguish between potentially harmful pollutants and naturally occurring trace constituents of the atmosphere. For example, ozone is both an important natural component that shields the terrestrial surface from harmful ultraviolet radiation and also a component of polluted atmospheres that produces harmful effects on people, plants, and materials. Antropogenic additions to the substantial amount of $CO_2$ naturally present in the atmosphere could be considered as a pollutant because of the possible effects on temperature and climate, but opinions are mixed as to whether these additions actually produce harmful effects. Water vapor would hardly be considered to be a pollutant, but its injection into the stratosphere could affect the climate. On the other hand, man-made additions of $SO_2$ and the oxides of nitrogen definitely produce harmful effects in urban regions and perhaps on a larger scale as well.

Hence, the topic of the study inevitably became remote measurement of trace constituents (both gaseous and particulate) in the atmosphere. A complete review of these constituents and the needs for their measurement is not only beyond the scope of this report, but fortunately is not necessary since most of the topics of interest have been extensively reviewed in NASA publications that are still current and definitive (NASA, 1971; Ludwig, 1969).[*] However, to provide some background

---

[*] References are listed at the end of the report.

information for readers who are unfamiliar with this topic, brief essays are provided on the gases and aerosols of primary interest. For the gases, summary charts are also provided. Following the example of the RMOP report, "Remote Measurement of Air Pollution" (NASA, 1971), distinctions are made among local, regional, and global scales of measurement, where the regional scale may be taken to have linear dimensions on the order of $10^3$ km. A differentiation is also made between the tropospheric and stratospheric regions (although the dividing altitude is somewhat arbitrary) because of some important differences in the effects of trace constituents in these two altitude regimes. Gases and particulate matter (aerosols) are considered separately.

## B.   Tropospheric Gases

The principal tropospheric gases of interest (apart from water vapor) are listed in Table II-1 together with some estimates of sources, emission rates, concentrations, and lifetimes. Brief discussions of these gases follow.

### 1.   Carbon Dioxide ($CO_2$)

The atmospheric content of $CO_2$ is an important determinant of the thermal balance of the atmosphere and hence of the temperature of the earth/atmosphere system. It is known that the mean concentration of $CO_2$ is slowly increasing at about 0.2% (or 0.7 ppm) per year. This could lead to an increase in the average temperature of the globe and possibly to major changes in the weather and ocean level.

### 2.   Carbon Monoxide (CO)

It has recently been found (Niki and Weinstock, 1972) that the natural lifetime of CO is much shorter than had previously been assumed.

TABLE II-1

CHARACTERISTICS OF ATMOSPHERIC TRACE GASES

| Pollutant | Major Sources | | Estimated Emission Rates | | Polluted-Atmosphere Concentrations | Atmospheric Background Concentrations | Calculated Atmospheric Residence Time |
|---|---|---|---|---|---|---|---|
| | Anthropogenic | Natural | Anthropogenic $(10^9$ kg/yr) | Natural $(10^9$ kg/yr) | | | |
| $CO_2$ | Combustion | Biological decay; release from oceans | 13,000 | $10^6$ | 350 ppm | 320 ppm | 2-4 years |
| CO | Auto exhaust; combustion | $CH_4$ oxidation | 250 | 3,000 | 5 ppm | 0.1 ppm | 0.1 year |
| $SO_2$ | Combustion of coal and oil | Volcanoes | 133 | Small | 1 ppm | 0.2-2 ppb | 4 days |
| $H_2S$ | Chemical proesses; sewage treatment | Volcanoes, biological action in swamps | 2.7 | 90 | 4 ppb | 0.2 ppb | 2 days |
| $O_3$ | Photochemical smog | Photolysis of $O_2$ (25-50 km) | Uncertain | Uncertain | 0.3 ppm | 0.01 ppm | 1 day |
| NO | Combustion | Bacterial action in soil | 48 | 460 | 0.2 ppm | 0.2-2 ppb | 1 day |
| $NO_2$ | None | Conversion of NO | Negligible | Negligible | 0.1 ppm | 0.5-4 ppb | 5 days |
| $N_2O$ | None | Biological action in soil | Small | 540 | 0.25 ppm | 0.25 ppm | 4 years |
| $NH_3$ | Waste treatment | Biological decay | 3.6 | 1,000 | 0.01 ppm | 6-20 ppb | 7 days |
| Hydrocarbons | Combustion exhaust; chemical processes | Biological processes | $CH_4$: 80 Others: uncertain | $CH_4$: 2,000 Others: Uncertain | $CH_4$: 3 ppm Others: 2 ppm | $CH_4$: 1.5 ppm Others: < 1 ppb | $CH_4$: 1 year Others: unknown |
| HCHO | Combustion exhaust; atmospheric reactions | Biological processes | 100 | 1,000 | 0.05 ppm | 1 ppb | 1-5 days |
| HCl | Chemical processes; rocket engine exhaust | Unknown | Uncertain | Unknown | 1-5 ppm | Unknown | Unknown |

This has required an increase by a factor of 40 in the estimated natural emission rate of CO. It is assumed that this enormous amount of CO (more than 10 times man's total contribution) comes from oxidation of $CH_4$, which is derived primarily from biological decomposition. Therefore, areas such as the Amazon jungle should be large sources of CO. The question of sinks for CO is still not completely resolved, although it appears that reaction with atmospheric OH radicals to form $CO_2$ is the dominant sink. CO is believed to be important in polluted atmospheres as an element in a chemical chain reaction that results in the rapid conversion of NO to $NO_2$.

3. Sulfur Dioxide ($SO_2$)

This compound is important primarily because of its tendency to oxidize in the atmosphere and form aerosols. These aerosols influence visibility and are involved in eye irritation and in plant damage. $SO_2$ also dissolves in water to form an acid rain, the residue of which is believed to be responsible for observed increases in soil acidity in certain regions.

4. Hydrogen Sulfide ($H_2S$)

Except on a strictly local basis where its odor and toxicity might present a problem, $H_2S$ is presently thought to be important only because it oxidizes to $SO_2$ and ultimately forms aerosols. The source and sink kinetics and the rate of conversion to aerosols are inadequately known to establish whether $H_2S$ is involved in presently unsuspected atmospheric chemical reactions.

5. Ozone ($O_3$)

Ozone is a major constituent of urban smog and also plays a major role in smog-related photochemical processes. Although there is a natural background of $O_3$ in the troposphere caused by downward diffusion from the stratosphere, the sources of greatest importance are photochemical reactions involving $NO_2$, NO, and hydrocarbons.

6. Nitrogen Oxides (NO and $NO_2$)

NO and $NO_2$, collectively or individually, are often designated as $NO_x$. Approximately 95% of the $NO_x$ in the atmosphere originates as NO from biological activity in the soil. Therefore, the relative contribution to the global $NO_x$ inventory by antropogenic activities is small. However, antropogenic contributions on a local scale are very significant. It is well known that generation of $NO_x$ by combustion is the primary cause of the photochemical smog that is so abundant in major urban areas.

7. Nitrous Oxide ($N_2O$)

The only known major source of $N_2O$ is biological action in soil. It is chemically inert in the troposphere and is of interest primarily because tropospheric $N_2O$ diffuses into the stratosphere.

8. Ammonia ($NH_3$)

On a global basis, essentially all the $NH_3$ comes from the decay of vegetation and animal matter in the soil. However, antropogenic contributions can be very significant on a local scale, since it is known (Cadle, 1972) that $NH_3$ reacts rapidly with smoggy air to form large, highly hygroscopic aerosols that can participate in local atmospheric chemical reactions.

9. Methane (CH$_4$) and Other Hydrocarbons

The major global source of this material also is decomposition of organic matter in the soil, although some is released from gas and petroleum activities. This gas is believed to be innocuous in the troposphere but it diffuses into the stratosphere. The numerous other hydrocarbons come primarily from combustion and chemical processes and are important because many of the noxious constituents of polluted air are derived from hydrocarbon reactions.

10. Formaldehyde (HCHO)

The major global source of HCHO is biological action, but on local levels photochemical smog is a major source. It is believed to be an eye irritant and it may be involved in plant damage. Its atmospheric chemistry is not well known, but it is believed to be involved in photochemical processes that form OH, HO$_2$, and CH$_3$O radicals.

11. Water Vapor (H$_2$O)

The major importance of water vapor in the troposphere is its influence on weather. It is also directly connected with the formation and size of atmospheric aerosols and hence is involved in nearly all atmospheric chemical reactions, and in determining visibility, an important index of pollution.

12. Hydrogen Chloride (HCl)

The natural background of HCl is negligibly small, but this gas has recently come into prominence as a pollutant because it is released in large quantities by certain solid-fueled rocket engines. In the troposphere it mixes readily with liquid aerosols to form a weak

hydrochloric acid solution that can precipitate as an acid rain. Although the effects can be deleterious to plants, people, and equipment, the problem exists only at the launch sites of the Atlantic and the Pacific missile ranges and at a few isolated test sites.

C.  Stratospheric Gases

Until recently, gases in the stratosphere were primarily of purely scientific interest because human activities had not significantly perturbed this normally stable region of the atmosphere where $O_3$ is produced by the interaction of solar ultraviolet radiation with molecular oxygen. The stratospheric ozone layer effectively prevents harmful solar ultraviolet radiation from reaching the surface of the earth. However, in the late 1960s a controversy arose over the possibility that exhaust emissions from supersonic transports (SSTs) might deplete the ozone layer and also alter the thermal balance of the earth-atmosphere system.

This concern about the effects of SSTs led to the establishment in 1970 of the Climatic Impact Assessment Program (CIAP) in the Department of Transportation having the objective of obtaining the necessary additional scientific information to evaluate the prospective effects of SST exhausts on the stratosphere. The final report on this investigation has recently become available (Grobecker, et al., 1974). The SST exhaust gases of primary interest are oxides of nitrogen ($NO_x$), oxides of carbon ($CO_x$), sulfur dioxide ($SO_2$), and water vapor. The CIAP program also focussed attention on the effects of diffusion into the stratosphere of gases of tropospheric origin. $SO_2$ is the primary source of the stratospheric aerosol (called the sulfate layer or the Junge layer). The stratospheric component of $H_2O$ seems to be changing, possibly as a result of volcanic activity, but perhaps influenced by diffusion of nitric acid ($HNO_3$), formaldehyde (HCHO), methane ($CH_4$), and nitrogen

11

compounds from the troposphere. All of the complex chemical reactions and the numerous intermediate chemical products (such as OH) are also of interest.

Subsequent to the advent of concern about the effects of SST exhaust products on the stratosphere, questions were raised about the possible adverse effects of rocket exhausts in this region. The principal concern is that injection of large amounts of HCl might reduce the concentration of stratospheric ozone. HCl is photodissociated into $H_2$ and $Cl_2$, and $Cl_2$ reduces $O_3$ to $O_2$ in a chain reaction in which each molecule of $Cl_2$ can reduce many molecules of $O_3$. The chemical byproducts of this process that are also of interest include ClO, $ClO_2$, $ClO_3$, OH, and the oxides of nitrogen. Injection of particulate matter and numerous other gases is also of concern.

In parallel with, and perhaps as a result of, questions about the prospective effects of HCl on the stratosphere, concern is also being expressed about the effects on the stratosphere of freons (also called chlorofluoromethanes and fluorocarbons), which contain chlorine that is released slowly by solar photodecomposition (Molina and Rowland, 1974; Cicerone, et al., 1974; Wofsy, et al., 1975). Freons are widely used as refrigerants and as propellants for spray cans. It is anticipated that these long-lived chemicals, which are being released into the troposphere in large quantities, will gradually diffuse into the stratosphere in future decades and produce effects similar to those discussed above in connection with HCl from rocket exhausts. There are many freons, designated as $CF_xCl_y$, but the principal ones are $CF_2Cl_2$ and $CFCl_3$.

D.   Need for Measurement of Gases

All of the aforementioned gases, as well as a large number of species resulting from interactions between and among these gases and both

sunlight and normal atmospheric constituents, are of interest to those concerned with air pollution, climatic and meteorological effects, and aerochemistry. For the purposes of this report, it is desirable to determine the measurement accuracies and the spatial and temporal resolutions that are needed. Unfortunately, this is a formidable task for which few guidelines are available.

For the stratosphere, spatial and temporal resolution requirements can be estimated from available data. According to the CIAP report (Grobecker et al., 1974), the ozone content varies on a typical day by a factor of 3 over the globe and by about 30% in a north-south distance of 2500 km at midlatitudes. Hence, spatial resolution horizontally in the range of from a few hundred up to perhaps a thousand kilometers should suffice. The vertical scale of ozone variation is compatible with a range resolution of 1 km. Day-to-day and week-to-week changes in ozone content are of the order of 25%, and changes in annual mean values are of the order of 10%. Since a single satellite in polar orbit observes the same space twice per day, average daily variations are only marginally observable from a single satellite.

For injected species, current estimates on dispersion rates predict a horizontal growth rate of 100 km to 200 km in three days from a point release, with an accompanying vertical dispersion of 0.1 km to 0.2 km. Thus, horizontal resolution of the order of 10 km would be required to observe the effects of SST and rocket flights. It is doubtful that the vertical dispersion could be resolved.

The situation in the troposphere is much more complicated and varied. On the local scale, spatial resolution (both horizontally and vertically) of 0.1 km is desirable for many purposes (e.g., studying the dispersion of emissions from smoke stacks), but urban models are currently based on cell sizes of 1 km horizontally with no vertical resolution. Regionally,

horizontal resolution in the range of 10 km to 100 km accompanied by a
vertical resolution of 0.1 km to 1 km would satisfy most needs. Globally,
horizontal resolution of 100 km to 1000 km with vertical resolution of
1 km to 10 km would suffice. In many cases, total vertical column content
averaged over several thousand kilometers would suffice.

Temporal resolution needs in the troposphere vary widely and are for
the most part poorly defined. For research purposes, intervals of from
minutes to several tens of minutes can be important. At the other extreme,
monitoring and control standards specify instantaneous peak readings
through 1-hour and 24-hour averages and up to annual averages.

Accuracy requirements in both the stratosphere and troposphere also
vary widely and tend to be poorly defined. In general, measurements
within an accuracy of 10% of local concentrations are considered to be
good to acceptable, while errors in excess of 50% produce data of marginal
value. The only available compendium of accuracy requirements is found
in Tables 1 and 2 of the RMOP report (NASA, 1971), which lists the best
estimates of knowledgeable experts in the field. Table II-2 is an ab-
stract of these estimates.

E. Aerosols

During the last few years the importance of atmospheric particles
has become the focus of considerable concern, especially in connection
with possible climatic changes that might result from modification of
the radiation balance by changes in particulate concentration. First
addressed in terms of the general effects of increasing urbanization
and industrial pollution, the problem has recently received special
attention in the context of proposed SST operations in the high atmo-
sphere (Nat. Acad. Sci., 1969; SCEP, 1970; SMIC, 1971; NASA, 1971;
Charlson, 1973; Elterman et al., 1973).

14

Table II-2

ACCURACY REQUIREMENTS FOR REMOTE MEASUREMENT OF GASES

| Constituent | Region | Accuracy Requirements | |
|---|---|---|---|
| | | Global | Regional |
| $CO_2$ | Total atmosphere | 0.5 ppm | 0.5 ppm |
| $SO_2$ | Stratosphere | 0.5 ppb | -- |
| $SO_2$ | Troposphere | -- | 10 ppb |
| $O_3$ | Stratosphere | Column content, 1% Vertical profile, 10% | -- |
| $O_3$ | Troposphere | -- | 10 ppb |
| $NO_x$ | Stratosphere | 10 ppb | 10-100 ppb |
| CO | Stratosphere | 10 ppb | -- |
| CO | Troposphere | -- | 10 ppb |
| $HNO_3$ | Stratosphere | 1 ppb | -- |
| Hydrocarbons | Troposphere | ? | 1 ppb (?) |
| $CH_4$ | Stratosphere | 0.2 ppm | -- |
| $CH_4$ | Troposphere | 0.5 ppm | -- |
| Freons | Total atmosphere | 0.001 ppb (?) | |
| $N_2O$ | Stratosphere | 50 ppb | -- |
| HCHO | Troposphere | -- | 1 ppb |
| $NH_3$ | Troposphere | -- | 10 ppb |
| HCl | Troposphere | -- | 0.5-1 ppm |

While the possibility of serious degradation of world or regional climates has been widely recognized and discussed, the effective

quantitative assessment of this possibility has not been possible with any
degree of conviction because, as is the case with many other atmospheric
factors and pollutants, too little is known about natural conditions and
their normal variability. This paucity of knowledge has been highlighted
by the DOT's studies to provide data upon which decisions can be made re-
garding national programs for supersonic transportation at high altitudes.
In all areas, the initial problem has been to learn more about existing
conditions, sometimes on the most elementary terms.

This has been particularly the case for the stratospheric aerosol.
Despite recently accelerated research efforts, knowledge of this layer
is still incomplete. Data have been acquired piecemeal in space and time
by a relatively limited number of remote-sensing and in situ observational
programs. The latter include the important, but quite sparse, inputs
made by a number of lidar groups around the world. The results are as
might be expected. Although the broad concept of a stratospheric particu-
late layer at approximately 20 km (the "Junge layer") is well demonstrated,
its seasonal and global distribution is only very sketchily known, and
the role of volcanic eruptions in generating and sustaining this layer is
understood only in the most general terms. For example, the overall de-
crease (by a factor of some 8 to 10) in the particulate loading of the
stratospheric layer over the ten years ending in October 1974, which has
been shown by many observational techniques, is ascribed to the depletion
of dust that was injected into the stratosphere principally by the Agung
volcanic eruption of 1963. Since October 1974, lidar, balloon, aircraft,
and twilight photometer observations have detected increased particulate
content at altitudes between 12 and 20 km comparable in intensity to at
least the largest amounts observed in the early 1960s from the Mt. Agung
event. The material now present is apparently due to the eruption of
Volcan de Fuego in Guatemala (October, 1974).

In the troposphere, conditions are not much better understood. Long-term changes in atmospheric turbidity associated with changes in population density and industrial pollution have been inferred by simple radiometric measurements and direct surface observations. The nature of pollution in the form of plumes or streams of high particulate concentration from industrial areas or cities is all too obvious, but much remains to be learned about the wider dispersion of such particulates and their transfer between different levels of the atmosphere. For example, even the origins of certain pollutant conditions are not well established. Even more needs to be determined about the role of particulate matter in modifying radiative energy-transfer processes and in providing condensation nuclei in such a way as to affect temperature and precipitation on a local, regional, or even a global scale.

The role of particulates in modifying local climate (e.g., as in the precipitation anomalies downwind of urban centers, such as is being studied in the METROMEX program) or climate on a larger scale (e.g., as in the transport of Saharan dust over much greater areas, as was studied in the BOMEX program) is of great importance.

On all these counts it is no wonder that every thoughtful review of the situation (Nat. Acad. Sci., 1969; SCEP, 1970; SMIC, 1971: NASA, 1971; Charlson, 1973; Elterman et al., 1973) has urged the acquisition of increased knowledge of the nature and distribution of atmospheric particulate contamination and, in many cases, has made recommendations to develop and advance remote-sensing capabilities. More specifically, the development of a satellite-borne lidar monitoring capability has been urged (NASA, 1971; Elterman et al., 1973).

# III PROPERTIES OF ATMOSPHERIC GASES AND THE ATMOSPHERE

## A. Gases

### 1. Physical Properties

The principal features of atmospheric gases that are important for remote measurement processes are the interaction with light of various wavelengths. However, the interactions between various gases and aerosols, especially water aerosols, are also important because they affect the amount of each gas that is in the vapor phase, in which the strongest interactions with light occur.

For example, $SO_2$, $NO_2$, $NH_3$, and HCHO are all soluble in water and are easily absorbed in liquids or adsorbed on wet surfaces. Therefore, in an atmosphere containing a large number of aerosols or particles with high surface area, it is possible that a significant portion of these species will be dissolved in aerosol droplets or adsorbed on particle surfaces rather than be present as free molecular gases. Since most of the analysis procedures currently in use for these gases involve either high temperature or "wet chemistry," the form in which the pollutant occurs makes little difference in the results of the measurements. However, if purely optical methods are used, the state or form becomes vitally important because the optical spectra and absorption coefficients are much different for a molecular gas than for an aqueous solution of that gas. The only way to evaluate gaseous and aqueous distributions of a pollutant in a real atmosphere would be set up a "standard" chemical method of analysis and a purely optical method side by side, and compare their data as a function of aerosol or particulate loading. To the best of our knowledge, no such experiment has been reported.

## 2.   Interactions with Light

### a.   Absorption

The fundamental relationship that defines the absorption of radiant energy is Beer's law,

$$I = I_o e^{-kcl} \qquad (III-1)$$

where

$I_o$ = The incident energy

$I$ = The transmitted energy

$k$ = The absorption coefficient

$c$ = The concentration or number density of the absorbing species in the path

$l$ = The length of the path.

The absorption coefficient, $k$, is a function of three parameters--the "line strength," the total pressure, and the illuminating wavelength.

Line strength is a fundamental property of the molecules and is a function of temperature.  Its net value is the product of the constant for a species, times the number of molecules present in the path.  Experimentally, the line strength is equivalent to the area under the absorption-line curve over the entire spectrum

$$S = \int_{-\infty}^{\infty} k(\nu)\, d\nu \quad .$$

The absorption coefficient, $k$, is dependent on the line-width and wavelength according to the relationship

$$k(\nu) = \frac{S\gamma}{\pi} \left[ \frac{1}{(\nu - \nu_0)^2 + \gamma^2} \right] \qquad \text{(III-2)}$$

where

$\quad\quad$ S = The line strength

$\quad\quad$ $\gamma$ = The line half-width at half intensity

$\quad\quad$ $\nu_0$ = The line center frequency

$\quad\quad$ $\nu$ = The frequency of interest.

The half-width $\gamma$ is a function of pressure and temperature according to the relationship

$$\gamma = \gamma_0 \left( \frac{P}{P_0} \right) \left( \frac{T_0}{T} \right)^n \qquad \text{(III-3)}$$

where

$\quad\quad$ $\gamma_0$ = The half-width at normal temperature and pressure

$\quad\quad$ n = An exponent in the range 0.5 to 0.62 depending on the type of broadening.

The behavior of the absorption coefficient as a function of distance from line center is illustrated in Figure III-1. In Figure III-1, curves A through E are in order of increasing total pressure. The area under each of the curves A through E is constant because of the constant line strength at constant temperature. At the line center, k is inversely proportional to the pressure. Thus, the absorption coefficient at line center increases very rapidly as the pressure decreases.

$\quad\quad$ The above relationships describe the approximate behavior of absorbing gases in the pressure-broadened region. This approximation is considered to be valid up to altitudes of 14 km, or a pressure of
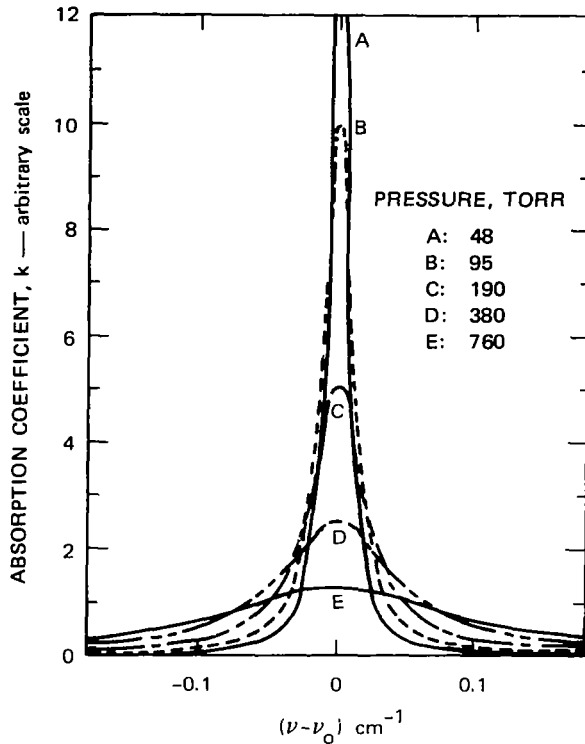
21

FIGURE III-1 ABSORPTION COEFFICIENT AS A FUNCTION
OF WAVELENGTH WITH TOTAL PRESSURE
AS A PARAMETER

142 mb (1013.2 mb is the pressure at sea level). At very low pressures, the absorption coefficient is determined by Doppler broadening rather than pressure-broadening. This Doppler-broadened region is considered to be valid at altitudes above 60 km or at pressures of less than 0.26 mb. The absorption coefficient in this region is given by

$$k = \left(\frac{\ln 2}{\pi}\right)^{1/2} \frac{S}{\gamma_D} \exp\left[(-\ln 2)\left(\frac{\nu - \nu_o}{\gamma_D}\right)^2\right]$$

where $\gamma_D$ is the Doppler-broadened half-width. Typical parameters in the Doppler-broadened regime at 300 $^\circ$K are a line width of about 0.001 $cm^{-1}$ and k values of about 2000.

Between 14 and 60 km (142 and 0.26 mb pressure) the Voight profile is used for determining the line shape and absorption coefficient.

This Voight profile is a complex mathematical expression that reduces to the Doppler behavior at low pressures and to the pressure-broadened behavior at high pressures, and is assumed to have approximately the correct behavior between these two regions. It has been found from calculations at various altitudes that the pressure-broadened behavior does not join smoothly with the Doppler-broadened behavior unless the intermediate Voight regime is used. The Voight regime encompasses a large altitude region of particular importance for ground-level monitoring from satellites.

The effect of illuminating the absorbing gas at frequencies off of line center is illustrated in Figure III-2. Curve A represents a case in which $\Delta\nu$ is so small that it is essentially at line center and k is inversely proportional to the pressure. Curves B through F illustrate that as $\Delta\nu$ increases by very small amounts the absorption coefficient at



$(\nu - \nu_o)$, cm$^{-1}$

A: 0.0016
B: 0.0032
C: 0.0065
D: 0.0125
E: 0.0250
F: 0.050
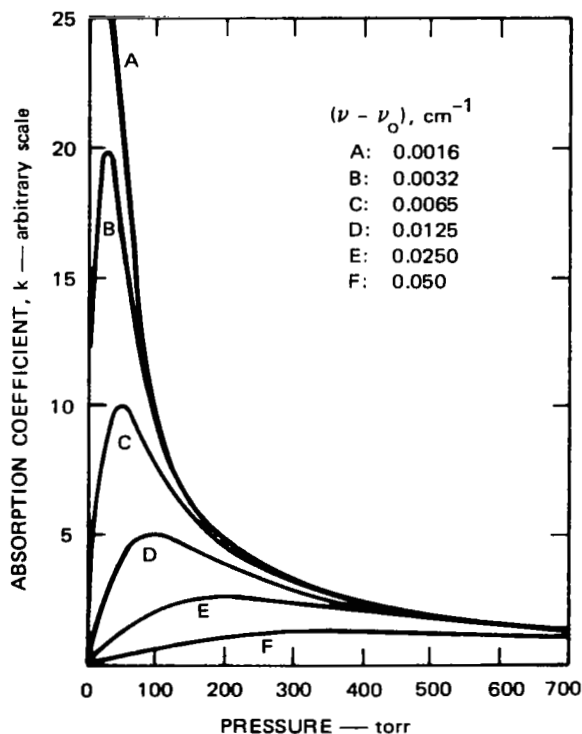
SOURCE: Hanst, 1971

FIGURE III-2 ABSORPTION COEFFICIENT AS A FUNCTION OF PRESSURE WITH DISTANCE FROM LINE CENTER AS A PARAMETER

1-atmosphere pressure (760 torr) changes very little. Therefore, an error in frequency of $\Delta \nu = 0.05$ cm$^{-1}$ probably affords a satisfactory match between $\nu$ and $\nu_0$ for ground-level measurement. However, at an altitude of 6 km (380 torr) an error of $\Delta \nu = 0.05$ cm$^{-1}$ would generate an error in k of 50%. At an altitude of 23 km (25 torr) an error of $\Delta \nu = 0.05$ cm$^{-1}$ would result in an apparent k value less than 1% of the true value. Even an offset of $\Delta \nu = 0.003$ cm$^{-1}$ would result in a 20% error. Therefore, if it is desired to measure stratospheric gases it will be necessary to have a spectral match between the illuminating frequency and the line center of $\Delta \nu$ less than 0.002 cm$^{-1}$. These examples illustrate in a general way the precision with which line locations and operating wavelengths must be known. The variations of the line widths of particular gases with pressure must be examined to determine the precision that is required for each case.

If it is desired to measure the ground-level concentration of $O_3$ from a satellite, the $\Delta \nu$ should be approximately 0.05 cm$^{-1}$. This would allow the illuminating beam to be strongly absorbed by the ground-level $O_3$ but be essentially unattenuated by the stratospheric $O_3$.

A great deal of "high-resolution" spectroscopic data has been taken on gases, and it might be assumed that it would be possible to compare tables of laser lines with tables of absorption lines to pick the optimum line pair to do the measurement. Unfortunately, these measurements were not made with adequate resolution or calibration accuracy. Some spectra are beginning to appear in the literature that are made using diode lasers that have a resolution of $10^{-5}$ cm$^{-1}$, and techniques are being developed to get wavelength calibrations of the same accuracy. However, the data that are presently available from such experiments are quite limited. Therefore, for the near future it will be necessary to utilize the best standard spectroscopic data that are available for estimating system performance.

These spectral data are used as inputs for the computer program to be discussed. This program computes an estimate of the expected system performance based on selected sets of spectral peaks and valleys. This estimate is valid for a feasibility analysis, but eventually it will be necessary to build a tunable laser and measure the absorption coefficient in the region of predicted optimum performance. Such a tunable laser will have to have a stability and a setting accuracy of better than $\pm 0.002$ cm$^{-1}$.

For the purposes of estimating system performance, a large amount of spectral information was collected on this project. The classes of data that were located are shown in Table III-1. The quality of these data and their usability for this project varied widely. The best data are contained in the AFCRL compilation (McClatchey et al., 1973). These data are in the form of a magnetic tape containing more than 100,000 spectral lines covering most of the data for $CO$, $CO_2$, $N_2O$, $H_2O$, $O_2$, $O_3$, and $CH_4$ between 1 μm and the far IR. These data are not complete but they are being updated and they represent the best data that can be obtained with standard spectrometers.

During this program, spectral data on NO and $SO_2$ were obtained from the literature and added to the AFCRL tape. It is believed that the resolution and accuracy of these data are equivalent to that of the main data bank. Data on several of the $SO_2$ lines were compared with those obtained using diode lasers, and the line-position accuracy was found to be $\pm 0.02$ cm$^{-1}$. This is excellent by spectroscopic standards but is an order of magnitude poorer than required for lidar measurements. Additional data on $SO_2$ and $NO_2$ are being generated at the University of Tennessee (Fox et al., 1970; Teowani, 1972; Corice et al., 1972) and will be incorporated into the tape as they become available.

Table III-1

## HIGH-RESOLUTION SPECTRA AVAILABLE

| Gases | Spectral Region | | | |
|---|---|---|---|---|
| | UV (180-400 nm) | Visible (400-700 nm) | Near IR (700-2000 nm) | IR (2-15 $\mu$m) |
| CO | X | | | X |
| $CO_2$ | X | | | X |
| $N_2O$ | X | | | X |
| Hydrocarbons | | | | X |
| NO | X | | | X |
| $NO_2$ | X | X | | X |
| $SO_2$ | X | | | X |
| PAN | | | | X |
| RCHO | | | | X |
| HCl | | | X | X |
| $NH_3$ | X | | | X |
| $H_2O$ | X | | X | X |
| $D_2O$ | | | | X |
| $O_3$ | X | | | X |

Many gases have absorption spectra in the ultraviolet spectral region. However, it is difficult to make use of UV absorption because of spectral interferences from other gases in the atmosphere, lack of detailed structure in the spectra, and absorption by $O_2$. For instance, CO has an absorption spectrum between 120 and 160 nm, but $O_2$ absorption prevents operation in this spectral region. $SO_2$ has a UV spectrum with good detail in an accessible spectral region where atmospheric transmission is reasonably good except for absorption by $O_3$, which produces a spectral interference problem.

In the visible region the only pollutant gas of interest that has a strong structured absorption is $NO_2$. The details of the spectrum are known and could be measured remotely using a laser operating in the blue region.

These absorption data are summarized in Figure III-3, which shows the locations of the principal absorption bands for atmospheric gases and the major pollutants. The absence of absorption lines in the 1-to-2-$\mu$m region where there should be overtone bands for some gases (for example, HCl and CO) probably indicates that data have not been taken in this spectral region.

b.    Data Deficiencies

Returning to Table III-1, it will be noted that there are only two gases for which high-resolution near-infrared spectra are presently available. This lack of data represents an area of investigation that has been largely ignored by spectroscopists because it is usually easier and more fruitful to work with the fundamental bands in the IR than to work with the overtone bands in the near IR (NIR). However, from the standpoint of remote air-pollution measurement, the NIR is an excellent region in which to work if sufficiently strong absorption lines can be found. At present there are photomultipliers that work out to about 1 $\mu$m and there is a good probability that this will be extended to about 2 $\mu$m in the near future. This region has some excellent windows and, most important, the Mie backscatter is much stronger in the NIR than it is in the IR. In the measurements of the NIR spectra of HCl at SRI it has been found that there is an overtone band that is readily observable at about 1.745 $\mu$m. The absorption coefficients appear to be strong enough to make it possible to observe a few ppm of HCl using remote-measurement techniques. There are good reasons to believe that it should

27
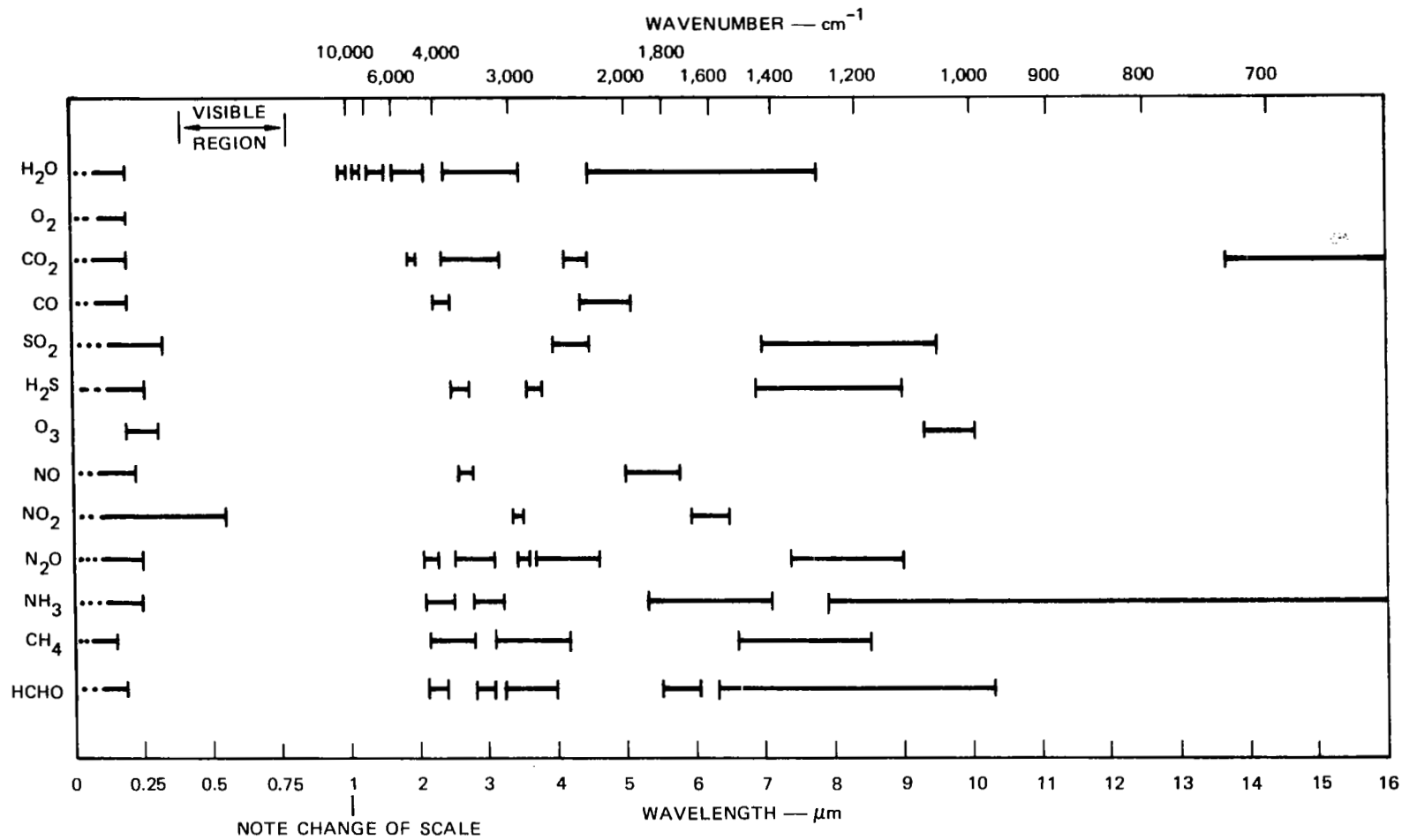
FIGURE III-3   ABSORPTION BANDS OF ATMOSPHERIC GASES

28

be possible to observe other gases in the NIR, but at present the spectral data do not appear to exist.

### c.   Fluorescence

Some gases fluoresce, which is defined as re-emission of energy previously absorbed at a shorter wavelength or band of wavelengths. At visible and ultraviolet wavelengths, fluorescence, when it occurs, involves electronic transitions of the molecules. In the infrared the vibrational transitions are excited. Fluorescence can be excited, selectively in some cases, by laser radiation. Fluorescence spectra are also different for different gases and thus offer a potential means of identification. Observation of laser-induced fluorescence therefore is a possible method for remote measurement of gases, including air pollutants. However, there are some inherent characteristics of molecules that create problems for this approach.

The lifetimes of the excited states are generally longer than the time intervals between collisions with air molecules at normal atmospheric pressures and temperatures, so that much of the energy stored in the excited states is lost by "quenching," or collisional de-excitation. Although not every collision results in a radiationless trasition in an excited molecule, quenching is very effective at most of the altitudes of interest for air pollutants. The average time between collisions at sea level is approximately $2 \times 10^{-10}$ s. The lifetimes of the vibrational states are typically in the range $10^{-2}$ to $10^{-1}$ s, so that infrared fluorescence is so heavily quenched that it cannot be detected except at very low pressures. The lifetimes of the states that produce fluorescence in the visible and ultraviolet are in the range of $10^{-9}$ to $10^{-4}$ s, which also leads to strong quenching even though fluorescence is observable.

Another problem is that even at low pressures where quenching is not a problem, many molecules of interest reradiate absorbed energy over such a wide band of wavelengths that the spectral density is low everywhere. The absorption and emission spectra of diatomic molecules (CO and NO) are line spectra that offer reasonable sensitivity. However, triatomic and larger polyatomic molecules have very complex absorption and fluorescence spectra that extend over hundreds of nanometers and appear to be essentially continuous at normal atmospheric pressures. The energy content per unit bandwidth is therefore low in comparison with diatomic molecules.

These broadband spectra also make identification by spectral characteristics difficult at best, and make identification impossible by measurement at only two or a few wavelengths. The problem is especially severe in mixtures of gases that have overlapping fluorescence spectra. A similar difficulty arises from the facts that fluorescence can also be excited in many aerosols by the same wavelengths used to excite gaseous fluorescence, and that the aerosol emissions may overlap the gaseous emission bands. Aerosols are abundant in most polluted atmospheres.

Many of the gases of interest do not fluoresce in the visible or UV range but photodissociate instead. This applies to $CO_2$, $N_2O$, $NH_3$, $O_3$, ethane, methane, and probably HCl and some other hydrocarbons. Often the dissociation products are excited in the process and relax to emit characteristic radiation, but identification can be difficult and collisional quenching is still a problem.

The absorption lines of many of the gases that fluoresce in the UV lie in spectral regions where atmospheric absorption of the excitation wavelength is severe. The fundamental absorption band for CO is at 154 nm, a wavelength for which the atmosphere is essentially opaque because of absorption by oxygen. The fundamental band for NO absorption is 227 nm, a wavelength that is strongly absorbed by ozone.

Because of these diffulties, laser-excited fluorescence
is not in general a promising method for remote measurement of air pollu-
tants, although there are some possible exceptions--for example, mea-
surement of high concentrations of $SO_2$ and NO at short ranges in the
smoke stacks of power plants.

B.  Aerosols

1.  Physical Properties

On a global basis, natural sources produce much greater quanti-
ties of aerosols than anthropogenic sources.  Soil dust supplies the
largest fraction of the total mass of atmospheric particles.  The spray
from ocean waves generates particles that are primarily droplets of
inorganic salts, but these particles can also contain large amounts of
organic material.  Many of the organic materials in sea water are very
surface-active and therefore are much more concentrated in the droplets
originating from surface spray than they are in the bulk of the water.
Volcanoes and fires also produce large quantities of particles.  The
above sources are the major sources of condensation nucleii for cloud
formation.

It has been estimated that trees and plants produce on the order
of $10^{12}$ kg per year of organic material in the air.  At least a part of
this material undergoes some form of chemical reaction in the air to
form aerosols.  These aerosols are visible as the "blue haze" often seen
over a forest.

Anthropogenic contributions to the particulate loading in the
atmosphere are probably only about 5% to 10% of that of natural sources
on a global basis.  However, on a local basis human activities are often
the dominant factors.  The most obvious materials are industrial dusts

31

such as cement, fly ash, and smoke.  These are also the most easily
dealt with because they can be filtered out of exhaust gases.

Much more difficult and subtle problems are caused by combus-
tion products from fossil fuels.  These exhaust gases usually contain
varying amounts of $NO_x$ and $SO_2$.  In the atmosphere, both of these gases
undergo chemical reactions that result in the formation of nitrate,
sulfate, or sulfuric-acid aerosols.

It is believed that the dominant removal process for atmospheric
particulates is precipitation.  Particles can be removed directly by be-
coming the condensation nuclei for rain or fog droplets or ice crystals.
Alternatively, they can be washed out of the atmosphere by collision
with falling raindrops or snowflakes.

In relatively dry areas gravitational settling as dry dust is
a more likely process.

Particulates can be modified in the atmosphere.  The major
changes that can occur are in size and in composition.  A change in size
or size distribution occurs because very small particles (less than
0.1 μm) collide and agglomerate to form larger particles.  Particles
larger than about 10 μm can settle out under the influence of gravity.
For these reasons, the size distribution of atmospheric particles usually
has a peak between 0.1 μm and 1 μm except in the immediate vicinity of
a large source of particles of some other size distribution.

Changes in the composition of particles occur primarily as a
consequence of their large area-to-volume ratio.  Because this ratio is
usually very large, they are ideal bodies for the absorption or adsorption
of gases in the atmosphere.  The surfaces of aerosols quickly reach
equilibrium with the surrounding atmosphere.  Therefore, a spray droplet
from an ocean wave will dry out as it blows inland and, assuming that
it contains hygroscopic salts, its size will depend on the relative

32

humidity of the air around it. If the droplet contains no organic material it will probably always have a monolayer of water on its surface. If it starts out with organic material, or if it passes through an atmosphere containing organics, the surface layer can be water, organic, or a mixture. If the particle passes through an atmosphere containing other gases, these will impinge on the surface. If the gas molecule is soluble in the liquid phase it will dissolve in the liquid. If it is not soluble, or if it is surface-active, it will adsorb on the surface. Thus, a particle that starts out as a droplet of "pure" seawater can have a subsequent history of being wet or almost dry, large or small, organic or inorganic, and spherical or irregular, all depending on the history of its passage through the atmosphere.

## 2. Interaction with Light

Aerosols interact with light by elastic scattering, absorption, and fluorescence. The scattering properties of aerosols are complicated functions of size, shape, surface condition, wavelength, polarization, and composition. There is no general mathematical description of scattering by aerosols, though the Mie theory of scattering by dielectric spheres is often used as an approximation. There are also some approximate theories of the angular dependence of forward scattering that can be used to obtain size information about single particles. Additional information about the scattering properties of aerosols is provided in Section VII-C.

Attenuation of light by aerosols is a complicated function of size, shape, wavelength, and composition. High concentrations produce strong attenuation at wavelengths comparable to or smaller than the characteristic dimensions of the constituent particles, but less at longer wavelengths. The structural features of the absorption spectra

33

are too broad and variable to be useful for identification or determination of composition.

Some aerosols fluoresce, generally in the visible and UV regions. The spectra are wide and lack features readily usable for identification. The principal effect of aerosol fluorescence is interference with attempts to measure gases by fluorescence.

C. Transmission of Optical Signals Through the Atmosphere

Water vapor and $CO_2$ have strong absorption bands in the infrared. In order to make remote measurements in this spectral region it will be necessary to operate in the atmospheric windows that are interspersed between these absorption bands. The difficulty of selecting the proper operating wavelength is illustated by Figure III-4. This shows that many of the absorption bands of pollutants lie in spectral regions where the atmosphere is opaque. It also shows that the spectra of many of the pollutants tend to overlap. In reality the situation is not as bad as it might appear from Figure III-4. High-resolution spectral data often
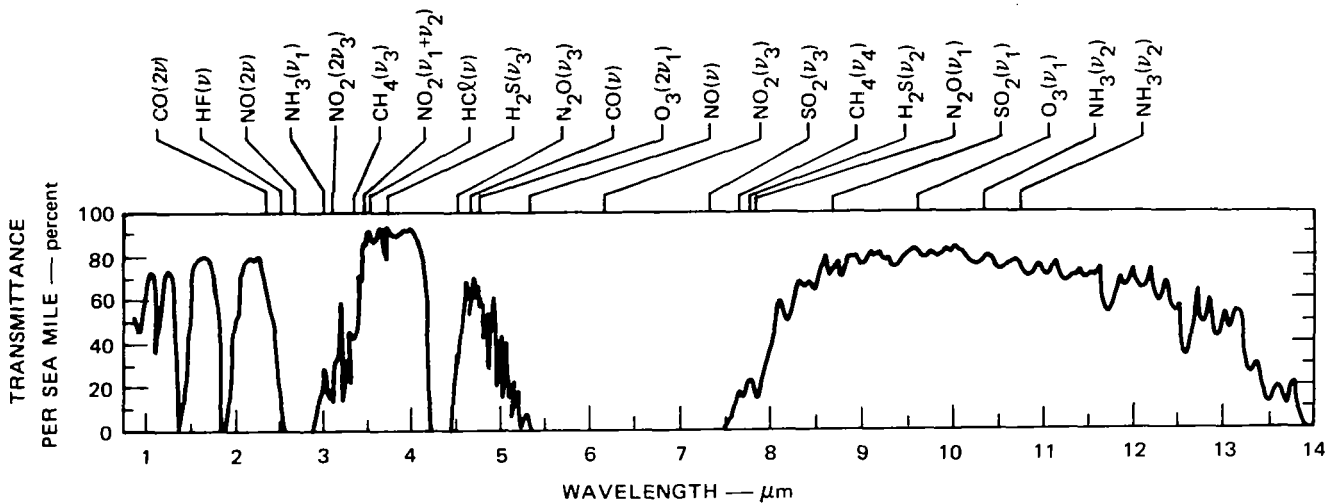


SOURCE: Kildal and Byer, 1971

FIGURE III-4    ATMOSPHERIC TRANSMITTANCE AND LOCATIONS OF POLLUTANT ABSORPTION BANDS

34

reveal narrow windows in regions where absorption seems to be severe at low resolution. For example, in Figure III-4 it can be noted that the fundamental NO band appears to coincide with a small window at about 5.3 μm. Figure III-5 shows this region at much higher resolution (and for a much shorter path length). Here it can be seen that the NO absorption peak at 5.330 μm indeed lies in a relatively good atmospheric transmission window. These data illustrate the reasons why the development of lidar for the remote measurement of air pollutants requires (1) use of the best available spectra to select potential spectral regions for the measurement of a given pollutant, (2) measurement of the atmospheric transmission coefficients and the pollutant absorption coefficients at resolutions at least as fine as the line widths of the lasers to be used for the measurement.
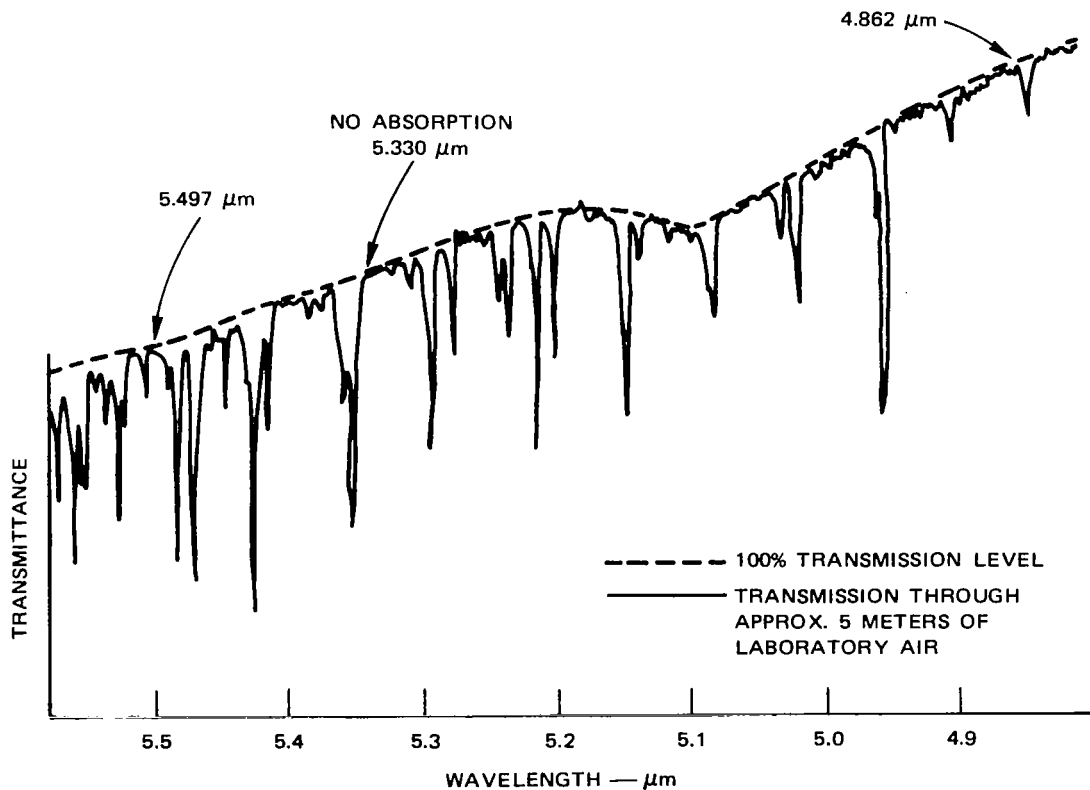


SOURCE: Hanst, 1971

FIGURE III-5    HIGH-RESOLUTION SPECTRUM OF AIR

## D. Other Atmospheric Properties

The other atmospheric properties of interest are elastic scattering of optical signals and of light from other sources (such as sunlight) by gases and aerosols; the transmission and scattering of light by clouds; and scintillation.

Scattering of optical signals by atmospheric gases and aerosols can be of significance in air-pollution measurements. The scattering cross sections of gases are small and vary as $\lambda^{-4}$ because the molecules are smaller than the wavelengths of interest. Backscattering produces measurable signals at considerable ranges on sensitive lidars. For example, signals are received from altitudes as high as 15 or 20 km with an SRI lidar operating at visible wavelengths, and measurements have been reported from altitudes of 75 or 80 km by the University of Jamaica in the West Indies (Kent et al., 1970) using a wavelength of 694 nm. Backscattering by gases is usually negligible at wavelengths longer than about 2 μm but is strong in the near-UV region where even small changes in wavelength can make a difference that must be taken into account in the differential-absorption measurement technique because of the $\lambda^{-4}$ dependence. Gases also scatter energy and thereby contribute to attenuation in both the illuminating beam and the return signal. The effects of this path loss are also wavelength-dependent and must be included in calculations.

Atmospheric scintillation, caused by turbulence produced by variable thermal effects, affects signal propagation and the interpretation of measurements. Scintillation is discussed in Section V-C.

# IV    MEASUREMENT METHODS AND PERFORMANCE ASSESSMENTS[*]

## A.    Methods of Remote Measurement

There are two classes of applicable methods for remote measurement of atmospheric pollutants.  The first involves backscattering in response to the incident illumination; the second uses absorption of the incident energy.  Table IV-1 shows the different categories within each class.

Elastically scattered energy has the same wavelength as the excitation.  It is customary to differentiate between the Rayleigh regime, in which the scattering objects are much smaller than the illuminating wavelength, and the Mie regime, in which object size is comparable to or larger than the wavelength.  These are usually referred to as "Rayleigh scattering" and "Mie scattering."  Neither is directly useful for measurement of gaseous pollutants, because of the absence of properties characteristic of particular gases.

Inelastic scattering includes ordinary fluorescence, resonant scattering, and Raman scattering.  Resonant scattering entails absorption at a wavelength corresponding to an electronic transition and re-emission at the same wavelength.  It is useful only for atomic species at very high altitudes.  Fluorescence usually refers to reradiation at one or more longer wavelengths and can apply to either atoms or molecules.

---

[*]This material was adapted from a previous SRI publication as the most efficient way of covering the topic for this report.

Table IV-1

PROCESSES FOR REMOTE MEASUREMENT

Backscattering

   1.  Elastic scattering

      a.  Rayleigh

      b.  Mie

   2.  Inelastic scattering

      a.  Resonant scattering

      b.  Fluorescence

      c.  Raman scattering

      d.  Resonant Raman scattering

Absorption

   1.  Double-ended, remote optical receiver

   2.  Double-ended, remote retroreflector[*]

   3.  Single-ended, remote topographical reflector

   4.  Single-ended, distributed scatters

[*]Considered to be double-ended because of need to emplace experimental equipment at a remote point.

Raman scattering results from excitation of either the vibrational-rotational or the pure rotational transitions. Re-emission takes place at lower frequencies[*] than the excitation and is offset from it by amounts that are characteristic of the scattering molecule and independent of the excitation wavelength. Simple molecules have only one or a

---

[*]The higher-frequency anti-Stokes lines are too weak to be considered for remote measurements.

very few significant Raman lines that provide simple and effective means for identification. However, complex molecules such as aldehydes and hydrocarbons have more complex spectra that make unique identification difficult. The resonant Raman effect, sometimes called "nearly resonant" Raman, is an enhancement of the Raman-scattering cross section that occurs as the incident wavelength is tuned near but not precisely on a sharp electronic transition peak. This effect is considered in detail in the Appendix.

All of the backscattering processes can provide range-resolved data by measurement of time delays in pulsed lidar systems. The system configuration for backscattering is illustrated in Figure IV-1.

In all of the absorption methods, observations are made at the wavelength of the incident radiation in absorption lines or bands characteristic of particular gases. Usually a simultaneous or sequential measurement is made at a nearby wavelength off the resonant absorption line to obviate the need for absolute-intensity measurements. This is called differential-absorption measurement. Conventional long-path spectroscopy measurements can be made either by using an optical receiver at the far end of the path or by using a reflector to return energy to a receiver collocated with the transmitter as shown in Figure IV-2. The alternative of using topographical targets as reflectors offers convenience at the expense of optical efficiency. These methods are capable only of measuring the total concentration, or column content, along the entire optical path, and cannot provide range-resolved data.

An absorption method based on backscattering from a continuous distribution of elastic scatterers can, however, provide range-resolved data. Elastic scattering can arise either from atmospheric gases or from naturally occurring particulates and aerosols. Since this method

$$\text{RANGE} = \frac{c\Delta t}{2}$$

$$\text{RANGE RESOLUTION} = \frac{c\tau}{2}$$

$$\text{ROUND-TRIP TIME DELAY} = \Delta\tau$$

$$\text{TRANSMITTED PULSE LENGTH} = \tau$$

SCATTERING MEDIUM

OPTICAL
DETECTOR

RECEIVING
TELESCOPE

BACKSCATTERED ENERGY

$\tau$

TRANSMITTED
PULSE

TRANSMITTING
TELESCOPE

DATA
SYSTEM

LASER
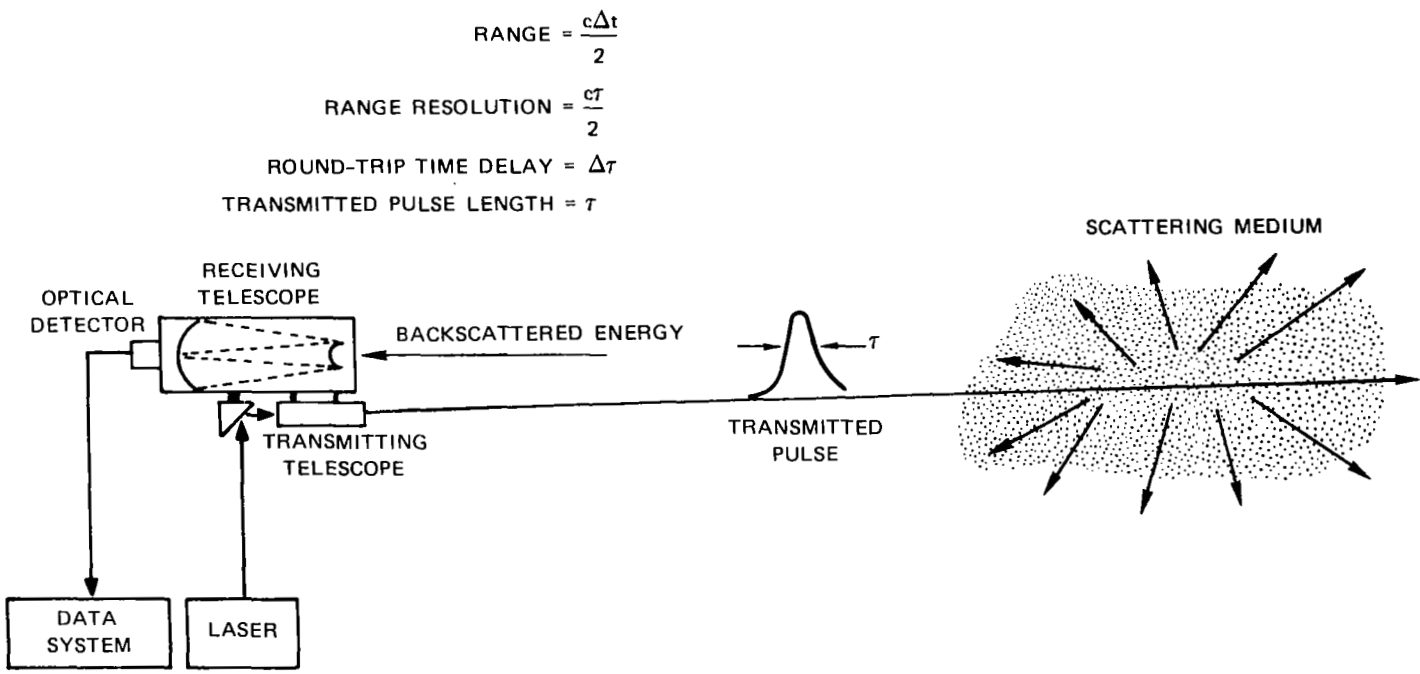
FIGURE IV-1   CONFIGURATION FOR REMOTE MEASUREMENT BY BACKSCATTERING

**(a) DOUBLE-ENDED MEASUREMENT**

**(b) SINGLE-ENDED MEASUREMENT**
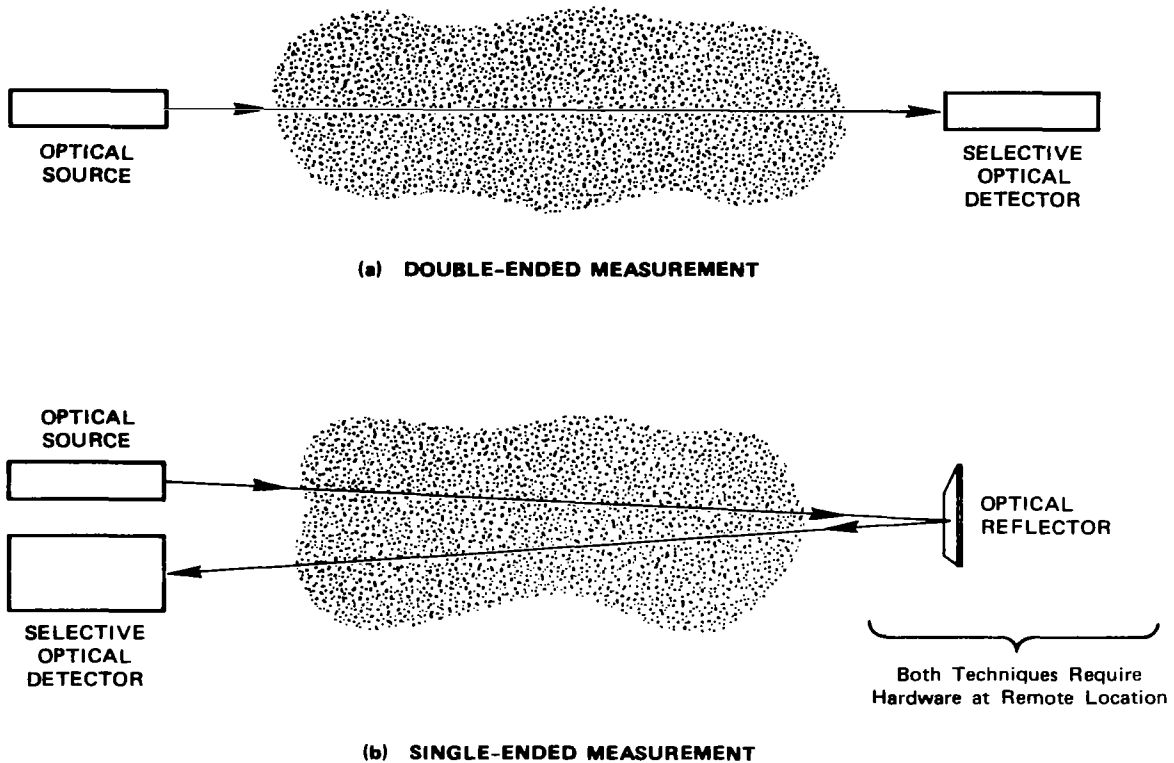
TA-654583-18

FIGURE IV-2   CONFIGURATIONS FOR LONG-PATH ABSORPTION MEASUREMENTS

is not as widely known as the others, a brief description seems in order. The method is illustrated in Figure IV-3. As shown in the inset, the pulsed laser transmitter emits signals at two wavelengths, labeled $\lambda_{on}$ and $\lambda_{off}$, corresponding to a peak and a trough, respectively, in the absorption spectrum of the pollutant of interest. Pulses arriving at the receiver at time $T_1$ will have traversed the path that includes Range Cell 1 but not Range Cell 2. Pulses arriving at time $T_2$ will have traversed the same path plus the increment represented by Range Cell 2. The amplitude difference between $T_1$ and $T_2$ is therefore proportional to the absorption increment produced by Range Cell 2, or, equivalently, Range Cell $\Delta$ if the centers of the other two range cells are considered as the sampling points. Quantitative determination of the amount of absorbing

41

RANGE CELL Δ

CONTINUOUSLY DISTRIBUTED
BACKSCATTERING MEDIUM

RANGE CELL 2

RANGE CELL 1

$\lambda_{off}, \lambda_{on}$

LASER
TRANSMITTER

$T_1$

$T_2$

OPTICAL
RECEIVER

ABSORPTION
LOSS

$\lambda_{on}$ $\lambda_{off}$
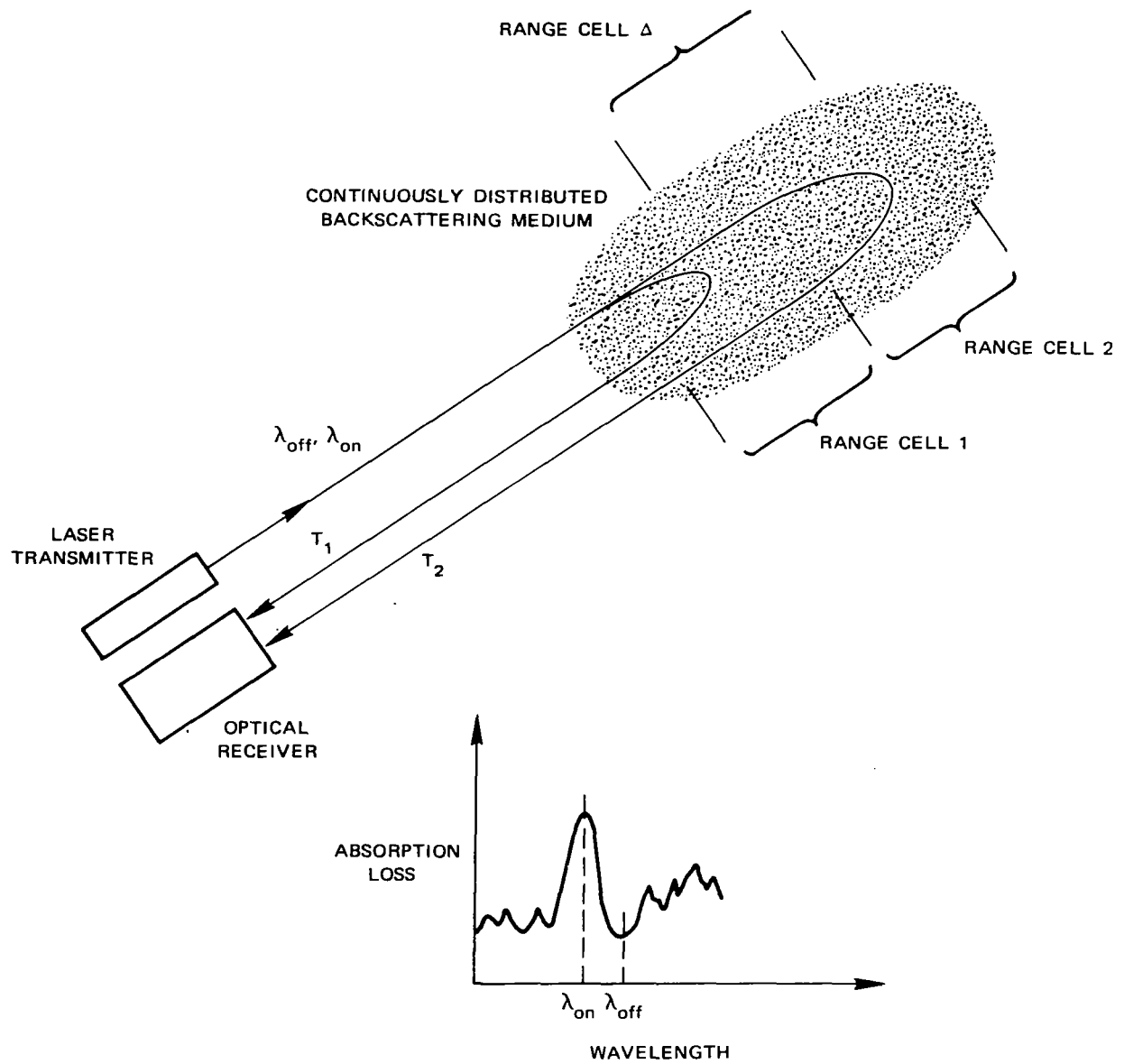
WAVELENGTH

TA-654583-16R

FIGURE IV-3    DIFFERENTIAL ABSORPTION USING DISTRIBUTED SCATTERERS

42

material in Range Cell $\Delta$ can be made by comparing the signal intensities at $\lambda_{on}$ and $\lambda_{off}$ with the known absorption losses at these two wavelengths for a calibrated gas sample. The result will be in units of concentration times the length of the range cell, usually expressed in terms of kilometer parts per million.

This technique was pioneered by Professor R. M. Schotland while at New York University,[*] first using a searchlight in the middle 1950s and later using thermally tuned crystal lasers (Schotland, 1964; Schotland et al., 1962 and 1964). However, the full potential of the method can be realized only with tunable laser sources, such as dye lasers and parametric oscillators.

B.  Comparisons of Double-Ended and Single-Ended Systems

  1.  Double-Ended Systems

For a given distance or range, double-ended systems for remote measurement of gases are inherently more sensitive than single-ended systems (Kildal and Byer, 1971; Byer, 1975). The primary reason is that the collection efficiency of a remotely located receiver and the reflection efficiency of a retroreflector are higher than the scattering efficiencies of either topographical reflectors or distributed scatterers.

This sensitivity advantage, however, is achieved at a great sacrifice in operational convenience and with loss of range-resolving capability. These disadvantages are deemed to outweigh the sensitivity advantage as explained below.

---

[*]Now with the Optics Sciences Center of the University of Arizona in Tucson.

### a.   Satellite-to-Satellite Configuration

This configuration offers some interesting possibilities for limb-scanning modes of operation, either with a transmitter in one satellite and a receiver on the other or with a lidar on one satellite and a passive retroreflector on the other.

For measurements of atmospheric constituents at ionospheric altitudes there are probably some distinct advantages for this configuration. Since Rayleigh and Mie scattering are extremely weak at these altitudes, the DIAL technique has little to offer. Resonant scattering is applicable only to a few atoms of interest. Hence, long-path absorption is the only available technique for many species. Thus, a satellite-to-satellite configuration may be advantageous in comparison with a single-ended system using echoes from clouds, terrestrial surfaces, or components of the lower atmosphere. On the other hand, the difficulty and technical complexity of acquisition and tracking, and of pointing with sufficient accuracy, the extremely narrow optical beams that would be required for this application are distinct disadvantages.

The study reported here was concerned with air pollutants and aerosols, which are found primarily in the troposphere and the stratosphere. Tropospheric measurements can be made with a satellite-to-satellite configuration and are being made from a single satellite using solar radiation. However, vertical resolution tends to be poor and interpretation of data from below the tropopause is not feasible at present. Limb scanning for measurement of stratospheric gases such as $O_3$, $NO_x$, chlorinated hydrocarbons (freons), and photochemical reaction products are interesting prospects that should probably be investigated, but observation time is used inefficiently because of the time lost when the beam is either intercepted by the earth or not traversing a region of interest.

The capabilities of single-ended active optical systems mounted on satellites and aircraft can be studied efficiently in parallel because of their many similarities. The satellite-to-satellite configuration requires a distinctly different analytical approach. Performance analyses for the latter configuration would have required a reduction of the effort on the single-ended studies that seemed more important.

On balance, it was concluded that the study effort should be concentrated on the single-ended satellite and aircraft cases, leaving the satellite-to-satellite configuration for possible future studies.

b.   Satellite-to-Ground Configuration

This configuration would require a large network of ground-based receivers or retroreflectors. Receivers capable of acquiring and tracking a satellite would be inordinately expensive. Moreover, since successive ground traces of a satellite at an altitude of 166 km are spaced by distances of the order of 1000 km (see Section VI-B-2), a single receiver could observe no more than one or two transits, which would provide a rather low data rate and poor coverage from each receiver site.

Retroreflectors can be relatively inexpensive and they could be deployed over large land areas at modest cost by use of air-drop techniques. Floating versions could be used at sea. However, their reflection efficiency would degrade with time in most climates unless they were periodically cleaned. It seems unlikely that the greater reflection efficiency or retroreflectors would be cost-effective in comparison with use of surface reflections, which is considered to be a single-ended operation.

## c. Ground-to-Satellite Configuration

A network of ground-based lidars observing one or more satellites equipped with retroreflectors would suffer from one of the serious disadvantages of the satellite-to-ground case--the wide spacing between successive orbits offers very poor coverage. The great distances to the satellite would also require nearly enough transmitter energy to provide a capability for range-resolved hemispheric coverage around the lidar site by using Mie scattering from atmospheric aerosols. Hence, the portion of satellite expenses allocated to pollution instrumentation could be expended more advantageously on a ground-based lidar.

## 2. Single-Ended Systems[*]

The several available techniques for remote measurement of gases have different advantages and disadvantages, and their sensitivity and suitability for air-pollution measurements vary widely. All except the differential-absorption technique were analyzed in detail in a recent paper by Kildal and Byer (1971). The differential-absorption method is analyzed in a paper by Byer and Garbuny (1973). Measures and Pilon (1972) have made a comparative study of fluorescence, Raman backscattering, and the differential-absorption technique for air-pollution measurements. These investigations have independently concluded that the performance potential of the differential-absorption technique is superior to that of any of the other methods. The reasons for this conclusion are elaborated in the above references, but it is worthwhile to review the subject briefly here.

---

[*] Some of the material presented here was taken from previous SRI publications. Adapting it to this section improved the efficiency of report preparation.

Some of the important differences among the various remote-measurement methods are shown in Table IV-2, which shows representative values of scattering and absorption cross sections and response times for the processes of interest.

Elastic scattering is not directly usable for remote measurement of gaseous air pollutants because of inadequate spectral selectivity, but the cross sections are of interest in connection with the intensity of backscattered energy for the differential-absorption technique.

The fluorescence cross sections are quite large at low pressures, but at atmospheric pressure collisional quenching reduces the effective cross sections by approximately five orders of magnitude. $NO_2$ fluoresces at visible wavelengths and $SO_2$, NO, and the ring hydrocarbons fluoresce in the near UV. However, aerosols and particulate matter normally occurring in polluted atmospheres also fluoresce in the same spectral regions as the pollution gases, so that masking and interference can present problems. Other gases, such as $N_2O$ and $H_2O$, do not fluoresce in spectral regions useful for remote probing.

The Raman cross sections are approximately six orders of magnitude below the quenched fluorescence cross sections. Therefore, the achievable range is quite small at pollutant concentrations of interest. The resonant Raman effect has often been proposed as a way around this difficulty. Indeed, if the resonant enhancement factor of $10^6$ reported for iodine vapor[*] by Fouche (1972) is found to apply to pollutants of interest, then resonant Raman will be a feasible technique under some conditions. However, there is no assurance that such large enhancements will be found for other molecules. In addition, the resonant Raman

---

[*] This value may be optimistic. See footnote for Table IV-2.

Table IV-2

REPRESENTATIVE CROSS SECTIONS AND LIFETIMES

| Process | Cross Section, $\sigma$ (cm$^2$) | Lifetime $\tau$ (s) | Typical Gases | Spectral Region |
|---|---|---|---|---|
| Elastic scattering<br>　Rayleigh<br>　Mie | $10^{-27}$<br>$10^{-21}$ to $10^{-24}$ | $10^{-18}$<br>$10^{-18}$ | $O_2$, $N_2$<br>Aerosols | Visible, near UV<br>IR to near UV |
| Fluorescence<br>　Atoms<br><br>　Molecules | $10^{-14}$ vacuum<br>$10^{-17}$ quenched<br>$10^{-18}$ vacuum<br>$10^{-23}$ quenched | $10^{-8}$ to $10^{-6}$<br><br>$10^{-8}$ to $10^{-1}$ | Hg, Na<br><br>$NO_2$, $SO_2$<br>$C_6H_6$, NO | UV, visible<br><br>Visible, near UV |
| Raman scattering | $10^{-30}$ | $10^{-12}$ to $10^{-15}$ | All molecules | All wavelengths |
| Resonant Raman scattering | $10^{-24}$* | $10^{-9}$ (?) | $I_2$, (others?) | Near UV |
| Absorption<br>　Atoms<br>　Molecules<br>　Molecules | $10^{-14}$<br>$10^{-18}$ to $10^{-21}$<br>$10^{-18}$ | | Hg, Na<br>All molecules<br>$SO_2$, $NO_2$,<br>$C_6H_6$, NO | UV, visible<br>IR<br>UV |

*A resonant enhancement of a factor of $10^6$ has been reported by Fouche (1972) for iodine vapor. At the Spring meeting of the Optical Society of America in New York (April 1972), H. J. Bernstein (National Research Council of Canada, Ottawa) reported an enhancement factor of $3 \times 10^2$ for iodine and similar values for $Cl_2$ and $Br_2$.

effect is important only for excitation near electronic transitions. Thus, of the pollution gases of interest only $NO_2$, $SO_2$, NO, $O_3$, and a few hydrocarbons could have enhanced cross sections. Moreover, since the resonant Raman enhancement occurs on the shoulder of the line profile and not at the peak (Penney and Silverstein, 1972), extremely precise control of the excitation wavelength would be required. This is undesirable at best in a field instrument, and may prove to be infeasible. In addition, the necessity of operating at the wavelength of a sharp absorption feature negates the principal advantage of a Raman lidar (the ability to measure all pollutants with a single transmitted wavelength) and forces the system configuration to become virtually identical with what is required for the more sensitive differential-absorption technique.

The differential-absorption technique suffers from none of the aforementioned difficulties. The cross sections are large, absorption cannot be collisionally quenched, and all the molecules of interest absorb in either the IR or the UV spectral region, or both.

Other problems can arise, however. Among these are coincidence of pollutant absorption lines with regions of strong atmospheric absorption,[*] spectral interferences from other pollutants or minor atmospheric constituents,[†] and failure to obtain a sufficiently large backscattered signal from aerosols at the longer IR wavelengths. In most instances these difficulties can be minimized by proper system design.

C.  Comparative Performances of Backscattering Technique

The performance capabilities of the measurement techniques that use backscattering are compared quantitatively in Figure IV-4, where

---

[*] This also applies to the other measurement techniques.
[†] This also applies to the other measurement techniques.
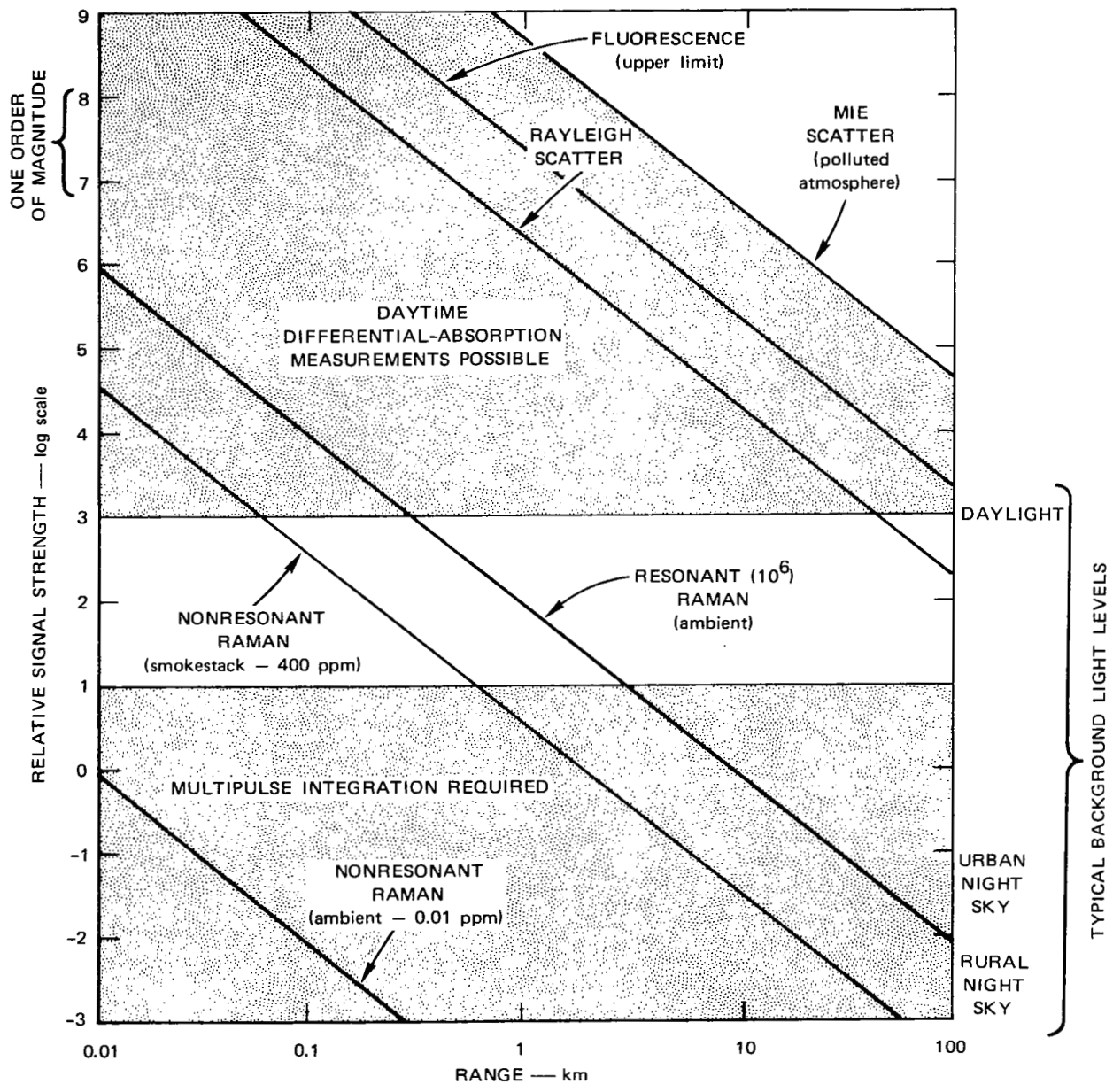
FIGURE IV-4   LIDAR PERFORMANCE CHART

50

received signal strength versus range is plotted for a number of differ-
ent conditions. To achieve meaningful comparisons in a single figure,
it is assumed that the instrumental capabilities for all the processes
to be compared are independent of wavelength and equivalent to the capa-
bilities of the existing SRI tunable dye lidar. This assumption is not
strictly valid in all details, but it permits a simple and meaningful
comparison of the relative merits of the several techniques. These
relationships were computed from the equation for received power for
the configuration shown in Figure IV-1, assuming that the receiving beam
is somewhat wider than the transmitted beam,

$$P_r = U_t \frac{A_r}{R^2} \frac{\lambda}{2h} \beta_{180} T_a^2 T_s \qquad \text{(IV-1)}$$

where

$P_r$ = Received signal strength, photons/s

$U_t$ = Transmitted energy = 0.25 J/pulse

$A_r$ = Effective area of optical receiver = 0.065 $m^2$

$R$ = Range, m

$\lambda$ = Wavelength $\approx$ 550 nm

$h$ = Planck's constant, $6.63 \times 10^{-34}$ J-s

$\beta_{180}$ = Volume backscatter coefficient ($m^{-1}$ $ster^{-1}$)

$T_a$ = Atmospheric transmittance = 0.5

$T_s$ = System efficiency = 0.5

Beamwidth = 0.5 mrad

Filter bandwidth = 1 nm (10 Å)

Pulse length = 300 ns.

Typically for Raman scattering $\beta_{180} \approx 7 \times 10^{-14}$ $m^{-1}$ $ster^{-1}$, and for Ray-
leigh scattering $\beta_{180} = 10^{-5}$ $m^{-1}$ $ster^{-1}$.

These numerical values are for an existing tunable dye lidar built by SRI. Thus, they are representative of current capabilities but do not reflect the performance that could be achieved with further effort. The purpose here is to compare the inherent sensitivities of the several backscattering methods. Detailed performance calculations are presented in Chapter VII.

Indicated on the right side of Figure IV-4 are typical background light levels for daylight, urban night sky, and rural night sky conditions. The lower shaded region indicates a returned signal level of less than one photoelectron per pulse per range cell. In this region integration of multiple pulses is not simply a technique for enhancing signal-to-noise ratio, it is a requirement for detecting even single photons. The lower portion of this region is therefore considered to be clearly infeasible for practical air-pollution measurements. The middle unshaded region is bounded on the top by the daylight background light level. Signal levels in this region indicate nighttime feasibility, and a marginal daylight capability with integration of multiple pulses required to obtain statistically meaningful results. Daylight operation is generally feasible in the portions of the graph that lie above the daylight background level.

All the backscattering processes can be represented by lines with signal strength varying as the inverse square of range for a given concentration of material. The line in the lower left corner is for the nonresonant Raman process[*] at a typical ambient concentration of 0.01 part per million (ppm). This clearly lies in the infeasible region. The next line up is for a concentration of 400 ppm, a typical value for

_____

[*] The $SO_2$ Raman cross section was used for this section, but the values are approximately the same for all the pollutants.

the smokestack of a coal-burning power plant. Daytime operation becomes marginal at a range of about 100 m, but nighttime operation would be feasible at several hundred meters with integration. The third line is for an assumed resonant Raman enhancement of a factor of $10^6$ for an ambient concentration of 0.01 ppm. For this condition, the single-pulse signal strength becomes comparable with the daylight background level at a range of only a few hundred meters.

The fourth line up is for Rayleigh scattering by atmospheric $N_2$ and $O_2$. This provides a very conservative lower limit (for the assumed wavelength, $\lambda \approx 550$ nm) of the amount of backscattered signal that will be obtained with the differential-absorption technique. Over continental land masses, the Mie scattering from naturally occurring aerosols would be at least an order of magnitude greater under clear conditions, and even greater than this in polluted air. Thus, the practical performance curve for the differential-absorption technique under the assumed conditions is determined by the Mie scattering line.

The next line shows an optimistic upper limit for fluorescence. It was obtained by using the UV fluorescence cross sections for NO (which probably has the largest fluorescence cross section of any gaseous pollutant), including the effects of collisional quenching.* The uppermost line is for a representative value of Mie scattering from aerosols in a polluted atmosphere.

Note that a material concentration level must be specified for each of the backscatter lines shown in Figure IV-4. This is necessary because the return-signal level is a direct function of the material concentration. This is not true for the differential-absorption technique because under the ambient conditions the return-signal amplitude is determined

---

\*
At sea level.

primarily by aerosol scattering and not by the concentration of the material being measured, although operating on a strong absorption line can negate this assertion. For this reason, the region in which daytime differential-absorption measurements can be made is shown as the upper shaded portion of the chart, and material concentrations are not shown on the chart.

D.    Minimum Measurable Concentrations

All lidar systems will be affected by noise and other error-producing mechanisms. One way of expressing these effects is to specify the minimum concentration of the desired material that can be measured in the presence of these mechanisms. This minimum detectable material concentration will, in general, be a function of the range or distance from the lidar system. The variation with range of minimum detectable material concentration will be different for differential absorption than it is for backscattering processes. An example of this difference is shown in Figure IV-5. For backscattering, the minimum measurable concentration varies as $1/R^2$ except at long ranges where energy absorption becomes important and at short ranges where the geometry of the optical system changes the slope of the curve. For differential absorption, the short-range performance is limited by the smallest power difference that can be detected by the system and the long-range performance is limited by insufficient optical signal compared to noise. For the example shown in Figure IV-5, the differential absorption system has better sensitivity for long ranges but poorer sensitivity for short ranges. This behavior occurs in many comparisons of the two techniques. Thus, it is not possible to describe which system is more sensitive unless the range behaviors are specified for both. These differences in behavior are the reasons why the two methods cannot be directly compared in Figure IV-4.
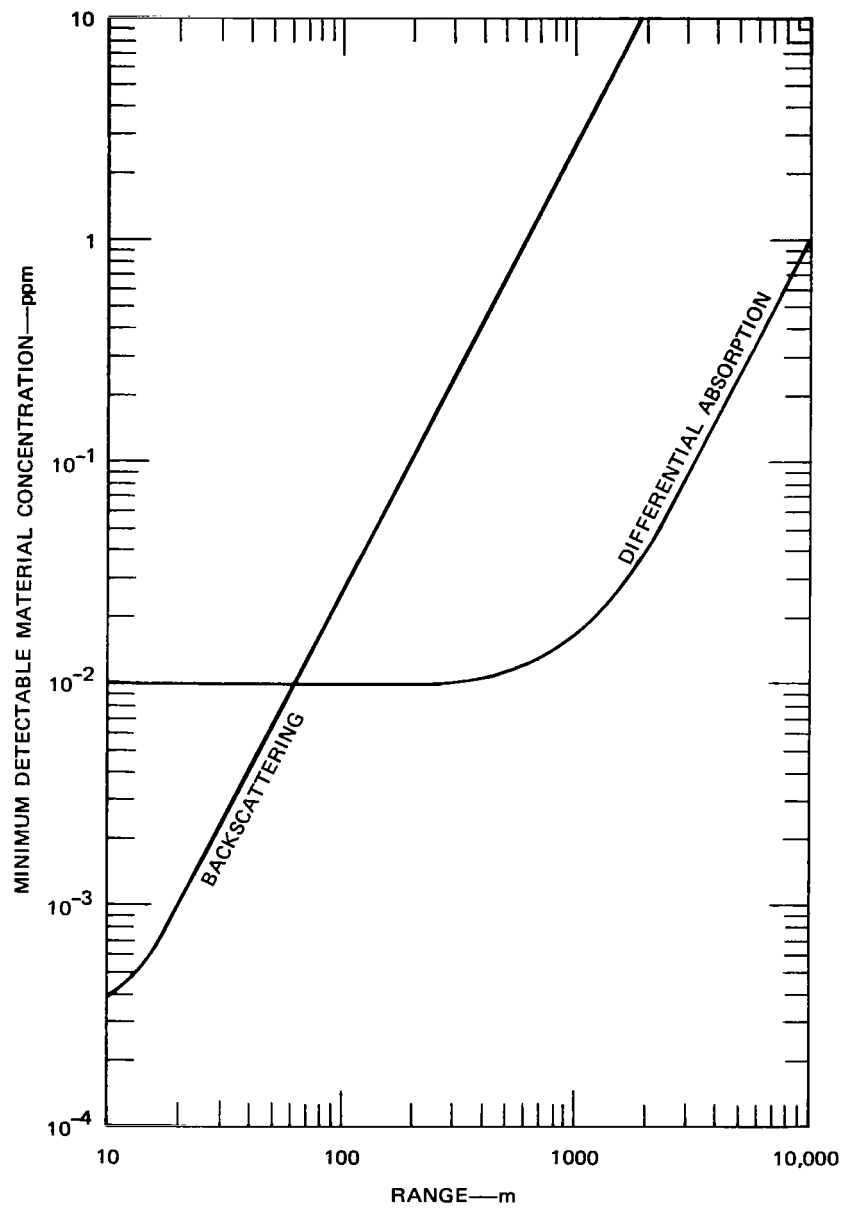
FIGURE IV-5   CAPABILITY COMPARISON FOR BACKSCATTERING AND DIFFERENTIAL-
ABSORPTION METHODS

The sensitivity in the region of relatively constant minimum detectable material concentration for the differential-absorption technique becomes a function of the differential-absorption coefficient of the gas to be measured once the minimum measurable difference signal of a lidar system is specified or determined. This dependence of the detection sensitivity on the differential-absorption coefficient is illustrated in Figure IV-6. This figure is based on a minimum measurable difference limit of 0.1 dB (2.3 percent) for a single pair of pulses. The differential-absorption coefficients for several gases having absorptions in the visible and UV spectral regions are shown in the upper row of labeled tick marks. The differential-absorption coefficients for those gases having absorptions in the IR spectral regions are shown in the lower row of tick marks. For example, $SO_2$ has a differential-absorption coefficient of approximately 17 $cm^{-1}$, yielding a detection sensitivity of 0.007 km-ppm, or 0.07 ppm with a range resolution of 100 m. This detection sensitivity may be increased as shown in Figure IV-6 by integrating multiple measurements. Note that for $NH_3$, NO, and $CO_2$ the detection sensitivity should be divided by 100. This is due to the large differential-absorption coefficient available for these materials, which would be off the scale of Figure IV-6 and which has been divided by 100 to allow plotting on that figure. With a 1-km range resolution, the detection-sensitivity scale will be the minimum detectable material concentration directly in parts/million. Under the assumed conditions it is possible to detect $SO_2$, $O_3$, NO, $NH_3$, $CO_2$, $CH_4$, CO, and $N_2O$ with a sensitivity of less than the typical ambient concentration of 10 parts per billion (ppb).

Recent experimental results (Grant, 1975 a,b) for UV and visible DIAL systems give detection sensitivities within approximately an order of magnitude of the results predicted in Figure IV-6. These results are for a general-purpose lidar apparatus and do not represent the results

56
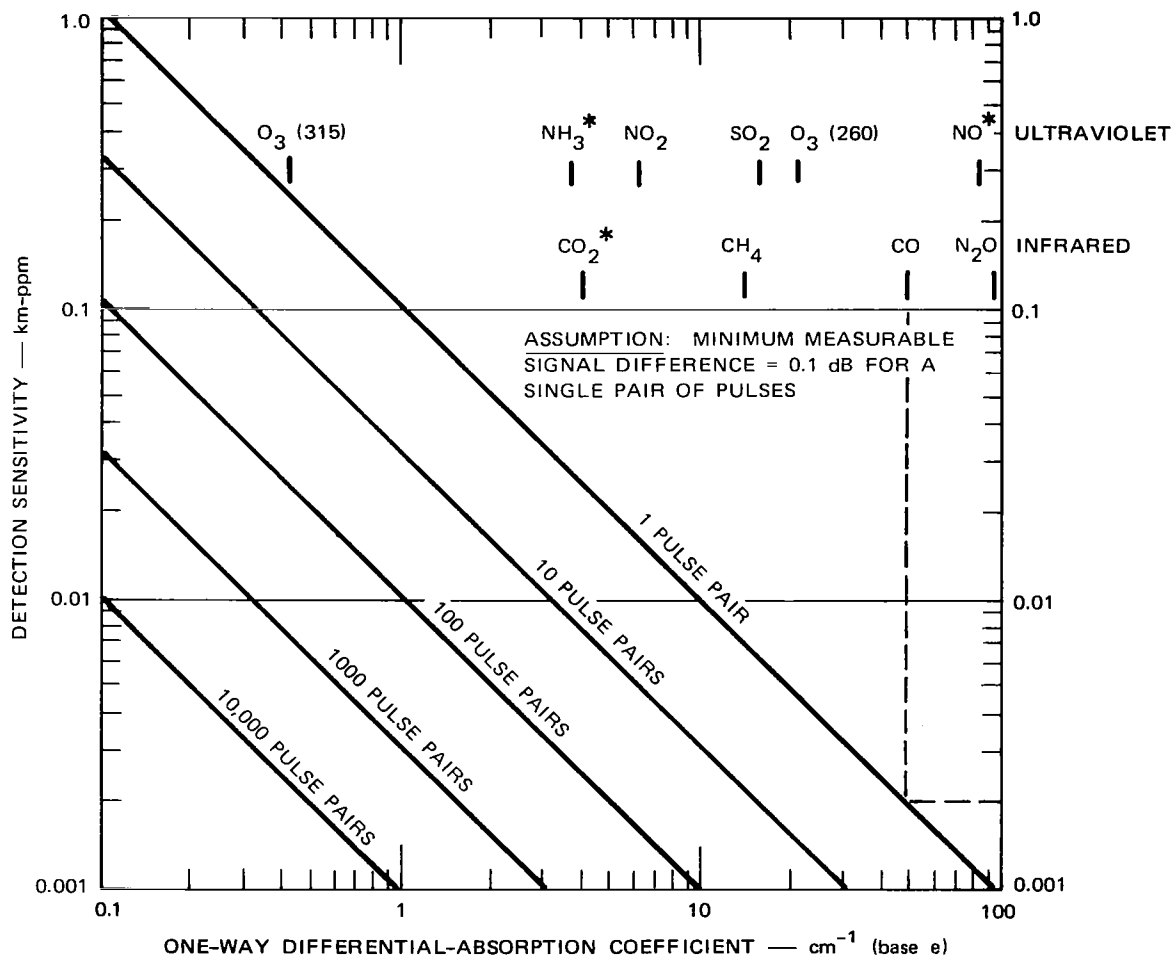
FIGURE IV-6   DETECTION SENSITIVITY vs DIFFERENTIAL-ABSORPTION COEFFICIENT

that could be achieved with an instrument specifically designed for field measurements of pollutants. The experimental detection sensitivities for $NO_2$, $SO_2$, and $O_3$ are 0.05, 0.06, and 0.075 km-ppm, respectively, at a range of approximately 300 m.

### E.    Column-Content Measurements

The comparisons of the previous sections have all been for systems that give range-resolved information. It is possible, particularly in the infrared, to obtain increased range for downward-looking systems by using (nondistributed) fixed reflectors such as the terrestrial surface, clouds, or retroreflectors. However, these fixed reflectors allow only column-content measurements to be made. A comparison of the relative lidar performance for column-content and range-resolved measurements is shown in Figure IV-7. Again, this figure is calculated for a system having a performance level approximating the present SRI dye lidar system. Its purpose is to show generally the comparative performance capabilities of column-content and range-resolved measurements. It should be noted that the performance difference between column-content and range-resolved measurements is greater in the infrared where the relative aerosol and Rayleigh returns are much lower than they are for the visible and UV spectral regions. The lines shown at the top of Figure IV-7 show typical altitude ranges for aircraft and satellites. The intersection of a vertical line for any altitude with any of the slanting lines gives the signal level that would be received by the lidar system under the selected conditions. For ground-based systems, the aerosol and Rayleigh returns would have to be modified for the vertical distributions of gases as shown by the curved dashed line below the Rayleigh line.
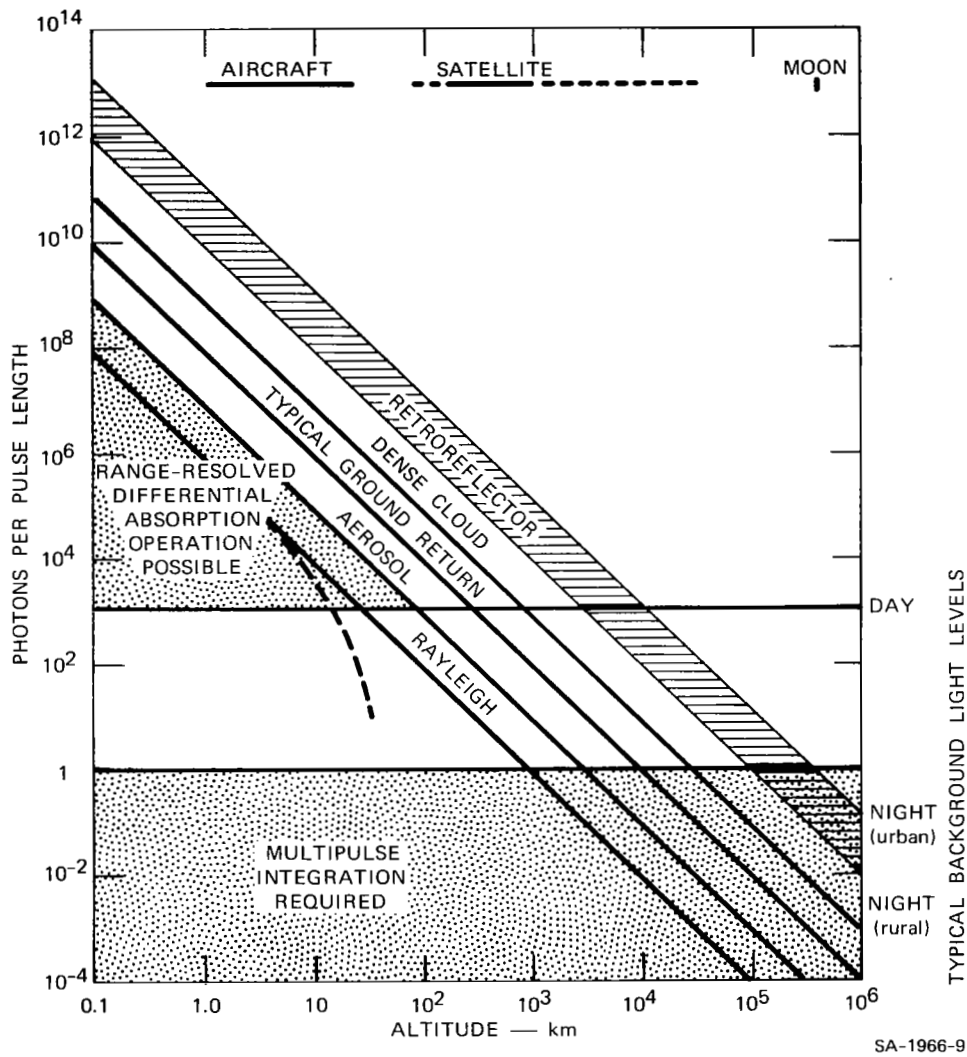
FIGURE IV-7    RELATIVE LIDAR PERFORMANCE FOR COLUMN-CONTENT AND RANGE-RESOLVED MEASUREMENTS

In Figure IV-7 the aerosol and Rayleigh return lines provide bounds for the range-resolved differential-absorption operation. The ground-return, dense-cloud, and retroreflector lines are for column-content measurements only, and give a rough indication of the increase in range that could be obtained by using these reflectors. The calculated improvement for retroreflectors involves additional assumptions about range, retroreflector area, and both transmitted and reflected-beam

59

divergences. For these reasons, the retroflector improvement is shown as a band rather than as a line to indicate that a range of performance improvements could be obtained. This band indicates the approximate performance improvement that may be obtained with a 10-cm$^2$ retroflector area, a 1-mrad transmitter beam, and a 0.1-mrad retroflector beam at a range of 1000 km.

## F.    A Note About the Volume Backscattering Coefficient

In deriving the lidar equation (Eq. (IV-1), the scattering medium is characterized by a volume backscattering coefficient, $\beta_{180}$. The concept of the volume backscatter coefficient as defined is no longer valid when the product $(\beta_{180})$ $c\tau/2$ approaches a value of $1/\pi$. The backscattering volume to which this coefficient applies is equal to the cross-sectional area of the beam times the resolution length of the system which is equal to half the transmitted pulse length, $c\tau/2$. It is assumed in the derivation that the scattering is uniform over this entire scattering volume. If this is the case, then the backscattered energy can be obtained by multiplying $\beta_{180}$ by the length of the resolution element in meters.

Note, however, that an increase in $\beta_{180}$ implies that the scattering medium is removing larger amounts of the transmitted energy from the beam through scattering at angles other than 180°. Thus, for large values of $\beta_{180}$ the beam may be significantly attenuated as it passes through one resolution length of the system, thus violating the original assumption of uniform scattering over the entire scattering volume. The extreme case occurs for a very dense scattering medium in which the beam cannot penetrate more than a small fraction of the pulse length into the medium before most of the transmitted energy is lost by scattering. This case closely approximates a reflecting plane surface, which is

characterized by a surface reflection coefficient rather than a volume backscattering coefficient.

The total energy scattered from any volume can never exceed that scattered by a plane surface of equal cross section having a reflection coefficient of unity. The two are equal when $\beta_{180}\, c\tau/2 = 2/\pi$. In the lidar equation, one may inadvertently assign a large $\beta_{180}$ to characterize a dense medium that scatters so strongly that the transmitted energy does not penetrate significantly into the medium. If the pulse length for the system is much longer than the penetration depth into the medium, the product of the required $\beta_{180}$ and the long pulse length could exceed $2/\pi$. This would indicate that more energy is scattered than is incident on the medium, which would violate energy conservation. This contradiction, which could result from misuse of the lidar equation, could not, of course, happen in the real world because the pulse would be strongly attenuated and energy would not be scattered uniformly over a path length comparable to the pulse length.

It is important, therefore, to examine the product $\beta_{180}\, c\tau/2$ for strongly scattering media to assure that this limiting condition is not being numerically exceeded. Alternatively, one may retain an attenuation coefficient that reflects the true attenuation caused by intense scattering. In digital-computer analysis of lidar returns, it may also be necessary to decrease the distance increments over which calculations are made in these strongly scattering media in order not to violate the condition indicated above on an incremental basis. By using either of these techniques, it is possible to ascertain the correct behavior of the scattering medium and thus correctly model the behavior of dense single-scattering media.

In practice, the inequality can be violated when very dense clouds are illuminated with pulses having durations in excess of approximately

61

0.5 μs.  However, the lidar equation ceases to be applicable because of
multiple-scattering effects at lower cloud densities than those that
would cause the inequality to be violated.


G.    Feasibility of Measuring Aerosol Properties

    Gas molecules in the atmosphere scatter light elastically just as
aerosols do.  Ground-based lidars operating at visible wavelengths
receive strong echoes from air molecules in the lower troposphere, and
it is not uncommon to detect molecular scattering from as high as 20 or
30 km.  The aerosols that are normally present in the atmosphere also
produce elastic scattering, and the backscattered signals from gases
and aerosols are indistinguishable without the use of polarization or
multiwavelength measurements.  Use of polarization and multiwavelength
techniques aids in the separation of the gaseous and particulate con-
tributions to a backscattered signal, but uncertainties, arising from
unknown particle-size distribution and polarization properties, will
often persist.  However, since the amount of scattering from a gas is
proportional to the density of the gas and depends in a known manner on
the lidar wavelength, the gaseous contribution to the total signal can
be computed if the lidar is calibrated, and if atmospheric pressure and
temperature and the round-trip attenuation are known.  Even if the lidar
is uncalibrated, an effective calibration can be accomplished if a layer
of negligible (or well-known) particulate scattering occurs within the
range from which lidar signals are analyzed.

    This procedure was first used by Fiocco and Grams (1964) in their
stratospheric aerosol studies, and it has become standard for virtually
all subsequent lidar investigations of the stratospheric aerosol.  The
scattering ratio, or ratio of total (molecular plus particulate) back-
scattering to molecular backscattering, is the fundamental result when

this procedure is employed. In the troposphere, where particulate extinction is frequently significant and unknown, this procedure is rarely applicable.

The importance of aerosols in meteorology, air pollution, weather modification, and the thermal balance of the earth-atmosphere system has generated considerable interest in measurements of the optical scattering properties of aerosols. Since the first lidar measurement of backscattering from tropospheric aerosols in 1963, similar observations have been made by many investigators and by now are considered to be routine. Such measurements can provide much useful information about movements of air masses and related phenomena where it is sufficient to detect the presence of aerosols, to observe the structures of distribution patterns, or to detect variations in concentration or mass distribution. The importance of this capability should not be minimized. However, the quantitative information content of lidar backscattering data about the number or mass concentration of aerosols and other physical properties is more difficult to evaluate. There are two reasons for this difficulty. In the first place, solving the lidar equation to obtain the atmospheric volume backscattering coefficient is difficult when attenuation is significant and aerosol properties are unknown or variable. In the second place, assuming that the volume backscattering coefficient can be obtained, it cannot easily be converted to mass or number because the volume backscattering coefficient of a collection of solid or liquid particles is a complex function of their distribution, wavelength, and concentration, and of the particle sizes, shapes, surface conditions, and real and imaginary components of the refractive index.

The general equations of radiative transfer that govern the passage of light through atmospheres of particles are known (Braslau and Dave, 1973), but exact solutions are virtually impossible to obtain. These

equations also require knowledge of the scattering of light by individual

particles, the properties of which are generally known poorly or not at

all. Thus, one is reduced to seeking approximate solutions and comparing

the results with various quantitative measurements to determine the degree

of validity of the approximations. The success of these efforts has

varied from rather poor to very good.

Extensive computations and many theoretical studies have been per-

formed on the scattering of light by atmospheres of particles, but the

majority of these have been based on spherical particles, the theoretical

cross section of which has been known since early in this century when

Mie (1908) published his theory of scattering from smooth dielectric

spheres.[*] It is possible to extend such calculations to distributions

of randomly oriented dielectric ellipsoids and discs, since the scatter-

ing cross sections of single particles having these shapes can be de-

scribed by known equations. Recently, scattering functions for randomly

oriented conducting wires have been determined. However, there is no

theoretical basis for believing that the detailed angular and polariza-

tion dependence of scattering by nonspherical aerosols can be reasonably

approximated by computations for such shapes. Also, there is no theo-

retical basis for computation of scattering from particles of other

shapes. Hence, use of approximations based on the Mie theory is the

best available computational alternative at present. For integrated

scattering properties (extinction, total scattered intensity, and so on)

associated with a polydispersion of particles, as occurs naturally, such

---

[*] The theory of scattering by a sphere is generally attributed to Mie,
since in 1908 he published a detailed account of the scattering of light
by suspensions of colloidal gold particles in liquids. In a review of
the history of the theory of scattering by spheres, Logan (1965) de-
scribes the important contributions by Clebsch, Love, Stokes, Rayleigh
and others in the latter half of the nineteenth century.

approximations are often useful and can be quite good (Collis and Uthe, 1972).

There is ample evidence that many aerosols are nonspherical. Dust, fine volcanic ash, ice crystals in cirrus clouds, snowflakes, salt crystals in maritime hazes, and smoke particles from forest fires and industrial operations are important sources of nonspherical particles. Cadle (1972) collected and analyzed samples of stratospheric aerosols and found large percentages that were nonspherical, although more recent measurements made in the CIAP* program have revealed few or no particles that are nonspherical at room temperatures. Many aerosols in polluted atmospheres are formed by absorption of foreign substances by water droplets; subsequent evaporation of the water leaves an agglomeration of residues having roughly spherical shapes but with wrinkled surfaces.

On the other hand, some aerosol components are either spherical or can be closely approximated by spheres. Small water droplets are good examples. Fly ash from smoke stacks is frequently composed of glasslike fuel residues that formed at temperatures above the melting point. Since surface tension is the dominant force in liquid droplets, many fly-ash particles are therefore approximately spherical† in shape. Thus, it can be expected that aerosols will range from collections of predominantly

---

*Climatic Impact Assessment Program, funded by the U.S. Department of Transportation. See Dynatrend (1973) and Russell, Viezee, and Hake (1973b). The question of the shape of stratospheric aerosol particles is evidently unresolved at present.

†Collected samples often contain cracked, hollow spherical shells. They probably are cracked during collection and subsequent handling. The scattering properties of hollow spheres might be quite different from the results of calculations based on the Mie theory for homogeneous spheres. The solution for concentric spheres of variable refractive index (Kerker, 1969) would be applicable in this case.

spherical particles to mixtures containing many distinctly nonspherical particles.

The effects of particle surface conditions on scattering from aerosols seem not to have been studied to any great extent. It is clear that surface modes of propagation are important in the Mie theory (see Collis and Uthe, 1972) which assumes smooth surfaces, and thus surface conditions must have effects on scattering. There is evidence that rough or wrinkled surfaces tend to interfere with surface modes of propagation and thereby damp out some resonance effects that are responsible for the large variations with frequency of backscattering cross sections of dielectric spheres. This effect probably improves the accuracy of the Mie theory approximation when averaged over a size distribution of particles with rough surfaces.

The other factors that enter the Mie theory explicitly are particle size relative to wavelength, and the real and imaginary parts of the complex index of refraction. It is also important to note the distinction between low concentrations of aerosols where the effects of multiple scattering can be neglected, and optically dense aerosols where multiple scattering cannot be ignored. Solution of the lidar equation when multiple scattering effects are significant is a difficult problem and the subject of current research. While progress in this area is being made, multiple scattering doubtless compounds an already difficult task.

The results of experiments to determine the validity of applying Mie theory to mixtures of nonspherical particles vary widely. Holland and Gagne (1970) injected an air stream laden with small silica particles into the scattering chamber of a recording polar nephelometer. The particles were extremely aspherical, having "flat plate-like shapes with irregular edges." The results clearly showed significant departures

66

from the Mie theory for backscattered intensity and for quantities sensi-
tive to polarization. For example, Mie theory predicts that for polarized
light the $F_{11}$ and $F_{22}$ elements of the scattering matrix are equal, but
the experiments yielded values of $F_{11}$ up to 3.5 times $F_{22}$. Moreover,
measured values of the matrix element $F_{12}$ had the opposite algebraic
sign from Mie theory prediction. The experiments also showed the exis-
tence of strong cross-polarized components at variance with the theory.
However, measured values of $F_{33}$ and $F_{22}$ agreed reasonably well with the
theory. The investigators also made a few runs with unpolarized light
that also generally agreed with the theory. Holland and Draper (1967)
performed similar measurements using a talc aerosol and unpolarized
light. The results showed reasonable agreement with Mie theory for
eight different wavelengths at scattering angles less than $120°$. At
larger scattering angles the theory overestimates the observed cross
sections substantially.

In general, it seems that the experiments with polarized light are
the ones that test the applicability of Mie theory to nonspherical
particles. The agreement with theory, when it occurs, is not unexpected.
Moreover, the agreement seems to improve when the collection of particles
produces an averaging effect over all or several of the controlling
parameters, as is the case for many naturally occurring aerosols. Collis
and Uthe (1972), among others, have had good success with this approach.
However, the sensitivity of the computed and measured cross sections to
scattering angle and refractive index in the vicinity of $\theta = 180°$ (the
backscattering case) requires further exploration to compare properly
experimental conclusions and theoretical predictions.

There is at least one case where the Mie theory is applicable and
in which it is possible to differentiate accurately between two types
of aerosol--namely, water droplets and ice crystals. Since surface

tension is the dominant force on suspended liquid droplets, they are spherical. The Mie theory shows that when multiple scattering can be neglected, the cross-polarized component of backscattering from dielectric spheres illuminated by plane-polarized radiation is zero because of spherical symmetry. Backscattered energy from ice crystals and other particles of irregular shape contains components of all polarizations. Hence, measurement of the depolarization ratio can be used to differentiate between spheres and irregular shapes. Component identification is possible, however, only when one has a priori knowledge that correlates shape with composition, as in clouds that contain only liquid droplets or ice crystals. Again, the occurrence of multiple scattering, which also leads to depolarization, can complicate the intepretation of polarization measurements. However, the dependence of depolarization on cloud penetration depth (Pal and Carswell, 1973) offers promise as a means of separating particle shape effects from multiple scattering effects.

For an optically thin aerosol assumed to contain spherical particles of uniform composition, both the backscattered energy and the absorbed energy can be determined analytically if the particle-size distribution and the index of refraction, $n = n_{re} - in_{im}$, are known, where the subscripts re and im indicate real and imaginary parts, respectively. The imaginary part accounts for absorption. The analytical approach can be found in many standard references. (See, for example, Van de Hulst, 1957; Deirmendjian, 1969; and Kerker, 1969.) By adjusting the size-distribution function and both components of the refractive index, it is possible to approximate the scattering properties of a variety of aerosols, though the fidelity is not always good. In this manner it is possible to construct models for fogs, drizzle, and a variety of clouds and hazes. Many examples are given by Deirmendjian (1969). These models are generally based on measured or theoretically estimated size distributions together with experimental values for at least the real part of

the refractive index. Frequently the value of $n_{im}$ is varied to obtain a fit between measured and calculated values of the scattering function. Experimental determination of $n_{im}$ and the size distribution are often subject to sizable errors, and it is sometimes difficult to assure that scattering measurements are made on the same kind of aerosol that was analyzed. Despite these difficulties and the existence of some significant discrepancies, many useful results have been obtained.

As shown by Collis et al. (1973), consideration of some dozen published theoretical investigations of the dependence of aerosol optical properties on their physical properties indicate that the uncertainties lie within reasonable bounds for many purposes. For example, inferences of mass or number concentration or extinction coefficient for a given backscattering coefficient generally vary by less than a factor of two when changes are made in the assumed particle size distribution, or by a factor of three for changes of the assumed refractive index. Larger changes (to a factor of 3.7 for size distribution and 10 for refractive index) occur only in isolated extreme cases. Similarly, in the case of particle shape a factor of 1.5 has been ascribed to small changes, with a factor of 10 being noted as a result of laboratory measurements of the differences in near-backscattering from the extreme cases of spheres and plates. The same reference (Collis et al., 1973) cites the results of some seven experimental investigations relating backscatter coefficient to extinction coefficient or to number or mass concentration. These investigations compare observations and theoretical determinations based upon reasonable assumptions. The results range from excellent to cases where differences amount to a factor of 3 or so.

In the partial or total absence of any other information, uncertainties of the order noted in lidar-derived data must thus be considered as very reasonable.

An interesting approach to the scattering properties of aerosols was recently developed by Grams et al. (1973). They determined the size distribution of an aerosol composed of soil particles by using an aerosol impactor or filter sampler. The value of the real part of the refractive index was determined by conventional microscopic techniques. Observing that the angular dependence of scattering by particles is appreciably affected by the absorption parameter $n_{im}$, polar scattering diagrams were measured and compared with Mie scattering calculations for the observed size distribution and the measured value of $n_{re}$. The value of $n_{im}$ that provided the best fit between measured and calculated scattering diagrams was interpreted as the best estimate for the true value of $n_{im}$ or, alternatively, of $n_{im}$ for an equivalent distribution of spheres with scattering properties equal to those of the measured particles. In some cases the calculated and measured curves fitted reasonably well. In others there were notable discrepancies. The experimental apparatus did not permit angular scattering measurements at 180°, the value for backscattering. By making backscattering measurements, it may be possible that this type of approach will lead to methods for relating backscattering properties of an aerosol to measurable characteristics of the constituents.

Predicting the scattering properties of an aerosol that can be described and measured is quite a different problem from inferring the characteristics of an unknown aerosol from measured values of the backscattering coefficient. Even if it can be safely assumed that the aerosol is composed of smooth spherical particles of uniform composition, one is faced with determining the size distribution and both $n_{re}$ and $n_{im}$ from a single measurement—viz., the magnitude of the backscattered energy. Clearly this is impossible unless there is some independent basis for quantitative information about two of the three properties. The backscattering coefficient seems to be particularly sensitive to

the value of $n_{im}$, which is difficult to determine even when one has an aerosol sample to measure. If, however, one is mainly interested in the backscattering and absorption properties of an aerosol layer as, for example, in climate studies, it is possible that these details can be ignored in favor of integrated layer properties.

It has often been suggested that a series of backscattering measurements taken at different wavelengths might reveal something about the size distribution, but so far very limited results (see, for example, Russell, Viezee, and Hake, 1973a) have been achieved along these lines with lidar data. However, successful inversions of multiwavelength radiometric data (for example, Yamamoto and Tanaka, 1969; Uthe and Russell, 1973) where more wavelengths are readily available have been accomplished and provide encouragement that lidar measurements may be successfully inverted in the future.

It seems worthwhile at this point to draw a distinction between tropospheric and stratospheric aerosols. The former are highly variable in composition so that it is difficult to characterize them and to correlate optical and physical properties. They are also highly variable in time and space. The characteristics and the effects of tropospheric aerosols are of greatest significance on local and regional, rather than global, scales. However, the data rate required to provide enough data points from a satellite to be useful on a local and regional basis is prohibitively high (see Section VI-B). Hence, aircraft rather than satellites are the more appropriate vehicles for making lidar measurements of tropospheric aerosols. Using lidar alone, extremely useful data can be gathered about the movement of air masses, the distribution and structure of particulate concentrations, the relative concentrations of aerosols, and similar information of importance to meteorology, air-pollution research, and air-pollution control. It seems likely that future research along the lines discussed by Grams et al. (1973) will

reveal how complementary data from other sources on the physical proper-
ties of tropospheric aerosols can be used to convert measured back-
scattering data into quantitative information on number or mass concen-
tration of particulate material, extinction coefficient, and scattering
coefficients for angles other than 180° and at wavelengths different
from the one(s) used to make the lidar measurements. Thus, despite the
limitations and uncertainties discussed above, airborne lidar (and also
groundbased lidar, for that matter) can now provide a wealth of useful
information about tropospheric aerosols, and the prospects are good that
further research will lead to results that are more quantitative than
those now available.

The capabilities and prospects for the stratospheric aerosols are
even more promising. The few ground-based lidar and airborne-sampling
measurements that have been made strongly suggest that the physical
properties of the stratospheric aerosol are stable over long periods of
time and that the variability of particle concentration occurs over
space and time scales that are compatible with data rates that can be
achieved with satellite-borne lidars. Even if the results could be
interpreted no more quantitatively or accurately than is now possible
for lidar measurements of tropospheric aerosols, the value of lidar ob-
servations carried out on a global scale over extended periods of time
would be very great. The sample frequency and spatial resolution could
be many orders of magnitude coarser than that needed for tropospheric
applications and still provide valuable data.

The lack of data about the stratospheric aerosols became so apparent
in consideration of the SST program that the Department of Transportation
established the CIAP. It is noteworthy that this program, which is
energetically pursuing the most intensive investigation to date of the
stratosphere, is only able to produce limited and relatively isolated

data on the stratospheric particulate content. Using lidar and in-situ aircraft and balloon-borne sampling, information has been gained on a coordinated basis but with a density in space and time that is so thin that it makes the lidar observations alone significant and relatively comprehensive, few and far between though the observations are. If such lidar observations, now carried out at two or three sites on a sporadic or at best monthly basis, could be extended to any substantial degree, a great advance would surely be made in characterizing the global and seasonal variations in the distribution of the stratosphere particulate content.

Even if only very gross horizontal and vertical resolution were possible, and perhaps only at night, lidar observations extended to a truly global scale by use of a satellite would be quite valuable even if the data rate limited observations to samples made at spatial inter-vals of many tens, or even hundreds of kilometers. The potential that such a capability would have, and indications of the form such data could take, is therefore offered in the following discussion of current lidar observation of stratospheric aerosols.

In support of the CIAP, a limited program of observations is being carried out by several groups. In addition to three groups operating lidars from fixed sites at the surface (NASA-Langley, NCAR, and SRI) a series of airborne lidar observations have been made to explore spatial variations in the stratospheric particulate layers on a continuous basis. The results of these observations to date have only been reported in a preliminary form (Schuster, Fernald, and Frush, 1973; Melfi, 1973; Dynatrend, 1973; Viezee, Hake, and Russell, 1973; and Russell, Viezee, and Hake, 1973a and b; and Russell et al. 1975). Such observations complement many earlier lidar observations that have been carried out since 1963 (Grams and Fiocco, 1967; Kent and Wright, 1970; Hirono et al., 1972; Gambling and Bartusek, 1972; Grams et al., 1973). In fact, lidar

data form one of the best sources of information on the stratospheric aerosol, particularly the so-called Junge layer at some 20 km altitude. For example the layer is known from lidar data to have decreased substantially (by approximately a factor of 10) in backscattering intensity (and hence, by inference, in mass concentration) since 1963 or 1964. Other valuable inferences as to the nature of the layer can now be made on the basis of lidar observations currently being taken with a density of coverage in time and altitude that would have been prohibitively expensive to provide using in-situ samplers.

Even without the auxiliary data or assumptions necessary to convert lidar data to absolute number or mass concentrations, the lidar data provide direct information on stratospheric aerosol content, given the reasonable assumption that particle size distributions and refractive properties do not vary in a capricious manner over large ranges from height to height, or within continuous layers from observation to observation. The profiles of scattering ratio and aerosol backscattering coefficient thus immediately reveal the presence, altitude, and variability (in space and time) of stratospheric aerosol layers.

As such, they can provide a valuable phenomenological basis for modeling and other studies that attempt to describe the dynamic, radiative, physical, and chemical processes responsible for natural and manmade changes in the stratosphere.

Even more encouraging results are in prospect for lidar measurements of stratospheric aerosols. The latest report from SRI in the CIAP series (Russell et al., 1975) presents results that show excellent agreement between mass concentrations determined directly by airborne sampling and those determined indirectly by lidar observations together with measured properties of samples taken from the stratosphere. Specifically, results obtained from a daytime overflight of a sampling aircraft were

compared with lidar observations made during the following night. The samples were analyzed for nonvolatile mass concentration and chemical composition. The results showed that the aerosol particles were droplets of a concentrated sulfuric-acid-and-water solution. Combining the aircraft-measured mass of sulfate ion with an estimate of ambient humidity resulted in a droplet mass concentration of $(9.8 \pm 1.8) \times 10^{-14}$ g/cm$^3$. Using an index of refraction based on the composition of the droplets, together with a realistic assumed size distribution of spherical particles, the lidar-derived value of mass concentration was $(9.4 \pm 2.3) \times 10^{-14}$ g/cm$^3$. The agreement between the two values is excellent. The lidar-inferred result is insensitive to assumed size distribution but quite sensitive to assumed refractive index. It is thus significant that the refractive index of the sample chemical composition produced such good agreement. It is also noteworthy that a near-cancellation of refractive index and density effects makes the lidar measurement of mass nearly independent of ambient humidity, whereas the aircraft-inferred value has a significant dependence on humidity (i.e., on acid-water solution density).

The effect of particle shape on the results is uncertain. If the droplets are in the liquid phase they are surely spheres. Thus, the freezing point of the sulfuric-acid solution is important. One tabulation shows the freezing point to be a sensitive function of specific gravity and pressure. It is therefore difficult at this time to tell whether the particles are liquid or solid in the stratosphere. However, the high viscosity of concentrated sulfuric acid leads to the expectation that even if the particles are solid (frozen) they will be amorphous rather than crystalline and therefore approximately spherical.

Further effort is evidently required, but it seems likely that the ambient stratospheric aerosols are sufficiently simple in composition and structure that the optical properties of interest can be determined

from measurable physical properties. However, the effects of large in-
jections of material from volcanic eruptions, such as those that have
occurred in October of 1974, must be considered. These effects would
probably complicate the quantitative interpretation of lidar returns,
but the returns themselves would still be valuable in monitoring the
dispersion and transformations of such an injection.

## H.    Cloud Measurements from Satellites

The possibilities for measuring cloud and atmospheric properties
with satellite-based lidar were studied in detail by W. E. Evens et al.
(1966) at SRI under an earlier NASA contract. This study emphasized
measurement of the height and density of cirrus clouds because the struc-
ture and circulation of cirrus clouds are good indicators of other mete-
orological conditions, especially large-scale circulation features such
as cyclones and jet streams. Also, even very low-density cirrus clouds
are capable of causing errors of several degrees in radiometric tempera-
ture measurements from space.

The satellite altitudes considered in the referenced study were in
the range from 1000 km to 1500 km. The principal lidar parameters used
in the study were a transmitted energy level of one joule per pulse and
a receiver aperture area of 1 $m^2$. The report concluded that it would be
barely possible to measure properties of low-density cirrus clouds even
at night because of excessive background light, and that reasonable
amounts of power would provide routine height and density data only for
cirrus clouds of greater density.

Measurement of atmospheric composition, density, or temperature
was found to require several orders of magnitude more power than was
likely to be feasible in satellites during the post-1966 decade. The
analysis indicated that detectable signals would be produced by reflections

76

from the terrestrial surface in the absence of clouds, but that atmospheric scattering would be very weak.

The principal differences between the work reported here and the earlier study **are satellite altitudes** (166 km versus 1000 km to 1500 km) and the far greater payloads that are possible with satellites in the class of the Space Shuttle. The altitude difference alone accounts for a sensitivity improvement of nearly two orders of magnitude for the lower altitude.

The heights of cirrus clouds can be measured when the clouds are sufficiently dense to provide detectable amounts of backscattered energy. The optical depth of cirrus clouds is also measurable by observing the rate of attenuation as the lidar signal propagates through the cloud. These measurements have often been made by ground-based lidars. A tunable transmitter is not required.

Satellite photographs are regularly used to measure the movement of cloud formations and weather patterns by observing successive locations of distinctive features. However, photographs can only display two-dimensional variations in scattered solar energy. A satellite-based lidar could add a third dimension by measuring the topside height of the cloud cover during both daylight and darkness. This would provide richer structural detail, which would be useful in plotting cloud movements in the daytime and would provide a nighttime capability that is now lacking.

The lidar characteristics required for cloud measurements from an altitude of 166 km, and the results of performance calculations, are presented in Section VI-D where it is shown that single-pulse measurements are possible with state-of-the-art lidar equipment. However, it is shown in Section VI-B that pulse rates of 22 to 38 Hz are required for a 20-km data grid from an altitude of 166 km. The rates increase to 350 to 611 pps

77

for a 5-km data grid. It seems unlikely that a 20-km data grid would be useful for cloud measurements. The 5-km grid, which is marginal at best, would be technically difficult to achieve. The relative advantages of active and passive systems, including accuracy and spatial resolution, should be carefully compared to determine whether the advantages of active systems are sufficient to warrant their use for cloud measurements from satellites.

I.    Other Possible Uses of the Scattering Ratio

The scattering ratio is simple in concept but there are difficulties in application. A principal one stems from the fact that molecular scattering depends on temperature and pressure, so that normal atmospheric temperature variations can be mistaken for gradients in aerosol concentration, and vice versa. Apart from this problem, however, the ratio could, in principle, be used as an indicator of aerosol content and provide a means of observing structure and concentration gradients in the aerosol. Since aerosols follow the movements of air masses, a satellite-based lidar could, in principle, measure the global circulation of clear-air masses by following the motion of distinctive structural features in the scattering ratio in much the same fashion as is now done using cloud photographs.

There are two prospective problems with this application that make evaluation difficult, apart from the uncertainty of distinguishing between transitory thermal effects and aerosol signals. It is explained in Section VI-B that pulse-repetition rates of several hundred per second are required to achieve a grid size of 5 km for data samples. It is unlikely that such high rates will be feasible at the required energy levels. Pulse rates of 20 to 40 Hz are required for a grid size of 20 km, a range of values that is more nearly feasible. It is uncertain whether a grid as coarse as 20 km would contain any concentration gradients or

structural patterns that could be recognized and followed. It will probably be necessary to try the experiment from a satellite in order to determine if it can be done.

The other difficulty stems from the fact that at midlatitudes a single satellite observes a given portion of the terrestrial surface only once in approximately 12 hours. It is not deemed likely that structural features of an aerosol backscattering pattern are stable enough to be identifiable over periods of 12 hours and longer.

The question has also been raised as to the usefulness of the scattering ratio in determining the effect of aerosols on the thermal balance of the earth-atmosphere system. This thermal balance is incompletely understood because of the complexity of the radiative transfer equations that describe all the interacting factors. There are several different mathematical models based on varying levels of approximation (see Grams et al., 1973). Aerosols comprise only part of the problem, but their major effects are important:

(1) To increase the amount of solar energy scattered into space.

(2) To absorb solar energy and reradiate a portion of it toward the earth.

(3) To reflect, or to absorb and reradiate, energy radiated by the earth.

Quantitative estimates of these effects require different levels of detailed information about the absorption and scattering properties of particles. The most direct relationship between lidar observables and the thermal balance is provided by the simple models of the earth-atmosphere system, which use the ratio of hemispheric backscatter, $\beta_H$, to absorption as a key parameter. Since lidar only measures the component of energy backscattered toward the lidar, $\beta_{180}$, the relationship between $\beta_H$ and $\beta_{180}$ must be determined before lidar data can be used

quantitatively. As noted earlier, this relationship is affected by the physical properties of the particles, and sometimes the dependence is critical. The needed relationship can be established for any aerosol having stable physical properties by taking samples and measuring the so-called phase diagram, the angular scattering pattern.

The complex atmospheric models require more detailed information about the angular dependence of scattering. However, for aerosols with stable physical properties it should still be possible to measure the phase diagrams of samples to relate lidar observables to the parameters used in the models.

Although the scattering ratio as measured by lidar only provides information about the spatial distribution and variability of an aerosol, it is precisely these quantities that are needed for both simple and complex models (once the scattering properties of the aerosols have been determined) to obtain quantitative estimates of the thermal balance. Moreover, these data are needed on a global basis. The number of ground stations required for adequate density of data points would be prohibitively expensive, but satellites and high-altitude aircraft could probably provide the requisite data at reasonable cost.

For the simple models, additional effort is needed to study the relationship between $\beta_H$ and $\beta_{180}$. It is known that $\beta_{180}$ is strongly dependent on $n_{im}$, the absorption term in the complex index of refraction. However, the scattering properties of the entire back hemisphere are similarly affected by $n_{im}$, so the ratio $\beta_H/\beta_{180}$ may be reasonably constant. More effort is needed to find out whether this ratio is critically dependent on the size distribution and other physical properties of aerosols.

Insofar as stratospheric aerosols are concerned, recent sampling data (see Russell et al., 1973b) found the aerosol to be sulfuric acid,

80

either frozen or as supercooled liquid droplets. In either case, $n_{im} = 0$ for visible wavelengths (Neuman, 1973). If this initial result is confirmed by further measurements, the necessary relationships between scattering properties and lidar observables will have been established, at least for the present. (Injection of dust into the stratosphere by future volcanic eruptions would perhaps alter the composition of the layer.)

It should be noted that the effects of aerosols on the thermal balance depend not only on the scattering properties of the particles but also on the absorption characteristics. Lidar is perhaps not the best means of measuring absorption since depletion of energy from the transmitted beam is caused by both scattering and absorption. However, if the scattering properties can be determined by other means, and if the aerosol is optically thin so that multiple scattering can be ignored and certain simplifying assumptions become valid (see Collis and Uthe, 1972), then the lidar data can also provide a measurement of absorption. If there is no absorption, as seems to be the case for the stratospheric aerosol at present, the lidar data alone will suffice once the scattering properties of the layer have been determined with adequate accuracy.

In many simple models the importance of aerosol layers on radiative transfer is considered in terms of the macroscopic effects of the layer as a whole. Such effects are assessed from limited knowledge of the detailed physical properties of the aerosols, or by using limited measurements or assumptions that determine the net or combined effects of many variables at the point of measurement. A common feature of these simple models is that the ratio of hemispheric backscattering to absorption for an aerosol layer is a critical parameter in determining whether the net effect of the layer will be heating or cooling. Lidar observations of direct (180°) backscatter could provide a useful input to these

models, but studies of the relationship between direct and hemispheric backscattering are required before the true applicability of the lidar measurements can be ascertained.

Since all radiative effects can be related completely by classical theory, considerable reliance has also been placed on the microscopic approach. Much attention has been devoted to the derivation of the required parameters by applying basic Mie theory, in various forms, to descriptions of an aerosol in terms of its particle-size distribution and refractive properties.

In considering the role of lidar measurements in aerosol climatic studies, it is important to recognize that such measurements do not lend themselves directly to the microscopic or complex numerical approach. The information that they provide is no less (and may well be more) valid in the context of the overall problem, however, which is to derive one kind of information from another. Thus, while monochromatic lidar can do little or nothing to determine the particle-size distribution of an aerosol, it can directly measure its backscattering coefficient. To determine, say, the hemispherical backscattering coefficient of an aerosol as a function of height from a lidar measurement of backscattering co-efficient by applying Mie theory to assumed particle characteristics is just as valid as any other approach based on the same or similar assump-tions, particularly if the other approach uses measurements that are less readily or precisely made.

If the attenuation per unit path length is not too great, it is possible to make direct measurements of the optical depth of a layer by lidar, although this measurement is limited to a single wavelength and must be extrapolated on a theoretical basis to other spectral regions before the results can be used directly in the radiative-transfer models.

Hence, the lidar-observed scattering ratio measured at a specified wavelength is a valid parameter that can be used to derive other atmospheric radiative parameters with as much justification as any of the other transformations commonly used in radiative transfer studies. Similarly, and more directly, lidar measurements of the total scattering coefficient or optical depth at a specified wavelength have validity and importance for such purposes.

Thus, the prospects are good that lidar data from satellites and globe-circling aircraft can provide global information of great value about the thermal balance of the earth-atmosphere system. It should be noted in this connection that the sparse measurements made to date indicate no significant diurnal changes in the stratospheric aerosol. If this conclusion is substantiated by further studies, then the lidar measurements need be made only at night when the greatly reduced background light level allows a corresponding reduction in transmitted signal intensity. However, temperature or pressure measurements must also be made if accurate results are to be obtained.
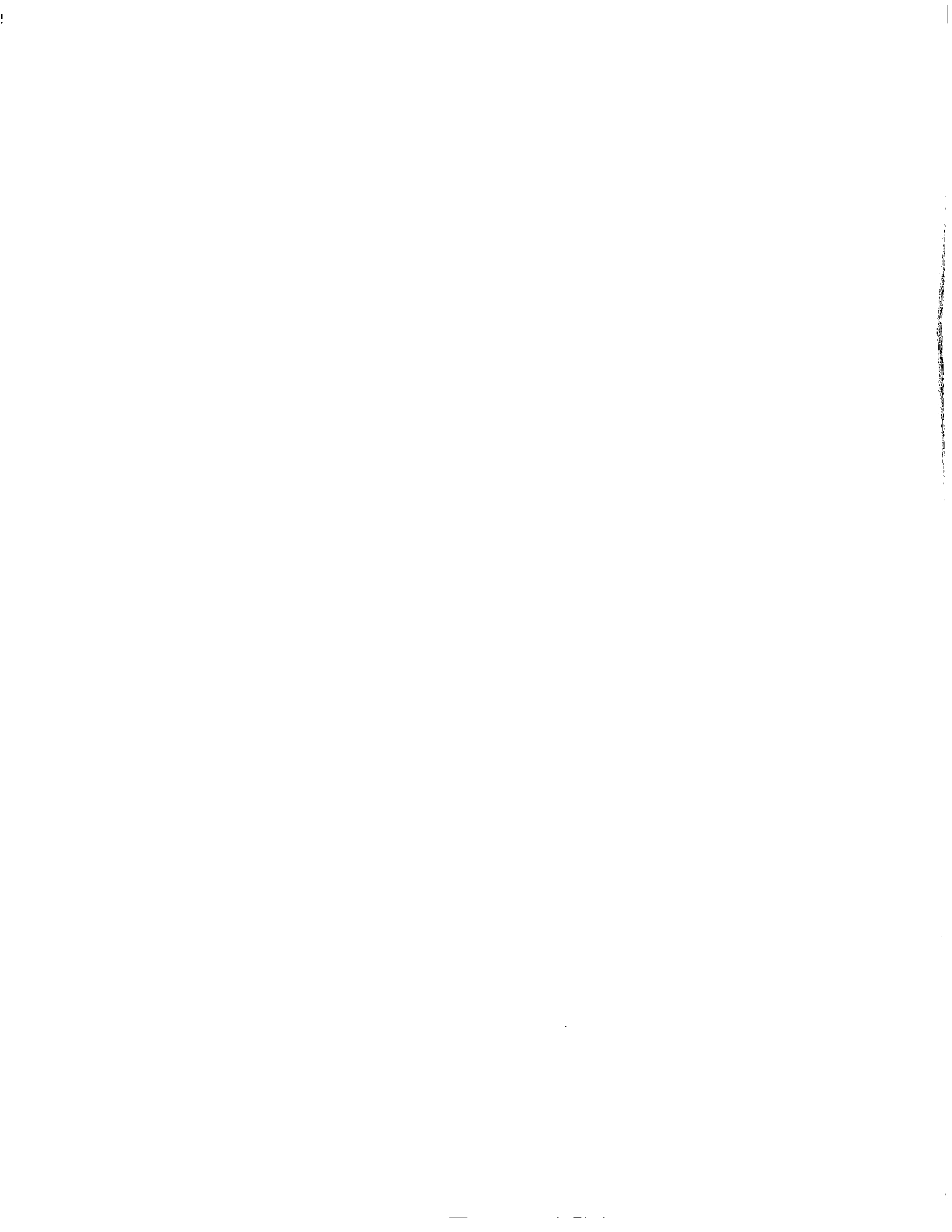
# V  DIAL SYSTEM ANALYSIS

## A.  Range-Resolved Systems

### 1.  Lidar Signal Strength

Lidar systems are most often used to measure the backscatter from a continuously distributed scattering medium or from a fixed target. The lidar equation relates the power received to the transmitted energy and the system parameters.  This equation has been described extensively in the literature (for example, see Collis, 1970).  The lidar equation presented in this section is more complex and extensive than the equation for conventional backscatter systems; the complexity is needed for the detailed error analysis included in a later section.

Differential-absorption lidars can be operated in either the range-resolved or the column-content mode.  The lidar equation, material-concentration equation, and error equations for both these modes of operation will be presented in this subsection and in Section V-B.

The range-resolved lidar equation in a form showing the major functional dependences of each term is:

$$P_{rec} = \frac{k_1}{2} \frac{c \, A_r(R)}{f(R)} \, U_T(t,N,\lambda) \, S(R,t,\lambda) \, \beta(R,t,\lambda) \, *$$

$$\exp \left[ -2 \int_0^R \left\{ \rho_D(R,t) \, K_D(\lambda,p,T) \right. \right.$$

$$+ \rho_{RAY}(R) \, K_{RAY}(\lambda) + \rho_{MIE}(R) \, K_{MIE}(\lambda,R)$$

$$\left. \left. + \rho_{I_1}(R,t) \, K_{I_1}(\lambda,p,T) + \ldots \rho_{I_j}(R,t) \, K_{I_j}(\lambda,p,T) \right\} dr \right]$$

$$+ k_2 \, P_{bkg}(t,\lambda) \qquad\qquad (V-1)$$

where

$$k_1, \; k_2 = \text{Fixed system constants}$$

$$c = \text{Velocity of light}$$

$$P_{rec}(R,t,\lambda) = \text{Received optical power, watts}$$

$$A_r(R) = \text{Effective receiver aperture area } (=A_r \text{ for large } R)$$

$$f(R) = \text{Geometrical power factor } (=R^2 \text{ for large } R)$$

$$U_T(t,N,\lambda) = \text{Transmitted laser pulse energy, joules}$$

$$S(R,t,\lambda) = \text{Scintillation factor}$$

$$\beta(R,t,\lambda) = \text{Volume backscatter coefficient, } m^{-1} \text{ ster}^{-1}$$

$$\rho_{RAY}(R) = \text{Atmospheric molecular concentration}$$

$$K_{RAY}(\lambda) = \text{Rayleigh extinction coefficient}$$

$$\rho_{MIE}(R) = \text{Atmospheric aerosol concentration}$$

$$K_{MIE}(\lambda,R) = \text{Mie extinction coefficient}$$

$$\rho_D(R,t) = \text{Concentration of desired material}$$

$K_D(\lambda,p,T)$ = Absorption coefficient of desired material

$\rho_{I_j}(R,t)$ = Concentration of interfering material, j

$K_{I_j}(\lambda,p,T)$ = Absorption coefficient of interfering material, j

$P_{BKG}(t,\lambda)$ = Received background optical power, watts.

Usually the right side of Eq. (V-1) is multiplied by the time interval, $\Delta t_r$, corresponding to one range interval, in which case $P_r$ is converted to photons per range cell.

Unlike the simplified general calculations resulting in Figure IV-4, the system calculations reported in Section VI are based on parameter values that closely approximate the specific real-world numbers expected for a given system. For example, $T_a$ is not fixed at a value of 0.5 as in the earlier example, but instead is evaluated from an atmospheric propagation model including all attenuating species and the appropriate altitude variation of each. The range of values of $T_a$ for the differential-absorption technique varies over several decades.

## 2. Material Concentration Derivation

Note that the material concentration appears in the integral exponent of Eq. (V-1). In order to find this quantity the lidar equation is solved by taking the logarithm of each side and using an approximate differential to eliminate the integral. Strictly speaking, this procedure restricts the validity of the solution to small range differentials. This results in:

$$\ln \frac{P(R) - P_{BKG}}{P(R + \Delta R) - P_{BKG}} = \frac{-2\Delta R}{R} + \ln \frac{\beta(R)}{\beta(R + \Delta R)} + \ln \frac{S(R)}{S(R + \Delta R)}$$

$$+ 2\Delta R \left[ \rho_{RAY} K_{RAY} + \rho_{MIE} K_{MIE} + \rho_D K_D + \rho_{I_1} K_{I_1} \cdots \rho_{I_j} K_{I_j} \right]_{r = R}$$

$$(V-2)$$

where

$P(R)$ = Received power at range $R$

$P(R + \Delta R)$ = Received power at range $R + R\Delta R$.

The lidar equation (V-1) has appeared in many publications in a form that ignores the background received power. For many applications the neglect of this background received power does not significantly affect the use of the lidar system. Note, however, in Eq. (V-2) that the background power appears as a subtractive term in a ratio of powers and thus must be included in order to achieve the correct mathematical expression. Although this effect is fairly obvious and can be important in practice, to the author's knowledge this is the first time the effect of the background has been specifically identified for DIAL systems.

Equation (V-2) is derived for both the peak and the valley (or off-peak) wavelength location. The two equations are solved simultaneously, yielding the following equation for material concentration, $\rho_D$, as a function of range:

$$\rho_D(R) = \frac{1}{2\Delta K_D \Delta R} \left[ \ln \frac{P_L(R) - P_{BKG(L)}}{P_L(R + \Delta R) - P_{BKG(L)}} - \ln \frac{P_W(R) - P_{BKG(W)}}{P_W(R + \Delta R) - P_{BKG}(W)} \right.$$

$$\left. + B + S + T + I \right]$$

$$(V-3)$$

where

$P_L$ = Power received at absorption or on-line wavelength

$P_W$ = Power received at valley or off-line wavelength

$P_{BKG(L)}$ = On-line background power

$P_{BKG(W)}$ = Off-line background power

$\Delta K_j = K_{L_j} - K_{W_j}$ = Differential absorption coefficient for material $j$

B = Systematic error term resulting from differences in backscatter

$$= \ln\left(\beta_L(R + \Delta R)/\beta_L(R)\right) - \ln\left(\beta_W(R + \Delta R)/\beta_W(R)\right)$$

S = Systematic error term resulting from scintillation

$$= \ln\left(S_L(R + \Delta R)/S_L(R)\right) - \ln\left(S_W(R + \Delta R)/S_W(R)\right)$$

T = Systematic error term resulting from Rayleigh and Mie extinction differences

$$= -2\Delta R \ (\rho_{RAY}\Delta K_{RAY} + \rho_{MIE}\Delta K_{MIE})$$

I = Systematic error term resulting from interfering materials

$$= -2\Delta R \ (\rho_{I_1}\Delta K_{I_1} + \ldots + \rho_{I_j}\Delta K_{I_j}).$$

This equation gives the range-resolved desired-material concentration as a function of the parameters indicated in the lidar equation. A similar analysis for visible-wavelength DIAL systems has been given (Schotland, 1974) and the notation of that analysis has been used, where applicable, for convenience in comparing the two results. The effects discussed in that reference will be summarized here but not given in detail. All of the terms in Eq. (V-3), including the four systematic

error terms, are also subject to random errors that in turn will produce an overall random error in the material concentration. The systematic errors and the overall random error are discussed in the next section of the report.

### 3. Error Analysis

#### a. General

This error-analysis section and the corresponding section (V-B-3) for column-content systems describe the sources of error for differential-absorption lidar (DIAL) systems and give mathematical expressions for each error source so that the magnitude of these errors can be quantitatively determined for a specific system configuration. The most accurate way to analyze errors in DIAL systems, especially at large error values, is to map each of the individual error distributions through the correct mathematical transformation to obtain an overall error distribution in the final measurement. To the authors' knowledge, this procedure has never been used, however, because of the very large number of calculations involved and because many of the individual error distribution functions are not well known. In most practical error analyses, some approximations are made to simplify the calculations. In the analysis presented here the errors from each individual source are assumed to be small and the mapping of each individual error to a total error in concentration measurement is done by using partial differentials with respect to each noise- or error-producing mechanism.

Also, it should be noted that additional complexities arise when a variety of probability distributions must be combined, or when various error mechanisms become partially correlated under certain system operating conditions. In order to avoid these complexities, individual error mechanisms are assumed to be independent and normally

distributed and the total error is assumed equal to the rms sum of the components.

A different approach toward error analysis, involving the representation of errors by signal-to-noise representations, was also made during the course of the project. This alternative approach toward error analysis is useful because it does not degrade as rapidly under certain large error conditions. However, this method does not provide a direct measure of the material concentration error, which is the preferred method of error presentation, and will therefore not be presented in detail in this report.

The derivation of errors for DIAL systems proceeds in four distinct stages. First, the received optical signal must be specified in terms of all significant parameters. This dependence is expressed in the detailed lidar Eq. (V-1). Next, the lidar equation is solved for the material concentration distribution including the presence of each error-producing term. Then this equation for the material concentration, Eq. (V-3), is differentiated with respect to each error-producing quantity. Finally, the probable error in material concentration is calculated as the rms sum of all the physical mechanisms causing individual error perturbations.

Two types of errors are considered: the first, systematic errors, are often correctable and are given by the error terms in the material concentration equation, (V-3); errors of the second type, random errors, are not correctable and are given by the random-error equation derived in the next section.

### b. Random-Error Derivation

An approximate value for the range-resolved random error in the desired material concentration can be obtained by taking the

partial derivative of Eq. (V-3) with respect to each of the variables. Each partial derivative then describes the effect of a random fluctuation in that variable on the desired material concentration measurement. If it is assumed that each of these variables is normally distributed and independent, then the total random error in the desired material concentration can be calculated as the rms sum of the individual components. This total rms sum, in which the error is expressed as a relative or percent error in material concentration, is given below. Note that the use of differential quantities may restrict the validity to small error values.

$$
\left( \frac{\partial \rho_D}{\rho_D} \right)^2 = \frac{1}{(2\rho_D \Delta K_D \Delta R)^2} \left[ \left( \frac{\partial P_L(R)}{P_L(R) - P_{BKG(L)}} \right)^2 \right.
$$

$$
+ \left( \frac{\partial P_L(R + \Delta R)}{P_L(R + \Delta R) - P_{BKG(L)}} \right)^2 + \left( \frac{\partial P_W(R)}{P_W(R) - P_{BKG(W)}} \right)^2
$$

$$
+ \left( \frac{\partial P_W(R + \Delta R)}{P_W(R + \Delta R) - P_{BKG(W)}} \right)^2 + \left( \frac{\partial P_{BKG(L)}}{P_L(R) - P_{BKG(L)}} \right)^2
$$

$$
+ \left( \frac{\partial P_{BKG(L)}}{P_L(R + \Delta R) - P_{BKG(L)}} \right)^2 + \left( \frac{\partial P_{BKG(W)}}{P_L(R) - P_{BKG(W)}} \right)^2
$$

$$
+ \left. \left( \frac{\partial P_{BKG(W)}}{P_W(R + \Delta R) - P_{BKG(W)}} \right)^2 \right]
$$

$$
+ \frac{1}{(\rho_D \Delta K_D \Delta R)^2} \left[ \left( \frac{\partial \beta(R)}{\beta(R)} \right)^2 + \left( \frac{\partial S(R)}{S(R)} \right)^2 \right] +
$$

$$+ \frac{1}{(\rho_D \Delta K_D)^2} \left[ \left( \rho_{RAY} \partial \Delta K_{RAY} \right)^2 + \left( \partial \rho_{RAY} \Delta K_{RAY} \right)^2 + \left( \rho_{MIE} \partial \Delta K_{MIE} \right)^2 \right.$$

$$\left. + \left( \partial \rho_{MIE} \Delta K_{MIE} \right)^2 \right]$$

$$+ \frac{1}{(\rho_D \Delta K_D)^2} \left[ \left( \rho_{I_1} \partial \Delta K_{I_1} \right)^2 + \left( \partial \rho_{I_1} \Delta K_{I_1} \right)^2 + \ldots + \left( \rho_{I_j} \partial \Delta K_{I_j} \right)^2 \right.$$

$$\left. + \left( \partial \rho_{I_j} \Delta K_{I_j} \right)^2 \right]$$

$$+ \left( \frac{\partial \Delta K_D}{\Delta K_D} \right)^2 \qquad\qquad (V-4)$$

where

$\partial x$ represents the absolute error in component x

$\partial x/x$ represents the relative error in component x

$\Delta R$ = Range resolution cell size.

The first eight terms in Eq. (V-4) represent the effect, on material concentration, of fluctuations in the received laser signals and fluctuations in the received background power. For those cases in which the signal-to-noise ratio is very large, it can be assumed that $P_{BKG}$ is approximately equal to zero and the first eight terms reduce to:

$$\left( \frac{\partial P_L(R)}{P_{L(R)}} \right)^2 + \left( \frac{\partial P_L(R + \Delta R)}{P_L(R + \Delta R)} \right)^2 + \left( \frac{\partial P_W(R)}{P_W(R)} \right)^2 + \left( \frac{\partial P_W(R + \Delta R)}{P_W(R + \Delta R)} \right)^2 \quad .$$

$$(V-5)$$

93

In many range-resolved DIAL measurements the range resolution is sufficiently high so that $P_L(R)$ is approximately equal to $P_L(R + \Delta R)$. Assuming **approximately equal** noise in adjacent range cells results in the following simplified equation for the range-resolved random material concentration error:

$$\left(\frac{\partial \rho_D}{\rho_D}\right)^2 = \frac{1}{2(\rho_D \Delta K_D \Delta R)^2} \left[\left(\frac{\partial P_L(R)}{P_L(R)}\right)^2 + \left(\frac{\partial P_W(R)}{P_W(R)}\right)^2\right]$$

$$+ \frac{1}{(\rho_D \Delta K_D \Delta R)^2} \left[\left(\frac{\partial \beta(R)}{\beta(R)}\right)^2 + \left(\frac{\partial S(R)}{S(R)}\right)^2\right]$$

$$+ \frac{1}{(\rho_D \Delta K_D)^2} \left[\left(\rho_{RAY} \partial \Delta K_{RAY}\right)^2 + \left(\partial \rho_{RAY} \Delta K_{RAY}\right)^2 + \left(\rho_{MIE} \partial \Delta K_{MIE}\right)^2\right.$$

$$\left. + \left(\partial \rho_{MIE} \Delta K_{MIE}\right)^2\right]$$

$$+ \frac{1}{(\rho_D \Delta K_D)^2} \left(\rho_{I_1} \partial \Delta K_{I_1}\right)^2 + \left(\partial \rho_{I_1} \Delta K_{I_1}\right)^2 + \ldots + \left(\rho_{I_j} \partial \Delta_{I_j}\right)^2$$

$$+ \left(\partial \rho_{I_j} \Delta K_{I_j}\right)^2\right]$$

$$+ \left(\frac{\partial \Delta K_D}{\Delta K_D}\right)^2 \quad . \tag{V-6}$$

Each of the differential terms on the right-hand side of Eq. (V-6) is a function of one or more physical noise- or error-producing mechanisms. These mechanisms and methods for their calculation are given

in Section V-C of this report. The magnitudes for these differential quantities are calculated from the appropriate equations for those physical mechanisms and the results are inserted in Eq. (V-6) to find the total random error in range-resolved material concentration.

## B. Column-Content Systems

### 1. Lidar Signal Strength

In the above derivation for the range-resolved material concentration, the return signal is backscattered from particulates or molecular species in the atmosphere. The material concentration can thus be determined as a function of range by processing the signal return at two or more different ranges. In column-content measurements the laser signal is received from a solid-object reflection and is used to measure only the total burden of material between the laser-platform location and the reflecting object (or target). Range-resolved measurements cannot be made directly with a single reflector.

Column-content measurements use the same differential-wavelength technique as is utilized for the range-resolved measurements. However, only a single differential in wavelength is used rather than the double differential in both wavelength and range as indicated in the above analysis. This simplifies both the equations and the operating system somewhat, although complications can arise in interpretation of the data over a wide altitude range.

The detailed lidar equation for a solid reflecting object (including the received background power) is given by:

$$P_r = k_1 P_T(t,N,\lambda) \, \frac{A_r(R)}{f(R)} \, \gamma(\lambda,t) \, S(R,t,\lambda) \, \exp\left[-2 \int_0^R \left\{ \rho_{RAY}(R) \, K_{RAY}(R) \right.\right.$$

$$+ \rho_{MIE}(R) \, K_{MIE}(R) + \rho_D(R,t) \, K_D(\lambda,p,T) + \rho_{I_1}(R,t) \, K_{I_1}(\lambda,p,T) \ldots$$

$$\left.\left. + \rho_{I_j}(R,t) \, K_{I_j}(\lambda,p,T) \right\} dr \right] + k_2 P_{BKG}(t,\lambda) \qquad (V\text{-}7)$$

where

$P_r$ = Receiver power

$P_T$ = Transmitted power

$\gamma$ = Target reflection coefficient.

This equation is similar to the range-resolved lidar equation except that a plain reflector is substituted for the distributed aerosol back-scattering medium. Note again that the background power level must be added to the received laser signal to obtain the total received power.


### 2. Material-Concentration Derivation

In order to find the material concentration, the lidar equation is again evaluated twice, once for the signal on the absorption-line wavelength and once for the signal off the absorption line. These two equations are logged and then differenced to obtain the following equation for the integrated optical absorption of the desired material over the entire column:

$$\int_0^R \rho_D K_{D_L} dr - \int_0^R \rho_D K_{D_W} dr = -1/2 \, \ell n \left[ \frac{\ell}{\omega} \right] + \int \Delta\alpha_{RAY} + \int \Delta\alpha_{MIE} + \int \Delta\alpha_I$$

where

$$\mathcal{L} = \dfrac{P_{r_L} - P_{BKG_L}}{P_{T_L} \dfrac{A_r}{f(R)_L} \gamma_L}$$

$$\omega = \dfrac{P_{r_W} - P_{BKG_W}}{P_{T_W} \dfrac{A_r}{f(R)_W} \gamma_W}$$

$$\int \Delta\alpha_{RAY} = \int_0^R \rho_{RAY_L} K_{RAY_L} \, dr - \int_0^R \rho_{RAY_W} K_{RAY_W} \, dr$$

$$\int \Delta\alpha_{MIE} = \int_0^R \rho_{MIE_L} K_{MIE_L} \, dr - \int_0^R \rho_{MIE_W} K_{MIE_W} \, dr$$

$$\int \Delta\alpha_I = \int_0^R \rho_{I_{1_L}} K_{I_{1_L}} \, dr - \int_0^R \rho_{I_{1_W}} K_{I_{1_W}} \, dr + \ldots$$

$$+ \int_0^R \rho_{I_{j_L}} K_{I_{j_L}} \, dr - \int_0^R \rho_{I_{j_W}} K_{I_{j_W}} \, dr \quad . \qquad (V\text{-}8)$$

The above equation is rather unwieldy to use because of the generality assumed in retaining integral quantities for all materials. The equation can be simplified by assuming that the differential absorption coefficient for the desired material is not a function of range and thus can be separated out. This results in:

$$\int_0^R \rho_D K_{D_L} \, dr - \int_0^R \rho_D K_{D_W} \, dr = \Delta K_D \int_0^R \rho_D \, dr \equiv \Delta K_D \int \rho_D \quad . \quad (V\text{-}9)$$

Similar simplifications can be made for Rayleigh, Mie, and interfering
material constituents as well. Note, however, that this simplification
does not apply for the case in which the absorption coefficient varies
significantly with altitude. This can be a particularly significant
effect when measuring the column-content of $O_3$ from a satellite because
the $O_3$ is distributed over a wide altitude range and has a widely varying
absorption coefficient. For these cases, the concept of an average
attenuation coefficient can be applied for first-order calculations. For
high accuracy, however, the integral formulations must be retained.

With the above simplification the equation for integrated
column-content material concentration reduces to:

$$\int_0^R \rho_D dr = \frac{\ln\left[\dfrac{P_{r_W} - P_{BKG_W}}{P_{r_L} - P_{BKG_L}}\right] + \ln\left[\dfrac{P_{T_L}\lambda_L f_W(R)}{P_{T_W}\lambda_W f_L(R)}\right] - 2\int \Delta\alpha_{RM} - 2\int \Delta\alpha_I}{2\,\Delta K_D}$$

(V-10)

where

$$\int \Delta\alpha_{RM} = \int \Delta\alpha_{RAY} + \int \Delta\alpha_{MIE}$$

$f_{L,W}(R)$ = Optical geometry factor for on- and off-line operation.

The first log term in Eq. (V-10) gives, in the absence of the
other terms, a column-content of desired material for an ideal system
operating in an ideal atmosphere. The second log term gives the systematic
errors that would be introduced by differences in transmitted power level,
ground reflection coefficient, or geometrical factors. Note that the
transmitted power on- and off-line is now a factor in producing a syste-
matic error in the column content measurement. Previously, because of
the range differentiation accomplished in the range-resolved DIAL tech-
nique, the transmitted power ratio canceled at least to first order.

This first-order cancellation is also true for the target reflection coefficient and geometrical effects in the range-resolved case.

The integral terms in Eq. (V-10) account for systematic errors introduced by Rayleigh and Mie attenuation (in this measurement the Rayleigh and Mie backscatter differences are not used) and the differential attenuation introduced by the sum of all the interfering materials. This equation not only gives the integrated desired-material concentration from the measured power level and differential-absorption coefficients, but also yields the systematic errors that would result from a variety of system and atmospheric imperfections. This equation is used in a manner analogous to the use of Eq. (V-3) for the range-resolved measurements.

### 3. Error Analysis

The column-content random errors are also calculated on a differential basis and the derivation is similar to the previous range-resolved DIAL error analysis. The column-content random error is given by:

$$
\left(\frac{\partial \int \rho_D}{\int \rho_D}\right)^2 = \frac{1}{\left(2\int \rho_D \Delta K_D\right)^2} \left\{ \left(\frac{\partial P_{r_W}}{P_{r_W} - P_{BKG_W}}\right)^2 + \left(\frac{\partial P_{r_L}}{P_{r_L} - P_{BKG_L}}\right)^2 \right.
$$

$$
+ \left[\frac{\partial\left(\frac{P_{T_L}}{P_{T_W}}\right)}{\frac{P_{T_L}}{P_{T_W}}}\right]^2 + \left[\frac{\partial\left(\frac{\gamma_L}{\gamma_W}\right)}{\left(\frac{\gamma_L}{\gamma_W}\right)}\right]^2 + \left[\frac{\partial\left(\frac{f_W(R)}{f_L(R)}\right)}{\frac{f_W(R)}{f_L(R)}}\right]^2 +
$$

(cont.)

99

$$+ 4 \left[ \partial \left( \int \Delta \partial_{RM} + \int \Delta \alpha_{I} \right) \right]^2 \Bigg\} + \left( \frac{\partial \Delta K_D}{\Delta K_D} \right)^2 \qquad . \qquad (V-11)$$

As in Eq. (V-10) this equation gives the expected random errors where the differential-absorption coefficient, $\Delta K_D$, is not a function of range and thus can be separated out as an independent constant. The first two terms in Eq. (V-11) give the power fluctuations due to noise and other mechanisms that produce fluctuations in the received signal. These mechanisms are essentially identical to those presented previously for the range-resolved DIAL system analysis. The next three terms in Eq. (V-11) yield the errors due to random fluctuations in the transmitted power level (after the measured power compensation has been made), noncompensated errors in target reflection coefficient, and random variations in geometry. The sixth term in Eq. (V-11) (in abbreviated form) accounts for random fluctuation in Rayleigh, Mie, and interfering-species attenuation. The last term accounts for random errors in the differntial-absorption coefficient of the desired material.

The random error in material concentration for both the column-content Eq. (V-11) and range-resolved Eq. (V-6) cases are functions of several lidar-equation variables. Each of these variables in turn may be a function of one or more noise- or error-producing physical mechanisms. The sources of these physical mechanisms are discussed in Section V-C.

C. DIAL-System Error Mechanisms

1. General

There are several noise- and error-producing mechanisms that can potentially contribute to measurement errors in DIAL systems. The more important of these processes are:

(a) Power fluctuations

- Detector noise

- Signal noise

- Background noise (photon fluctuations)

- Excess background fluctuations

- Digitization errors

- Analog signal-processing errors

- Background subtraction errors

- Bias and bias-offset errors

- Geometrical-optics effects

- Pulse-shape effects

- Laser-power variations

- Ground-reflectivity changes

(b) Backscatter variations

(c) Scintillation effects

(d) Rayleigh attenuation fluctuations

(e) Mie attenuation fluctuations

(f) Interfering-material errors

(g) Errors in desired-material differential-absorption coefficient.

The lettered categories in the above listing correspond to individual terms in the error equation, Eq. (V-6). Within each of these lettered categories one or more physical mechanisms are indicated that may contribute to the overall error in each category. The number and type of physical mechanisms that must be included in each category will vary depending on the specific system components and on the specific system application.

The next subsections of the report discuss the general nature of these various physical mechanisms as they apply to DIAL system error

analysis. Specific effects and tradeoffs associated with individual mechanisms are given in more detail.

## 2.   Power Fluctuations

Power fluctuations are often associated only with detector noise and signal noise. Although it is true that these may be limiting factors for power fluctuations in idealized systems, it is evident that several other mechanisms must be included to characterize adequately the power fluctuations that occur in more realistic nonideal systems and environments.

Detector noise has been discussed widely in the available literature and will differ in detail for various types of detectors. To characterize detector noise at this level of detail would require several detector and system parameters to account for the exact detector noise under a wide variety of system and operating conditions. It is believed that this level of detail is not warranted for the present system analysis. The neglect of these additional variables, however, is not believed to affect the outcome of the system studies to a significant degree.

For the system performance calculations presented here, optical detectors are characterized by noise equivalent power (NEP) and quantum efficiency. This characterization is particularly convenient for the present analysis because the NEP is directly equivalent to the power fluctuations caused by detector noise.

Signal noise consists of fluctuations in the received optical signal due to the photon nature of light. This noise mechanism is distinct from the internal detector noise and would still be present even for ideal optical detectors. If the total received optical signal is

expressed in photons, then the fluctuations in this received optical signal are given by the square root of the number of photons received.

In the absence of a received laser signal the only optical signal incident on the detector is due to the background observed by the receiver. The photon fluctuations associated with this background signal are the minimum possible for an ideal optical-receiver system. These fluctuations are equal to the square root of the received background signal.

The background fluctuations are the limiting factor only if the incident background light level is constant except for these fluctuations. Under many field conditions (i.e., moving platforms, atmospheric scintillation, plume turbulence, and other effects) the background is far from constant. For the case in which the average received photon flux is very large, these "excess background fluctuations" can be considerably larger than the fluctuations due only to the photon nature of the background light. The magnitude of this effect can vary widely, depending on the system configuration and application. In this report the excess background fluctuations are represented by a factor multiplying the received background signal.

Digitization errors occur in systems that either count photons or convert the analog detector output to a digital signal for further processing. In either case, the system has a minimum digitization increment. This increment can produce a significant digitization error in the measured material concentration under certain operating conditions. This error is represented in the system calculations by a factor that multiplies the total power received.

It may be possible to implement some systems without requiring digitization and digital processing of the received signals. In these cases there will be analog signal-processing errors that will provide

limitations similar to the above digitization errors. The actual calculation of the analog processing errors can be approximated by:

$$\text{Error} = E_6 \, \ell n \left[ E_3 \frac{E_1 P(R) + E_2(-P_{BKG})}{E_1 P(R + \Delta R) + E_2(-P_{BKG})} + E_4 \right] + E_5 \qquad \text{(V-12)}$$

where $E_1$ through $E_6$ represent analog processing errors associated with each step in the analog signal-processing. Because the actual error value is very system-specific, this error is also assumed equal to a factor times the received optical power.

Background subtraction errors are associated with the signal-processing requirement of subtracting the received background optical signal from the total received signal to obtain the portion that is associated only with the transmitted laser signal. In some systems it is convenient to represent this error by a separate term that is equal to a calculated factor times the background optical level. In the analysis, this error was added to the background multiplicative term associated with the excess background fluctuations and is not considered as a separate error term. The actual value of this error would be very system-specific.

It should be noted that the DIAL technique requires operation both on and off an attenuation line. This can introduce inherent differences in the observed background level on and off the attenuation line. It is not appropriate, therefore, to assume that the background power level is constant on and off the attenuation line. A background-power-level determination must be made at each wavelength and used in the appropriate background subtraction. If only a single background determination is made, a systematic error will be introduced, the magnitude of which can be determined by Eq. (V-3).

A background enhancement effect can occur for hot gases in the infrared spectral region, especially in emissions from smoke stacks where the on-line background emission level may be greater than the thermal background to produce a difference in background radiation at the two wavelengths of operation.

In many cases it can be assumed that the background light level is constant (i.e., no excess background fluctuations) during the measurement of a range cell at (R) and a range cell at (R + ΔR). Because of the nature of the first-order signal processing the "constant" excess background fluctuation will cancel out for range-resolved measurements.

A useful alternative description of the background fluctuation phenomenon states that for the short time interval required to make the two power measurements at (R) and (R + ΔR), the excess background fluctuations are correlated and, because of the nature of the signal processing, do not affect the measurement accuracy. However, as the time interval increases and these fluctuations become uncorrelated, the error smoothly approaches the maximum power fluctuation assumed for the excess background fluctuations.

Bias and bias offset errors occur primarily in infrared systems that employ bias circuits with direct coupling of the output signal; they are most significant in analog signal-processing systems. In other systems, however, this source of error can be negligible. Because of their lack of generality, bias errors were neglected in the computations.

Errors arising from geometrical-optics effects occur primarily when two lasers or two optical receiver channels are used simultaneously. In these cases the two channels may not illuminate or view the same region of space, resulting in a slightly different optical signal level that is most conveniently represented by a power fluctuation. This effect has been observed experimentally even with the use of a single laser and a

single optical receiver. This type of error is also very system-specific and can vary widely in importance. Because of its lack of generality this error term has also been neglected in the calculations even though it may be significant in individual cases.

Laser pulse-shape effects can be significant for systems in which sampling is done with little or no multipulse averaging of received signals. These effects were also neglected in the system analysis because pulse shape is a detailed characteristic of a lidar transmitter that is not known in advance.

Laser power variations are a direct source of error in column-content measurements. It is assumed that corrections for laser power variations will be made, but that a residual fluctuation that is uncorrectable will remain. This residual fluctuation is assumed to be equal to a factor times the received laser power.

Ground reflectivity also introduces a direct error contribution in column-content measurements. This mechanism is also represented by a constant factor times the received optical signal level.

It is evident from the above discussions that not all of the power fluctuations are significant for all DIAL systems. Those that have been retained in the calculations in this report are divided into four categories. These are:

- Detector noise
- Power-measurement error
- Signal-plus-background noise flucutations
- Excess background fluctuations.

In the random error equation (V-6), the first two terms are calculated from these four categories and combined as follows:

$$[\delta P_{L,W}(R)]^2 = N_1^2 + N_2^2 + N_3^2 + N_4^2 \qquad \text{(V-13)}$$

where

$P_{L,W}$ = Received optical signal power on- or off-line respectively

$N_1$ = Detector noise

= Detector NEP (in photons)

$N_2$ = Power measurement error

= $K_{N2}P_{L,W}(R)$

$N_3$ = Received-signal photon-fluctuation error

= $(P_{BKG}$ in photons) + $(P_{L,W}R$ in photons$)^{1/2}$

$N_4$ = Excess background fluctuations

= $K_{N4}P_{BKG}$(in photons).

## 3.   Backscatter and Scintillation Variations

Backscatter variations are assumed to be caused·by fluctuations
in the scattering medium.  This medium may be either molecular gases or
particulates, resulting in either Rayleigh or Mie scattering.  Scintilla-
tion variations are associated with the propagation of optical signals
through the atmosphere and are assumed to be caused by changes in the
index of refraction of the propagating medium.  In most cases, there is
a close interaction between variations in the scattering medium and
variations in the index of refraction of the propagating medium, and thus
the two effects, although treated separately, are often closely cor-
related in time and space.

Separation of the volume backscatter coefficient into the product
of a density and a cross section in the form $\beta = \rho\sigma$ facilitates understanding

of the backscatter variations. For an ideal uniform aerosol type and concentration, $\beta(R)$ = constant and, therefore, from Eq. (V-3) the systematic interference term, B, is zero.

For a nonuniform spatial distribution of the same aerosol, $\rho = f(R)$, $\sigma \neq f(R)$, yielding $\beta(B) \neq$ constant and $\beta(\lambda) \neq f(r)$.

$$\frac{\beta_L(R + \Delta R)}{\beta_L(R)} = \frac{\beta_W(R + \Delta R)}{\beta_W(R)} \qquad . \qquad \text{(V-14)}$$

Therefore B is again zero.

A different situation arises for a nonuniform distribution of both aerosol concentration and aerosol type. For this case,

$$\frac{\beta_L(R + \Delta R)}{\beta_L(R)} \neq \frac{\beta_W(R + \Delta R)}{\beta_W(R)} \qquad \text{(V-15)}$$

and a systematic error results. This case typically occurs near the edges of inversion layers or is associated with turbulent smoke plumes. The magnitude of B in Eq. (V-3) depends on the combined spatial and wavelength correlation for that particular case. In the calculations made for this report, neither inversion layers nor smoke plumes were considered; therefore, B is assumed to be zero.

Random fluctuations in backscatter are described by Eq. (V-6). This effect is represented by a calculated factor times the received optical signal level. Little is known about the spatial, temporal, and wavelength dependence of fluctuations in backscatter, especially at IR wavelengths. An accurate evaluation of this effect requires a more detailed theoretical and experimental basis than is presently available.

Atmospheric scintillation is usually considered in terms of one-way propagation of optical signals through the atmosphere. However, scintillation can also affect the performance of lidar systems, which use two-way optical propagation. In many cases, the optical path for transmission is almost identical to the optical path for reception but with a very short time dealy. This use of the same optical path for transmission and reception, together with the significantly different geometry associated with backscatter systems, can produce significant differences between the detailed behavior of atmospheric scintillation in backscattering systems and its behavior in one-way transmission systems. Transmission scintillation is better known and understood than is backscatter scintillation. To the authors' knowledge, no theoretical treatment or detailed experimental investigation has been made of backscatter scintillation. Although it may be possible to use knowledge of transmission scintillation to infer the effects for the backscatter configuration, this was not attempted in this study.

The effects of scintillation on double-ended (one-way) optical propagation paths have been studied both experimentally and theoretically (Tatarski, 1960; Lawrence and Strohbehn, 1970). However, atmospheric scintillation effects involving 180-degree backscatter have apparently received practically no attention either theoretically or experimentally. A recent survey article by Lawrence and Strohbehn (1970) demonstrates that under most conditions the power spectrum of intensity fluctuations for one-way propagation decreases above approximately 100 Hz, and is quite small above 1000 Hz. In the absence of data for two-way propagation, the best approximation is to assume that the high-frequency power spectra for one-way and two-way propagation are the same. Hence, the atmosphere can perhaps be considered stable insofar as scintillation is concerned for time intervals smaller than 1 ms. The differential-absorption measurement must be completed within this time interval if scintillation effects are

109

to be reduced or avoided. The most straightforward way to meet this requirement is to emit the two pulses of slightly differing wavelengths simultaneously. If the round-trip delay time is short enough, the gradients in refractive index will not change materially during the measurement interval and both signals will traverse nearly identical paths in both directions. Spatial fluctuations within each range cell will be averaged out for each pulse. Variations from one cell to another will be the same for each pulse and will therefore be subtracted out during data processing.

Lacking experimental data about the effects of scintillation on backscattered lidar signals, the echoes from a number of vertical atmospheric probes made at SRI with a ruby lidar were examined. The intervals between pulses exceeded one second. Although a detailed statistical analysis was not made, the pulse-to-pulse fluctuations appeared to be approximately 0.1 dB, or 2.3%. This conclusion implies that it may be possible to operate with pulse separations of much more than 1 ms. Furthermore, it seems likely that scintillation effects on backscattered signals from satellite-based lidars will be even smaller because the large beam areas in the atmosphere resulting from beam spreading over long distances will provide a measure of spatial averaging. However, this speculation must be verified and quantified before it can be used as a basis for alleviating the requirement for close spacing of pulses within a pulse pair.

Scintillation effects can occur because of variations in either absorption or refraction in the propagating medium. Scintillation in absorption coefficient due to small-scale changes in atmospheric temperature and pressure is not expected to be significant and is neglected in the calculations in this report. Fluctuations due to changes in refraction are included in the backscatter variations discussed above and are

not handled as a separate term in the analysis. Systematic errors due to scintillation are assumed to be zero. It should be noted that although these assumptions are appropriate for the present analyses, they are not necessarily valid for use in other DIAL applications.

### 4. Attenuation Fluctuations

Attenuation fluctuations include variations in both Rayleigh and Mie attenuation, variations in the attenuation of all interfering species, and errors in the determination of the differential-absorption coefficient of the species being measured. The latter errors are included because, even though they do not affect the propagation of optical signals through the atmosphere, they are closely related to other absorption or attenuation fluctuations.

Rayleigh and Mie attenuation can introduce both systematic and random errors. The systematic errors are calculated as shown in Eq. (V-3) using the calculated attenuation differences that are applicable to each specific system and situation. The magnitude of this effect will be dependent on altitude (range), and the calculation is performed within each range cell. Random errors due to Rayleigh and Mie attenuation are represented by a constant factor multiplying the received-optical-signal level.

### 5. Spectral Interference

Interference from overlapping spectra of other materials can cause substantial errors in the measurement of a desired material. The level of interference is usually assumed to be unacceptable when

$$\rho_i \Delta K_i \geq \rho_d \Delta K_d \quad , \qquad (V-16)$$

111

where subscripts i and d designate interfering and desired materials, respectively. This condition produces a larger differential signal for the interfering material than for the desired material.

The preferred procedure used for minimizing this type of error is to find the best spectral region for minimizing absorption by the interfering-material while retaining adequate range and sensitivity for the desired material. This trade-off is often quite complex in the case of an altitude-dependent material such as $O_3$, for which no wavelength pair is optimum for monitoring at all altitudes. If a search of all available measuring wavelengths still indicates a significant interfering material error, then some means of compensating for the interfering-material error is desirable. This can be accomplished most conveniently in a tunable lidar by changing from two-wavelength operation to multi-wavelength operation.

Eliminating all the interference terms in Eq. (V-3) except those involving interfering materials results in:

$$\ln P_{L_M} - \ln P_{W_M} = \rho_1 \Delta K_{11} + \rho_2 \Delta K_{21} \qquad \text{(V-17)}$$

where

$P_{L_M}$ = Received lidar power ratio on-line for material M

$P_{W_M}$ = Received lidar power ratio off-line for material M

$\Delta K_{i,j}$ = Differential-absorption coefficient for material i at wavelength pair j.

Defining the log power terms as the differential signal matrix, $\Delta P$, these equations are conveniently represented in matrix form as

$$[\Delta P] = [\rho] \, [\Delta K] \quad , \qquad \text{(V-18)}$$

112

giving the material-concentration matrix directly as

$$[\rho] = [\Delta P] \, [\Delta K]^{-1} \quad . \qquad\qquad (V-19)$$

The method of calculation of errors for multi-wavelength operation is the same as shown in Sections V-A and V-B. The complete error analysis for this case, however, is quite tedious because of the large number of terms involved. Because of the complexity of this detailed error analysis for multi-wavelength operation, an alternative way of representing residual random interfering-material errors is given by the next-to-last term in Eq. (V-6). This approximation gives the residual errors that occur after the first-order interfering-material compensation has been made.

The error in differential attenuation is equal to the error in the product of $\rho\Delta K$. This results in two error components given by

$$\partial(\rho\Delta K) = \rho\partial(\Delta K) + \Delta K \, \partial\rho \quad . \qquad\qquad (V-20)$$

The effect on the concentration error due to both components is shown in Eq. (V-6). In most cases, however, the differential absorption for the interfering material will be well known at the two wavelengths of operation. This means that the error in interfering-material absorption coefficient, $\partial\Delta K$, can usually be neglected compared to the error in material concentration, $\partial\rho$.

It is useful to consider the wavelength-dependent attenuation caused by Rayleigh and Mie scattering as equivalent to an interfering material because these processes also introduce a differential signal into the measurement. This differential signal can often be neglected for closely spaced lines. However, some measurements (such as of ozone in some parts of the UV spectral region) may require a relatively wide

113

spacing of the two wavelengths. Such a wide spacing can produce significant differences in the Rayleigh and Mie scattering cross sections. In these cases, it is sometimes possible to compensate partially for the effect because of the predictability of the wavelength dependence of the scattering cross sections. The Rayleigh cross section varies as $\lambda^{-4}$, but for wavelength regions below the ultraviolet Rayleigh scattering is less significant than Mie scattering. The dependence of Mie backscattering on wavelength is highly variable, particularly in the infrared, and depends on several properties of the aerosol.

Systematic errors due to interfering species are calculated as shown in Eq. (V-3). Random fluctuations for both attenuation and density are represented by a constant multiplicative factor as shown in Eq. (V-6). For the calculations in Chapter VII, it is assumed that the measuring systems do not invoke interfering-material compensation and that the systematic errors due to interfering materials are dominant over the residual or random errors due to interfering materials. The reverse would normally occur if interference compensation were utilized.

As shown in Eq. (V-3), to convert between the variables in the lidar equation such as power, backscattering coefficient, etc., and desired material concentration, it is necessary to know the differential-absorption coefficient of the desired material. Uncertainties in the desired material differential-absorption coefficient thus produce errors in material concentration. The causes of uncertainties in the desired-material differential-absorption coefficient are many and varied and are very specific to the system configuration and the application. The uncertainty in the desired-material differential-attenuation-coefficient is given by a constant term in Eq. (V-6).

The absorption coefficient for gaseous materials is a function of pressure, temperature, and wavelength. The small-scale pressure and

temperature variations in the atmosphere on a spatial scale comparable
to the range resolution of a pulsed DIAL system do not produce significant
changes in absorption coefficient for either the desired material or the
interfering materials. However, for measurements from satellites, the
gross changes in pressure and temperature through the entire atmosphere
will produce large changes in the absorption coefficient for infrared
wavelengths. If the concentration of material is the desired output,
rather than a simple measure of absorption or attenuation, then the
absorption coefficient of the material must be known at each altitude.
This coefficient is most conveniently determined by reference to the
stored atmospheric models, and this is the procedure used in the compu-
tations made for the study reported here.

Variations in laser wavelength on a pulse-to-pulse basis
cause random errors in measurement of the concentration of the desired
material because of the wavelength dependence of the absorption coef-
ficient. The reasons for these variations differ appreciably from system
to system depending on the details of design and construction. Since
these details cannot be specified in a feasibility study, a constant
numerical error was assumed for the random component of absorption-
coefficient variation in the calculations.

Absorption coefficients can also vary in some species because
of chemical effects, particularly dimerization that can occur in the
atmosphere. For example, $NO_2$ can dimerize to $N_2O_4$. (However, the spectra
for $NO_2$ and $N_2O_4$ are easily distinguishable. In fact, the preferred
wavelength regions for measuring $NO_2$ are those where the $N_2O_4$ absorption is
not significant.) Similar effects occur in more complex molecules although
the temperature and wavelength characteristics are generally also more
complex and in some cases there do not appear to be opportunities for
choosing wavelengths for which the temperature effects can be eliminated.

Fortunately, the materials considered in this study are all simple molecules that do not exhibit chemical effects on absorption coefficient to a significant degree.

### 6. Signal Integration

The accuracy of lidar measurements can usually be improved if the signal return from many pulses can be integrated. The exact specification of this accuracy improvement is complex because of the large number of different types of noise and error mechanisms that must be taken into account. The different regimes in range and power level for the various noise and error mechanisms must also be considered. In addition, not all noise mechanisms are affected equally by multipulse integration, and the improvement for each mechanism must be determined separately for each specific system and application.

To indicate the degree of improvement that can be obtained through multipulse integration, some generally applicable improvement factor must be chosen. An often-used approximation for the improvement factor with multipulse integration is $\sqrt{n}$, where n is the number of pulses integrated. This factor is appropriate for most of the noise and error mechanisms discussed in this report and is generally valid as a representation of multipulse-integration improvement for a wide variety of systems operating under a number of different conditions.

Note in particular that atmospheric scintillation produces a limit on the improvement achievable with signal integration. For a single pulse pair, when the signals are transmitted simultaneously, the effects of scintillation may be canceled out to first order under certain conditions and thus produce a small error in the measurement. If more than one pulse pair is integrated, however, the scintillation will produce an additional error term that is not present in the simultaneous,

single-pulse-pair case. Thus, it may happen that a number of pulses
must be integrated in order to achieve the same performance level that
could be attained in the single-simultaneous-pulse-pair case. Thus,
the benefits and tradeoffs associated with multipulse integration are
very system- and application-specific and must be examined on a case-by-
case basis.

# VI  DIAL SYSTEM PARAMETERS, OPERATIONAL CONSIDERATIONS, AND COMPONENT CAPABILITIES

## A.  Introduction

In the design of specific DIAL-system hardware, various operational considerations and component capabilities must be taken into account to meet desired performance requirements for particular monitoring applications.  These additional considerations normally have primary impacts on one of the subsystems or components of the overall DIAL system.  This chapter is divided into three major sections, corresponding to the major subsystems:  the optical transmitter, the optical receiver, and the electronic and mechanical components.  In each section the effects of the operational considerations and component capabilities on overall system performance and the selection of system parameters are discussed.

## B.  Optical Transmitters

### 1.  Tunable Optical Sources

#### a.  General Observations

Use of the word "tunable" is slightly misleading, since for any single pollutant the differential-absorption technique requires only two signals at specific fixed wavelengths.  However, except in the cases where one of the discrete wavelengths available from a conventional fixed-wavelength laser coincides with an absorption line of interest, or can be tuned into coincidence, the output wavelength of the laser must be adjustable over a significant range to achieve precise coincidence. The wider the tunable range the greater the variety of absorption lines that are accessible with a single device.  Hence, the signal sources that

are of greatest interest and value are those that can be tuned over an appreciable range of wavelengths. The tunable devices of greatest current interest are dye lasers and optical parametric oscillators (OPOs), but new types of high-pressure gas lasers now under development may offer the best prospects for future tunable systems in the IR. A detailed exposition on each of these laser types is not feasible here, but the principal features and characteristics are discussed below.

### b.    Flashlamp-Pumped Dye Lasers

Flashlamp-pumped dye lasers are similar to conventional solid-state lasers except that the laser crystal (ruby, YAG, glass, for instance) is replaced by a hollow glass or quartz cylinder containing a fluorescent organic dye dissolved in a suitable solvent. The dye absorbs a portion of the light generated by the flashlamp and stores the energy briefly in excited fluorescent states from which stimulated emission can be induced. The output can be tuned over a large portion of the fluorescence linewidth. Oscillator/amplifier combinations can be used to achieve improved wavelength control and higher output energy levels.

The optical cavities require a tunable dispersive element such as a rotatable grating or mirror/prism combination for tuning and a partially reflecting mirror for output coupling. Achievable linewidths with a single grating or prism are in the range of a few tenths of a nanometer. By adding a high-quality etalon (a form of Fabry-Perot interferometer) the output linewidths can be reduced to as little as 1 or 2 picometers (pm).* Reducing the linewidth reduces the output energy level, but usually by a less than proportionate amount. With care and

---

*1000 pm = 1 nm.

high-quality components, a linewidth reduction by a factor of 1000 can often be achieved with a concomitant energy reduction of about a factor of 10 or less, but these numbers depend somewhat on the dye system.

At average power levels above the low milliwatt range, dye lasers require a flowing dye solution to avoid optical distortion from thermal gradients in the dye, and a means of cooling the flashlamps, usually a flowing water system. The maximum flow rate of the dye solution is usually limited by cavitation and the formation of bubbles in the dye cell, which scatter energy out of the optical resonator and stop the lasing action. This in turn limits the pulse-repetition rate. Typical values for conventional-flow lasers are 1 to 3 pps for water-soluble dyes and 4 to 30 pps for dyes that require alcohol or more complex organic solvents. Transverse-flow lasers can run at 100 Hz or more.

Flashlamp-pumped dye lasers present many severe problems for operation in satellites. The efficiency of these lasers (ratio of laser output energy to flashlamp input energy) is generally in the range of 0.1% to 1%. This imposes a severe limitation on operating such a laser in a satellite because of the large amount of input energy that must be supplied and the amount of heat that must be dissipated.

Output-energy levels in excess of 10 J/pulse have been achieved in broadband modes (linewidths of the order of tens of nanometers). Output levels in the range of 0.5 J to 1.0 J/pulse have been achieved with linewidths of a few picometers, but this is presently feasible with only a few dyes and only in selected spectral regions. Tuning ranges for a single dye vary from as little as a few nanometers to as much as several tens of nanometers. The spectrum from approximately 330 nm to 970 nm can be covered with known flashlamp-pumped dye systems, but achievable energy levels vary by about an order of magnitude over this range.

The flashlamps have limited operating lifetimes, usually measured as the total number of flashes expected before failure or degradation below a stated threshold of light output. Under conservative operating conditions, life expectancies for linear flashlamps are of the order of 500,000 flashes, which is approximately six hours of operating time at 22 Hz.

Another problem is that most of the useful dyes are more efficient when dissolved in alcohols and complex organic solvents that are either combustible or toxic, or both. The close proximity of high-voltage components and potentially explosive solvents would present some special problems in designing for safety. Enclosing the laser in an invert gas, using fast-acting electrical shutoff and venting systems, and the use of thixotropic agents to gel the dye system if a break occurred could probably solve the safety problems, but it would be preferable to avoid the problems by using safe solvents such as water.

Despite these difficulties, flashlamp-pumped dye lasers and associated components comprise a rapidly developing field in which many innovations and breakthroughs can be expected in the future. Substantial sums are being invested in this area by both governmental agencies and private industry. There are predictions that several joules per pulse at picometer linewidths will be available in the future, and that repetition rates of tens of pulses per second will be possible at these output levels. If these forecasts are achieved and some of the other problems solved or alleviated, then flashlamp-pumped dye lasers may become suitable for space missions.

It should be noted that many of the aforementioned problems would be much less severe in aircraft than in satellites because of the shorter mission durations and the greatly reduced premium on output energy, efficiency, power availability, and waste-heat disposal. Because

of the relaxed requirements, dye-laser technology is already suitable for aircraft applications.

### c. Laser-Pumped Dye Lasers

Fluorescent organic dyes can also be pumped by light from another laser. Although this approach is generally less efficient than flashlamp pumping because two optical-energy conversions are required, it does offer some advantages. The principal one is that the pulse length of a Q-switched pump laser can be only a few tens of nanoseconds. Thus, both excitation and emission occur in an interval that is short in comparison with the time constants for deexcitation by transfer of energy to triplet states; this makes it possible to obtain good lasing action from some dyes that work poorly or not at all when excited by flashlamps. Laser pumping of dyes also produces less heating of the dye solution, permits the use of a more stable optical system for the dye laser, and permits close optical coupling that makes optimum use of the available pump energy.

There is also an important disadvantage to the use of laser-pumped dye lasers for measuring air pollutants. Since fluorescence always occurs at longer wavelengths than those of excitation, the wavelengths of the pump sources must be shorter than those used for measurement. Thus, currently available dyes require pumping at either short visible or ultraviolet wavelengths. This requires either an $N_2$ laser or harmonic operation of crystal lasers. Also, the only pollutant of interest that interacts with wavelengths that can be generated by dyes pumped by these lasers is $NO_2$ which can be reached more easily and efficiently by flashlamp-pumped dye lasers.

Even if some future development produced an efficient laser capable of pumping dyes at wavelengths shorter than 300 nm, there are no

known dye lasers at wavelengths shorter than 330 nm. In addition, it seems likely that photodissociation of the dyes by such a short-wavelength pump would prevent practical applications in the range of UV wavelengths useful for measuring air pollutants. Hence, laser-pumped dye lasers seem to be poor prospects for the purposes under study.

### d. Optical Parametric Oscillators

Consideration of OPOs began in 1961 when Franken et al. (1961) demonstrated second-harmonic generation at optical wavelengths using nonlinear properties of materials. Giordmaine and Miller (1965) demonstrated the first tunable OPO in 1965. Developments have proceeded rapidly since that time and it is now possible to obtain tunable energy throughout the visible region, over a portion of the near-UV, and over most of the IR between 1 µm and 20 µm. It is not practical to undertake here more than a brief summary of the work because it is so extensive and complex. A survey article by Harris (1969) listed 98 references. A soon-to-be published updated survey article by Byer (1975b) lists 288 references.

A schematic diagram of an OPO is shown in Figure VI-1. An incident signal $\omega_p$, called the pump frequency, is focused into a non-linear crystal. An optical resonance at frequency $\omega_s$ produces oscillation at that frequency. In the process, a third frequency, $\omega_i$, called the idler frequency, is generated in accordance with the relationship

$$\omega_p = \omega_s + \omega_i.$$

As with a laser, the OPO generates coherent light with an efficiency that increases greatly as the threshold is exceeded. Energy can be extracted at either the signal or the idler wavelengths in the single resonant configuration or at both wavelengths, if desired, in the doubly resonant configuration. These same configurations can be used
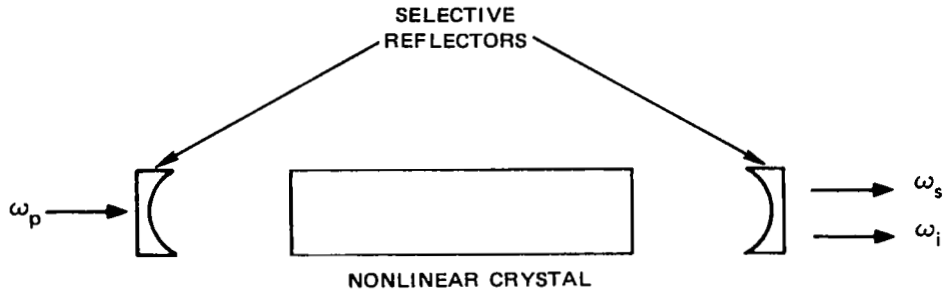
FIGURE VI-1 SCHEMATIC OF AN OPTICAL PARAMETRIC OSCILLATOR

for second-harmonic generation (frequency doubling) and parametric up-conversion (sum generation). That is, energy may be introduced at the signal and idler frequencies and extracted at the pump frequency.

The linewidths attainable with parametric oscillators depend upon such factors as the optical qualities of the crystals, of the resonator elements, and of the other components. Linewidths of $1$ cm$^{-1}$ (equal to 0.1 nm, or 1 Å, at a wavelength of 1 μm) are readily achieved, and widths as small as 0.001 cm$^{-1}$ (equal to 0.1 pm or $10^{-3}$ Å at $\lambda = 1$ μm) can be achieved. Unlike the dye laser, which manifests a power loss as the linewidth is decreased, the OPO maintains full efficiency as the linewidth is narrowed.

The nonlinear reactance on which the OPO is based arises from the nonlinear polarizability of the crystals at high field intensities. Achievement of significant parametric amplification (or reduction of the oscillation threshold) requires phase matching of the signal, idler and pump waves in the crystal. For collinear waves, this requires that

$$\omega_s n_s + \omega_i n_i = \omega_p n_p \qquad \text{(VI-1)}$$

125

where

$n_s$ = Refractive index at signal frequency

$n_i$ = Refractive index at idler frequency

$n_p$ = Refractive index at pump frequency.

For a fixed pump frequency, changing any of the refractive indices alters the signal and idler wavelengths at which high gain or oscillation occur, thus providing a means for tuning $\omega_s$ and $\omega_i$.

Birefringence in anisotropic crystals makes the refractive indices strongly dependent on the propagation angles in the crystal, so that tuning can be accomplished by rotating the crystals. The refractive indices are also temperature-dependent, so that thermal tuning is also possible. Impressed electrostatic fields can also be used for rapid tuning over limited ranges. In combination with varying $\omega_p$, these features make it possible to tune an OPO over a wide range of operating wavelengths, the range being primarily limited by the range of parameters over which phase matching can be maintained or by the transparency limits of the crystal. These effects are illustrated in Figure VI-2, which shows the tuning curve for a lithium niobate ($LiNbO_3$) crystal for phase matching at 90 degrees to the crystal axis. Additional tuning range can be achieved by altering the angle.

In general, the efficiency of an OPO improves as the field intensity at the pump frequency is increased and as interaction length increases, although there are limits on the useful crystal length (Byer, 1975b). However, the maximum allowable intensities are set either by damage to the crystal or by thermal effects. These limitations, as well as the need for excellent optical properties, place a premium on the achievement of high quality in the production of large crystals. Other limitations on the capabilities of OPOs include a limited pump-light
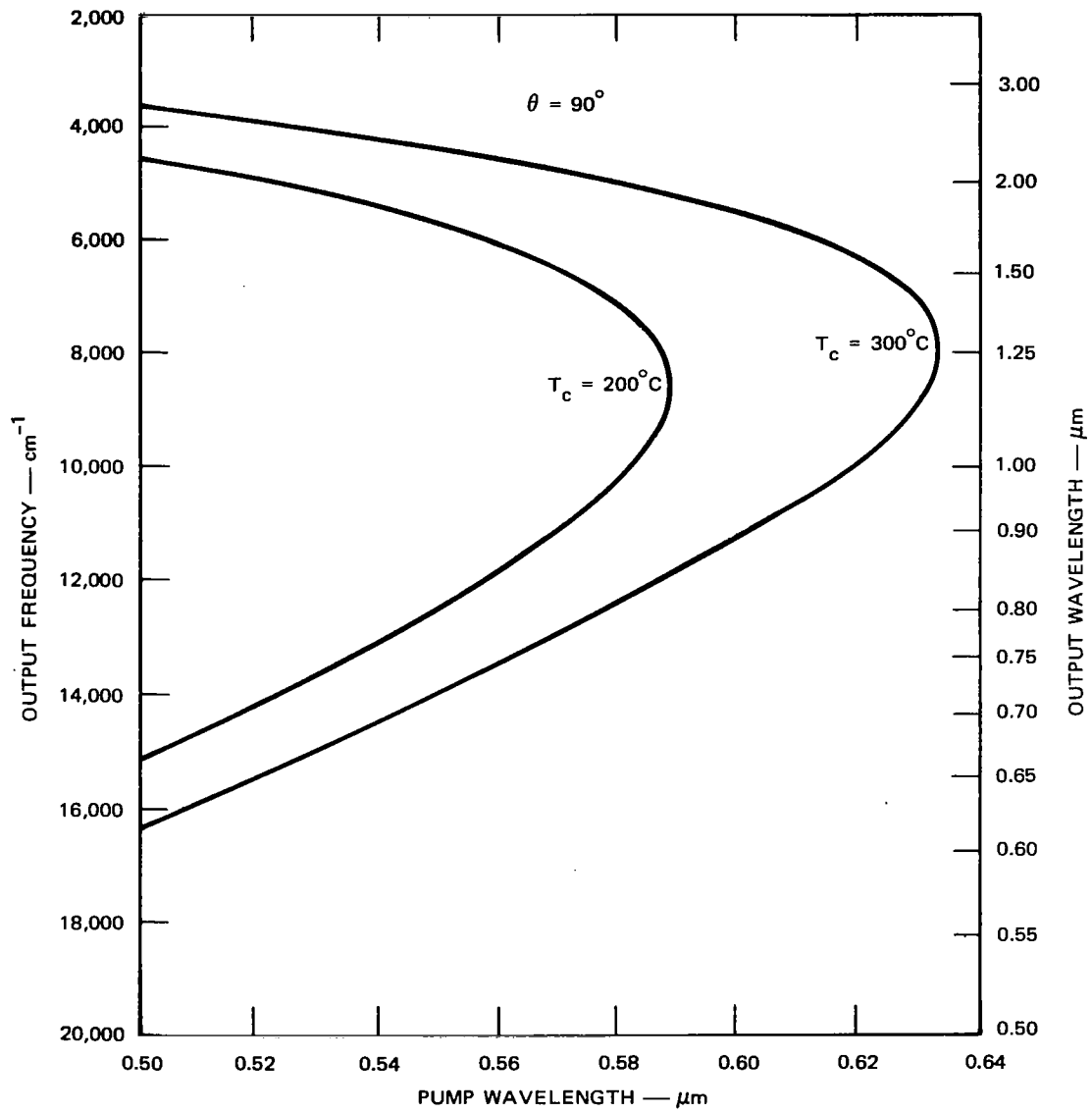
FIGURE VI-2    TUNING CURVES FOR A 90-DEGREE PHASE-MATCHED LITHIUM NIOBATE
PARAMETRIC OSCILLATOR PUMPED WITH A TUNABLE SOURCE.    Source:
Byer, 1973.

127

acceptance angle, a requirement for high mode purity in the pump, and a necessity for high-quality optical coatings in the laser components.

It is only possible to discuss the highlights of this interesting but complex topic in a report of reasonable length. Fortunately, Byer (1975b) covers all the important technical matters completely and succinctly, and the reader interested in more details is urged to read this reference. Our discussion here of OPOs closes with a summary of the present state of the art and some observations concerning future prospects.

At present the theory of OPOs is well established and the practical aspects are adequately understood, although further advances will be made. Successful operation of a number of parametric oscillators has experimentally demonstrated the relationships among theory, measurable parameters, and performance capabilities. The further development of OPOs and extension of their capabilities into new frequency ranges and increased energy and power levels is still severely limited by the characteristics of available materials and the limitations of existing pump sources.

At present, the demonstrated tuning range of OPOs extends from 0.54 μm to 4.8 μm. Measured properties of known crystals assure that this tuning range will be extended to at least 18 μm. Efficiencies of up to 50% have been demonstrated, with 30% being perhaps a more realistic general expectation.[*] This is probably adequate for the purposes under consideration here. Output energy levels of the order of 1 mJ per pulse at 70 Hz have been achieved. This is an adequate pulse rate for most purposes, but considerably more energy per pulse is needed. It

---

[*] These values are for the energy in $\omega_s + \omega_i$. The values for conversion to $\omega_s$ only are smaller.

should be emphasized, however, that present pulse energy levels and average power are not limited by fundamental factors, and that additional effort on material properties and pump sources will almost certainly lead to improvements in output levels. The achievable bandwidths of as low as 30 MHz are adequate for conventional detectors, but may be too wide for some heterodyne applications. Additional work is needed on efficient pump sources capable of generating about 10 J/pulse at a variety of wavelengths.

### e. Other Tunable Lasers

Other types of tunable lasers that have been studied in recent years are the diode laser, the Raman spin-flip laser, the isotope-tuned laser, and the TEA laser. Some observations about the characteristics and the future prospects for these lasers follow.

The wavelength of the lead-salt or lead-tin-telluride semiconductor diode laser (Hinkley and Kelley, 1971) can be varied by several means. The composition, expressed as $Pb_{1-x}Sn_x Te$, can be altered chemically by adjustment of the composition factor, x, to emit anywhere in the wavelength range from 6.5 μm to 32 μm. Other diode lasers cover the range 0.63 μm to 34 μm. For any given value of x, an individual laser can be tuned by applying pressure, by imposing a magnetic field, or by varying the temperature. The most convenient tuning means is to alter the refractive index through a temperature variation by changing the current through the diode. Typically, a single device can be tuned over a frequency range of up to 4 $cm^{-1}$. However, because of changes in operation from one cavity mode to another, a single diode cannot be tuned continuously over this range. Emission occurs in continuous bands up to 0.8 $cm^{-1}$ wide that occupy about half the total tuning range of 4 $cm^{-1}$.

Diode lasers have a number of shortcomings for the uses envisaged here. Presently they require cryogenic cooling. Until recently, liquid-helium temperatures were needed for CW operation, with pulsed operation possible at the temperature of liquid nitrogen--77 $^{\circ}$K. Melngallis (1973) reported CW operation at temperatures up to 70 $^{\circ}$K. High-power cryogenic operation is at best awkward in a laboratory and is of dubious practicality in a satellite. Melngallis (1973) also reported achievement of 100 mW output power at wavelengths around 3.5 $\mu$m. This power levels is inadequate for use with conventional detectors for the uses envisioned here but may be useful in a heterodyne system, particularly from the 12- and 3-km aircraft altitudes.

The Raman spin-flip laser (Patel, 1973) at present tunes over two limited portions of the IR spectrum--5.5 $\mu$m to 6.5 $\mu$m, and 11 $\mu$m to 15 $\mu$m. The tuning ranges within these bands do not provide full coverage. Cryogenic temperatures are required and precise temperature control is necessary to maintain accurate frequency calibration. Although these lasers are small, their available output energy is too small for remote measurement of air pollutants from satellites or aircraft.

Certain types of low-pressure gas lasers, including $CO_2$ and CO lasers, are capable of producing many closely spaced lines in the IR emission bands of the fill gases. These emission bands and their harmonics can be shifted significantly by substituting isotopes of the constituent gases. The lines in these shifted bands are different for each isotopic combination, thereby providing a measure of wavelength adjustability, though not continuous tunability. Several studies have been made of the applicability of this technique to the remote measurement of air pollutants (Jacobs and Snowman, 1967; Menzies, George, and Bhaumik, 1970; Newman and Trusty, 1971; Hanst, 1971b; and Snowman, 1972).

The literature on TEA (Transversely Excited Atmospheric) lasers is extensive, and much of the work is classified military information. Successful lasing action has been obtained in a number of IR bands from several gases, including $CO_2$, CO, HBr, HF, and $N_2O$. At pressures of approximately one atmosphere, these lasers operate at any of several discrete wavelengths in a band.

$CO_2$ oscillators and amplifiers have received the greatest attention because of their high efficiency--typically 30% and 10%, respectively. The operating region is a band lying between 9.6 μm and 11 μm. Following several years of experimentation and development, $CO_2$ lasers are now reliable, efficient, and commercially available, and they can produce energy levels in excess of hundreds of joules per pulse. The output of these lasers can be doubled and tripled to obtain wavelengths of 5.3 μm and 3.53 μm that can be used to pump OPOs. Tripling by doubling and summing in one operation in a single crystal can be accomplished with 15% efficiency.

f.    New Types of Tunable Lasers Under Investigation

At high pressures, the transition wavelengths of some gas lasers are broadened into continuous bands so that tuning over an entire band is possible if the desired levels can be excited and utilized before collisional quenching depletes the energy stored in the excited states. Two means of exciting these states in a variety of gases are under intensive investigation--electrical discharges and electron-beam excitation. The general area of high-pressure gas lasers has been listed as one of high-priority research by the Laser Research Committee of the Department of Defense. It seems reasonable to suppose that important new capabilities will become available in the future.

Excitation of high-pressure gases by electrical discharges is an outgrowth of the TEA-laser development effort, though progress has not been easy or straightforward. For example, although the stored energy increases with pressure, so does the required voltage. It takes 65 to 70 kV to produce the discharge at 10 atmospheres, and this must be accomplished with a pulse of about 1 μs. At higher pressures the field intensities become so great that optical-resonator components are damaged. Danilychev (1973) has made a 60-atmosphere $CO_2$ laser with energy storage density of 100 J/liter at one atmosphere. He is confident that the engineering problems can be solved and that with a large volume of gas in a container 12 cm in diameter he will be able to produce more than $10^7$ watts at 50% efficiency and tunable over the entire band. Furthermore, he expects similar achievements at other IR wavelengths with CO, $NO_2$, $N_2O$, HF, and even hydrogen, but these experiments have not yet been attempted.

Hess at NASA-Langley Research Center and Mooradian at MIT-Lincoln Laboratory are also working on high-pressure $CO_2$ lasers. Their results are encouraging but have not yet been published.

Both electron beams and short pulses of light have been used to produce ionization to initiate uniform discharges in TEA lasers. More recently, however, both methods have been used for direct excitation of a high-pressure gas.

g.   Limiting Factors for Laser Output Levels

Several well-established limits affect the amount of output energy that can be achieved from a single laser. Although these do not impose absolute upper limits on future energy levels, they do tend to channel future development efforts in particular directions. A brief review of the limits will be of value in assessing future prospects.

One limiting factor is the breakdown power level for gases. At one atmosphere, gases become ionized at a power density on the order of $10^{10}$ W/cm$^2$. The breakdown level decreases to about $10^9$ W/cm$^2$ at a pressure of 10 atmospheres. A minimum is reached at about 20 atmospheres. The breakdown level increases with increasing pressure above 20 atmospheres and with decreasing pressure at very low pressures. This limiting factor affects the minimum dimensions of optical components in lasers, but not severely under the conditions envisaged here. At pulse lengths of the order of $10^{-6}$ s, $10^{10}$ W/cm$^2$ is reached at an energy level of $10^4$ J/cm$^2$.

The energy density at which the surfaces of optical components are damaged imposes a more severe limitation. In the IR and visible regions the practical operating limit for most high-quality optical components is in the range of 2 to 4 J/cm$^2$. In some cases it is possible to work at 10 J/cm$^2$, but 4 J/cm$^2$ is more realistic. In the UV region the limits are lower because absorption is greater and materials are more susceptible to two-photon absorption and to ionization. These values are for clean surfaces. Dust on the surfaces lowers the operating level by a large amount. This limit applies primarily to optical windows and crystal faces. Some authorities doubt that it will ever be possible to obtain high energy densities at wavelengths shorter than 400 nm.

Nonlinear optical materials are subject to internal damage at energy densities that vary from one material to another (see Byer, 1975b) and depend somewhat on the method of preparation. KDP can withstand up to 4 J/cm$^2$, but most other materials are limited to 1 J/cm$^2$ or less.

There is also an imperfectly understood energy limitation at about 4 J/cm$^2$ in $CO_2$ lasers. It is related to a gas breakdown problem, and nonlinear ionization processes seem to be involved.

These energy density limits of a few joules per $cm^2$ are all related to the fact that at these levels the electric-field strengths in the optical electromagnetic fields are close to the static dielectric-breakdown points. It is unrealistic to expect to exceed this limit significantly. The implication is that 10-J pulses are going to require components with diameters in the range of 3 to 5 cm. This is not difficult for gas lasers or for windows, but it presents some imposing problems for dye lasers, solid-state (doped crystal) lasers, and especially for nonlinear materials. Techniques for producing larger crystals are now under development, but historically progress toward this goal has been slow.

A further limit is imposed on the laser inversion density and volume by superfluorescence. If the single-photon emission rates are short enough ($\approx 1$ $s^{-1}$), the populated excited states cannot remain populated long enough to store energy beyond certain limits. This suggests that future high-power-laser research be oriented toward systems where the metastable levels cannot be depopulated by single-photon transitions, but can be depopulated by anti-Stokes Raman radiation or by externally supplied radiation.

Another limit is the pumping depth, expressed in units such as atmosphere-centimeters. Both photons and electrons have limited penetration depths into the lasing medium because of their intense interaction with the medium. It is suggested that other pumping sources be sought that have greater penetration depths, such as x-rays and neutrons.

Several types of high-energy lasers under development for military applications are capable of generating much higher energy levels than those considered above. Also, parallel operation of multiple sources can produce energy levels that exceed the damage threshold of optical

components. However, fuel consumption rates and storage limitations prevent such systems from operating for periods longer than a few minutes. In addition, most of these high-energy systems produce continuous rather than pulsed signals, which makes both range-resolved and column-content measurements difficult. Although modulation techniques could obviate . this difficulty, they have not yet been developed for high-energy lasers.

h.   An Assessment of Future Prospects for High-Energy
     Tunable Lasers

Predictions of future capabilities in a complex technical area that is changing rapidly are inherently uncertain. However, some well-established reference points provide a basis for at least near-future predictions and, apart from the possibility of technical breakthroughs, offer a basis for longer-range estimates.

In the long-wavelength portion of the spectrum of interest, Byer at Stanford University is doing exploratory work to develop laboratory sources in the 1-to-4 and 7-to-18 μm region. Within the next year or so he expects to demonstrate a few tens of millijoules per pulse at approximately 10 pps over 1 to 4 μm.

The highest energy and power levels obtained with any laser, and at the best efficiencies, are afforded by the continuous-wave (or long-pulse) $CO_2$ lasers operating around 10 μm. These devices can deliver kilojoules per pulse at efficiencies in the range of 10% to 30%. The highest power levels are obtained with electron-beam pumping; this approach appears promising for satellites because the large sizes and weights of ground-based electron-beam sources can be greatly reduced in a space environment. Other modes of operation (such as TEA lasers) are capable of providing hundreds of joules per pulse around 10 μm in $CO_2$.

High-pressure $CO_2$ lasers capable of operating throughout the 9.6-to-11-μm band at reasonable efficiencies and at energy levels of the order of 10 to 100 J/pulse are good prospects. Use of isotopes can expand the wavelength range to approximately 9 μm to 12 μm. The efficiency with which this energy can be converted to shorter-wavelength regions is uncertain, but second-harmonic generation is unlikely to exceed 33% efficiency. Third-harmonic generation by optically pumping gases or nonlinear materials is a possibility for achieving 3.4 μm tunable energy, perhaps at up to 25% efficiency. With large crystals that have just become available, doubling and frequency addition can probably provide at least 10 J/pulse tunable over essentially the entire infrared region of interest.

Between 0.5 μm and 4.5 μm, OPOs pumped by Nd:YAG or dye lasers will also be competitive as widely tunable sources for some time to come. Oscillator/amplifier combinations using Nd in glass that can produce 200 to 300 J/pulse are now available. An output of 10 J/pulse at 10 to 20 Hz is more reasonable. This would be an impressive source in terms of present capabilities. The output could be converted into tunable energy in the 1.5-to-4.5-μm-band at efficiencies of up to perhaps 40% or 50% by $LiNiO_3$ or other crystals that can probably be obtained to provide 4 to 5 J/pulse as a reasonable estimate.

Nd:YAG lasers can also be doubled efficiently (~ 50%) in CDA crystals to obtain maximum energies of 5 to 40 J/pulse at 0.532 μm. This could be used to pump a dye laser at 50% to 60% efficiency, but wavelengths between 0.5 μm and 1.06 μm are not useful for measuring air pollutants. Tripling to obtain energy at 353 nm to pump dyes to produce 440-nm radiation for measurement of $NO_2$ is a possibility. Flashlamp-pumped dye lasers, however, could probably do as well, even though they are more complicated to operate and maintain.

Apart from new types of lasers now in the exploratory research phase, frequency-doubled tunable dye lasers offer the best prospects for tunable radiation in the near UV. Until new crystals are discovered and perfected, phase-matching limitations will prevent attainment of wavelengths shorter than approximately 215 nm. Output levels in excess of a few J/pulse are unlikely from such sources. Parametric oscillators pumped by frequency-doubled dye lasers or the third or fourth harmonic of Nd:YAG may be future possibilities, but energy levels in excess of 1 J/pulse are unlikely for the near-UV spectrum.

These estimates of future capabilities are summarized in Figure VI-3. They are based on reasonable extrapolations of existing technology, subject to known constraints on energy densities.

Prospects of achieving continuously tunable energy levels in the 100-J/pulse range with devices compatible with non-military operations and capable of sustained operation seem rather poor at present. However, research on high-energy lasers (some are tunable) is being carried on by large, well-funded groups at the Lawrence Livermore Laboratory in Livermore, California, and at Los Alamos, New Mexico, as well as in a number of militarily funded laboratories and at least two industrial laboratories seeking such lasers for isotope separation. Thus, research on tunable lasers that has in the past been dominated by organizations (college laboratories and a few government/industrial laboratories) that were motivated more by desire for knowledge and understanding than by needs to achieve specified performance objectives has now become a well-funded goal-oriented operation. These goals are not well matched to the needs of remote air-pollution measurement, but they may nonetheless develop new approaches and techniques that could be made to meet these needs. A well-coordinated and adequately funded research program to meet the specific needs of remote measurement of air pollutants
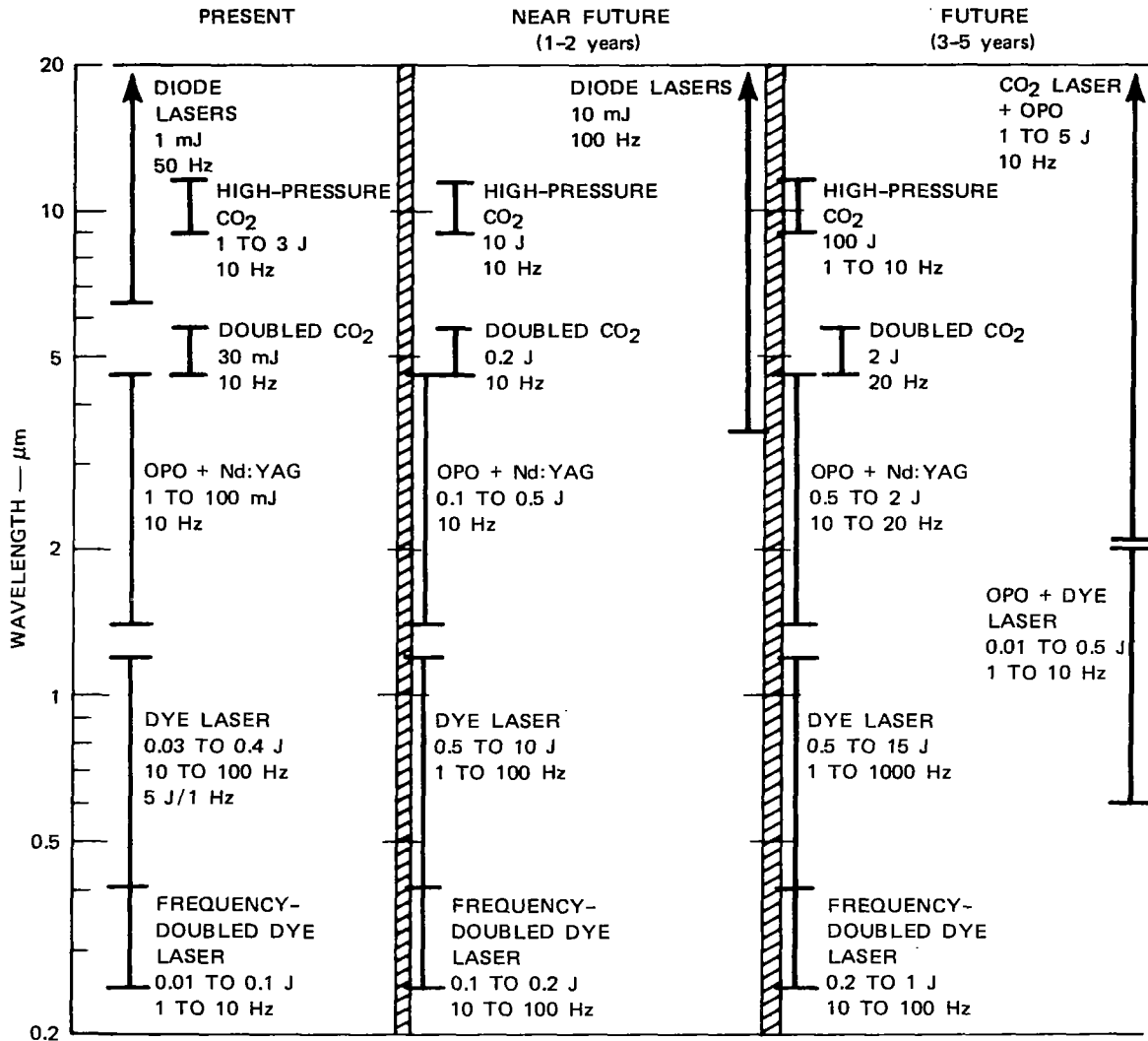
FIGURE VI-3    ESTIMATES OF FUTURE CAPABILITIES OF LASERS

should offer good prospects of achieving energy levels in the 10-to-100-J/pulse range at rates of 10 to 20 Hz with reasonable efficiency within 5 to 10 years.

## 2. Earth Coverage

For the purposes of this study, a single satellite altitude of 166 km was specified, with the orbital inclination lying between 55

degrees and 28 degrees. Two aircraft altitudes, 3 km and 12 km, were specified. The grid size of interest for global measurements from satellites was specified as being in the range of 5 to 20 km, and multishot laser firings with the option of pointing the optical system was considered as a possible mode of operation. These parameters have important implications for the minimum permissible pulse-repetition rates and for multipulse integration to improve the signal-to-noise ratio (SNR).

The ground-trace velocity (based on a stationary earth) of a satellite at an altitude of 166 km is approximately 7.6 km/s. The distance moved in the 1 ms limit imposed by scintillation on the round-trip echo time of a single-pulse-pair is less than 5% of the beam diameter (166 m) at ground level for a 1-mrad FOV. Thus, ground-trace velocity would not be a limiting factor even if sequential pulses spaced one echo interval apart were otherwise feasible.

Since the required data rates affect the pulse-repetition rate and the energy levels required for the laser transmitters, the implications for data rates of the specified orbital parameters and data-grid sizes must be considered.

For a circular orbit, the orbital period is given by (TRW, 1967)

$$T = 1.41 \left[(R + h)/R\right]^{3/2} \qquad \text{(VI-2)}$$

where

  h = Orbit height above the surface of the earth = 166 km, and

  R = Equatorial radius of the earth = 6378.16 km.

These values yield an orbital period of T = 1.4654 hours = 87.924 minutes and a ground-trace velocity (relative to a nonrotating earth) of 7.597 km/s. For an average earth rotational period of 23.9345 hours, the linear velocity at the equator due to rotation is 1674.368 km/hr. This

provides a westward drift of equatorial crossings of 2453.62 km. Ignoring a small correction due to a nonspherical earth, this figure is independent of orbital inclination. The perpendicular distance, D, between successive same-direction crossings of the equator is given by

$$D = 2453.62 \sin \alpha \qquad\qquad \text{(VI-3)}$$

where $\alpha$ is the orbital inclination. The geometry is indicated in Figure VI-4. However, the equatorial velocity of the earth, 1674.68 km/hr,
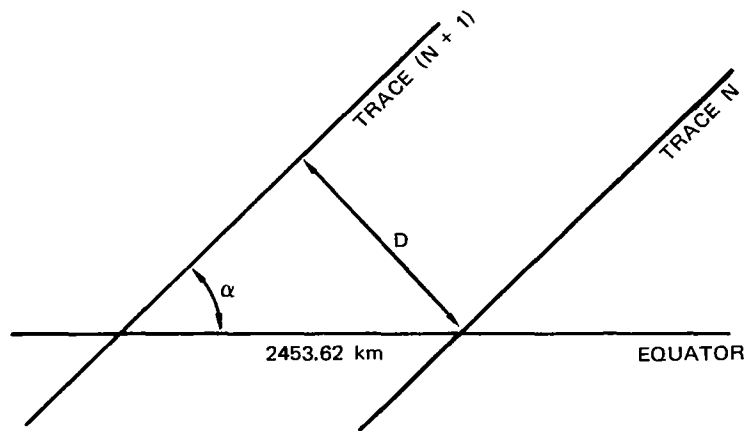


FIGURE VI-4    GEOMETRY FOR DETERMINING GROUND-
                TRACE SEPARATION AT THE EQUATOR

must be added vectorially to the ground projection of satellite velocity to determine the correct trace separations. This alters the effective inclination angles slightly. The resulting corrected values of effective orbital inclination angle ($\alpha'$), ground-trace velocity ($v'$), and trace separation ($D'$) are given in Table VI-1. This table also gives the pulse-repetition rates in pulses per second (Hz) required to scan the areas between successive traces with grid sizes of 5 km and 20 km.

It is perhaps surprising to observe that the pulse rates for a given grid size and inclination angle are identical for the posigrade and retrograde orbits. However, a short trigonometric analysis

140

Table VI-1

GROUND-TRACE PARAMETERS AND REQUIRED LASER PULSE RATES

| Orbit | $\alpha$ | $\alpha'$ | $v'$ (km/s) | $D'$ | Laser PRF (Hz) Grid Size 5 km | Laser PRF (Hz) Grid Size 20 km |
|-------|-----|-------|-----|---------|-----|----|
| Posigrade | 28 | 26-1/2 | 8.01 | 1092.25 | 350 | 22 |
| | 55 | 52-1/4 | 7.87 | 1939.41 | 611 | 38 |
| Retrograde | 28 | 29-3/4 | 7.19 | 1217.14 | 350 | 22 |
| | 55 | 58 | 7.34 | 2080.22 | 611 | 38 |

$\alpha$ = Orbital inclination angle

$\alpha'$ = Effective orbital inclination angle

$v'$ = Ground-trace velocity

$D'$ = Trace separation.

demonstrates that the product $(v'D')$ has the same value for any value of $\alpha$ independent of the orbital direction.

For a lidar system in an aircraft scanning through an angle $Y$ to each side of the ground trace, the pulse rate for a grid size $\Delta X$ is given by

$$PRF = \frac{2hv\ (\sin\ Y)}{(\Delta X)^2} \quad , \qquad (VI-4)$$

where

h = Aircraft altitude

v = Aircraft velocity.

Local monitoring of air pollutants, for which a grid size of 100 m is appropriate, could be accomplished from an aircraft at an altitude of 3 km flying at a velocity of 75 m/s (167 mph) and scanning ±22-1/2 degrees.

This results in 17.4 Hz and a scanned strip width of 2.3 km. For regional monitoring, a grid size of 500 m from an altitude of 12 km would be suitable. Again scanning ±22-1/2 degrees but flying at a velocity of 100 m/s (223 mph), the required rate is 3.7 Hz and the width of the scanned strip is 9.2 km. Clearly, these values are quite flexible since the scan angle and both the altitude and the velocity of the aircraft can be varied widely. In general, the required pulse rates for airborne systems are easily accommodated in the range of 3 to 15 Hz.

### 3. Size, Weight, and Power Requirements

It is one thing to conclude that equipment and components required for the lidars under consideration in this study are either technically feasible now or can become so within a few years if adequate resources are allocated to an appropriate research and development program. The logistic feasibility of operating equipment with the required capabilities in either an aircraft or a satellite is another matter. A groundbased tunable lidar built by SRI for measuring gaseous species at altitudes of the order of 100 km at a data rate of 1/4 to 1/2 Hz occupies a substantial portion of a 40-foot trailer and consumes a few kilowatts of power. Another SRI fixed-wavelength lidar for aerosol backscattering measurements fills most of the space in a special van-type body on a light-duty pickup truck. Other lidars built at the NASA Langley Research Center and elsewhere are of comparable size. Although these units were not optimized for aircraft and satellite operation, their sizes, weights, and power consumptions are impressive.

There are but few examples of space-qualified lasers. A recently published paper (Yang, 1973) describes a Nd:glass laser that delivers 3.3 J/kg (1.5 J/lb) with a volumetric efficiency of $4.9 \times 10^3$ $J/m^3$ (0.8 $J/in^3$). However, this laser is not capable of rapid, continuous

142

pulsing. The size and weight of storage capacitors, high-voltage converter, and cooling equipment for pulse rates of 30 Hz would increase overall size and weight requirements by two or three orders of magnitude. This would put the weight requirements in the 600-to-6000-kg (1300-to-13,000-lb) category and the volume requirements in the 0.4-to-4-$m^3$ range. A reasonably detailed design study would be needed to arrive at more definitive estimates.

Power consumption will be a major problem for satellite-based high-power lidars intended for continuous operation. With the exception of the $CO_2$ TEA laser, the best efficiencies achievable with current lasers are of the order of one percent, and many lasers are an order of magnitude less efficient. From Table VI-1, it can be seen that the required pulse-repetition rates vary from 22 to 38 Hz for the 20-km data grid and from 350 to 611 Hz for the 5-km grid. The differential-absorption measurement method requires at least two pulses for each data point. At 2 J per pulse pair and the average rate of 30 Hz for the larger grid size, the power required for the laser alone would be 6 kW at 1% efficiency. The requirement increases to 60 kW for 20 J per pulse pair. Both levels are substantially in excess of the guideline values of 1.5 to 2 kW for the power level that might be made available for a lidar in a large satellite such as the Space Shuttle vehicle. Disposing of the waste heat from such inefficient conversion of electrical energy to light would impose an additional burden on the capabilities of any reasonable satellite. Since additional power would be required for other components, including a data system and telemetry equipment, it seems clear that a satellite-borne lidar would require stored fuel and an electrical generating system at energy levels of 20 J per pulse pair or higher, unless the efficiency of the laser could be greatly improved.

143

Prospective overall efficiencies for frequency-doubled tunable dye lasers for the near UV are well below 1%. Tunable signals derived from Nd:YAG sources will have efficiencies in the range 0.1% to 0.5%, depending on the nonlinear crystals used and the number of conversion stages required. The two stages of energy conversion required to obtain tunable energy in the 3-to-10-μm range from $CO_2$ lasers probably limit overall efficiency to 10% or less. Of the presently known techniques, only high-pressure $CO_2$ lasers for the 9.6-to-11-μm band offer prospects for efficiencies significantly in excess of one percent. Of the cases discussed in Chapter VII only $O_3$ has absorption lines in this band. Thus, efficiencies of the order of 1% to 10% at best are in prospect until new technological approaches are developed.

It probably will not be feasible to provide continuously the 60 kW of power that would be required at 10% efficiency for an energy level of 200 J per pulse pair. Providing energy at the 20-J-per-pulse-pair level for the 350-to-611 Hz rate required for the 5-km data grid also appears infeasible.

The pulse-repetition-rate estimate for aircraft is 3 to 15 Hz. Using the highest figure and 20 J per pulse pair leads to a power requirement of 30 kW (≈ 40 hp) for a laser efficiency of 1%. This is a substantial amount of power, but it could be provided aboard any of several aircraft that might be considered for such a mission. Even at lower laser efficiencies it would be feasible, though expensive, to generate the power for laser sources operating at the required energy levels. Hence, it should be feasible to provide the power required for operation of lidars aboard aircraft even with appropriate allowances for power for auxiliary equipment.

## 4. Eye Safety

The high energy levels and power densities that can be produced by laser radiation from telescopes of modest size can be hazardous to human eyes even at considerable distances. The Z-136 Committee on the Safe Use of Lasers, a committee of the American National Standards Institute, has set tentative maximum intensity levels for eye safety. The recommended maximum permissible exposure (MPE) in the visible region from 0.4 µm to 0.694 µm is $5 \times 10^{-7}$ $J/cm^2$, increasing linearly to $2.5 \times 10^{-6}$ $J/cm^2$ at 1.06 µm. It stays constant at that level to 1.4 µm. From 1.4 µm to 13 µm the MPE is given by $0.56\ T^{1/4}$ $J/cm^2$, which yields 13 m $J/cm^2$ for a pulse length of 300 ns. In the UV region, the MPE is governed by a curve determined by the corneal absorption spectrum in the region from 200 nm to 310 nm. The curve decreases from $2 \times 10^{-4}$ $J/cm^2$ at 310 nm to a minimum of $3 \times 10^{-6}$ $J/cm^2$ at 260 nm, and then rises to $10^{-4}$ $J/cm^2$ at 200 nm. From 310 nm to 400 nm the MPE is $10^{-3}$ $J/cm^2$. It should be noted that at 0.4 µm and at 1.4 µm there are substantial discontinuities in the permitted pulse energy. Despite the wording of the standard, there seems to be some question about the actual safety level that is tolerable near these discontinuous points.

Using these safety criteria at ground level, the maximum safe transmitted pulse energy as a function of wavelength is shown in Figure VI-5 for a satellite altitude of 166 km and the two aircraft altitudes of 12 and 3 km. Also indicated for each of these three altitudes are three transmitter beamwidths: 1 mrad, 0.33 mrad, and 0.1 mrad. Increasing the transmitter beamwidth which requires an increase in the receiver FOV, would permit transmission of more pulse energy without exceeding the eye-safety limit. However, if the receiver system, which should have an FOV at least as large as the transmitter beamwidth, is limited by the received background radiation, the SNR will not necessarily increase at the receiver
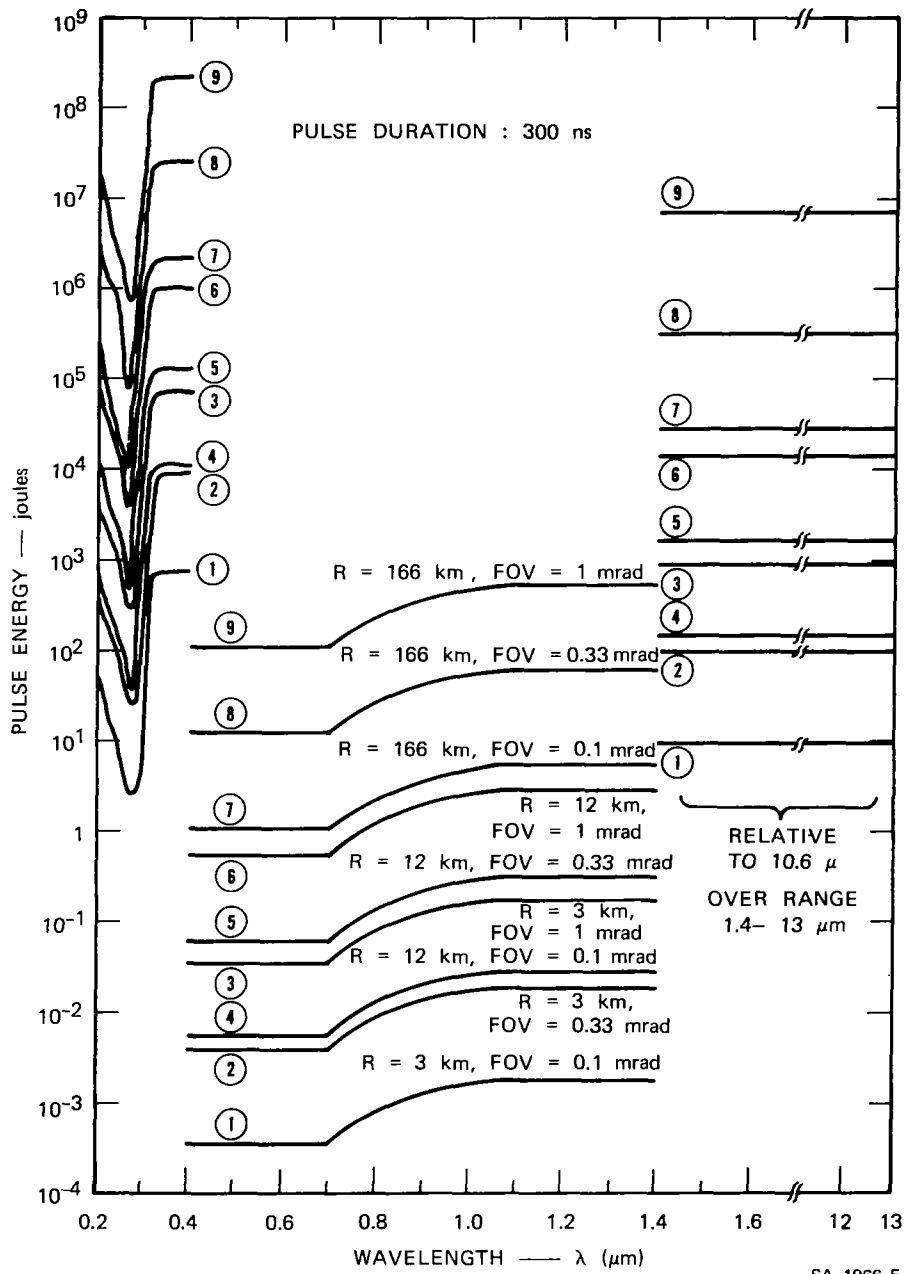
PULSE DURATION : 300 ns

PULSE ENERGY — joules

$10^9$
$10^8$
$10^7$
$10^6$
$10^5$
$10^4$
$10^3$
$10^2$
$10^1$
1
$10^{-1}$
$10^{-2}$
$10^{-3}$
$10^{-4}$

⑨
⑧
⑦
⑥
⑤
③
④
②
①
⑨
⑧
⑦
⑥
⑤
③
④
②
①

R = 166 km , FOV = 1 mrad
R = 166 km , FOV = 0.33 mrad
R = 166 km , FOV = 0.1 mrad
R = 12 km, FOV = 1 mrad
R = 12 km, FOV = 0.33 mrad
R = 3 km, FOV = 1 mrad
R = 12 km, FOV = 0.1 mrad
R = 3 km, FOV = 0.33 mrad
R = 3 km, FOV = 0.1 mrad

⑨
⑧
⑦
⑥
⑤
③
④
②
①

RELATIVE
TO 10.6 $\mu$
OVER RANGE
1.4– 13 $\mu$m

0.2    0.4    0.6    0.8    1.0    1.2    1.4    1.6    12    13

WAVELENGTH —— $\lambda$ ($\mu$m)

SA-1966-5

FIGURE VI-5    EYE-SAFE ENERGY AS A FUNCTION OF WAVELENGTH

146

despite the fact that a larger pulse energy is transmitted. Thus, the eye-safety consideration can set a limit on the SNR performance of the optical system for background-limited operation.

## C. Optical Receivers

### 1. Optical Detectors

The most important characteristic of optical detectors that affects their suitability for remote air-pollution measurements is the noise associated with the detector. It is possible, in principle, and it is often feasible in practice, to reduce external noise to negligible levels by reducing the FOV of the optical system and the bandwidth of the optical interference filter. Thus, in the limit the dominant noise will come from the detector, the preamplifier, or the signal statistics.

Detectors for lidar systems are normally operated in either a photon-counting or power-detecting mode. Photon counting is preferred whenever possible, but is usually restricted to systems using photo-multiplier tubes (PMTs) in the UV, visible, and very-near-IR spectral regions (Hake et al., 1971). Photon counters are not currently available for IR wavelength longer than about 1 $\mu$m. At longer wavelengths, power detectors, typically photoconductors, are used instead. Because of the difference in system performance in the photon-counting and power-detection modes, and because visible and IR detectors have different sources of noise and behave differently with respect to cooling, comparison of the relative performance of optical detectors over the entire wavelength range of interest entails a degree of complexity. The literature on this topic is extensive. The major features are summarized in the following paragraphs.

## a. Visible and UV Detectors

Photomultipliers (PMTs) are the most sensitive detectors for the visible and UV spectral regions. However, PMTs have electron emission from the detector surface (dark current) that produces a noise signal even in the absence of incident light. Additional noise is introduced by the secondary-emission process, in which both the signal and the dark current are amplified. This electron-multiplication process is a relatively-low-noise operation, with typical noise factors being approximately 1.5 for a factor-of-3 gain per stage (Melchior et al., 1970). The newer negative-electron-affinity surfaces can provide gain factors of 20 to 50 per stage, with a noise factor even lower than 1.5. The use of small detector areas, cooling, and electric or magnetic focusing can reduce the magnitude of the noise to an equivalent optical input signal on the order of a few photons per second. In most lidar systems this is a negligible noise level because of the short gate time (approximately 1 $\mu$s or less with pulsed lidar systems). The net gain and output signal level of good PMTs are high enough that the noise figure is established by the PMT rather than by subsequent amplification processes. The noise properties of electron amplification are usually included in the specification of the tube, and the equivalent-noise input includes the amplification-noise factor. Such tubes are available for operation throughout the near UV and visible and out to approximately 1 $\mu$m in the IR.

Existing PMT performance levels were used in this study for assessing both present and near-future capabilities. The detector noise level at visible wavelengths is typically at least three orders of magnitude lower than the daylight background level due to scattered sunlight. Thus, even for future systems using narrowbandwidth optical filters and perhaps also a narrower FOV, the performance of visible-wavelength detector systems is still likely to be limited by scattered

148

solar radiation. In the UV region, where the large ozone attenuation provides a dark background for aircraft altitudes, the detector may produce more noise than the background. However, the noise level for both noise sources can be reduced to about one photon per pulse length if necessary, thus making the contribution of these noise sources negligible.

A comparison between UV/visible detectors and IR detectors can be made by using a noise-equivalent power (NEP) description. It will become evident in the next subsection that visible-wavelength PMT performance exceeds the capabilities of conventional IR detectors.

### b.    IR Detectors

The situation for the IR region is more complex because of the larger number of detection processes and noise mechanisms that occur in IR detectors. For the near IR, photodiodes, and especially avalanche photodiodes, provide excellent performance. The more technologically advanced silicon diodes provide response out to wavelengths slightly longer than 1 μm. Germanium diodes can be used out to about 1.5 μm, and indium arsenide and indium antimonide can be used to provide responses to approximately 3.5 μm and 5.5 μm, respectively. For longer wavelengths, more complicated mixed-crystal diodes, such as mercury-cadmium-telluride ($Hg_{1-x}Cd_xTe$), can be used.

Avalanche photodiodes have the advantage of providing a moderate current gain that reduces the noise contribution of the pre-amplifier. Multiplication factors for avalanche photodiodes are typically $10^2$ to $10^4$, which are substantially smaller than those achieved in photomultipliers. In addition to the lower gain there is a larger noise contribution relative to PMTs that is associated with the solid-state multiplication process. Also, avalanche devices are normally operated

at the dark-current-breakdown point and thus require precise control of the operating point to achieve satisfactory operation. As the technology improves for longer-wavelength materials, such as gallium arsenide, indium antimonide, and indium arsenide, practical avalanche photodiodes for these wavelength regions should also become available.

Much of the recent IR-detector development has been oriented toward achieving IR detectors capable of low-noise operation at higher temperatures. For example, background-limited performance has been achieved in Hg-Cd-Te photoconductors in the 8-$\mu$m region, cooled only to 77 $^\circ$K. Recently, proton bombardment has been used as a method for fabricating high-sensitivity photodetectors, and it may have potential for yielding high-quality detectors in the small sizes required for the applications considered here.

The most common IR detectors are photoconductive (PC), photovoltaic (PV), and photoelectromagnetic (PEM) detectors. The primary internal noise sources for these detectors are generation-recombination noise and thermal noise. In poorer-quality detectors there may also be significant current-noise contributions due to poor contacts or undesirable surface conditions on the detector crystal.

The large number of sources of detector noise and of detector types, and the resulting difficulty of comparing the various detectors, has led to the use of a single phenomonological figure of merit called detectivity, $D^*$, defined by

$$D^* = \frac{(A)^{1/2} (BW)^{1/2}}{NEP} \text{ cm } (Hz)^{1/2}/\text{watt} \qquad (VI-5)$$
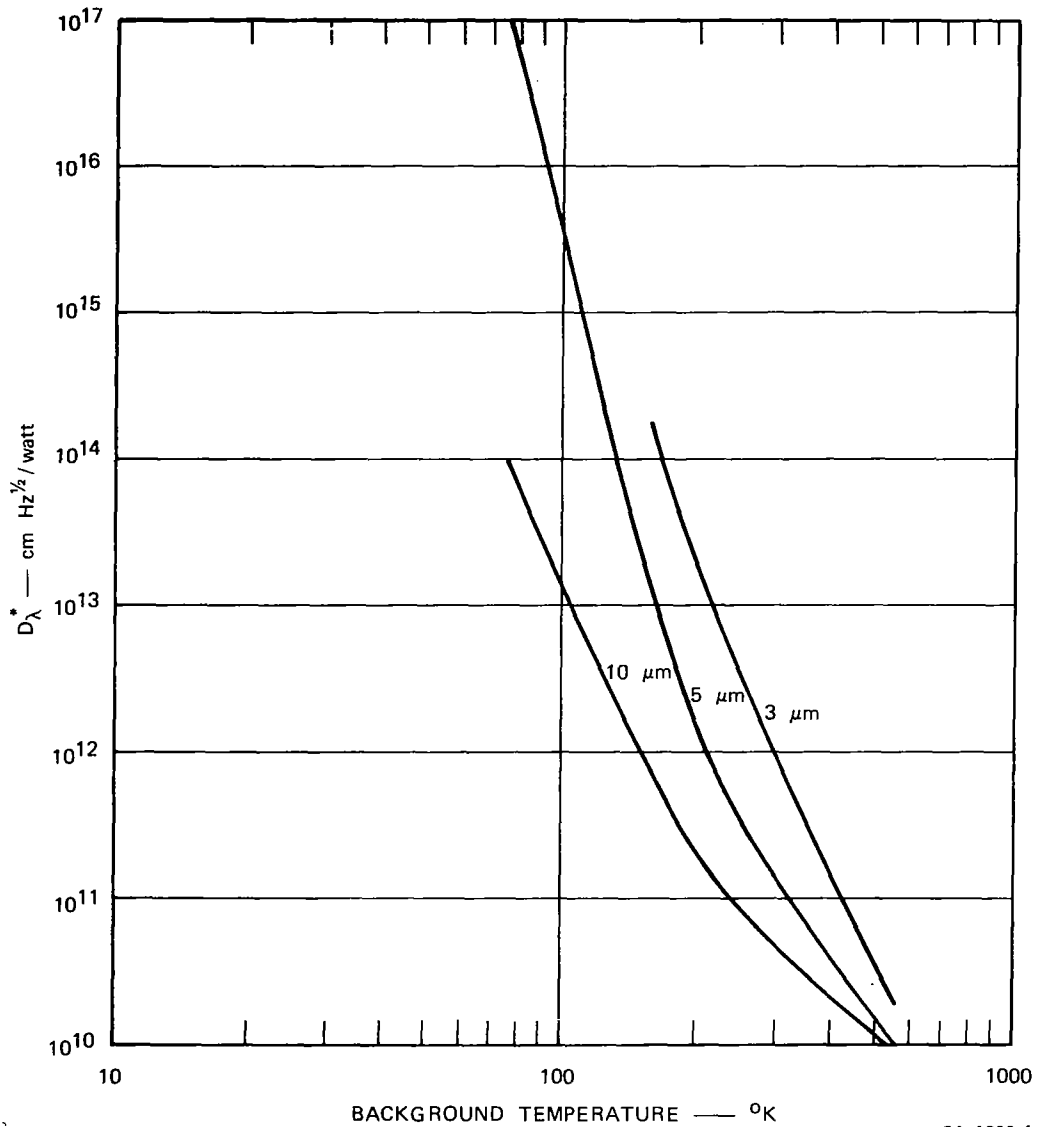
where

$A$ = Detector area, $cm^2$

$BW$ = Post-detection bandwidth, Hz

$NEP$ = Noise-equivalent power, watts.

$D^*$ is determined experimentally under specified conditions by illuminating the detector with thermal radiation from a calibrated source at a known temperature. This radiation is periodically interrupted or chopped at a specified rate. $D^*$ is usually normalized to a post-detection bandwidth of 1 Hz. The experimental conditions are usually given by three numbers in parentheses following $D^*$. Thus, $D^*$ (500, 900, 1) indicates a calibrated source temperature of 500 $^\circ$K, a chopping frequency of 900 Hz, and a post-detection bandwidth of 1 Hz.

The responses of most types of detectors are also dependent on the wavelength of the incident radiation. In these cases the values of NEP and $D^*$ are determined by measurements made with monochromatic illumination instead of wideband thermal radiation, and there is a wavelength, $\lambda_p$, at which the best detector performance is obtained. The value of $\lambda_p$ is often substituted for the source temperature in the parentheses, in which case the detectivity is expressed in the form $D^*_{\lambda_p}$ (2.8, 900, 1) for $\lambda_p = 2.8$ µm.

A typical data sheet for a detector also states the field of view (FOV) of the detector and the temperature of the background for the $D^*$ measurement. However, the relative contributions to the NEP of background radiation and internally generated detector noise are usually not specified. An upper bound on the amount by which $D^*$ can be improved by lowering the background temperature is illustrated in Figure VI-6, which gives the photon-limited value of $D^*$ as a function of background temperature at 3, 5, and 10 µm (Kruse et al., 1962). It is evident that substantial increases in $D^*$ are theoretically achievable at all three

FIGURE VI-6    DETECTIVITY AS A FUNCTION OF BACKGROUND TEMPERATURE

wavelengths with reasonable degrees of cooling. However, these curves
are applicable only in the limit where internal detector noise is much
lower than photon, or signal-statistics, noise. The amount of improvement
that can actually be achieved by surrounding the detector with a cooled
enclosure having an aperture just large enough to accommodate the desired
FOV of the receiving system will not be as large as indicated by Figure
VI-6.

Several NEP characteristics of detectors over the wave-
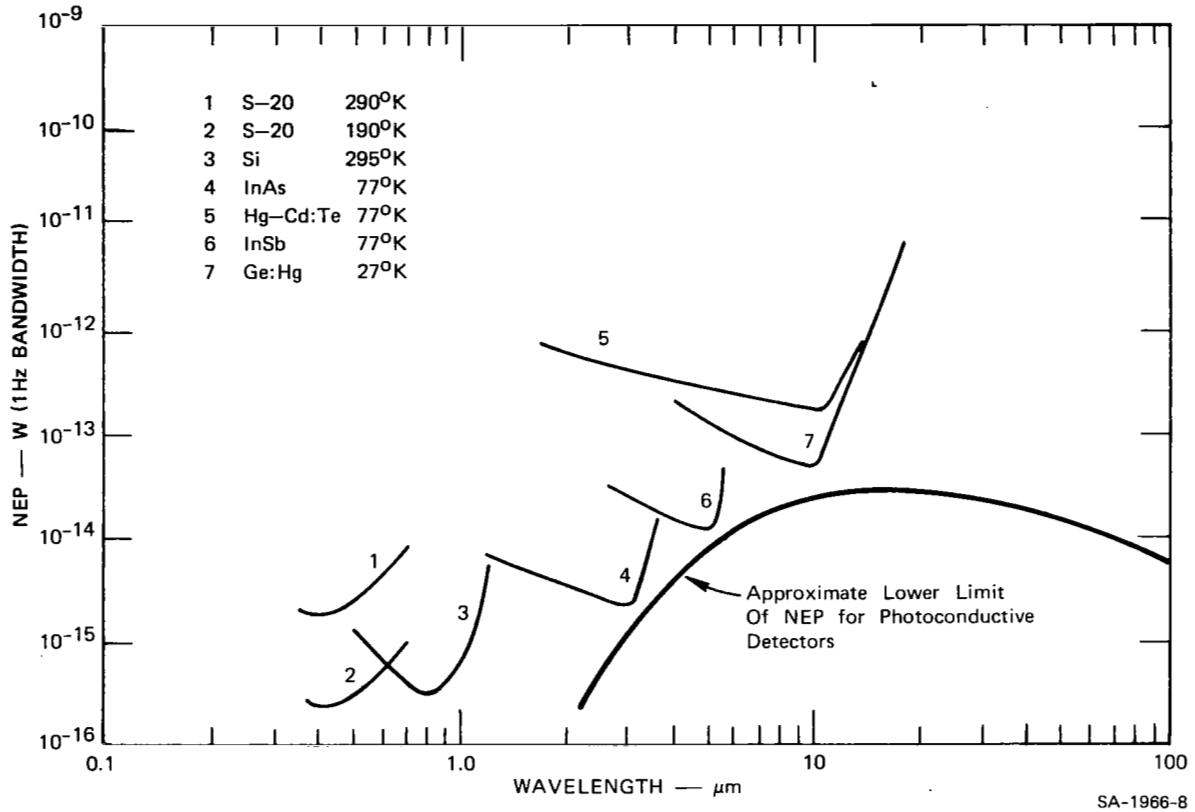length range of interest are shown in Figure VI-7.  Curves 1 and 2 are



FIGURE VI-7    NOISE EQUIVALENT POWER FOR SEVERAL TYPES OF DETECTOR

for PMTs.  The other curves are for IR detectors.  The IR detectors and
the limiting IR curve are for a 0.1-mm-square detector operating in a
cooled enclosure.  These performance curves were based on the assumption
that improvement by a factor of 10 could be achieved by cooling the
enclosure.

The FOV of the lidar receiver also has a detector-related
aspect.  In IR systems intended for passive detection of thermal radiation
it often happens that the FOV is large enough that the external background
radiation is greater than internal detector noise.  For an active lidar

153

system receiving echoes from very small illuminated areas, the background
radiation is a noise with which the signal must compete. Hence, the
sensitivity of the system can be improved by reducing the FOV until the
background noise is less than the detector noise. The relationship be-
tween FOV and sensitivity for background-limited operation is shown in
Figure VI-8, with θ, the FOV, given in both degrees and milliradians.
It is clear that apart from limitations that may arise from other causes,
small FOVs offer an improvement in sensitivity down to the point where the
system becomes limited by internal noise. However, there are minimum
size limits for detectors, determined by other optical considerations,
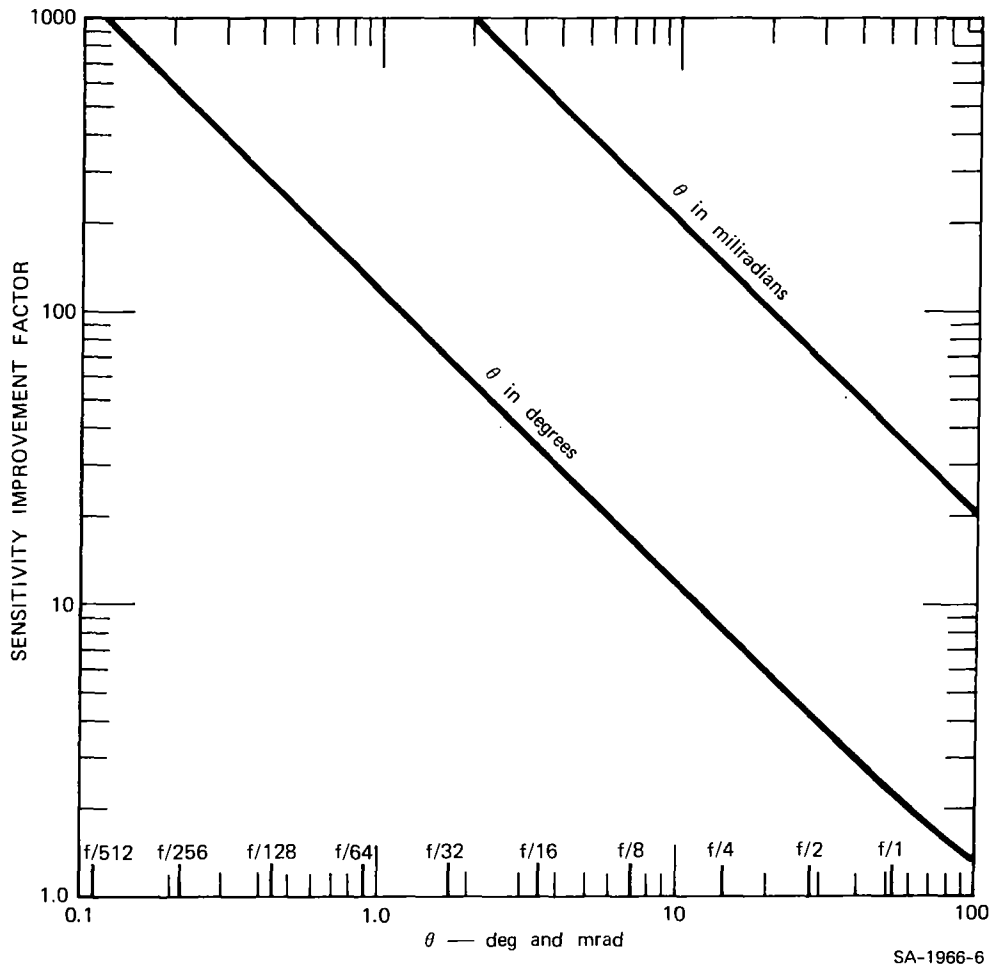


FIGURE VI-8    DETECTOR IMPROVEMENT FACTOR AS A FUNCTION OF FIELD
OF VIEW, θ

154

which establish minimum achievable FOVs for the receiving system.  For
the work reported here, the minimum detector size was taken to be 0.1 mm.
The post-detection bandwidth used for the calculations was 1 MHz.

Another factor that may be significant in detector per-
formance is the noise of the amplifier that follows the optical detector
(Anderson and McMurty, 1966; Melchior et al., 1970).  In photomultipliers,
amplification is accomplished by electron multiplication, which provides
large amplification factors with only a relatively small increase in
noise.  Most infrared power detectors, on the other hand, do not have
internal gain and thus must be followed by a very good low-noise ampli-
fier in order to obtain the high performance levels indicated in Figure
VI-7.  It was assumed in this investigation that adequately low-noised
preamplifiers would be available in order that the optical detector would
determine the noise performance of the overall system.  In practice, this
may require the use of cooled parametric amplifiers or other ultra-low-
noise techniques.

Another type of noise usually associated with the detector,
although not caused by imperfections in the detector, arises because the
optical signal is composed of discrete photons.  The Poisson statistics
of randomly arriving photons lead to a noise level proportional to $\sqrt{n}$,
where n is the number of photons received in a specified time interval.
Thus, the SNR for signal-statistics noise is given by $n/\sqrt{n} = \sqrt{n}$.  This
noise is sometimes a system limitation for infrared detectors but is
more often associated with the use of photomultiplier tubes in the UV
and visible-wavelength ranges.

The level of performance that will be achievable in the
future with narrow-bandwidth, narrow-FOV conventional IR detectors is
difficult to predict because of the large number of different types of
materials and operating modes.  Also, the technology of these detectors

155

is still evolving and a continuously improving performance level can be expected. Specific detector developments, tailored for the detection of specific materials, may yield performance levels that are substantially better than those presently available.

### c.    Other Types of Detector

In comparison with the conventional IR detectors, heterodyne detectors and parametric up-converters of IR radiation to the visible region may provide substantial improvements in performance. Both of these devices are well suited to narrow FOVs and narrow bandwidths, characteristics that tend to minimize the importance of these devices for the more usual wideband blackbody detection applications. In addition, microwave biasing of photoconductors to reduce contact noise has also been used to improve the performance of photoconductors, although the complexity of the method tends to discourage its use for mass-produced IR detectors (Sommers, 1970).

Heterodyne detectors use a nonlinear optical element in which the received optical signal is mixed with an optical local oscillator to produce a radio-frequency (RF) output signal. This RF signal is then amplified and detected. The operating principles are similar to those of radio-frequency superheterodyne receivers. The primary increase in sensitivity that is obtainable through heterodyne detection is due to the narrow bandwidths and smaller FOVs that are achievable through this technique. The optical bandwidth of the device is essentially equal to the bandwidth of the RF amplifier following the optical mixer. This bandwidth can be many orders of magnitude smaller than that obtainable through conventional optical filtering techniques, thus reducing the background noise to very low values. The internal noise levels can be reduced to values equal to or less than those obtainable in conventional IR

detectors. The limiting noise level for both the conventional detectors and the optical mixers is the thermal noise associated with the detector resistance, which can be reduced through cooling. Adequate nonlinearity must be maintained in the optical mixing element at low temperatures to realize the benefits of reducing internal noise.

Thus, the heterodyne detector appears to offer the best performance potential obtainable with any of the alternative detector techniques. However, because of the extremely narrow bandwidths involved, the lasers used in such a system must also have extremely narrow bandwidths in order for the full laser energy to be effective in the system. This changes the laser evaluation criterion from the maximum power output per pulse to the maximum energy per unit frequency interval. Therefore, better performance might be achievable with a heterodyne receiver and less laser power, providing the bandwidth can be narrowed by a factor larger than the laser power reduction.

The limits on bandwidth are dictated by the pressure-broadened line width and the range resolution required for pulsed systems. The pressure-broadened line width of typical IR absorption lines is approximately 3 GHz. System bandwidths larger than this would have part of their energy outside the absorption band and thus would not be effective. This sets an upper limit on the bandwidth required for the system. The lower limit is set by the bandwidth required to achieve the desired range resolution. (A bandwidth of 1 MHz provides a range resolution of approximately 150 m.) It is also possible to operate CW range-resolved systems in which narrower bandwidths can be used. These systems involve integration of the signals for a time span, however, and their use for satellite-based systems has not been fully investigated. For the present purpose, the 1-MHz bandwidth is considered to be the minimum required to achieve the desired range resolution.

Optical heterodyne receivers have been built at several laboratories and have achieved performance levels within less than a factor of 2 of the theoretical minimum, the photon-noise limit. Some have been used in operational systems. However, the frequency stabilities and bandwidths of laser transmitters are limiting factors, especially for continuously tunable pulsed sources. The noise effects caused by atmospheric variations may also impose limitations on achievable performance, but information on this topic is limited at present.

Optical parametric up-converters are based on the same type of nonlinear optical interaction used in OPOs. The up-converters provide a theoretically noiseless conversion of IR photons to visible photons. Because visible photons are more energetic than IR photons, this corresponds to a noise-free amplification of the input signal. The conversion of IR photons to the visible region makes possible the use of photomultipliers for detection and signal amplification of the electrons emitted from the photocathode. The primary loss mechanism is the relatively low quantum efficiency of photocathode surfaces. The use of photomultipliers also permits photon counting to be done in the IR region through the up-conversion of single IR photons. The primary disadvantage of up-converters is that the fractional bandwidth is approximately 0.1% to 0.01%, which does not provide as high a background rejection as would be available using heterodyne detectors or, in some cases, from the 0.0075% bandwidth available with the Carson Skyspear Ⓡ filter techniques. Also, the technology of up-converter construction is not as advanced as other optical techniques, particularly optical heterodyne detection, and thus requires additional development to reach the high levels of performance that are theoretically available.

A detailed investigation of the performance capabilities of the advanced techniques discussed above was not possible under the

present contract. However, since heterodyne detectors have closely approached the photon noise limit, it was assumed in the calculations that lidar sensitivity would be limited by photon fluctuation noise rather than internal detector noise.[*] A more detailed investigation of the use of these nonconventional IR detectors to determine the increase in performance level that could be achieved would be beneficial in determining the future performance level that could be achieved for realistic IR lidar systems. It would be important, however, to keep in mind the specialized requirements for this particular detector application. Many heterodyne detector systems appear to have been developed specifically for communications applications and may not be entirely suitable for use with active lidar remote-sensing systems.

### 2. Other Receiver Optical Components

The primary function of the receiving optical components is energy collection. Images are not required at any point in the lidar system. Hence, some of the optical-design requirements can be less exacting than for imaging systems. The receiving optical system should be designed for collecting the received energy over the smallest field of view that allows a reliable mechanical alignment of transmitter and receiver beams to be maintained. The transmitted beam is normally somewhat narrower than the receiver beam so that some misalignment can be tolerated. Values of 0.1 to 1 mrad were chosen for the receiver field of view for the system calculations because values of slightly less than 1 mrad can be maintained consistently with the lidar system now in use; therefore, this range of values seemed to be reasonable for both sattelites and aircraft.

---

[*] This assumption is indicated for those detailed system-performance analysis runs that are labeled as using heterodyne detectors in Figures VII-8 and VII-9.

Large f-number optical receiving systems aid in the narrowband optical filtering that is necessary for reducing the background light level. These filters achieve their narrowest bandwidth when parallel beams of light pass through the filter. The optical system should be designed to achieve this condition as closely as possible.

Increasing the size of the receiver aperture increases the SNR if the system is limited by internal noise. Once the background noise exceeds the internal noise, however, the system becomes background-limited, and further increases in receiving aperture will not increase the SNR. Under some conditions, it may still be advantageous to increase the area of the receiving aperture because the detection probability can be improved with a larger total collected signal. This type of improvement would require a more detailed noise and signal analysis, taking account of the statistical properties of both signals and noises. This level of detail is not necessary to determine the general feasibility of the concept of using lidars for remote measurement of gases. It is only necessary to provide a more precise specification of the errors that could occur in operational systems.

With only one exception, none of the other optical components required for an airborne or satellite-borne lidar instrument present any special requirements, other than those normally associated with aircraft and space operations. The exception is narrowband interference filters. The bandwidth assumed for many of the computations is 0.0075%, which is only 0.04 nm (0.4 Å) in the center of the visible spectrum. The Perkin-Elmer Corporation markets filters having approximately this linewidth and fairly good transmittance ($\sim$ 30%) for use in the visible and infrared regions of the spectrum. Carson Astronomical Instruments, Inc., of Valencia, California, also has a line of filters with subangstrom line-widths and good transmittance ($\sim$ 50%) for use in the visible region.

However, comparable filters seem not to be available for IR and near-UV wavelengths. Conversations with personnel from Carson Astronomical indicated a high probability that with additional research the applicable techniques could be extended into these spectral regions. This seemed to the authors to be a reasonable forecast of a future capability, but linewidths of 0.0075% cannot be considered as assured performance levels for all wavelenghts of interest.

### 3. Background Radiation

A receiving telescope pointing downward from a platform at some specified altitude has in its field of view a portion of the earth and of the atmosphere, both of which can emit or scatter optical energy. In the daytime, solar energy scattered by both the earth and the atmosphere is dominant from the near-UV into the near-IR. At longer wavelengths, thermal radiation from the earth is more important.

Background radiation can arise from many sources (see Kruse, 1962; Valley, 1965; Vassiliadis, 1965), several of which are illustrated in Figure VI-9. This figure also shows the very large dynamic range of the background radiation level, varying over approximately 12 orders of magnitude from a condition of viewing the sun to viewing a dark rural nighttime sky. The standard background conditions chosen for this project are a sunlit earth having an equivalent black-body temperature of 288 $^\circ$K. This background was chosen because it represents the highest value that will normally be encountered when a satellite or aircraft lidar system views the surface of the earth.

As noted earlier, the amount of background radiation admitted to the detector of the lidar system can be reduced by using a narrow field of view and a narrowband interference filter in the receiving system.
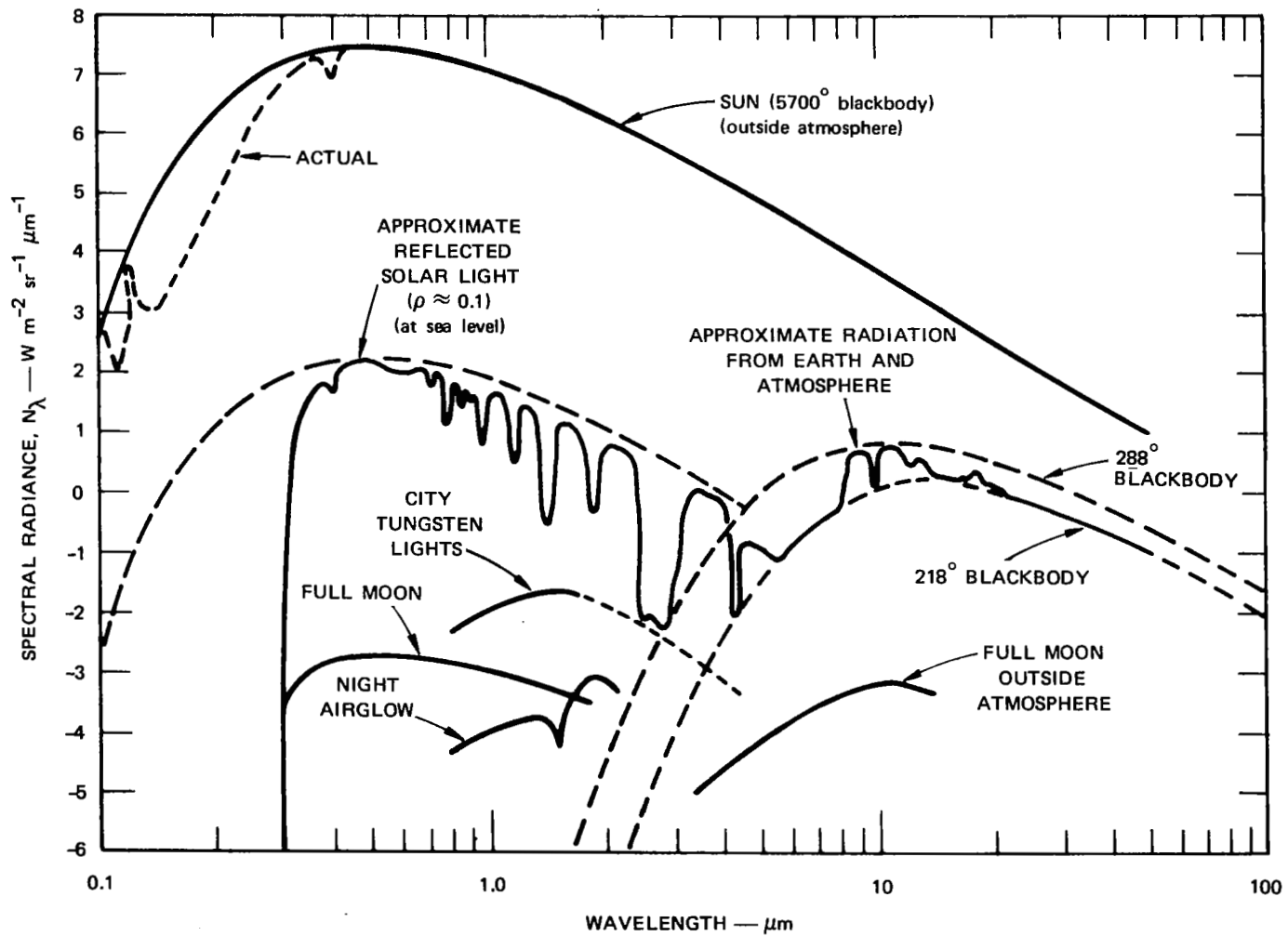
161

FIGURE VI-9   TYPICAL BACKGROUND RADIATION LEVELS

Two spectral regions seem most desirable for operation from the point of view of minimizing the background radiation. The first is in the UV from approximately 200 to 300 nm, where the ozone layer provides a dark background for aircraft altitudes below the stratosphere. The second is around 3 μm in the infrared, where the solar radiation has dropped off considerably from the level in the visible region and the 288 °K background radiation has not yet reached a peak signal level. The power density, $P_B$, at the receiver due to this background radiation from the earth is given by

$$P_B = \frac{B_R A_v \Delta\lambda}{R^2} \text{ watts} \qquad \text{(VI-6)}$$

where

$B_R$ = Spectral radiance in the field of view, watts/m$^2$/μm/ster

$A_v$ = Area of radiating body in the field of view, m$^2$

$\Delta\lambda$ = Optical-filter bandwidth, μm

$R$ = Distance (range to earth), m.

Nighttime operation is possible for some systems that are rendered inoperable by the large daylight background. These obviously must be systems that operate at wavelengths shorter than 3 μm where solar radiation is the predominant background source.

The reflection coefficient of the earth is a complex function of the material surface being viewed and of the wavelength (Valley, 1965; Evans et al., 1966). Most materials and wavelengths can be accounted for by a range of reflection coefficient from 0.01 to 1. A large number of materials have reflection coefficients of approximately 0.1 over a wide range of wavelengths. For the purposes of this report, the terrestrial surface is assumed to be a Lambertain reflector having a reflection

coefficient of 0.1 at all wavelengths. With this assumption the spectral radiance can be calculated from the irradiance by

$$B_r = \frac{Ir}{\pi} \qquad\qquad (VI-7)$$

where

I = Irradiance

r = Reflection coefficient.

## D. Electronic and Mechanical Components

Only two other groups of components--the scanning optical system and the data system--offer enough potential complexity to cause concern about operational feasibility.

The transmitting and receiving telescopes must maintain alignment as they are scanned back and forth at right angles to the ground trace of either a satellite or an aircraft. A receiving telescope area of 1 $m^2$ was assumed for most satellite-based system calculations. This diameter could be reduced to approximately 0.3 $m^2$ at the cost of a ten-fold increase in transmitted power level and may have to be reduced to 0.1 $m^2$ for heterodyne detectors. This trade-off appears feasible for aircraft but not for a satellite at 166 km.

A non-imaging scanning telescope one meter in diameter is a sizable item of optical equipment for either an aircraft or a satellite, but several studies have concluded that even larger optical systems are now feasible. The most stringent operational requirement arises in the case of a satellite where scanning through angles of 146 degrees to 162 degrees at rates of approximately 60 degrees/s is required. But this does not appear to present any insuperable obstacles.

It is not immediately apparent whether the data systems should be configured for large storage capacity with fast readout to fixed ground stations for processing, or for on-board processing to reduce the data-storage requirements. For all satellite applications, except $O_3$ measurements, there would be no point in recording data above an altitude of 30 km because negligible amount of most pollutant materials are present above that altitude. Recording below 30 km would lead to 600 range cells per pulse pair at a range resolution of 0.1 km. Digitizing at 8 bits per sample leads to $1.44 \times 10^5$ bits/s at 30 Hz. Conventional 9-track computer tape stores $1.28 \times 10^4$ bits/inch, so that a tape speed of 11.25 inches/s would suffice. A standard 400-foot reel would thus last 40 minutes, requiring 2.2 reels per orbit or 36 reels per day. If the seven NASA ground communication terminals now in use* were uniformly spaced, fewer than six tapes would be required. Thus, ten tapes seems to be a reasonable estimate. Though this is a large number, it does not appear to be an excessive requirement, especially in view of the fact that cloud cover would greatly reduce the amount of useful tropospheric data that could be taken. A recent proposal for a comparable satellite data system, including telemetry equipment, estimated a weight of approximately 100 lbs and power consumption of 200 watts.

The amount of data to be stored could be reduced by partial on-board processing, although this may restrict subsequent use of the data for some uses. Since the data storage and dumping requirements appear reasonable, it seems doubtful that complete on-board processing would be advantageous. The requirements for aircraft operation could certainly be met by storage for later processing on the ground.

---

*Some of these stations apparently are being closed.

There are no other electronic component requirements for either airborne or satellite-borne lidar equipment that apparently cannot be met with state-of-the-art technology.

# VII   DETAILED PERFORMANCE CALCULATIONS
## AND TRADE-OFF STUDIES

## A.   Introduction

There are 35 principal environmental and lidar system parameter variables used in evaluating measurement capabilities.   These are:

(1)   Altitude

(2)   Desired material (material to be monitored)

(3)   Desired range-resolution

(4)   Operating wavelengths

(5)   Laser energy

(6)   Area of optical-receiver aperture

(7)   Receiver field-of-view

(8)   Receiver optical bandwidth

(9)   Detector noise level

(10)   System transmission efficiency

(11)   Background light level

(12)   Transmitted pulse length

(13)   Receiver time resolution

(14)   Ground-reflection coefficient

(15)   Receiver electronic bandwidth

(16)   Pulse-repetition frequency

(17)   Material concentrations in the atmosphere

(18)   Aerosol scatter characteristics

(19)   Numerical values for each of the 17 distinct error mechanisms considered.

The number of variables and the complexities of their relationships necessitated analysis by computer, as described in Section VII-C.

For a scanning system, the angle between the line of sight and the vertical direction must be varied in about ten steps. Ten pollutants of interest plus hydrocarbons are listed in Table II-1, and all of them have several absorption bands. One satellite altitude, 166 km, and two aircraft altitudes, 3 km and 12 km, were specified for this study, and a contract modification stated that at least four lines pairs were to be investigated for each gas studied.

Since even a few values for each of these variables would have required an impractically large number of computer runs, it was necessary to make a selection to keep the number of computations within reasonable bounds. The guidance letter of 20 November 1972 recommended that emphasis be placed on $SO_2$, $O_3$, $NO_2$, and aerosols. It was decided to add CO and $N_2O$ to this list and to study $O_3$ in two wavebands to provide data for all of the wavelength regions of interest. Even with only six wavelength regions for study, it became evident that it would be impractical to vary all the parameters over all values of interest.

The primary compromise that was adopted in attempting to find combinations of wavelengths and reasonable system parameters was to emphasize the satellite cases and provide a lesser degree of optimization for the aircraft cases. As a result, many cases were run on the computer in which identical wavelength values were used for both satellite and aircraft altitudes or for both the 3- and 12-km aircraft altitudes where the aircraft wavelengths were different from the satellite-altitude wavelength. This practice provided at reduced cost a large number of data runs for aircraft cases, but many of the values were selected to improve the performance of satellite-based systems. Thus, the aircraft cases should not be considered to be optimized to the degree that the satellite cases are. The results presented here are, therefore, not necessarily representative of the best performance that could be achieved

with aircraft-based systems, nor descriptive of the most reasonable system designs for operation in aircraft. Despite this lack of optimization, however, a high degree of performance is achievable at the present time from the aircraft platform altitudes.

Some of the system variables were either fixed or varied over a limited range in only a few runs. Usually, the performance was calculated for both a single pulse pair and for integration of a reasonable number of pulses (usually between 100 and 1000 pulse pairs). Because of the effects of satellite velocity and the great difficulty of scanning to illuminate the same volume of air in integrating multiple pulses, it was assumed that the multiple-pulse-integration case represented a distributed rather than a single-point measurement. Also, only vertically directed signals were considered on the premise that if vertical measurements proved feasible, scanning could be explored separately, and that if vertical measurements proved infeasible, scanning would not be of interest.

Even with these restrictions, several thousand cases were run and analyzed. To present and discuss the results of all these cases would be an overwhelming task. It would also serve no useful purpose, because many of the runs resulted in one or more of the error curves being at an unreasonably high level, and thus unacceptable, at all ranges. In addition, several changes were made in the computer program during the investigation to correct errors, to make it more facile or versatile, or to aid in interpreting the results. Despite these difficulties, something of value was learned from nearly every run, including even ones that were made before the program errors were corrected, since only parts of the data were affected by the errors. However, the different sets of data all have some features that would mystify most readers, and an unreasonable amount of text would be required for explanation and clarification.

Thirty-three cases (plus supplementary material) have been selected for presentation and discussion from among the many that were run. Some of these are the end results of extensive trade-off studies that the authors believe adequately explored the reasonable alternatives. Others are the results of incomplete trade-off studies that were terminated because they did not seem to be leading toward very promising or encouraging performance capabilities. In some instances, studies were terminated because of depletion of financial resources.

The method of approach to these trade-off studies entailed development of an initial system configuration based on current technological capabilities for each combination of pollutant and absorption bands. Examination of the absorption spectra of the pollutants and the atmospheric gases led to selection of a set of promising operating wavelengths. These trial systems were tested and evaluated on the computer for each pair of wavelengths. The results were then studied and used as bases for judicious changes in one or more system parameters, including the operating wavelength. The cycle was then repeated a number of times. The initial intent was to iterate this process until a satisfactory combination of parameters and performance capabilities was achieved or until it could be seen that no prospectively feasible set of lidar system characteristics would provide acceptable performance. This plan was modified somewhat to include an effort to determine what would be needed to achieve at least a marginal capability, even if this required component characteristics far beyond reasonable projections of future technology.

It seems simple, in principle, to devise logical and straightforward procedures for developing an optimum set of system parameters for each application. In practice, this proved to be impractical because of the complex interrelationships among the several measures of performance capability and the various system parameters. Even if one is intimately

familiar with the computer program and how it processes both input information and stored data, it is very difficult to determine from a printout sheet or the plotted graphs which parameters to change and by what amounts. After running hundreds of cases, the project staff members developed a degree of skill in successively choosing parameters in a way that evolved toward a desired objective in a reasonably efficient and direct manner. This is not a readily describable or transferable skill, but it is believed that some of the ingredients will be made apparent by the following discussions.

The results of the calculations for the various materials and platform altitudes are presented in the following order in this chapter:

    (1)   Results for satellite gases (altitude = 166 km)

        &bull;  Range-resolved measurements
           $(O_3[UV], O_3[IR], NO_2, SO_2, CO, N_2O)$

        &bull;  Column-content measurements

        &bull;  Cloud measurements

        &bull;  High-altitude aerosol measurements

    (2)   Results for aircraft cases

        &bull;  Range-resolved measurements from 12 km

        &bull;  Range-resolved measurements from 3 km

    (3)   Ground-based upward-looking measurements.

Graphs of the results of the computer runs are presented as complete sets in a single illustration for each case so that the reader can examine each case without turning several pages. The format for this data presentation is given in Section VII-D.

## B.   System Trade-Off Considerations

One of the most important overall system considerations is the choice of absorption coefficient to obtain the maximum sensitivity for the range

of operation desired. This trade-off is needed because of the behavior
of the return-signal strength with respect both to range and to the values
of the absorption and scattering coefficients of the material of interest.
Before proceeding to the more difficult differential measurement, it is
useful to examine this effect in terms of a conventional backscatter lidar
system operating at a single wavelength.

Consider a conventional lidar system receiving signals backscattered
from a scattering medium having a wide range of scattering coefficients.
Increasing the scattering coefficient increases the percentage of back-
scattered energy but also increases the attenuation of the transmitted
beam. The effect of this variation in scattering coefficient is shown
in Figure VII-1. An increase in scattering coefficient is shown to



SA-1966-10
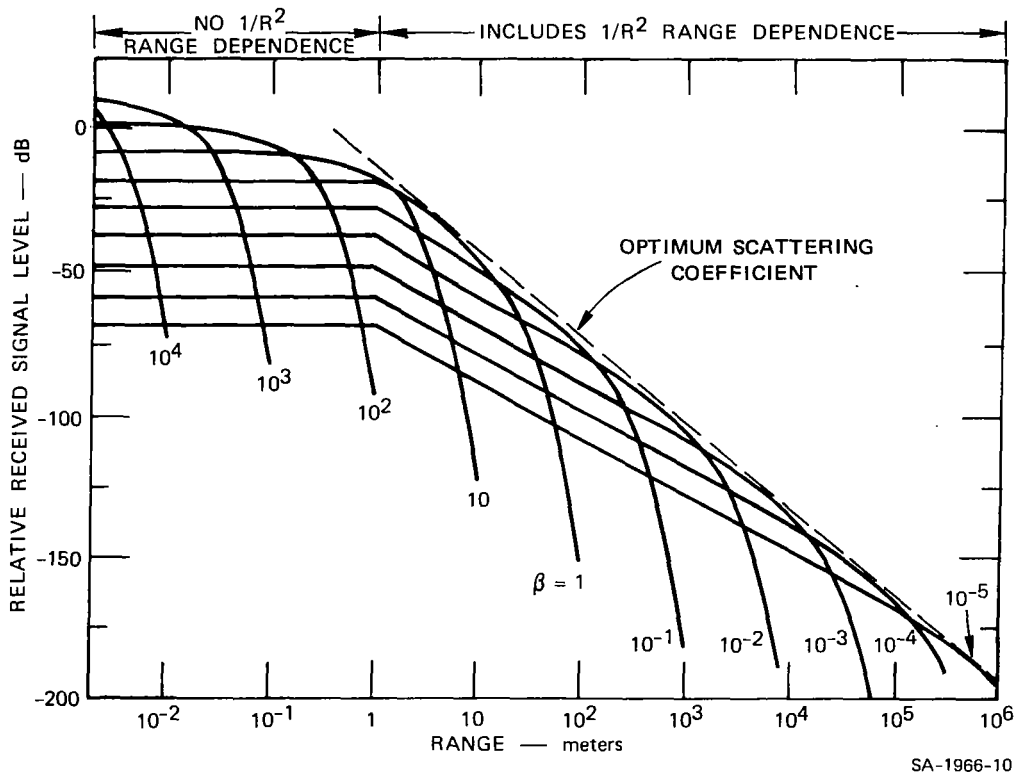
FIGURE VII-1    RECEIVED SIGNAL AS A FUNCTION OF RANGE FOR A VARIABLE-
SCATTER MEDIUM

172

produce larger return signals for short ranges; however, at longer ranges the increasing attenuation due to scattering reduces the value of the return signal to less than what would have been obtained with a smaller scattering coefficient. It is apparent that for operation at a particular range, there is an optimum value of scattering coefficient that maximizes the return signal. Smaller values would not scatter a sufficiently large portion of the signal and larger values would produce too large an attenuation in the intervening atmosphere. The optimum scattering cross section as a function of range is shown by the dashed line in Figure VII-1.

A similar effect occurs for the differential-absorption measurement, in which it is desirable to maximize the differential absorption per range cell without causing an excessive attenuation in the intervening medium. Figure VII-1 becomes also relevant to the differential-absorption case if the scattering coefficient is replaced by the differential-absorption coefficient for the gas to be measured. However, the result can be interpreted literally only for very special cases. In most cases other factors have a substantial influence on the optimum absorption coefficient for a particular range, and these factors cannot be shown in a single, two-dimensional graph. These additional factors include, for example, the presence of a substantial absorption coefficient that is independent of wavelength. This additional attenuation can reduce the signal level and in some cases can force a choice of wavelengths that offer substantially less differential absorption in order to reduce the total attenuation to an acceptable level. Also, the type of limiting noise or error-producing factor must be taken into account because some errors, such as scintillation, are independent of signal-strength while others, such as background noise, can be reduced by increasing the transmitted signal strength. Thus, the selection of an optimum differential-absorption coefficient is not as simple as a choice of optimum backscattering

173

coefficient for conventional lidar systems. Fortunately, judicious use of a computer program for a series of different wavelength pairs can indicate the best choice of differential-absorption coefficient for a given material measurement.

Another system trade-off involves the transmission of maximum energy without exceeding eye-safety limitations. The parameters involved are discussed in an earlier section on eye safety. The design procedure to obtain maximum performance in this trade-off is to attempt first to achieve background-limited operation, and then to set the field of view to attain an eye-safe energy level. This system will then achieve the eye-safety-limited signal-to-background-noise ratio, independently of field of view, operating altitude, or transmitted energy, providing the eye-safety limit is maintained.

The system design is, of course, subject to all the technical trade-offs normally encountered in optical and lidar systems that are intended to operate over the wide wavelength ranges and under the environmental conditions that would be encountered. Detailed discussion of these other trade-offs seems superfluous here, since they are considered at length in many standard references.


C.   Computational Procedures

An extensive computer program has been prepared by SRI to solve a variety of problems associated with the transmission of optical signals through simulated atmospheres. It is called the Modular Atmospheric Propagation Program (MAPP). The program is in modular form and for this project has been set up to do three types of calculations. These are (1) atmospheric transmission calculations, (2) lidar-system performance calculations, and (3) error analyses for the differential-absorption technique. A brief description of what MAPP does is provided here.

174

The atmospheric propagation calculations are of two types--absorption
and scattering. Because the calculations must include the entire atmo-
sphere from the ground up to satellite altitudes, extensive stored models
for the atmosphere are used to account for variations in temperature,
pressure, and material concentration of both naturally occurring materials
and pollutant materials. Standard-atmosphere profiles are used for the
naturally occurring materials and for uniformly-mixed pollutant materials.
Exponential-decay models are used for pollutant materials that are not
uniformly mixed. A capability for offset exponential decays, starting
at a particular altitude, is incorporated to approximate the conditions
that occur under atmospheric inversions. Layers of pollutants or clouds
can also be included at appropriate altitudes.

Attenuation calculations are done by first calculating the attenua-
tion from each material for each range cell of interest, taking into
account the appropriate profile data. These separate attenuations are
then combined to get partial or total attenuations for other parts of
the program. In addition to the atmospheric-model-profile information,
the spectral-attenuation characteristics for each material are also
stored in the program data bank. These spectral data appear in two
forms: continuous spectrum information, primarily for the UV and short-
wavelength visible regions, and line absorption data, primarily in the
IR and long-wavelength visible regions. Attenuation from aerosols is
taken into account by using an appropriate aerosol model and concentra-
tion. Attenuation from Rayleigh scattering, which is significant pri-
marily in the UV, is also included.

The continuous spectrum information is stored as a table of cor-
responding values of absorption coefficient and wavelength. Attenuations
at intermediate wavelengths are obtained by interpolation. The line
data are stored as a table of line strengths, half-widths at half-heights,

and a temperature-related constant, at the corresponding wavelengths. These data are then used to calculate and absorption-line profile taking into account the appropriate pressure and temperature dependence for the material. These absorption-line profiles are assumed to follow the usual pressure-broadened, Doppler, or Voight shapes (Long, 1966). The pressure-broadened shapes are used for altitudes below about 14 km, the Doppler shapes for altitudes above about 60 km, and the Voight shapes between approximately 14 km and 60 km.

The second type of atmospheric propagation calculation is scattering. Both gaseous (Rayleigh) and aerosol (Mie) scattering are included. Only single scattering is accounted for in the present program configuration. Multiple scattering, which can be significant in denser aerosols and clouds, is not considered. The primary scattering process for most of the visible and IR regions is aerosol scattering.

The scattering properties of aerosols have been studied by many people (see, for example, Plass, 1966; Deirmendjian, 1964; Deirmendjian et al., 1961; Rusk, 1971; Holland and Draper, 1967; Holland and Gagne, 1970; Bullrich, 1963; McCormick et al., 1968; and Dave, 1969). Various size-distribution models have been proposed to describe the scattering characteristics of aerosols. Deirmendjian (1969) probably offers the most comprehensive treatment of the subject. However, since there are many types of aerosols, and wide ranges of variability within each type, there is a problem in deciding which model to use for system performance calculations. For polluted urban atmospheres, a heavy haze model would be appropriate, but there are both continental and maritime varieties. For relatively unpolluted rural areas over land masses, a light continental haze model seems more appropriate. The primary one used in this study is the maritime haze because of the global nature of this application.

It should be noted that the experimental basis for these aerosol models is limited to measurements made in the near-UV, visible, and near-IR spectral regions. Thus, there is no assurance that calculations at longer IR wavelengths based on these models will yield valid results. Apparently there is little long-wavelength experimental scattering data for aerosols. Hence, the only alternative for system performance calculations is to use the existing models and be prepared to alter the conclusions in the future if experimental data are found to be at variance with these models. The scattering models used are from Deirmendjian (1969) and are summarized in Figures VII-2 and VII-3. These figures show the two types of scattering data that are significant. Figure VII-2 shows the volume backscattering coefficient, which determines, in part, the backscattered laser signal strength. Figure VII-3 shows the extinction coefficient, which determines the attenuation of the propagating optical beam caused by Mie scattering. These figures show the scattering properties of the four models used in the calculations--cumulus clouds, high-altitude or cirrus clouds, tropospheric or low-altitude aerosols, and stratospheric or high-altitude aerosols. The two haze models follow the often-used $1/\lambda$ approximation for the wavelength variation in the visible region, but beyond 2 to 3 $\mu$m there are large changes due to the varying index of refraction of water. The extinction curve for Rayleigh scattering is also shown; its importance in the UV is evident. Scattering at angles other than $180^\circ$ is not considered in the present program configuration.

The aerosol profiles are handled in two ways by the MAPP computer program. The first way utilizes a composite aerosol distribution combining standard atmosphere data and new data for stratospheric aerosols, which is believed to represent high altitudes better than the older standard atmosphere data. The aerosol concentration profile from zero to 8 km was taken from Valley (1965). Balloon and lidar data taken at
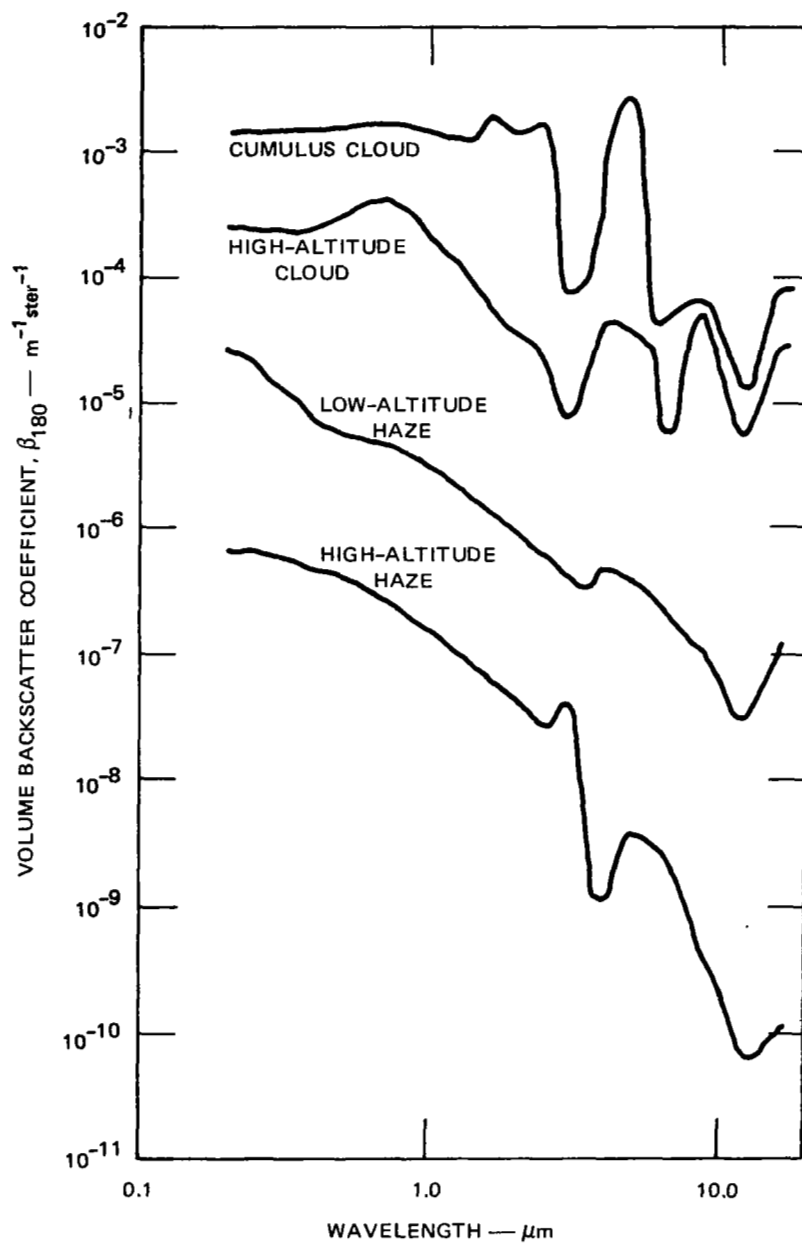
177

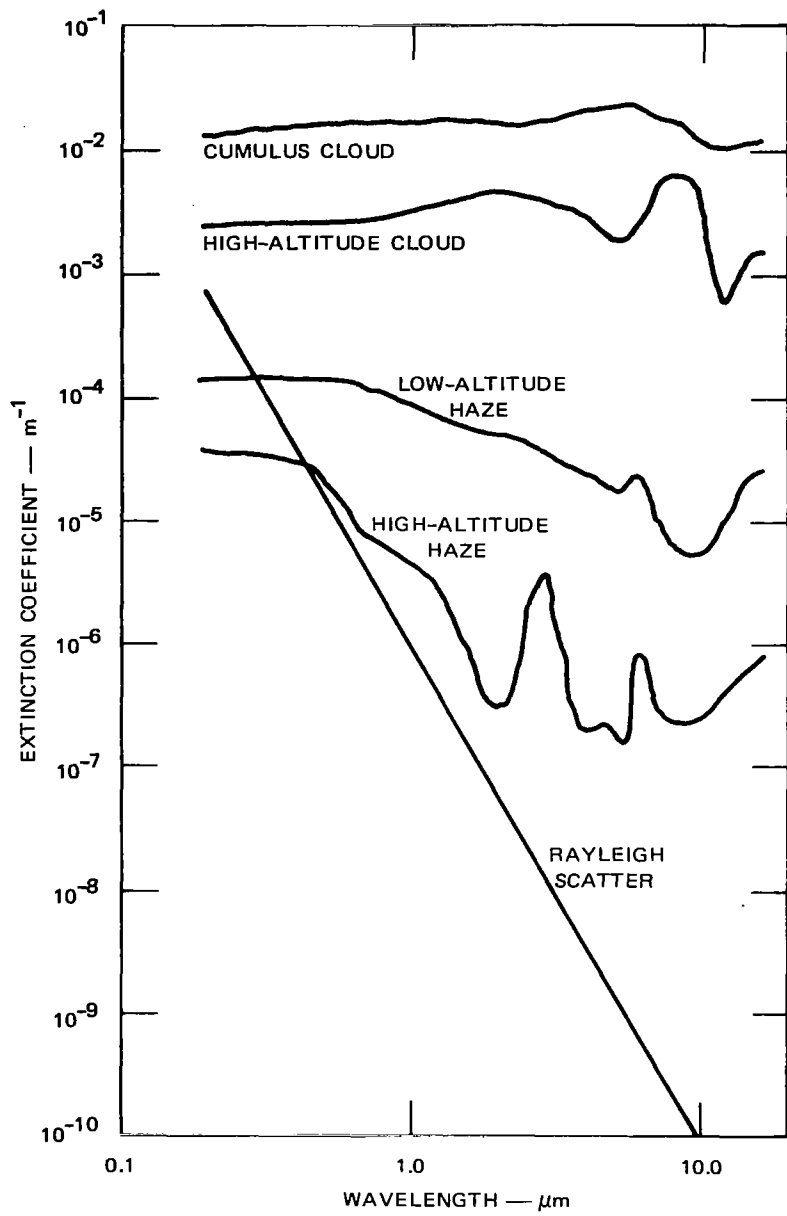FIGURE VII-2   AEROSOL VOLUME BACKSCATTER COEFFICIENT AS A FUNCTION OF WAVELENGTH

178

FIGURE VII-3   AEROSOL EXTINCTION COEFFICIENT AS A FUNCTION OF WAVELENGTH

Laramie, Wyoming, under the Climatic Impact Assessment Program (Melfi et al., 1973) in September 1972 were used for altitudes above 8 km. The fine structure that appears in the stratosphere on these records was smoothed. An exponential decay was used above approximately 30 km, the limit of the CIAP data. The resulting composite distribution is shown in Figure VII-4. This produces a composite curve similar to that shown for a standard atmosphere (Valley, 1965) with a more accurate representation of the high altitude aerosol region.

The second method for handling aerosols within the MAPP program involves two separate altitude distributions, first, a low-altitude



SA-1966-11
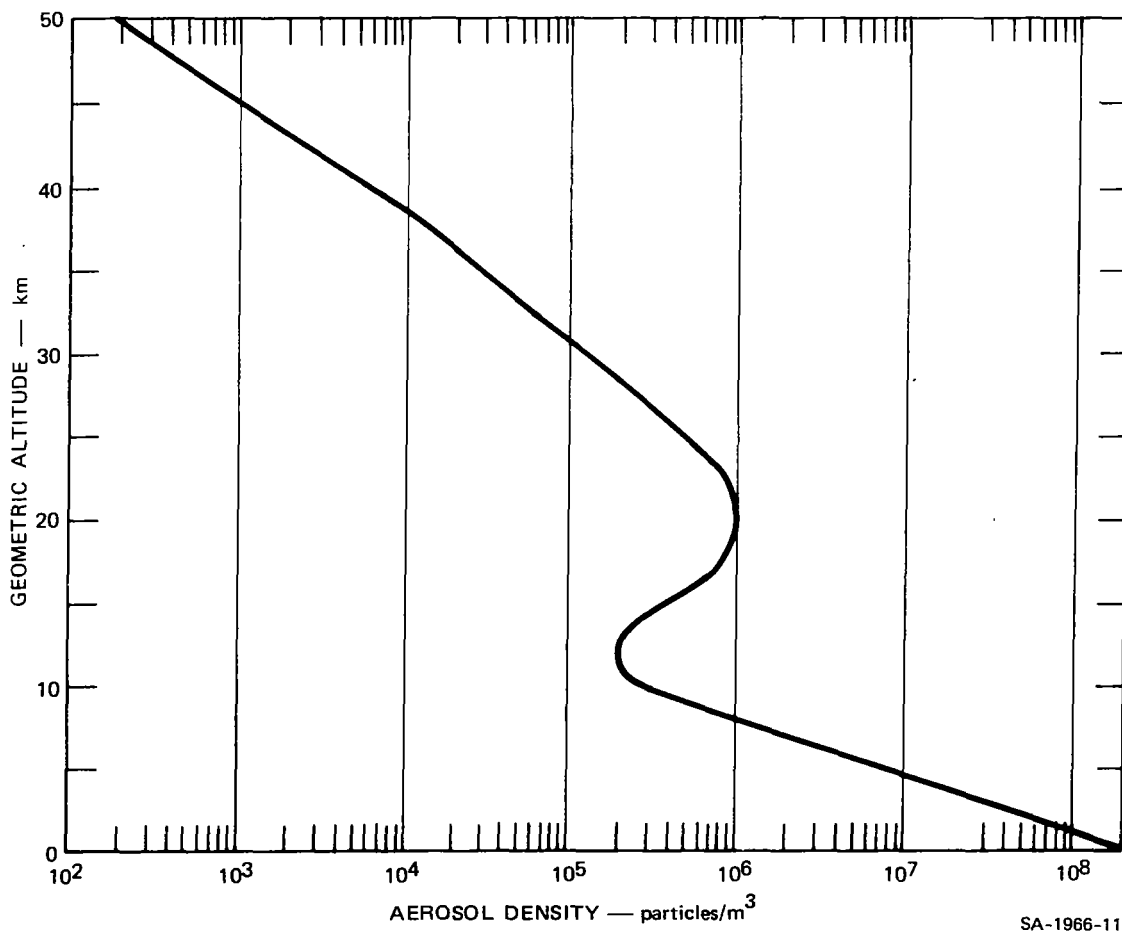
FIGURE VII-4   COMPOSITE AEROSOL DISTRIBUTION

standard atmosphere profile extended in altitude to the stratosphere but not having a stratosphereic bulge, and second, a separate distribution for the high-altitude aerosol extending downward into the troposphere with a decreasing distribution. These two distributions are shown in Figures VII-5 and VII-6. The advantage of the two separate distributions is that different haze models can be ascribed to both the low- and high-altitude aerosol regions, thus giving a more accurate representation of aerosol scattering as a function of wavelength than would be obtained by using the single composite aerosol distribution shown in Figure VII-4. For this reason, most calculations were done using the separate distributions for the high- and low-altitude regions.

Once the scattering and attenuation properties of all materials of interest are determined as a function of distance along the optical propagation path, the system calculations can proceed. It is usually of great interest to know the cumulative attenuation caused by all materials along the optical propagation path as a function of range from the lidar platform location. This information is presented in graphical form for each of the two operating wavelengths. This graph is a plot of cumulative attenuation as a function of altitude and has uniform axes for all cases presented in this report. The attenuation is cumulative, starting at the location of the lidar platform and increasing with increasing distance from that location. Cumulative attenuation is given for both operating wavelengths, as shown by the solid and dotted lines in the example of Figure VII-7. For this example, the lidar is located at an aircraft altitude of 12 km. The attenuation for both wavelengths at this altitude is obviously zero, as indicated by the dip in the curves shown at 12 km in the figure. In some cases the material of interest may extend both above and below the platform altitude. In these cases, the graphs of cumulative attenuation are shown both above and below the platform altitude. In other cases it may be shown only in one direction,
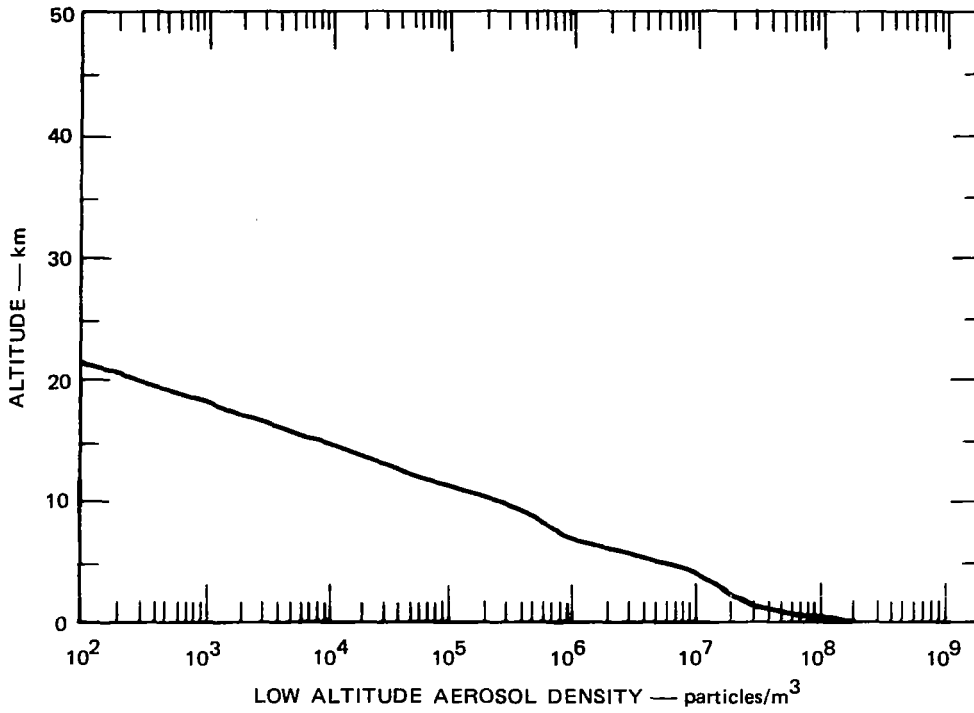
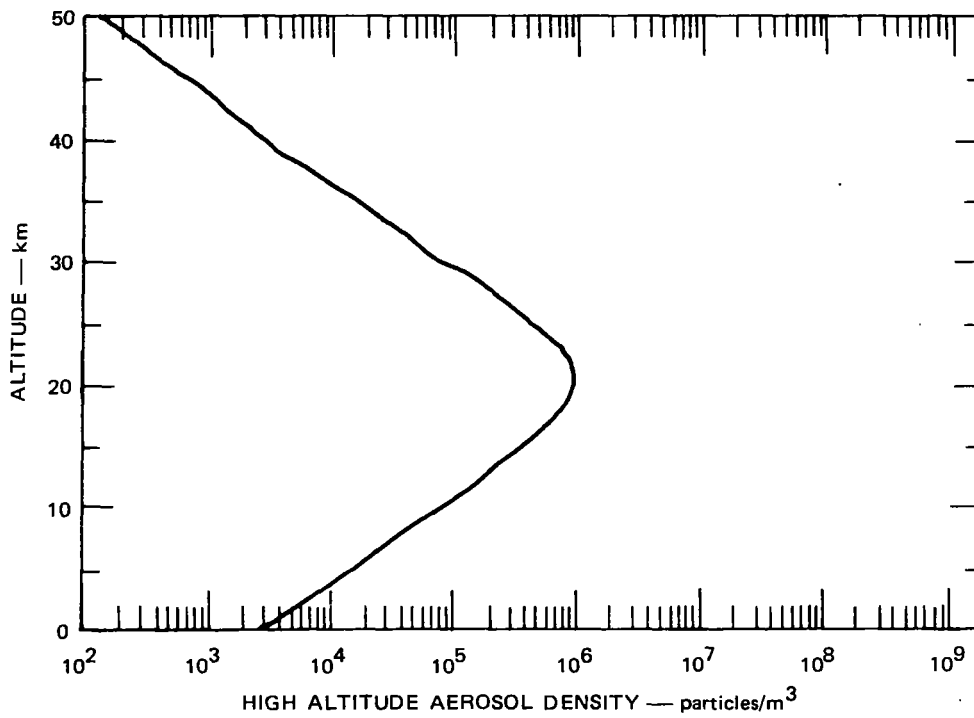FIGURE VII-5    LOW-ALTITUDE AEROSOL DISTRIBUTION



FIGURE VII-6    HIGH-ALTITUDE AEROSOL DISTRIBUTION

182

usually below the altitude of the lidar. Normally, these attenuations are the sum of contributions from all materials existing in the modeled atmosphere. Exceptions to this are indicated in specific cases.

The MAPP computer program, in addition to producing graphs of overall system performance, also produces a large amount of printed "intermediate" output data such as the attenuation and scattering properties of each individual material. Although these intermediate data are very useful in choosing an optimum system configuration for a specific application, the large quantity of data precludes inclusion in this report. Only the final quantities of primary interest are presented.

The system calculations begin with a determination of the received signal strength as calculated by the lidar equation (V-1). This received signal strength is calculated by a straightforward substitution of the appropriate system and atmospheric variables in this equation, and is presented in graphical form, an example of which is shown in Figure VII-8. Again, the graphs of signal strength as a function of altitude have identical axes in order to maintain a uniform graphical presentation throughout the report. The received signal strengths for the two operating wavelengths are shown by the solid and dotted lines, respectively. Unlike the cumulative attenuation, which increases at increasing distances from the lidar platform altitude, the received signal strength decreases with increasing distance from the lidar platform. For short distances away from the lidar location, the $1/R^2$ component of distance variation produces a very rapid dropoff in signal strength. However, this effect diminishes at larger distances. The effect is somewhat exaggerated because of the logarithimic altitude scales used in the graphs.

Note, however, that an interesting difference occurs between upward-looking and downward-looking lidar systems. In downward-looking lidar systems the $1/R^2$ signal-strength variation is largely compensated by the
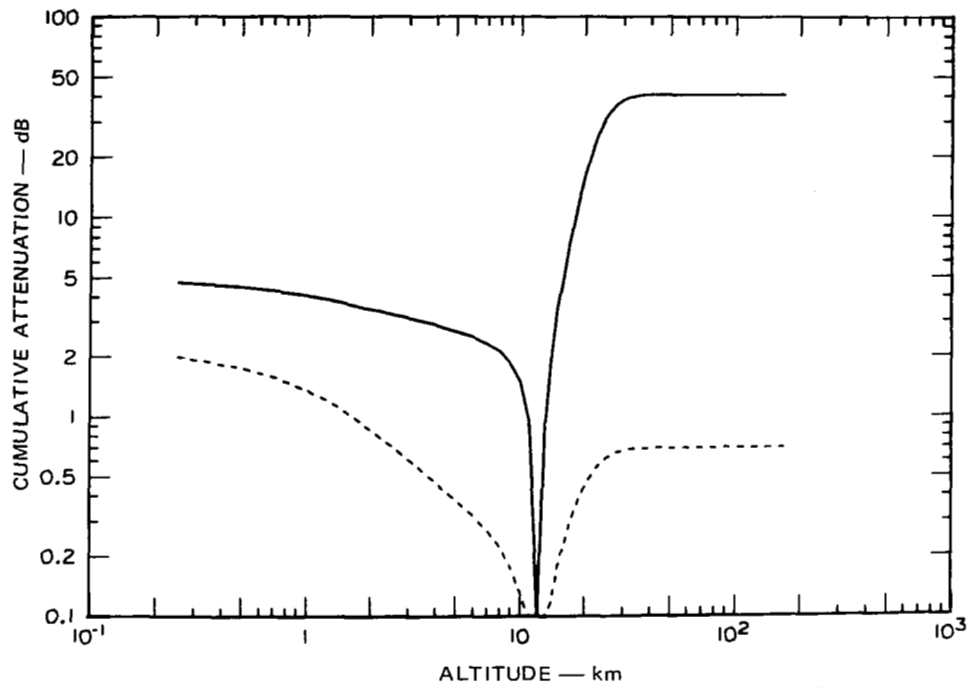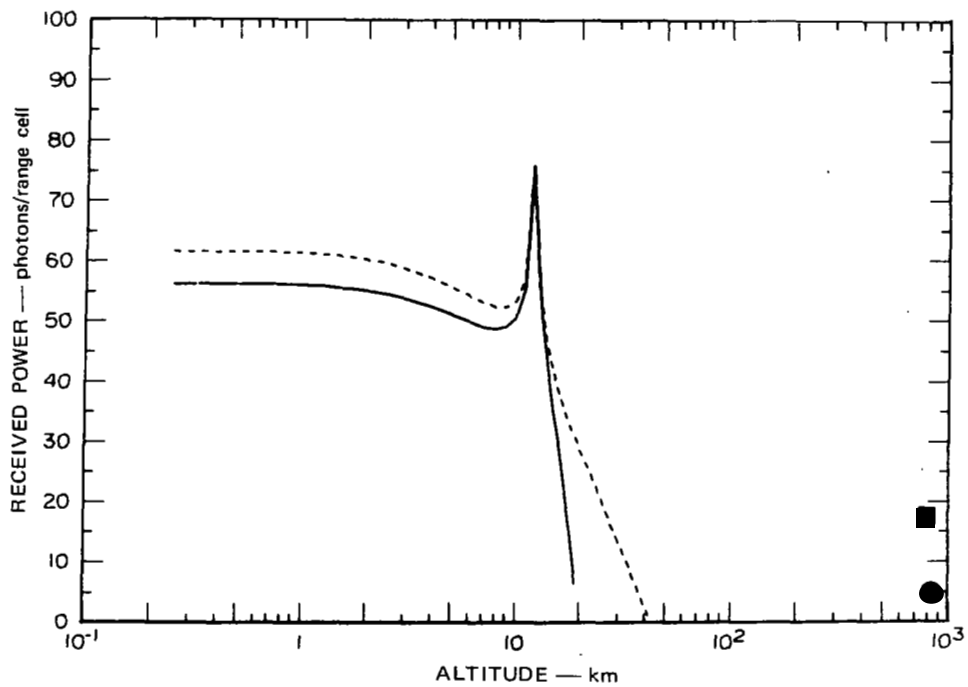
FIGURE VII-7    EXAMPLE OF CUMULATIVE ATTENUATION GRAPH



FIGURE VII-8    EXAMPLE OF SIGNAL-STRENGTH GRAPH

184

increased backscattering that occurs at lower altitudes, thus producing a signal strength as a function of altitude that is fairly constant. For upward-looking lidar systems, however, the $1/R^2$ decrease in signal strength reinforces the decreased amount of backscattering to produce a very rapid dropoff in signal strength as can be seen in Figure VII-8.

In system studies it is often useful to know the SNR that is achievable for the system being considered. For this reason, two optical-receiver noise limits are also presented on this graph. The detector noise described in Section V-C is indicated by the symbol ■ and the background noise is given by the symbol ●. These two symbols appear on the right-hand edge of the figure and are in the same units as received signal strength so that a direct comparison of SNRs as a function of range can be determined from this graph.

At this point the MAPP computer program has stored within it the calculated received signal strength as a function of range that would occur at the two operating wavelengths of an actual lidar system. These calculated signal strengths include the effects of interfering materials, system imperfections, and small differences in atmospheric scatter. It is then possible to process these calculated signal returns in a manner identical to the signal processing that would be accomplished in a real operating lidar system.

The most important calculation done in a real DIAL system is the calculation of desired-material concentration as a function of range using Eq. (V-3). This calculation is done in the MAPP computer program, which contains models for the spatial distribution of all constituents, including the desired material. These models are used in conjunction with a system model to predict the signal and noise levels that would occur in a real system. These simulated signals are then used to predict the distribution of desired material that would be measured by the model

185

system. Thus, two distributions are available within the program, the first being the "actual" distribution of the desired material, and the second being the "measured" distribution as shown in Figure VII-9. The difference between these two distributions is the predicted error in the measurement. In Figure VII-9, the "true" or model concentration is given by the solid line, and the calculated concentration is given by the square symbols. It should be noted that, because of the nature of Eq. (V-3), only systematic errors are indicated in this comparison. Nevertheless, this figure gives a quick indication of the performance capabilities of a system in which no compensation for systematic errors is assumed. This was the case for all systems described in this report except where specific exceptions are noted.

The concentration scale shown in Figure VII-9 extend in both the positive and the negative direction. A negative desired-material
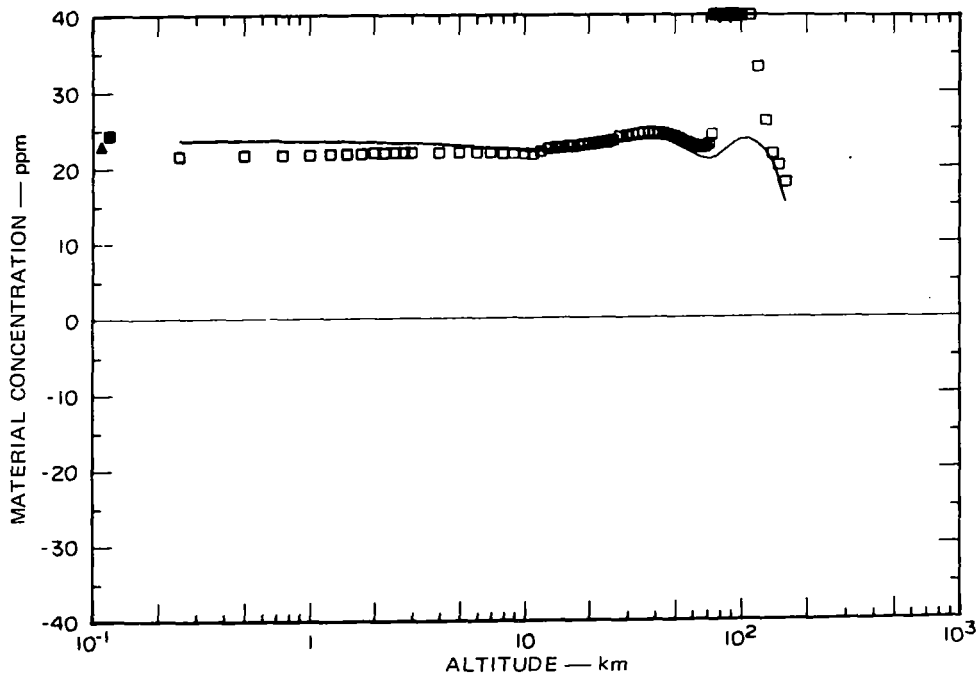


FIGURE VII-9    EXAMPLE OF CALCULATED AND MODEL MATERIAL CONCENTRATIONS AS A FUNCTION OF RANGE

concentration, although not physically realizable, could be indicated by a DIAL system in the presence of severe systematic errors due, for example, to large quantities of interfering materials. A few examples of this phenomenon are shown in the detailed systems analysis of Sections VII-E and VII-F.

In addition to the range-resolved measurements in which material concentration is presented as a function of range, both the modeled and calculated integrated quantities measured by the column-content mode of operation are also indicated in the figure. The calculated column-content concentration is indicated on the left edge of the figure by the symbol ■ and the modeled desired-material concentration by the symbol ▲. Thus, this figure indicates both the column-content and the range-resolved performance capabilities of the system. For a number of reasons, column-content figures are not given for all cases. For example, column-content data are of minor interest for the 3-km cases and for those cases (such as $O_3$) where the concentration varies radically as a function of altitude.

The last major system calculations entail a determination of the magnitudes of errors caused by noise and the other sources of error discussed in Section V-C. These various errors are consolidated into three groups. The total error in each group is graphed in units of material concentration, in parts per million, as a function of range.

The first error group contains the errors due to interfering materials. Because this report considers only those systems in which compensation is not made for errors due to interfering materials, the interfering-material error is primarily systematic in nature. This error component, in units of concentration, is given by Eq. (V-3). The second category comprises errors caused by noise and includes the four noise-error groupings discussed in Section V-C. These errors are random and thus, unlike the interfering-material errors are not correctable by

187

compensation or computation techniques. The third group of errors is called "miscellaneous" and includes all the other errors discussed in Section V-C that are not included in the interfering-material or noise categories. Fortunately, for most system configurations these miscellaneous error sources are less important than either interfering materials or noise errors for the conditions examined in this report.

These three groups were chosen as a compromise between simplicity of presentation and interpretation of the results in terms of corrective measures to improve system performance. Additional data not suitable for inclusion in a report but useful for understanding system performance are provided by the MAPP in the form of printed data.

A typical graph of these three error categories is shown in Figure VII-10. The interfering-material error is shown by the solid line, the noise error is given by the dotted line, and the miscellaneous errors
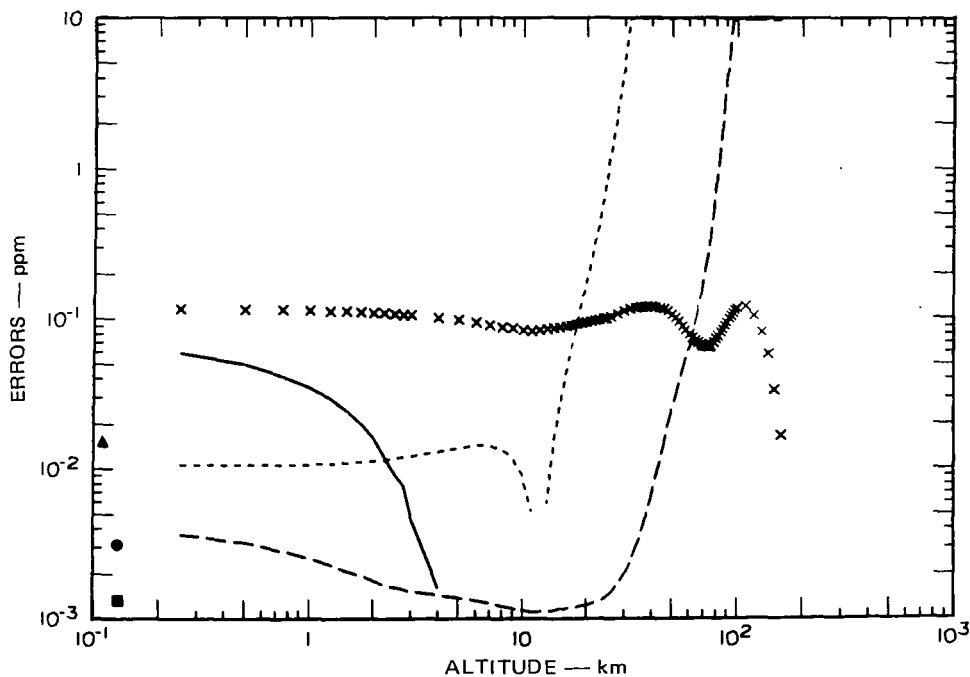


FIGURE VII-10    EXAMPLE OF ERROR-PRESENTATION GRAPH

are given by the dashed line. Also shown on this figure is the assumed desired-material concentration as a function of range, indicated by the symbol X. This inclusion of the model distribution facilitates comparison of the system performance limits, indicated by the three error curves, with the concentration of desired material to be monitored. Thus, when the error in material concentration from any or all of the indicated error categories is well below the modeled concentration, it can be concluded that the modeled concentration would be accurately determined with the specified lidar system.

The minimum detectable material concentration (MDMC) is defined here to be the material concentration that equals the calculated measurement error when the error is expressed in units of concentration. The MDMC can also be interpreted as the minimum detectable change in material concentration. Each of the three categories of error can be considered as establishing an MDMC for that category. The overall MDMC is the rms value of the three components for the statistical distributions assumed in this report.

In addition to the range-resolved errors, the column-content measurement errors are also indicated in Figure VII-10 for the cases where column-content measurements are important. These errors appear on the left-hand edge of the graph and are given by three symbols corresponding to the same error groupings used for the range-resolved calculations. The interfering-material error is indicated by the symbol $\blacktriangle$, the noise error by the symbol $\bullet$, and the miscellaneous errors by the symbol $\blacksquare$. In some cases the numerical values for the individual categories are different from the range-resolved cases.

These detailed numerical error calculations are based on the equations given in Sections V-A and V-B. For most of the calculations, a standard set of input error values was chosen to facilitate comparison

189

of performance for different altitudes and different materials. Exceptions to these standard values are noted in individual discussions of specific cases. These standard error-mechanism values are shown in Table VII-1.

Table VII-1

ASSUMED VALUES OF STANDARD ERROR MECHANISM

| Error Mechanism | Assumed Error Value |
|---|---|
| Power measurement | 0.001 |
| Background fluctuations | 0.001 |
| Backscatter fluctuations ($\delta\beta$) | 0.001 |
| Scintillation fluctuations ($\delta S$) | 0.01 |
| Rayleigh attenuation fluctuations $\delta(\Delta K)$ | 0.0001 |
| Rayleigh density fluctuations $\delta(\rho)$ | 0.0001 |
| Mie attenuation fluctuations | 0.001 |
| Mie density fluctuation | 0.001 |
| Interfering-material attenuation fluctuation | 0.01 |
| Interfering-material density fluctuation | 0.05 |
| Desired-material differential attenuation coefficient uncertainty $\delta(\Delta K_D)$ | 0.01 |
| Transmitted-power normalization error | 0.005 |
| Ground-reflection error | 0.001 |
| Optical-geometry error | 0.0001 |
| Integrated column-content interfering-material random error | 0.05 |
| Range-resolved interfering-material-attenuation random fluctuations | 0.01 |
| Range-resolved interfering-material-density random fluctuations | 0.05 |

In the system calculations it was assumed that the interfering-material error components due to the wavelength dependence of Rayleigh and Mie scattering have been compensated in the measurement procedure; thus, they are not included in the calculations. However, the entire interfering-material error for any or all interfering gaseous species is included in the calculations. It was also assumed that interfering-material compensation is not implemented for these interfering gaseous species, although compensation would be possible in many cases. Estimates of performance possibilities for interference compensation are given on a case-by-case basis in the system-analysis section.

### D.  Data-Presentation Format

Most of the detailed system calculations use identical axes for the graphical outputs produced by the MAPP computer program. This facilitates comparison of the detailed performance summaries for different conditions and different cases and also allows the use of a standard format data for presentation. Each performance summary consists of four graphs of the types presented in Figures VII-7 through VII-10 above. These graphs show the cumulative attenuation, the received signal strength, the calcu-lated and modeled material concentration as a function of range, and the computed errors in the measurements of material concentrations as functions of range. A legend explaining the axes, symbols, and con-ventions used in the performance summaries is presented as a foldout in Figure VII-11.

A summary of the system characteristics for each of the cases analyzed is given in Section VII-H and appears for the 166-km cases in Table VII-8, and for the 12-km and 3-km aircraft cases in Table VII-9. These two foldout tables can be used in conjunction with the systems analyses described in Sections VII-E through G.

## E.  Calculations for Satellite Cases

### 1.  Range-Resolved Measurements

#### a.  Ozone at UV Wavelengths

The first detailed systems analysis in this subsection is for a differential-absorption lidar system that is designed to measure $O_3$ and uses the ultraviolet (UV) absorption region of $O_3$ for monitoring. ($O_3$ also has an infrared absorption region that is discussed in Section VII-E-1-b, below.)  The first system to be discussed is theoretically capable of monitoring $O_3$ both near the ground and in the stratosphere with acceptable performance in both altitude regions.  However, because this system is beyond the projected capabilities of predicted lasers, a second system is described that could measure the upper-atmospheric $O_3$ layer with acceptable errors but which would provide only marginal performance for the low-altitude $O_3$ measurements.

Approximately 10 wavelength pairs were examined in order to find the pair that provided the best performance level for monitoring $O_3$ in the UV from ground level to the stratosphere.  The best pair proved to be 301.6 and 310.9 nm.  This pair provides a reasonable differential absorption for monitoring $O_3$ from the satellite altitude.  The attenuation on the higher attenuation line (there is no peak and valley in this spectral region for $O_3$) is slightly higher than desirable and results in a moderately low signal for that wavelength (301.6 nm).  However, the interfering-material errors for this case are smaller than those for other wavelength pairs, and are minimized because of the larger differential absorption of $O_3$ for this wavelength pair.

The cumulative attenuation for both wavelength locations is shown in Figure VII-12(a).  Note that in both of these curves the cumulative attenuation rises sharply at about 40 km and reaches almost

**Top-left panel** (CUMMULATIVE ATTENUATION — dB vs ALTITUDE—km):
- ——— ATTENUATION AT $\lambda_1$
- - - - - - - ATTENUATION AT $\lambda_2$

**Top-right panel** (RECEIVED POWER — photons/range cell):
- ——— SCATTERED SIGNAL STRENGTH AT $\lambda_1$
- - - - - - - SCATTERED SIGNAL STRENGTH AT $\lambda_2$
- ✕ GROUND REFLECTED SIGNAL AT $\lambda_1$
- ◆ GROUND REFLECTED SIGNAL AT $\lambda_2$
- ■ DETECTOR NOISE LEVEL
- ● BACKGROUND NOISE LEVEL

**Bottom-left panel** (MATERIAL CONCENTRATION — ppm vs ALTITUDE—km):
- ——— MODEL DISTRIBUTION
- □□□□□□□□□□ CALCULATED DISTRIBUTION FROM SIMULATED SIGNALS
- ▲ COLUMN-CONTENT MODEL VALUE
- ■ COLUMN-CONTENT CALCULATED VALUE

**Bottom-right panel** (ERRORS—ppm vs ALTITUDE —km):
- ✕✕✕✕✕✕✕✕✕ DESIRED—MATERIAL DISTRIBUTION FROM MODEL

| COLUMN-CONTENT | ERRORS | RANGE-RESOLVED |
|---|---|---|
| ▲ | INTERFERING MATERIAL | ——— |
| ● | NOISE | - - - - - - - |
| ■ | MISCELLANEOUS | — — — |

FIGURE VII-11    LEGEND FOR DETAILED PERFORMANCE SUMMARIES
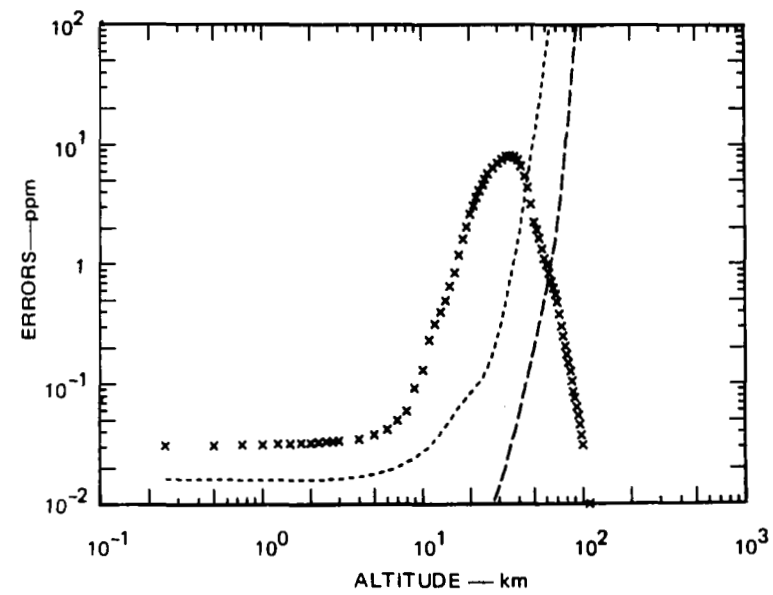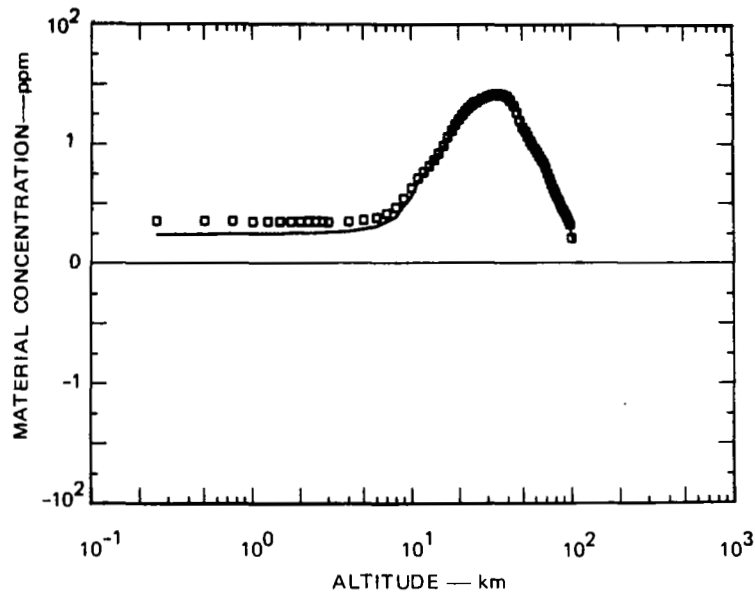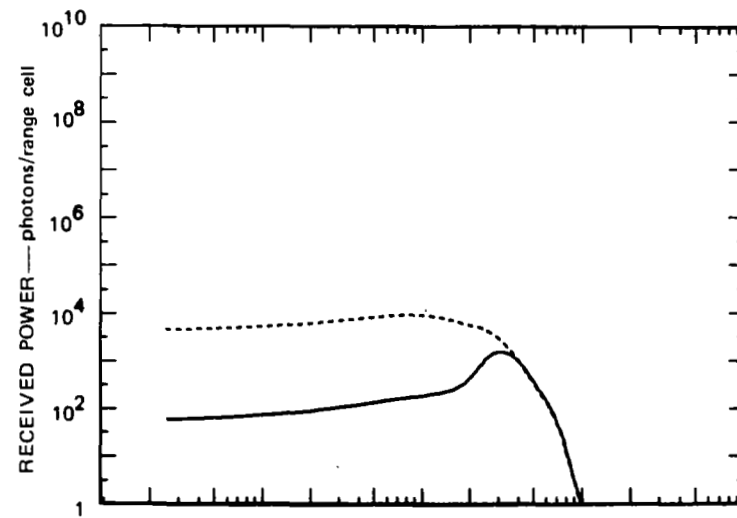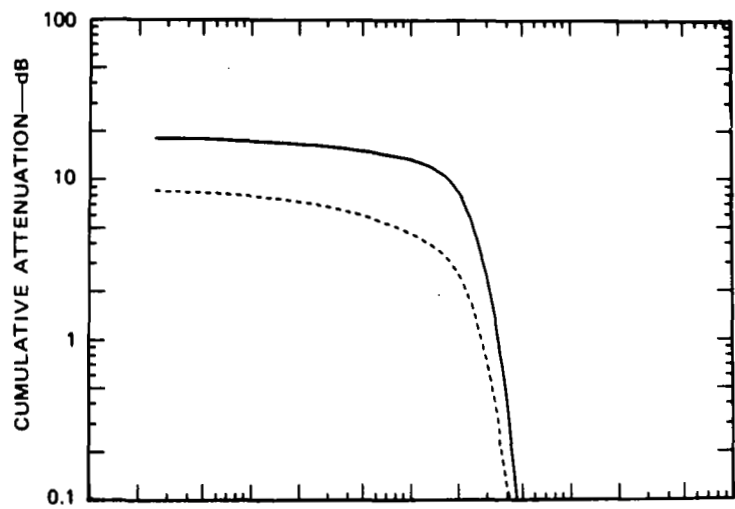
FIGURE VII-12    DETAILED PERFORMANCE SUMMARY FOR $O_3$ AT 300 nm FOR H = 166 km

its highest value at around 15 km. This sharp rise at high altitude is due to the high-altitude ozone layer between 15 and 30 km. This layer contains about four times the amount of ozone in the region below 15 km. Thus, there is about four times as much attenuation in the high-altitude region as there is below 15 km.[*] Note also that at every altitude there is a difference in the cumulative attenuation between the two curves of Figure VII-12(a). This difference is due to the difference in absorption that is the basis for the differential-absorption measurement technique.

The received signal at each of the two wavelengths is shown in Figure VII-12(b). The dotted cruve shows the signal for the wavelength of lower attenuation (310.9 nm), corresponding to the dotted attenuation curve shown in Figure VII-12(a). If this were a single-wavelength lidar system, it would provide good performance for altitudes up to 80 or 90 km, where the signal rapidly decreases to less than 1 photon per range cell. The solid curve in Figure VII-12(b) shows the received signal for the wavelength of higher attenuation, 301.6 nm; it exhibits an unusual peak at about 30 km. This peak occurs because at very high altitudes, the received signal strength increases with decreasing altitude because of enhanced Rayleigh scattering that results from increased atmospheric density. This accounts for the increasing signal level down to about 40 km. From Figure VII-12(a), it is apparent that the attenuation rises rapidly below 40 km. This additional attenuation is caused by $O_3$ and produces a rapid decrease in received signal power down to about 15 km. In the high-altitude ozone layer, the attenuation increases more rapidly than the backscatter signal, thus producing a

---

[*] A typical behavior for cumulative attenuation in which a high-altitude layer is not present is shown later in Figure VII-18.

decrease in the received-signal intensity. Below the high-altitude ozone layer, at about 15 km, the received signal stays almost constant down to the ground.

The large altitude region over which the received signal for the less strongly absorbed line remains constant in Figure VII-12(b) is due to the delicate balancing of several factors--the $1/R^2$ signal dependence, the increased attenuation from both $O_3$ and interfering materials at that wavelength, and the increase in the backscattered signal with decreasing altitude caused both by the higher concentration of gases and the enhanced aerosol scattering at lower altitudes. In this particular case, these effects combine to produce a received signal that varies less than ±2 dB from essentially ground level to almost 30 km.

The differential attenuation for this wavelength pair is reasonably good but produces a maximum cumulative attenuation of approximately 20 dB on the more strongly absorbed line. For the 10-J energy level and 1-$m^2$ receiver aperture assumed for this case, the signal level near the ground for the more strongly attenuated line is less than 100 photons per pulse at the satellite receiver altidues; thus, the noise fluctuation in the received signal is large.

The large signal-noise fluctuations produced when fewer than 100 photons per pulse are received can be reduced by integration of multiple pulses. Figure VII-12(d) shows the errors in material concentration that would result from integration of 100 pulse pairs. The dotted line shows the error due to noise, which is the most significant error in this case. This error is approximately half the model $O_3$ concentration (shown by the Xs) up to approximately 40 km.

Integration of 1000 pulse pairs would provide a measurement capability for $O_3$ up to approximately 12 km for the background concentration of 10 ppb.

Figure VII-12(c) indicates a simulated display of the quantity of $O_3$ measured by the system, including systematic errors but not random errors, and on the same graph also indicates the assumed $O_3$ distribution in the atmospheric model (solid line). Perfect operation of the system would result in a coincidence of these two curves. Although it is off the scale of the graph in Figure VII-12(c), interfering-material errors provide a sensitivity limitation of 0.008 ppm for $O_3$ at low altitudes.

The primary interfering material at low altitudes is $SO_2$. Because of the large difference in wavelength necessary to achieve adequate differential absorption for $O_3$, a large differential backscatter component is produced by the Rayleigh contribution. In this wavelength region the differential in Rayleigh scatter is approximately 10 times as large as the differential absorption due to $SO_2$, but fortunately has less effect than the differential absorption due to $SO_2$. Decreasing the wavelength spacing to minimize this scatter differential, however, decreases the $O_3$ absorption coefficient to the point where the overall system performance is impaired. Thus, the wavelength pair chosen for this example is considered to be the best pair available for this particular monitoring application.

The 10-J energy level necessary to achieve this performance level is beyond the capabilities predicted for UV lasers in the next 3-to-5 years. The estimated future capabilities of frequency-doubled dye lasers is limited to approximately a 1-J energy level. The performance that could be obtained with a 1-J energy level and a 0.1-$m^2$ aperture is shown in Figure VII-13. The wavelength locations are 303.6 and 310.9 nm. These wavelengths were chosen in order to reduce the total attenuation slightly, thus increasing the minimum signal level received. At the 1-J and 0.1-$m^2$ aperture indicated, this wavelength tradeoff results in better
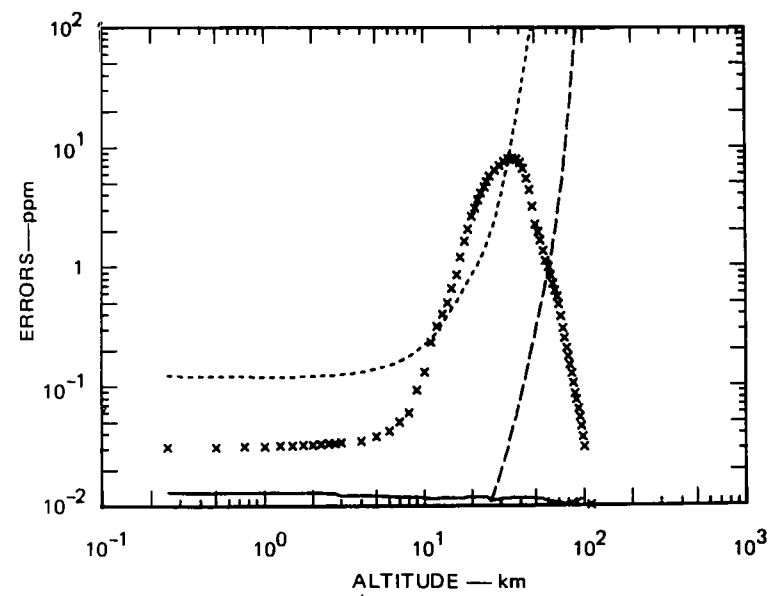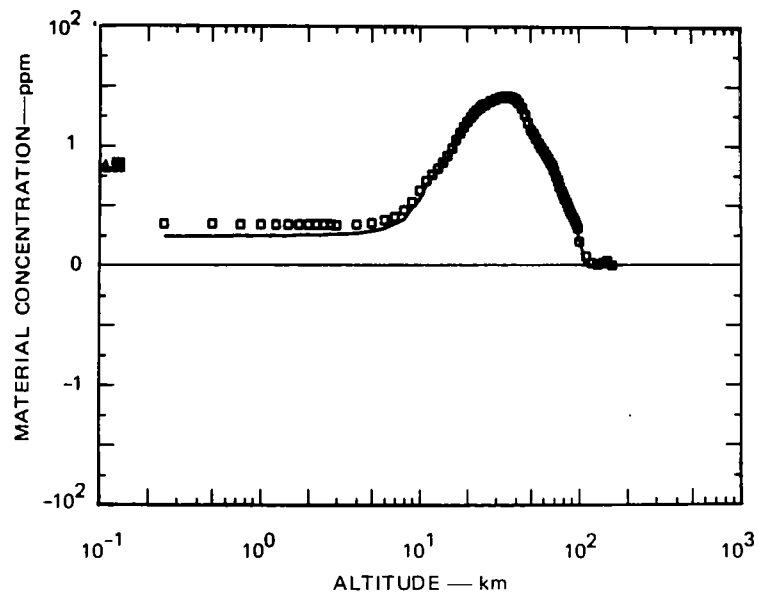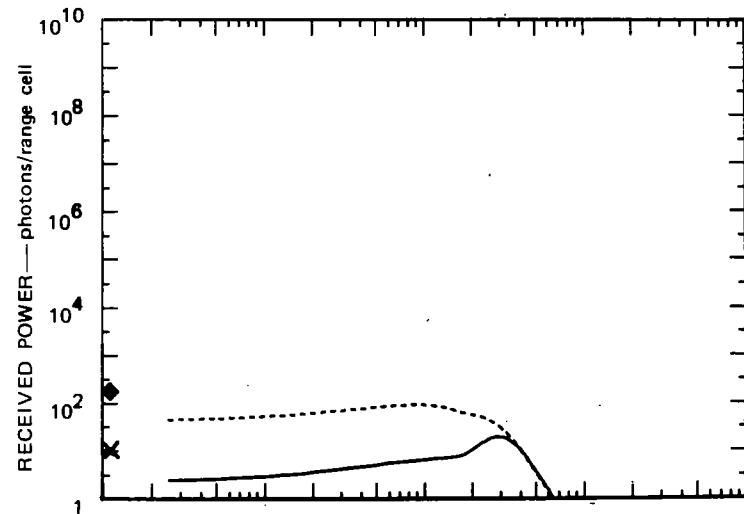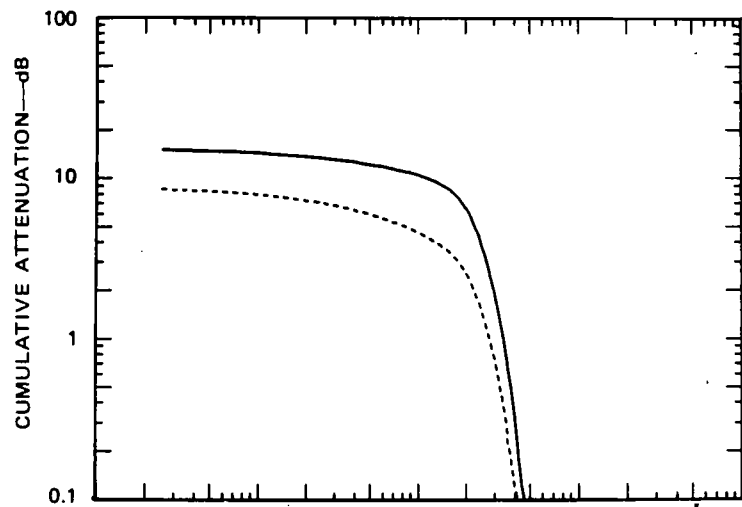
199

FIGURE VII-13    DETAILED PERFORMANCE SUMMARY FOR LOWER-ENERGY SYSTEM TO MONITOR $O_3$ AT 300 nm
FOR H = 166 km

system performance than would occur with more attenuation. This wavelength pair also provided the best performance for column-content $O_3$ measurements. Reference to Figure VII-13(a) shows the slightly reduced attenuation for the more strongly absorbing line also results in a slightly reduced differential absorption coefficient for $O_3$ for this wavelength pair. Note, however, that even with the reduced energy and aperture the signal levels shown in Figure VII-13(b) are not reduced proportionately because of the decrease in attenuation of the 303.6-nm line. Figure VII-13(d) shows that the calculated error at low altitudes exceeds the assumed model distribution, thus precluding low-altitude $O_3$ measurements. From approximately 15 to 30 km, however, the error is less than the assumed $O_3$ distribution and thus provides an adequate measurement capability for $O_3$ in that altitude regime.

The errors shown in this figure assume integration of 100 pulse pairs. If this number is increased to approximately 2000 pulse pairs, then the error (or MDMC) would be approximately equal to the assumed concentration at ground level. Measurements of the 10 ppb background concentration would not be possible for the low-altitude $O_3$ distribution.

### b.  Ozone at IR Wavelengths

Ozone has a large number of absorption lines in the infrared near 10 μm, many of which were studied. Of these, the wavelengths of 1057.677 $cm^{-1}$ and 1057.950 $cm^{-1}$ yielded the best performance. It does not seem likely that a significant improvement in performance could be obtained through a more exhaustive analysis of the many other absorption lines of $O_3$. The attenuation coefficients for this wavelength pair are appropriate for the range and energy levels assumed for the satellite-based lidar system. Also, this line pair has a moderately low

interfering-material error, which if necessary, could be reduced through compensation by measurement of the interfering species.

The results of the detailed system analysis are shown in Figure VII-14. The cumulative attenuation shown in Figure VII-14(a) indicates that a substantial differential absorption is available with this wavelength pair. This results in a large differential signal as indicated in Figure VII-14(b). The 100-J energy level and 1-m$^2$ receiver aperture produce a large signal return even on the more strongly attenuated line and even with the amount of backscatter predicted at 10 μm. The more rapid fall-off of signal in the IR with increasing altitude, as compared to the previous UV case, results from the fact that the return signal in the IR is caused primarily by aerosol backscattering, which falls off more rapidly with altitude than backscattering from atmospheric gases in the UV. The strong dependence on aerosol scattering at IR wavelengths is indicated by the prominent "bump" or "bulge" in received signals at 20 km caused by the aerosol layer at that altitude.

Note, however, that in comparison with the UV case the backscatter from the high-altitude aerosol layer **is reduced** by a larger amount than is the backscatter in the lower atmosphere because a high-altitude haze model is used. This results in a more serious degradation of the high-altitude $O_3$-measuring capability than for the low-altitude $O_3$ measurements. Figure VII-14(c) shows that the systematic errors due primarily to interfering materials are essentially negligible for this measurement because the measured and model $O_3$ distributions are virtually identical. Figure VII-14(d) shows that at low altitudes the error in material concentration is less than the background concentration of 0.01 ppm up to approximately 2 km. However, starting at about 8 km the error is approximately equal to the assumed $O_3$ distribution up to about 25 km, equal to the assumed $O_3$ distribution up to about 25 km, above which the
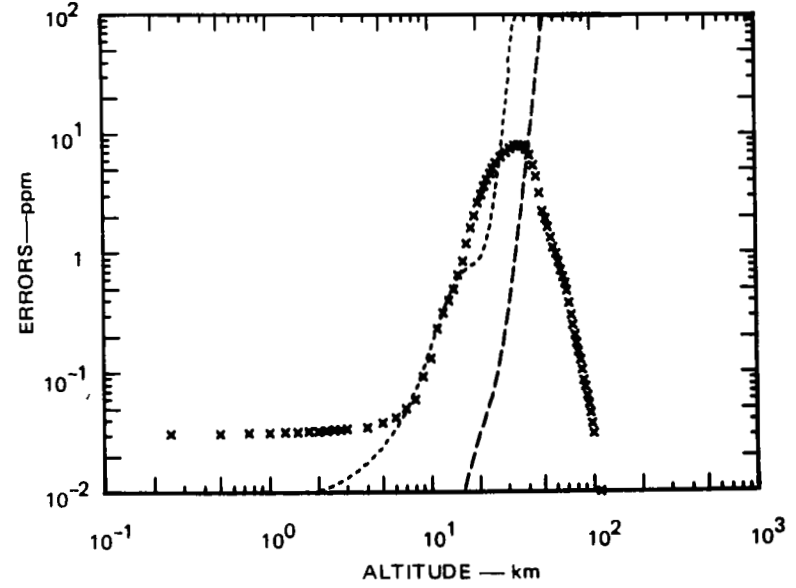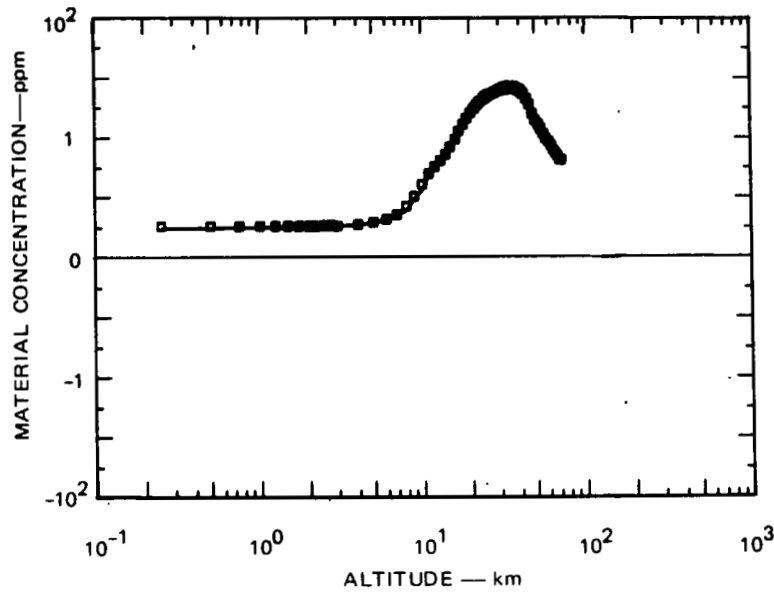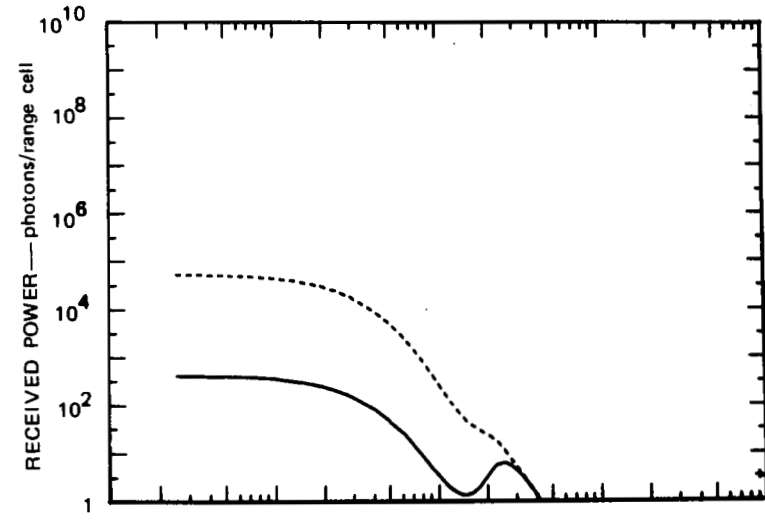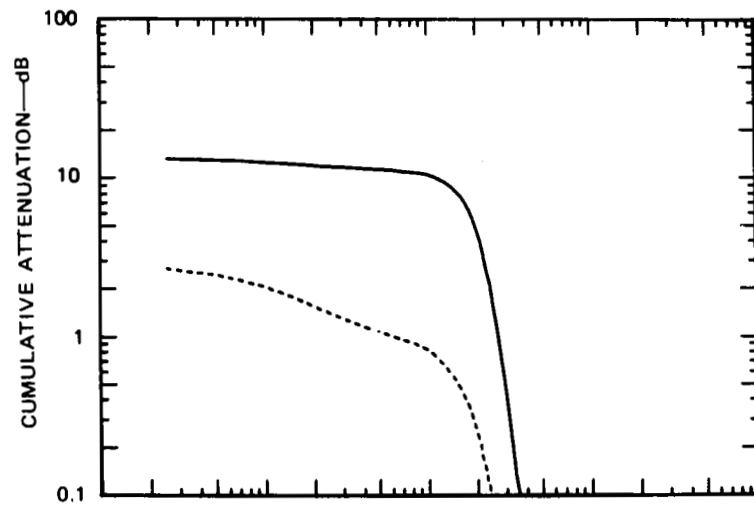
FIGURE VII-14    DETAILED PERFORMANCE SUMMARY FOR $O_3$ AT 10 $\mu$m FOR H = 166 km

above which the error greatly exceeds the model concentration. Therefore, this case indicates poor results for measuring stratospheric $O_3$. However, the natural variability of $O_3$ is such that the calculated accuracy of measurement would provide useful results for the altitude range of 10 to 30 km on many occasions.

Integration of 100 pulse pairs was assumed for this case. Increasing the number of integrated pulse pairs to 1000 would provide good accuracy up to approximately 30 km.

Although not shown on the graph, the interfering-material errors are approximately 0.004 ppm at ground level and dropping off rapidly with altitude.

The performance levels achieved with the 100-J laser, 1-$m^2$ aperture, a heterodyne detector,[*] and integration of 100 pulse pairs as assumed for this example are not sufficiently good to allow adequate performance to be achieved by substituting a lower energy level, a conventional detector, or a smaller aperture. For example, use of a 10-J laser with a 0.1-$m^2$ aperture and a heterodyne detector results in an error in material concentration of approximately 0.1 ppm at ground level, which is ten times the background concentration.

c.    Sulfur Dioxide at UV Wavelengths

Reference to Figure VII-15(a) shows that the differential attenuation available for measuring $SO_2$ is quite small even though the attenuation level for the two wavelengths is fairly large due to the strong $O_3$ absorption at these wavelengths.

---

[*] The feasibility of using a 1 $m^2$ aperture in combination with a heterodyne detector at ranges shorter than 166 km has not been established.
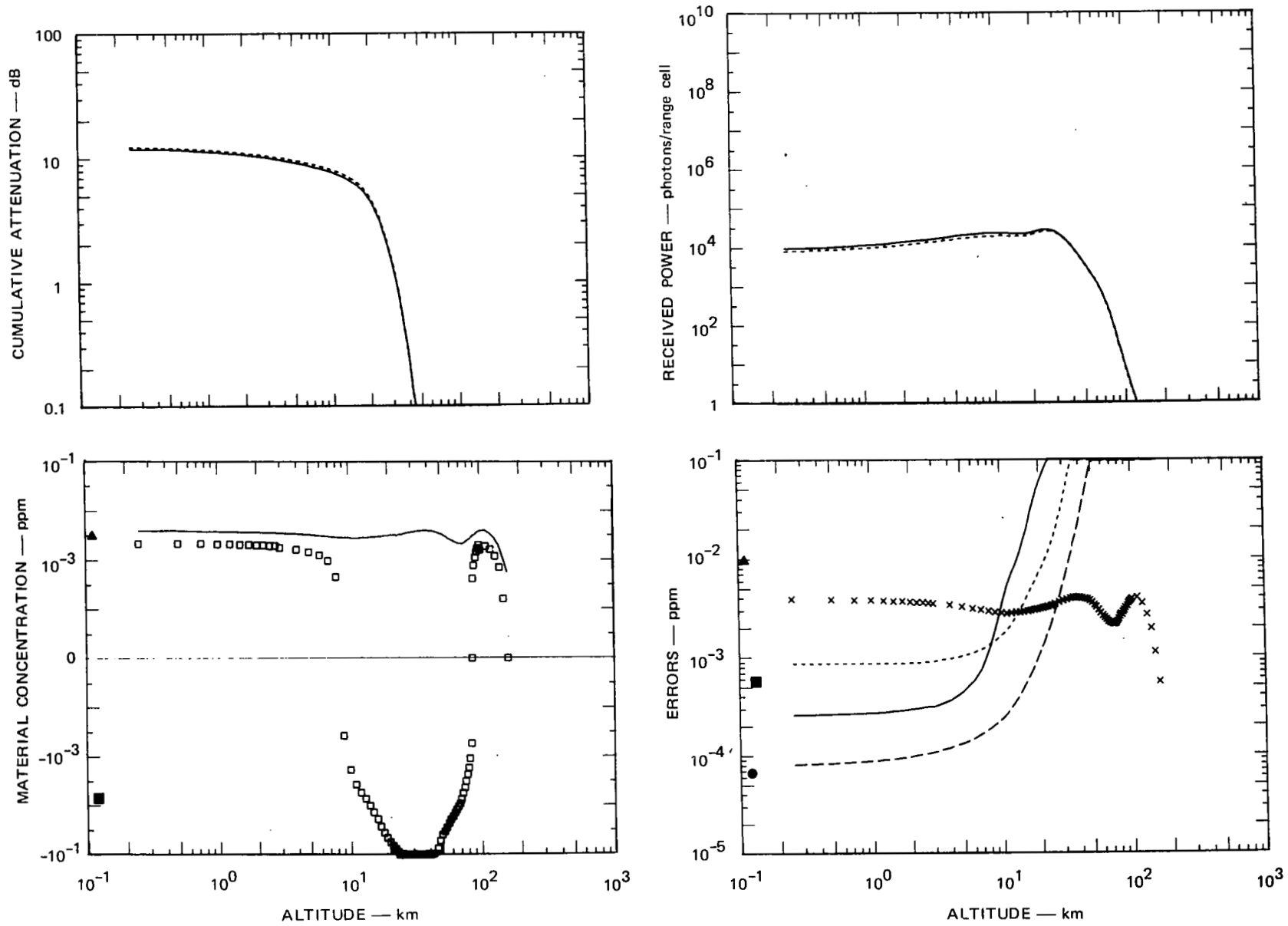
FIGURE VII-15    DETAILED PERFORMANCE SUMMARY FOR SO$_2$ AT 300 nm FOR H = 166 km

The high-altitude $O_3$ concentration responsible for this large attenuation is also evident from the cumulative-attenuation curves that build up to high values as the attenuation is accumulated through the high-altitude $O_3$ layer. Because of the large attenuation in the high-altitude $O_3$ layer and the need to penetrate this layer to make low-altitude measurements, choosing $SO_2$ lines is very critical with respect to $O_3$ interference. This particular line pair afforded the smallest interfering-material error of the several line pairs tried. The small differential attenuation for $SO_2$ results in large errors in the measured concentration because of the effects of noise and other sources of error despite the adequate signal levels that are received in all altitude regions, as shown in Figure VII-15(b).

The systematic errors introduced by the differential absorption of $O_3$ are quite evident in Figure VII-15(c). The squares indicate the $SO_2$ distribution that would be measured by the simulated system, and it is apparent that for the upper altitudes the measured $SO_2$ concentration differs substantially from the assumed concentration as indicated by the solid line in the graph. Fortunately, the errors below 5 or 6 km due to the interference from $O_3$ are not large. Reference to Figure VII-15(d) shows that the error in material concentration below 8 km is limited by noise (indicated by the dotted line) rather than interfering materials, although there is a fairly large error due to $O_3$. The MDMC is below the upper limit on background concentration (2 ppb) and would thus provide a measurement capability for $SO_2$ below approximately 5 to 6 km.

Unfortunately, the 100-J laser assumed in this calculation is beyond the future capabilities extrapolated for UV lasers. Because of the high attenuation by $O_3$ and the small differential signal for $SO_2$ the performance level achievable with 100 J is only a factor of 5 below the model concentration. Thus, a reduction in laser energy to the 1-J future capability estimated for UV lasers would result in unacceptable performance.

## d. Nitrogen Dioxide at Visible Wavelengths

The performance summary for measuring $NO_2$ at visible wavelengths is given in Figure VII-16. The line pair chosen provided the maximum differential absorption available for $NO_2$ in the visible spectrum. Despite this choice, the cumulative differential absorption is quite low, as can be seen from Figure VII-16(a). This is due in part to the low absorption coefficient for $NO_2$ in the visible region, and in part to the rural pollution model for $NO_2$, which has a small $NO_2$ concentration. The small differential absorption makes $NO_2$ monitoring difficult because the resulting differential signal is small, as seen in Figure VII-16(b).

It was assumed for this calculation that the significant differential in backscattering by aerosols and atmospheric gases had been corrected, which removes almost all of the systematic errors associated with interfering materials and produces the excellent agreement between measured and modeled material distribution shown in Figure VII-16(c). Thus, with a 10-J energy level, a $1\text{-m}^2$ aperture, and integration of 100 pulse pairs, the MDMC is less than 0.001 ppm below 2 km and does not equal the assumed model distribution until approximately 9 km.

Integration of 1000 pulse pairs would provide an approximately equal performance level for an assumed 1 ppb background concentration. Thus, if the $NO_2$ concentration is less than the 4 ppb maximum estimate in Table II-1, an adequate performance level could still be obtained.

The assumed 10-J laser energy level is believed to be possible during the near-future time period (1 to 2 years); thus, the calculated $NO_2$ monitoring capability would be possible with the relatively good performance level indicated in Figure VII-16(d) in this time scale. A somewhat degraded measurement capability could be realized with a 1-to-5-J energy level, thus changing the time estimate from the near future to the present.
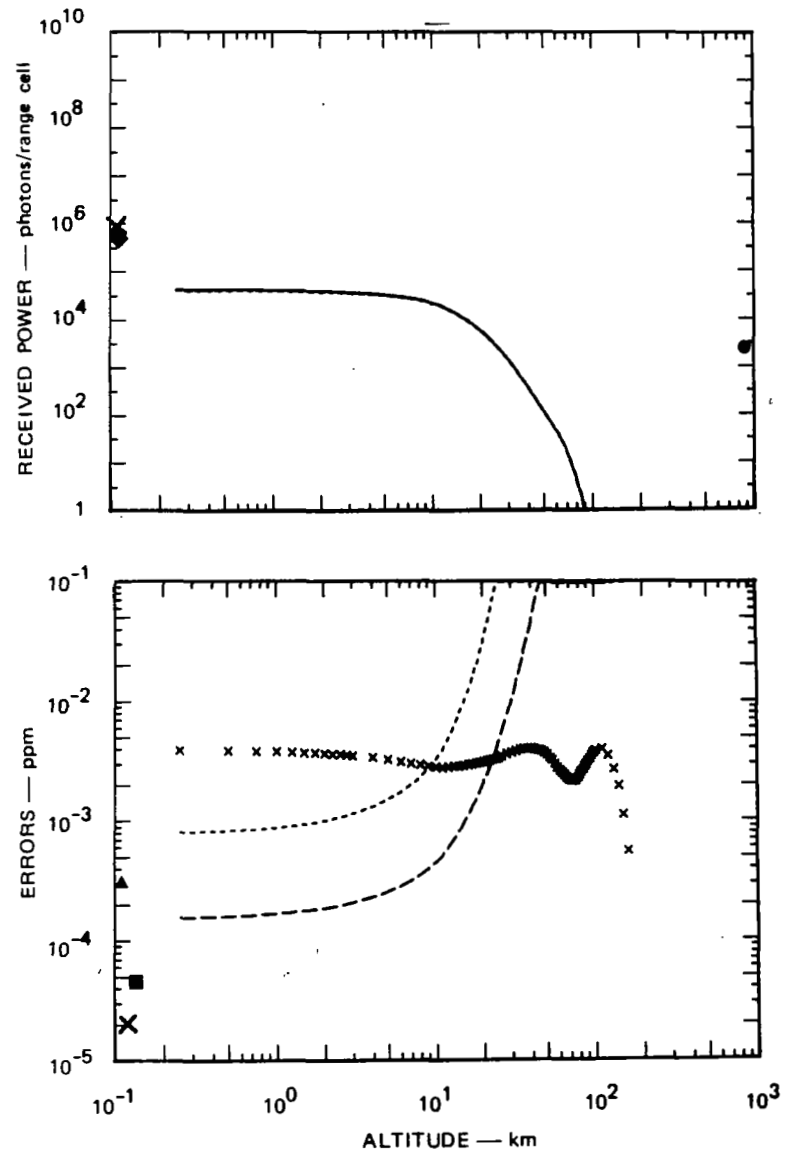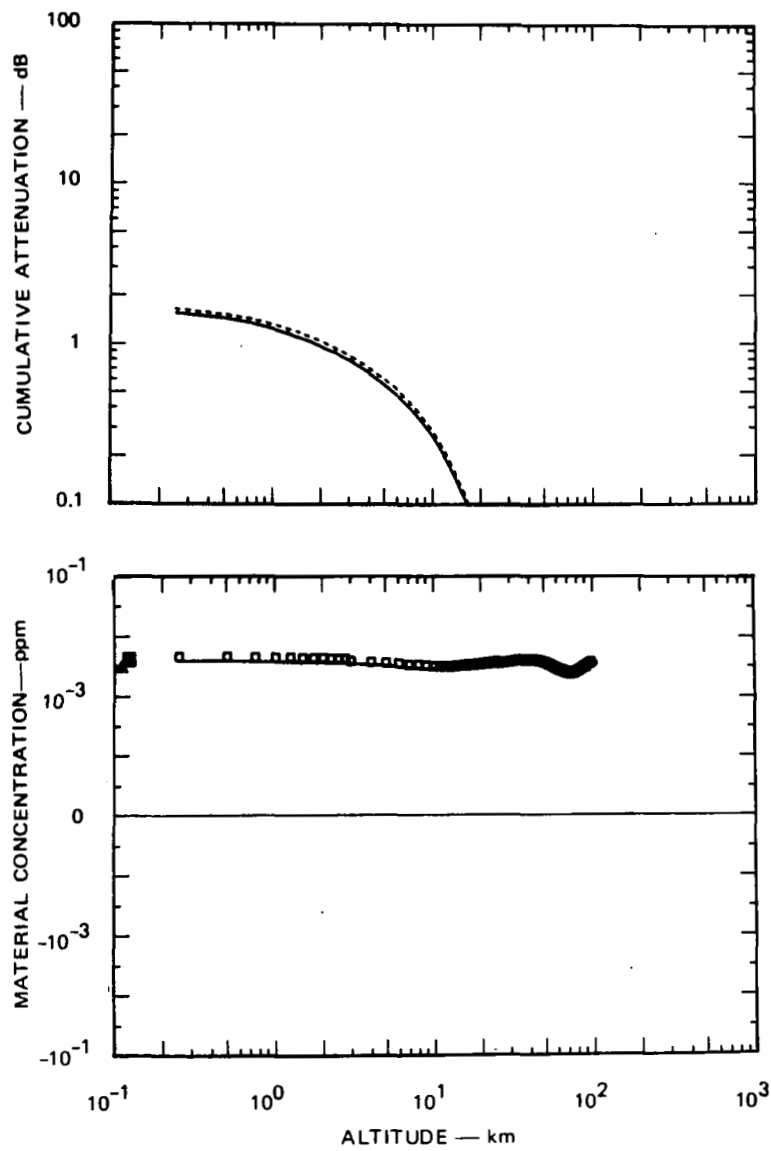
206

FIGURE VII-16   DETAILED PERFORMANCE SUMMARY FOR NO$_2$ AT 450 nm FOR H = 166 km

A rural model for pollutant concentrations was assumed for all the satellite cases. An urban pollution model would have approximately ten times the $NO_2$ concentration used for this example. This increased concentration would produce about ten times as large a differential signal as is shown here, which would improve the overall performance level. The overall effect of increased levels of all pollutants in urban models, however, is complex and could lead to a performance change that is either substantially above or substantially below the estimated performance change extrapolated by just an increase in $NO_2$ concentration alone. For this reason, the entire problem would have to be rerun to predict accurately the operation under urban pollution conditions. In addition, it is believed that the satellite operation was primarily applicable to global monitoring, which would be at rural concentration levels. A satellite capability for only urban concentrations was not believed to be useful; therefore, the urban investigations were not run.

e.   Carbon Monoxide at IR Wavelengths

Figure VII-17 shows the performance summary for CO in the 4-to-5-μm band. This spectral region is one in which both CO and $N_2O$ lines appear in close proximity. It was hoped that it would be possible to monitor both materials on a noninterfering basis with a single narrowly tunable laser. Approximately 30 spectral lines were tried in various combinations to find combinations with good performance levels. For most of the line pairs investigated, CO shows relatively small interference from $N_2O$ or other materials. However, the effects of interfering materials, although not large, is apparent at low altitudes in Figure VII-17(c). Below about 2 km the squares deviate slightly from the solid line, indicating a slight difference between the model distribution and the measured distribution of CO.
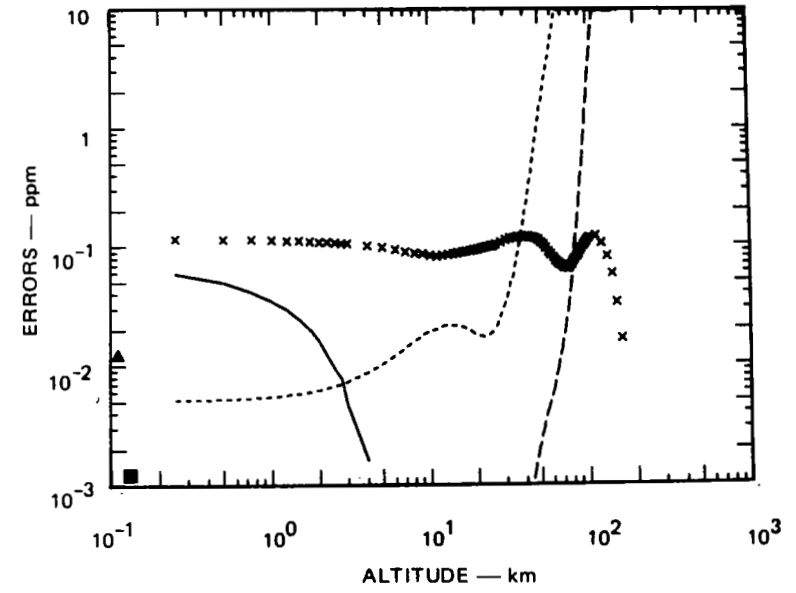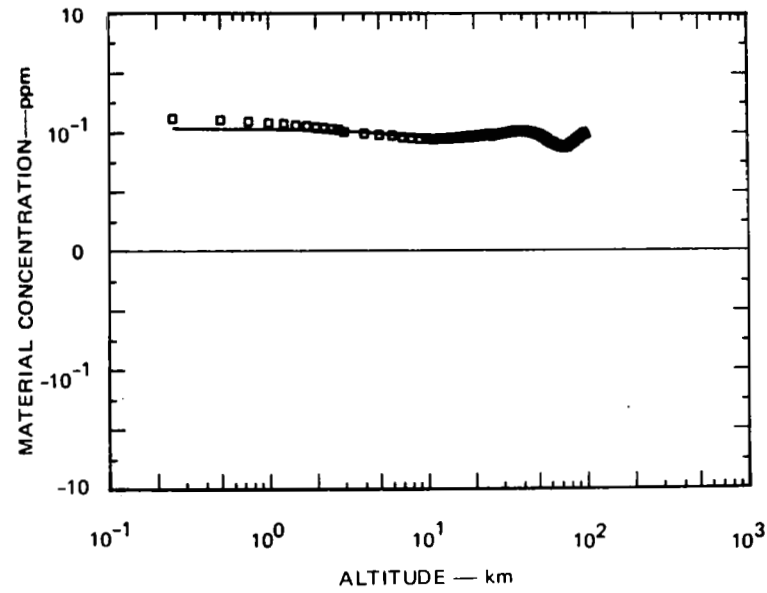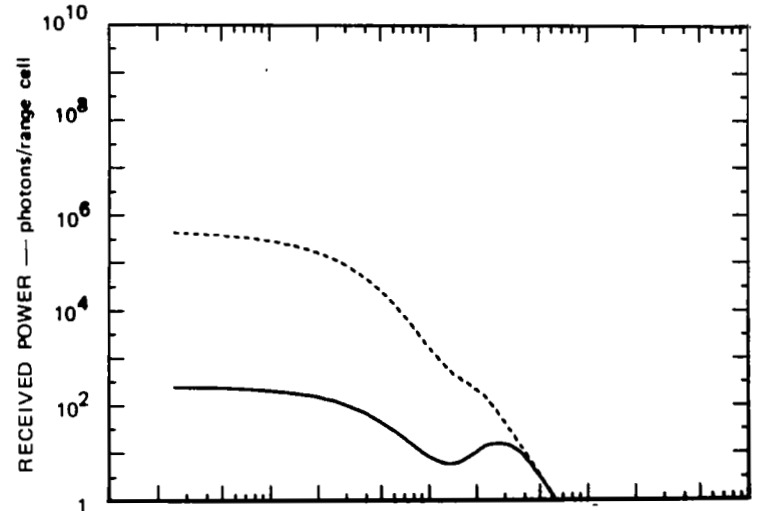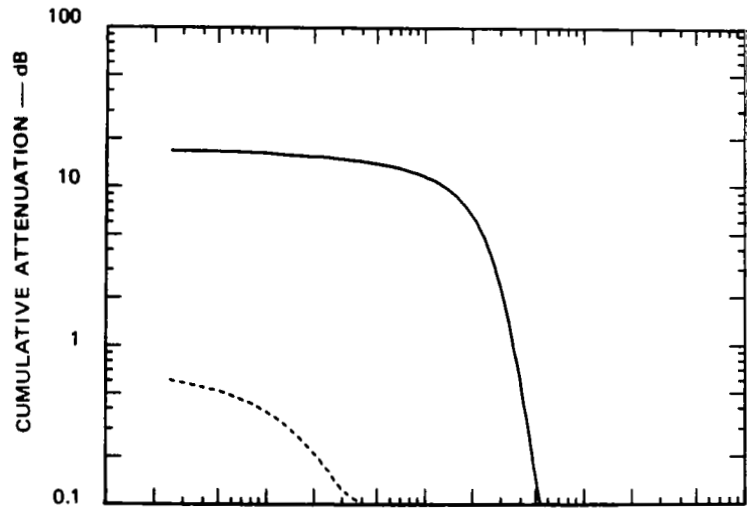
FIGURE VII-17    DETAILED PERFORMANCE SUMMARY FOR CO AT 4.5 μm FOR H = 166 km

Figure VII-17(d) indicates that the errors in material concentration are limited by the systematic error due to interfering materials at low altitudes, as indicated by the solid line in the graph. The noise error is dominant above approximately 3 km, although it is substantially below the model concentration at all altitudes where a measurement of CO would be desired. The primary interfering material is water vapor. Hence, performance could be improved dramatically by compensation for a measured water-vapor content. It is expected that a compensated measurement of this type would be limited by noise at all altitudes and would look much like the dotted curve shown in Figure VII-17(d).

The excellent performance achieved with the assumed 100-J laser would make feasible the use of lower-energy lasers that could still provide adequate performance. However, because of the limit laser energies predicted for this wavelength region, an extensive analysis of performance for lower energy levels was not performed. It is estimated, however, that a system using a 1-J laser, 1-m$^2$ aperture, and a heterodyne detector[*] would, with integration of 100 pulse pairs, produce an MDMC of approximately one-tenth the assumed distribution. This energy level is predicted to be achievable in the future (3 to 5 year) time scale by use of an optical parametric oscillator driven by either a doubled $CO_2$ laser or a Nd:YAG laser.

It is likely that an examination of other line pairs in the portion of the $N_2O$ spectrum further removed from the CO line would produce a substantially decreased interfering-material error without seriously degrading the other errors in the system. The practical value of doing this, however, is doubtful because of the 100-J assumed energy level for

---

[*]Note that the compatibility of a heterodyne detector and a 1-m$^2$ aperture has not been established for ranges of 166 km and less.

the present calculations. It does not appear possible to reduce the noise error by a significant amount, and thus to reduce the required energy level to substantially less than 100 J, even with the selection of other lines having lower interfering-material errors. Thus, although monitoring of CO from 166 km appears to be feasible only with multipulse integration, prospects for space-averaged measurements over horizontal distances of several hundred kilometers are promising.

### f. Nitrous Oxide at IR Wavelengths

An energy level of 1 J and a receiver aperture of $0.1 \text{ m}^2$, and wavelengths of $2219.808 \text{ cm}^{-1}$ and $2221.06 \text{ cm}^{-1}$ were chosen for this example following a series of performance analyses. (Another wavelength pair has been found subsequently that provides better interfering-material performance than the selected wavelengths.) A summary of the computed system performance is shown in Figure VII-18. The maximum attenuation indicated in Figure VII-18(a) is reasonable for the assumed conditions although the differential attenuation is smaller than would be desired because of the significant attenuation on the lower-attenuation line. The signal levels are quite low because of the small aperture and low laser energy. However, with the assumed heterodyne detector a noise-limited error in material concentration of approximately half the modeled concentration is obtained up to an altitude of approximately 5 km with integration of 100 pulse pairs. A significant, although not dominant, interfering-material error approximately equal to the noise error also occurs at low altitudes. Reference to Figure VII-17(c), however, indicates that the deviation between measured and modeled $N_2O$ distribution is not significant in this low-altitude regime. This interfering-material error could be reduced to a negligible value by selection of a different line pair.
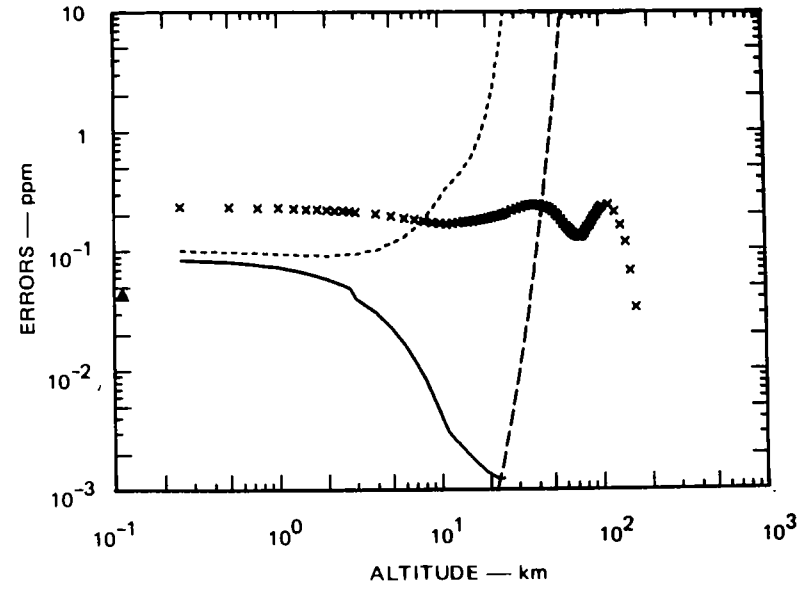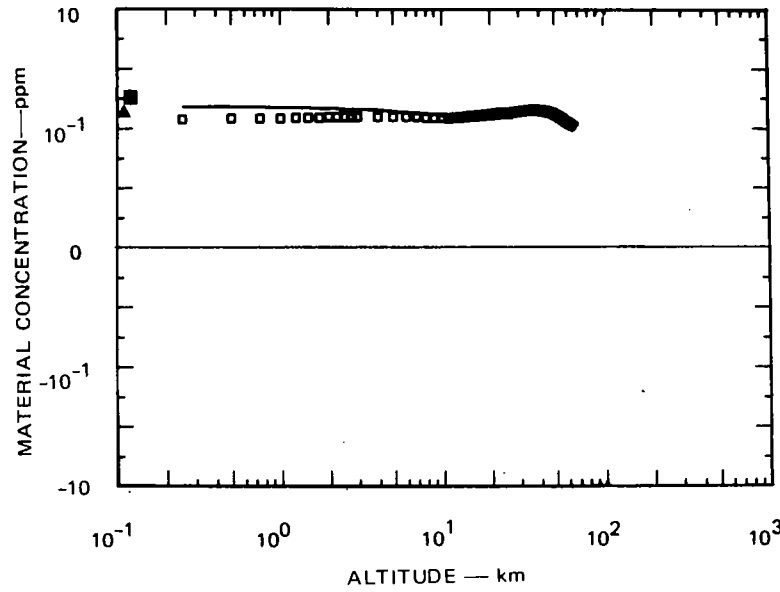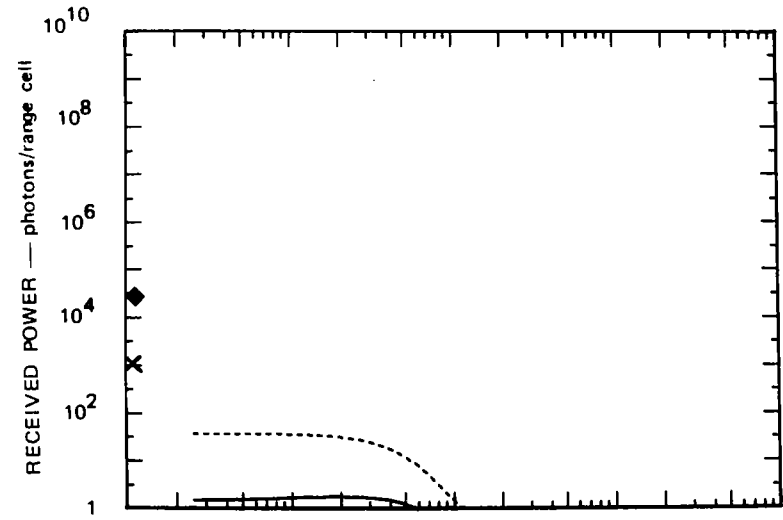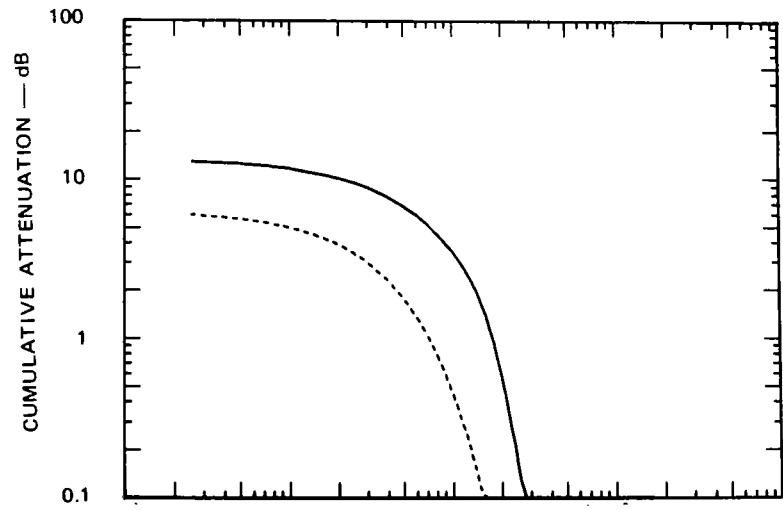
FIGURE VII-18   DETAILED PERFORMANCE SUMMARY FOR $N_2O$ AT 4.5 $\mu$m FOR H = 166 km

A new line pair at 2222.751 cm$^{-1}$ and 2222.46 cm$^{-1}$ can provide substantially improved performance with respect to interfering materials. This wavelength pair will reduce the interfering-material errors by more than a factor of 10 with only a small change in other system performance parameters. This reduction in errors from interfering materials would probably make compensation unnecessary for monitoring $N_2O$, which, in combination with a larger aperture, would produce a very promising satellite system.

### g. Summary of Range-Resolved Cases from 166 km Altitude

A summary of the projected feasibility of measurements from the satellite altitude of 166 km is given in Table VII-2.

### 2. Column-Content Measurements

Measurement of the column content of a material is easier than a range-resolved measurement of the same material. There are two basic reasons. The first reason is that the signal reflected from the ground, with the assumed 10% Lambertian reflector characteristic, is larger than the signal backscattered from the aerosols used in these calculations. The ground-reflected signal exceeds the scattered signal from approximately 5 dB in the UV to almost 40 dB at approximately 10 µm. This large signal difference in the IR makes column-content measurements possible with systems that are simpler than those required for range-resolved measurements. For example, the 100-J laser energy required for range-resolved $O_3$ measurements in the IR imposes severe requirements on the satellite lidar system. In contrast, column-content measurements of $O_3$ can be made in the IR with high accuracy (better than 1%) by using a 10-J laser that has already been demonstrated.

Table VII-2

SUMMARY OF RESULTS FOR RANGE-RESOLVED CALCULATIONS
FOR A PLATFORM ALTITUDE OF 166 km

| Time Period For | Material | MDMC or Altitude* Range | Assumed Laser Energy (J) |
|---|---|---|---|
| Present (0-1 year) | $NO_2$ | 0.004 ppm | 1-2 |
| Near-future (1-2 years) | $O_3$ (IR) | 0-2 km | 10 |
| | $NO_2$ | 0.001 ppm | 10 |
| Future (3-5 years) | $O_3$ (UV) | 15-30 km | 1 |
| | $N_2O$ | 0.1 ppm | 1 |
| | CO | 0.1 ppm | 1 |
| | $O_3$ (IR) | 0.009 ppm | 100 |
| Extended (> 5 years) | $O_3$ (UV) | 0.008 ppm | 10 |
| | $SO_2$ | 0.0009 ppm | 100 |
| | CO | 0.008 ppm | 100 |

*Either ground-level minimum detectable material
concentration (in ppm), or altitude range for
satisfactory performance.

The second reason for the superior performance of column-content measurements is that the normalizing factor relating errors in concentration to power fluctuations [see Eq. (V-10)] contains the full column-content differential absorption rather than the samll differential absorption associated with each individual range cell. For example, if the total absorption for a column-content measurement is divided into 1-km

range increments for a range-resolved measurement, the power-fluctuation errors due to noise would be increased by a factor of approximately 50.

Because of the reduced laser energy requirements, column-content measurements are feasible now for $NO_2$ and $N_2O$ and are predicted to be feasible for $O_3$ (IR), CO, and $SO_2$ in the near future.

The errors in the integrated column-content measurement of each material caused by interfering materials, noise, and miscellaneous mechanisms are shown in Table VII-3. It is assumed that errors from interfering materials are not compensated. Ppm entries are not given for $O_3$ because of the large variation in concentration as a function of altitude. Some equivalent ppm numbers are missing for other entries where they are very small compared to other indicated error sources. The number of pulse pairs that must be integrated and the laser energy required to achieve the stated performance are also given in Table VII-3. The other system parameters assumed for these calculations are shown in Section VII-H (Table VII-8).

The most favorable case in Table VII-3 is measurement of $O_3$ in the 10-μm band where integration of 10 pulses at 10 J per pulse yields a measurement error of less than 1% for the combined total of uncompensated interfering materials, noise, and miscellaneous errors. This excellent performance is achievable in the near-future time period by use of high-pressure $CO_2$ gas lasers. A somewhat degraded preformance is possible using presently available $CO_2$ lasers.

The indicated capabilities for measuring $O_3$ in the UV spectral region are also good. In this case, interfering-material and miscellaneous errors are less than 1%, but there is a 15% noise error in the measurement even with a 1-J laser (achievable in the future time period) and integration of 100 pulse pairs. The combination of larger noise error, greater number of pulse pairs to be integrated, and longer time before projected

Table VII-3

PREDICTED PERFORMANCE FOR 166-km COLUMN-CONTENT MEASUREMENTS

| Material | Errors in Integrated Column-Content Measurement | | | Number of Pulse Pairs Integrated | Laser Energy |
| | Caused by Interfering Materials[*] | Caused by Noise | Caused by Miscellaneous Mechanisms | | |
|---|---|---|---|---|---|
| $O_3$ (UV) | < 1% | 15% | < 1% | 100 | 1 |
| $O_3$ (IR) | < 1% | < 1% | < 1% | 10 | 10 |
| $SO_2$ (UV) | 300% | 35% | 1.8% | 100 | 0.2 |
| $NO_2$ (vis.) | 10% (0.0003 ppm) | 1.5% | 1.4% | 100 | 1 |
| CO (IR) | 12% | 1% | 0.12% | 100 | 0.5 |
| $N_2O$ (IR) | 22% (0.04 ppm) | 2% | 0.15% | 100 | 0.1 |

[*]Assuming no compensation.

216

feasibility for the UV system indicates that the IR spectral region is promising for column-content measurements of $O_3$.

The $SO_2$ column-content measurements are subject to large interference by $O_3$ as indicated by the 300% interfering-material error shown in Table VII-3. This large error could be reduced substantially by compensation. The 35% noise error could be reduced by increasing the assumed transmitted energy level of 0.2 J or the number of pulses that are integrated. Integration of 400 pulse pairs will provide comparable performance for the maximum background concentration of 2 ppb. Because of the much greater interfering-material error, however, no further attempt was made to reduce this noise by increasing the system capabilities. An MDMC of 0.0004 ppm is obtainable with interference compensation and integration of 1000 pulses.

An adequate performance level for $NO_2$ measurements can be achieved with available tunable dye lasers. Compensation for the interfering-material error of 10%, caused primarily by differential scatter effects, can be accomplished by auxiliary measurements and empirical procedures. Integration of 100 pulse pairs is required for this performance level at a background concentration of 4 ppb. Integration of 1000 pulses would give comparable performance for a background concentration of 1 ppb.

An adequate level of performance can also be achieved for CO monitoring within the near future. The largest error is the 12% interfering-material error, which could be reduced to approximately the 1% level by interference compensation. This improvement would result in excellent performance within the near-future time periods. Operation with presently available technology would result in a noise error that is slightly less than the interfering-material error.

Excellent performance is also obtainable for monitoring $N_2O$ if compensation for the 22% interfering-material error can be accomplished through auxiliary measurements.

217

### 3. Cloud-Measurements for a Satellite at 166 km Altitude

The Statement of Work requires consideration of the feasibility of measuring cloud heights and optical thicknesses. A definitive study of this topic for satellites was made earlier at SRI by Evans et al. (1966). The general conclusion was that the technology available at that time was inadequate for such measurements for the 1000-km orbital altitude under consideration. The larger payloads and lower orbital altitudes specified for this study make it appropriate to reconsider the possibilities.

The three quantities of interest in cloud measurements are height (especially the height of the top of the cloud), thickness, and optical depth. The optical depth is the cumulative one-way attenuation through a cloud; it is a quantity calculated by the computer program as described below.

The five types of clouds considered were stratus, cumulus, and three types of cirrus, designated as thin, medium, and thick. A summary of the cloud parameters used for the calculations is given in Table VII-4. The designations of thin, medium, and thick for cirrus clouds refer to a difference in aerosol number density within the cloud rather than to a thickness in kilometers.

The attenuation and volume backscattering coefficient for each of the cases was calculated from the appropriate Deirmendjian haze model as indicated in Table VII-4 and described in Section VII-C. The models are based on single scattering; results should be interpreted with caution for dense clouds in which multiple-scattering effects are important.

The measurement of cloud parameters does not require a tunable lidar system. Because the technology for ruby lasers is more advanced than that of dye lasers, an operating wavelength of 694.3 nm was chosen for these calculations. The system parameters are shown in Section VII-H (Table VII-8).

## Table VII-4

### PARAMETERS OF CLOUD MODELS

| Cloud Type | Deirmendjian Haze Model | Density $\left(\dfrac{\text{particles}}{\text{cm}^3}\right)$ | Cloud-Top Altitude (km) | Thickness (km) |
|---|---|---|---|---|
| Thin cirrus | C3 | 1 | 10 | 1 |
| Medium cirrus | C3 | 10 | 10 | 1 |
| Thick cirrus | C3 | 100 | 10 | 1 |
| Stratus | C1 | 100 | 3 | 1 |
| Cumulus | C1 | 1000 | 1.5 | 1 |

For each of the five cloud cases a graph of cumulative attenuation and received signal is given. The legend for these figures is the same as that presented in Figures VII-11(a) and VII-11(b).

Figure VII-19 shows the lidar system performance for a clear atmosphere without clouds. Figure VII-19(a) shows the cumulative attenuation starting at the satellite and accumulating toward the ground, and Figure VII-19(b) gives the received signal power at the satellite as a function of altitude. The ground-return signal, detector noise level, and background-noise level are shown at the edges of the graphs. The attenuation losses are due primarily to scattering by gases and aerosols. The aerosol losses are much larger than the gaseous losses. The received signal is scattered from both gases and aerosols, with approximately 90% of the return signal due to the Rayleigh (gaseous) scatter and the remainder due to aerosol scatter.

Figure VII-20 shows the system performance for thin cirrus clouds at 10 km. Note the abrupt step of 0.2 dB at 10 km in the cumulative-attenuation curve. This step is also the calculated optical depth of the cirrus clouds. (The assumed 0.1-dB resolution of signal intensity implies
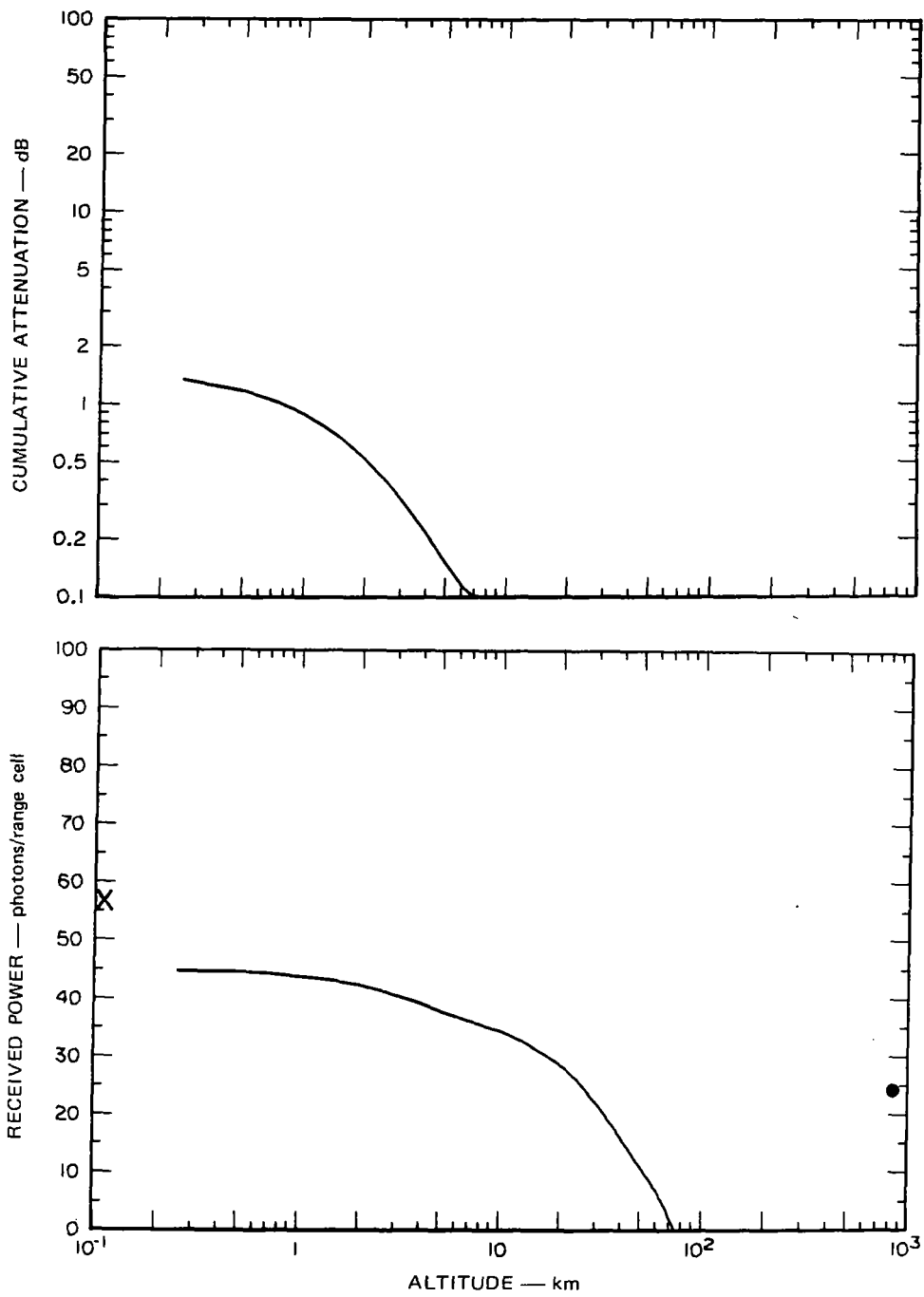
219

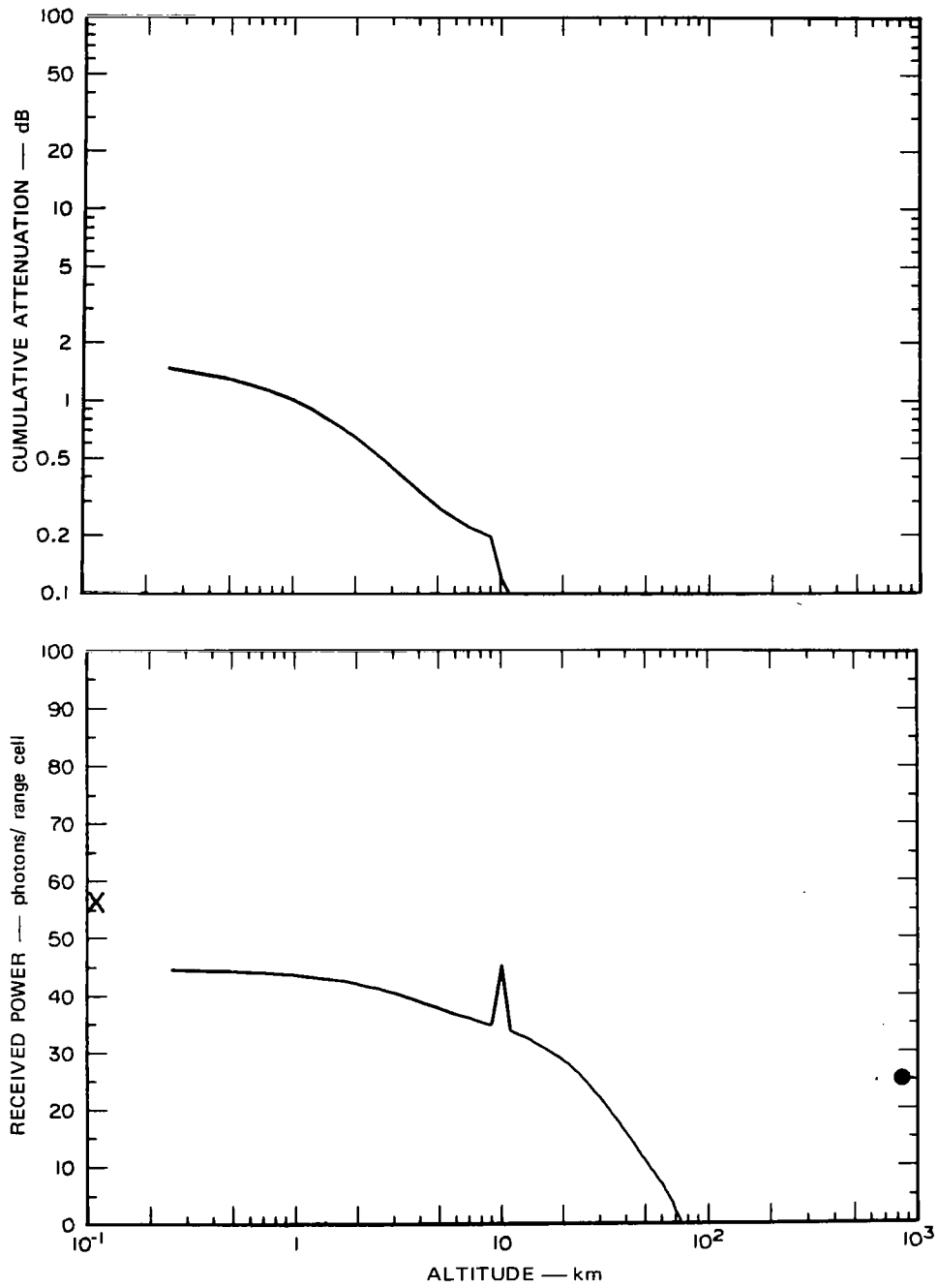FIGURE VII-19    ATTENUATION AND RECEIVED SIGNAL FOR CLEAR STANDARD
ATMOSPHERE

FIGURE VII-20    ATTENUATION AND RECEIVED SIGNAL FOR THIN CIRRUS CLOUD

221

a measurement error in optical depth of 0.2 dB.)  There is a significant increase in the return signal at 10 km from the thin cirrus clouds, and the entire curve below 20 km is above the background noise level.  This allows the height and optical depth of the thin cirrus to be measured. The cloud thickness of 1 km could be more accurately measured with a range resolution of 100 m than with the assumed resolution of 1 km.

Figure VII-21 shows the results for medium cirrus clouds at 10 km.  The optical depth of 1.3 dB in the cumulative-attenuation curve at 10 km is apparent as a slight offset in the received-signal curve. In theory, the signal level above and below the clouds could be measured and the magnitude of the step could be determined.  In practice, there may be more scattering variations and cloud nonuniformities than are shown in this theoretical example, and the measurement of a 1.3-dB optical depth may not be very accurate even with a 0.1-dB resolution system.

The backscattered signal from the medium cirrus is large enough to enable measurement of both cloud height and thickness because both the upper and lower boundaries of the clouds are detectable, even in daylight.  However, the thickness would not be determined accurately with the assumed 1-km range resolution.

Figure VII-22 shows the results for a thick cirrus cloud at an altitude of 10 km, with an optical depth of 13 dB.  This optical depth produces an offset in the received signal of 26 dB, which could be measured except for the fact that the signal level from below the cloud is smaller than the daylight background-noise level.  Hence, the optical depth of this cloud cannot be measured except at night.  Note, however, that the thickness of the cloud can still be measured because the lower edge of the cloud has a relatively sharp discontinuity in signal level
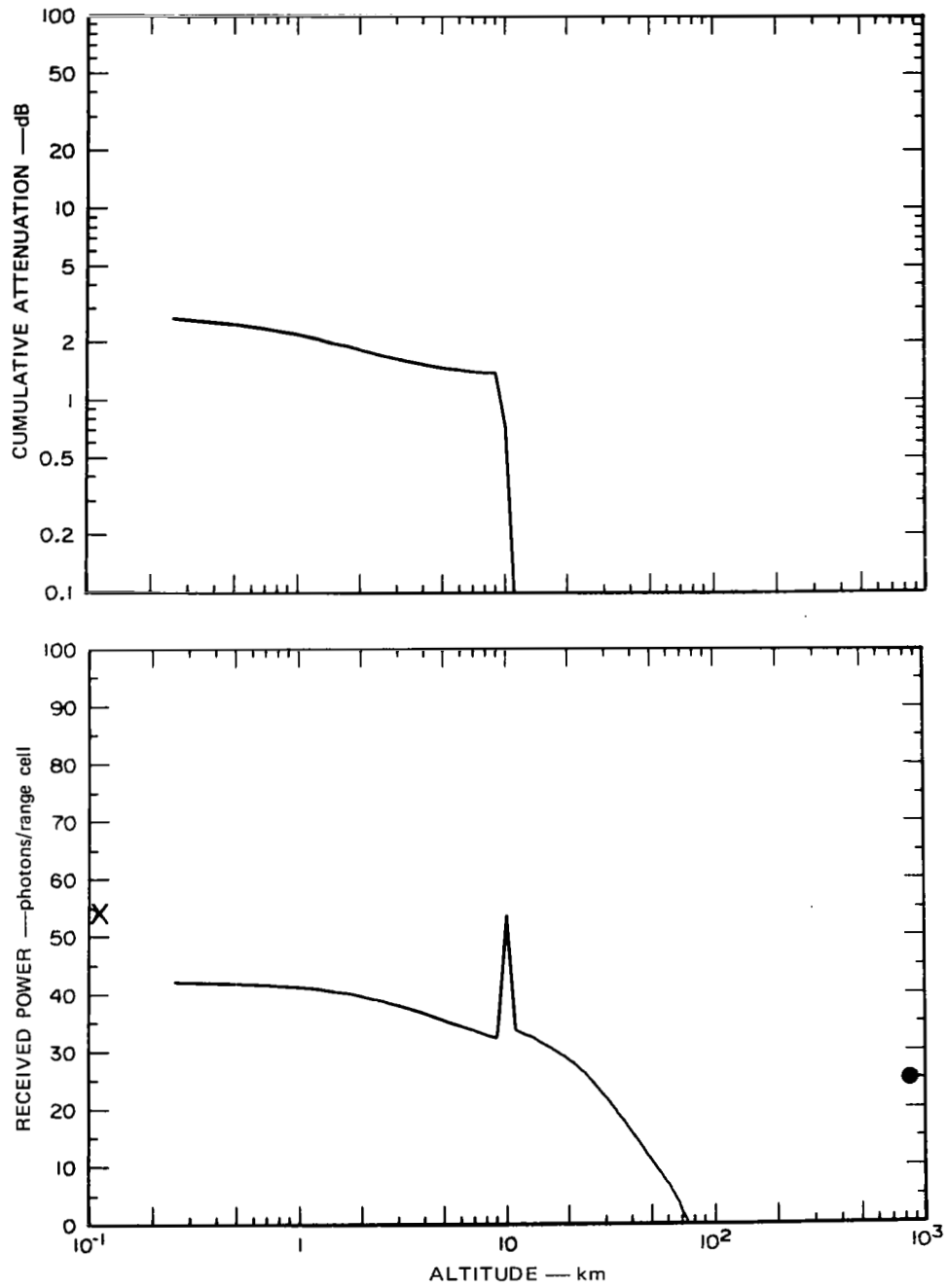
FIGURE VII-21    ATTENUATION AND RECEIVED SIGNAL FOR MEDIUM CIRRUS CLOUD
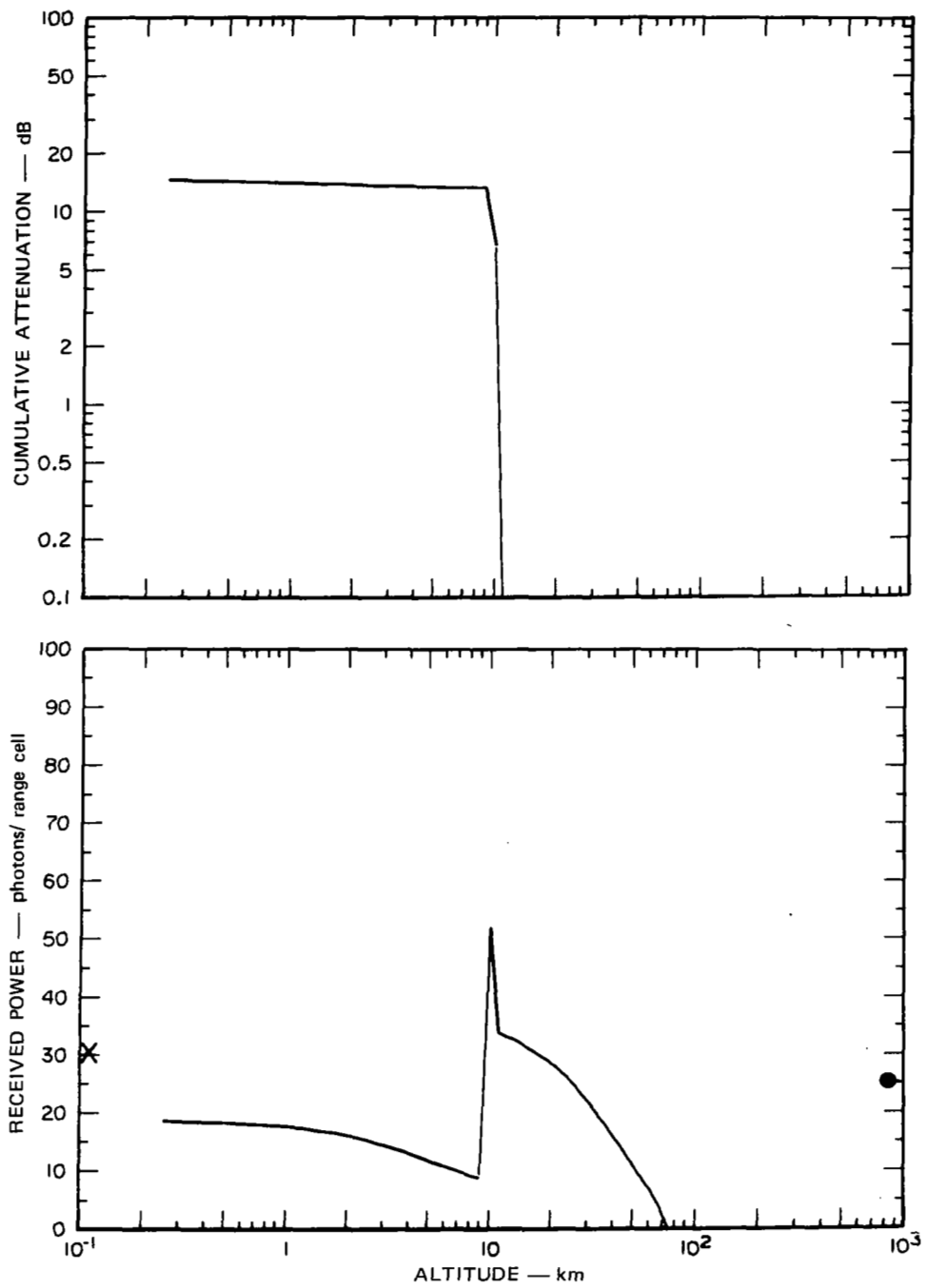
FIGURE VII-22    ATTENUATION AND RECEIVED SIGNAL FOR THICK CIRRUS CLOUD

that is sufficiently above the background-noise level to enable the bottom height of the cloud to be determined within the accuracy of the 1-km resolution.

Figure VII-23 shows the system performance for a medium stratus cloud at an altitude of 3 km. It is clear that the top height of the cloud can be determined in the daytime; however, the attenuation through the cloud is so large that the bottom portion of the cloud and anything lower in altitude cannot be seen, even at night. Thus, thickness and optical-depth measurements cannot be made.

Figure VII-24 shows the results for a dense cumulus cloud at an altitude of 1.5 km. The top-height measurement is feasible but the attenuation through the cloud is even higher than for the medium stratus; thus the comments concerning optical depth and thickness measurements for the stratus clouds apply to the cumulus cloud as well.

A summary of the capabilities of the 4-J ruby lidar system for making cloud measurements from 166 km is given in Table VII-5. A system with a larger energy output ($>40$ J) could also make daytime optical-depth measurements in thick cirrus and could also operate with a decreased range resolution, but otherwise the capabilities would be similar for a higher-power system. An improved instrument resolution would improve the accuracy of the cirrus optical-depth measurements.

Table VII-5

SUMMARY OF CLOUD CALCULATIONS

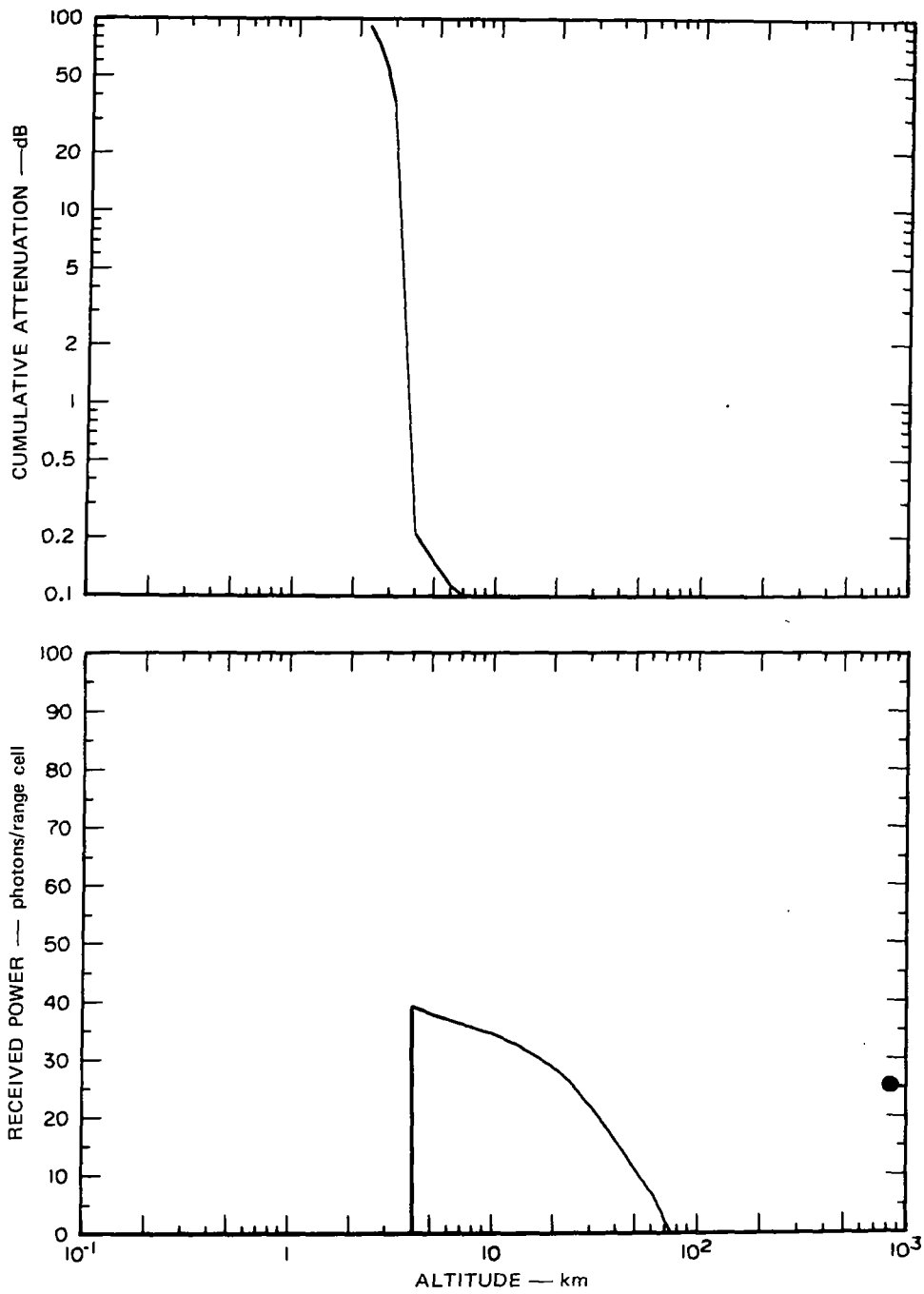| Cloud Type | Measurement Capability For: | | |
|---|---|---|---|
| | Height | Thickness | Optical Depth |
| Thin cirrus | Yes | Yes | Yes |
| Medium cirrus | Yes | Yes | Yes |
| Thick cirrus | Yes | Yes | No |
| Stratus | Yes | No | No |
| Cumulus | Yes | No | No |

FIGURE VII-23    ATTENUATION AND RECEIVED SIGNAL FOR STRATUS CLOUD
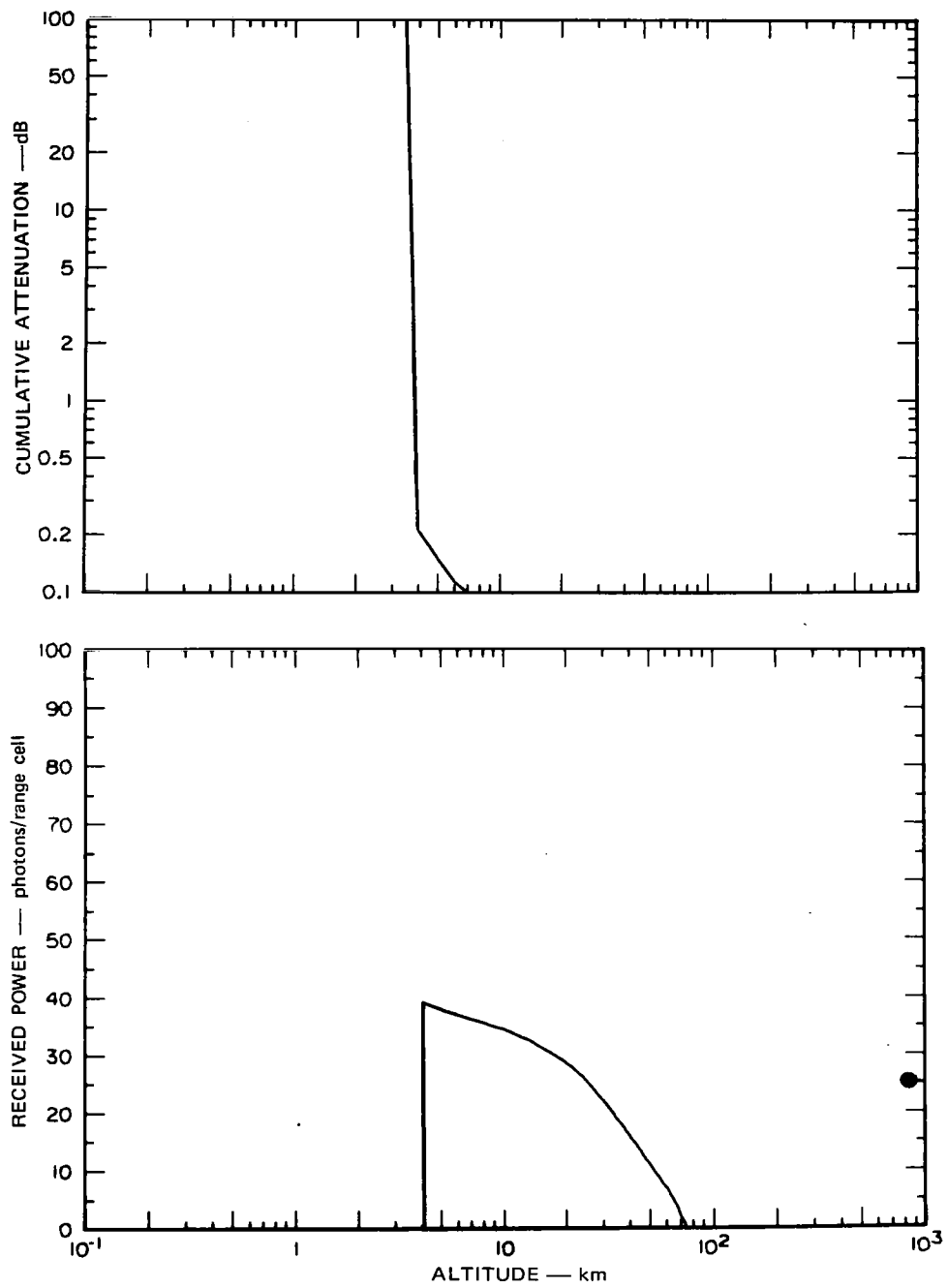
FIGURE VII-24    ATTENUATION AND RECEIVED SIGNAL FOR CUMULUS CLOUD

## 4. High-Altitude Aerosol Measurements

Backscattering from aerosols varies slowly with wavelength. Fixed-wavelength nontunable lasers are therefore suitable for measurement of the high-altitude aerosol layer. The superior performance capabilities of ruby and neodymium YAG lasers, which operate at 0.6943 $\mu$m and 1.06 $\mu$m, respectively, make them suitable for monitoring the high-altitude aerosol layer from satellites.

In addition to the cumulative-attenuation and received-signal curves shown for the cloud cases, a scattering quotient was computed as a function of altitude for these examples. This scattering quotient is the ratio of Mie scatter to Rayleigh scatter and is an excellent index of the high-altitude aerosol "visibility" in the presence of Rayleigh scatter. The ratio of Mie to Rayleigh scatter is preferred over the more commonly used ratio of total (Rayleigh plus Mie) scatter to Rayleigh scatter because it allows much better graphical accuracy for conditions of small aerosol scatter. The ratio of total scatter to Rayleigh scatter can be obtained simply by adding unity to the ratio used here.

Figure VII-25 shows the scattering quotient as a function of altitude for operation at the ruby wavelength of 0.6943 $\mu$m. This graph is for a clear standard atmosphere and shows a scattering quotient of approximately 0.11 at 25 km, corresponding to a scattering ratio of 1.11. The scattering quotient has a peak at 25 km and decreases to low values at about 15 and 40 km. To monitor the entire high-altitude aerosol layer, the system should operate at both the 15-km and the 40-km limit.

The received signal at 0.6943 $\mu$m shown in Figure VII-26 is approximately at the daylight background-noise level at about 22 km and does not rise to 6 dB above the background noise until about 10 km.
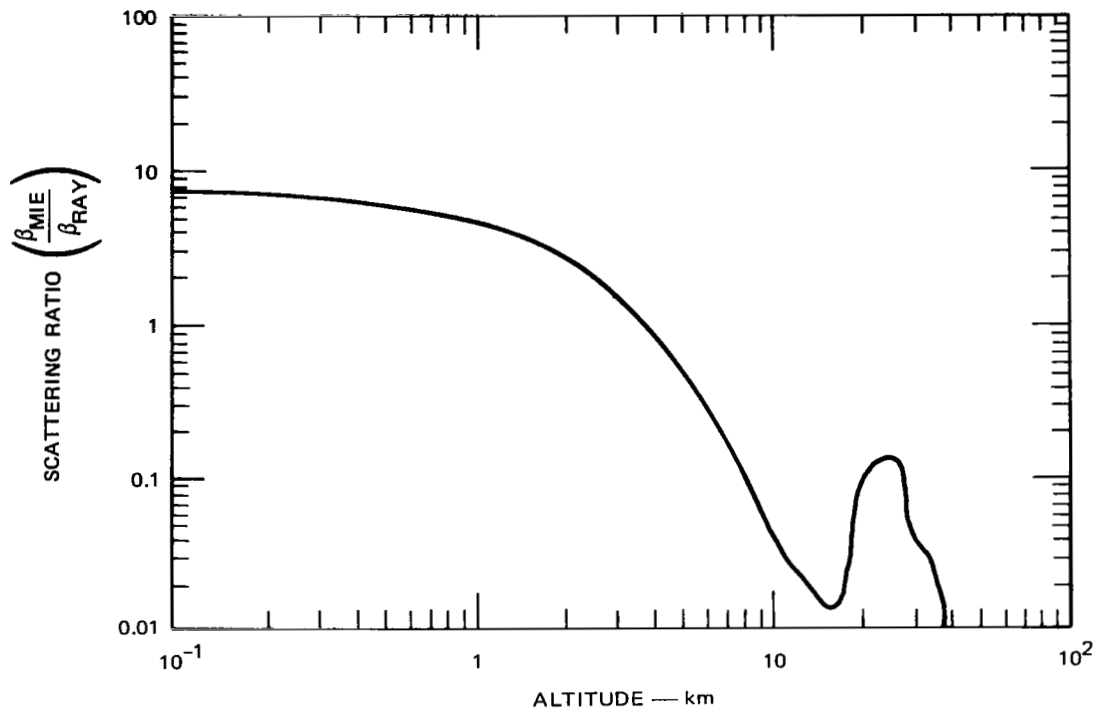
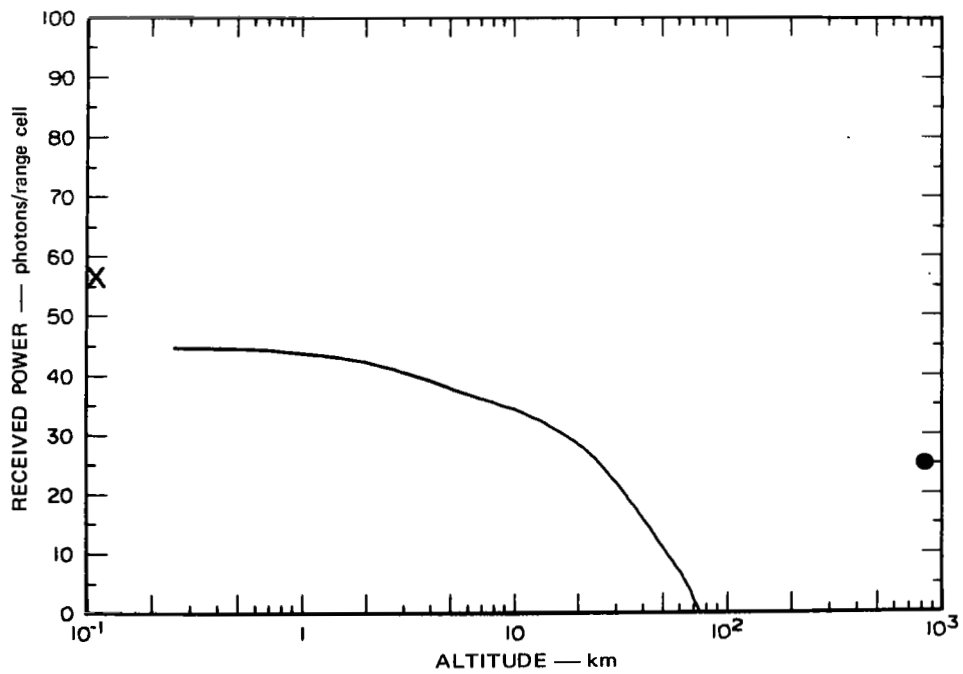FIGURE VII-25    SCATTERING RATIO AS A FUNCTION OF ALTITUDE AT 694.3 nm



FIGURE VII-26    RECEIVED SIGNAL AS A FUNCTION OF ALTITUDE AT 694.3 nm

229

Thus, single-pulse measurements in daylight are not possible with the postulated system. Note, however, that changes are only expected in the high-altitude aerosol layer from day to night. Therefore, nocturnal measurements of this layer are of interest. For the system parameters used in this example, night operation is limited by photon fluctuations rather than by detector noise. Under some conditions, however, performance can be limited by detector noise and perhaps by background noise (for example, when urban areas are in the field of view).

The reasonable minimum operating level of 100 photons per pulse, yielding a 10% fluctuation, occurs at about 30 km. Therefore, the postulated system would not provide accurate measurements up to the desired 40-km altitude. Since the photon fluctuation level is approximately 4% even at the 22-km peak and the aerosol component is only 11% of the total backscattered signal, the fluctuation noise would cause large errors in the measurement of the aerosol. Thus, the postulated system must be judged marginal. Operation at a 40-J level, however, would be satisfactory.

The cumulative attenuation curve, Figure VII-27, rises to a value of about 1.2 dB at ground level. Only about 0.13 dB of this attenuation is due to the Rayleigh component, the remainder being due to the aerosol component. Thus, the cumulative attenuation can be considered to be essentially due to the aerosol.

The performance of the 1.06-$\mu$m system is shown in Figures VII-28, VII-29, and VII-30. The scattering quotient in Figure VII-28 has a peak value of 0.4 at 23 km, corresponding to a 40% contribution from the aerosol and a scattering ratio of 1.4. This large value of the scattering quotient would produce good accuracy for measuring the high-altitude aerosol layer. Note that the scattering quotient still decreases to low values at 15 and 40 km, as in the previous case, but
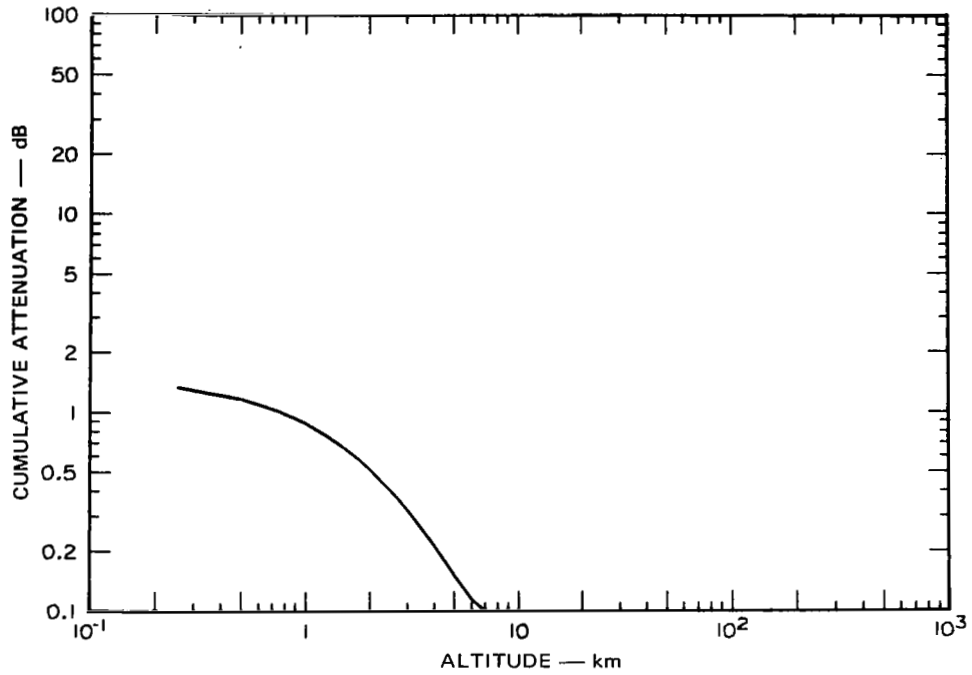
230

FIGURE VII-27    ATTENUATION AS A FUNCTION OF ALTITUDE AT 694.3 nm
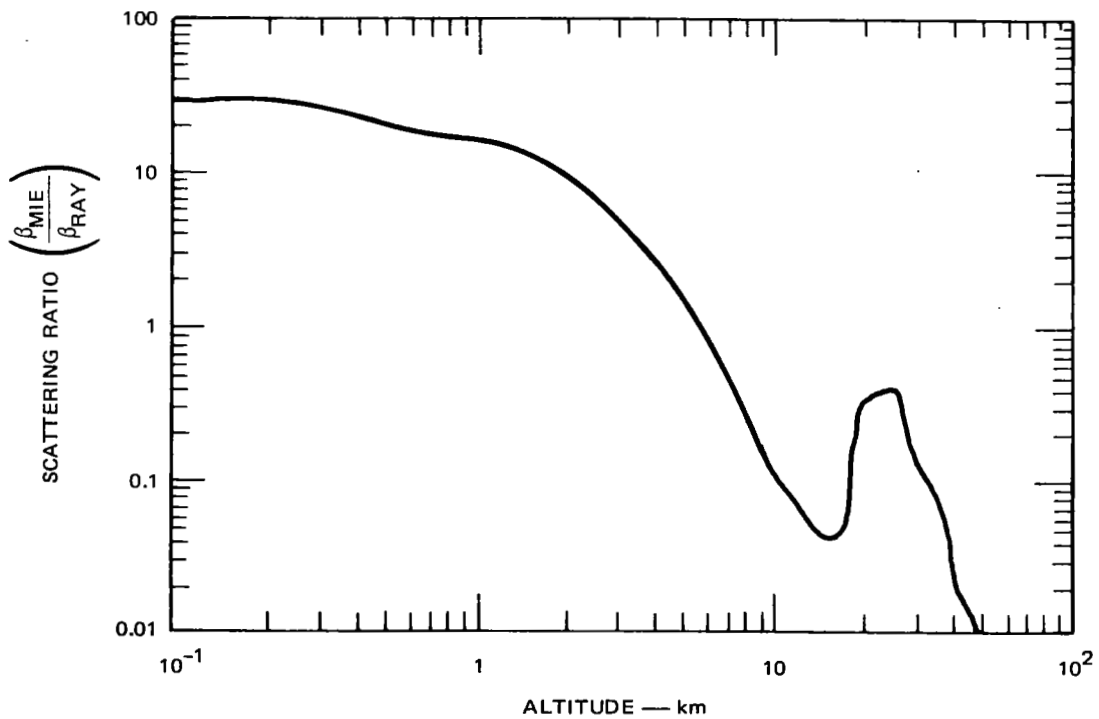


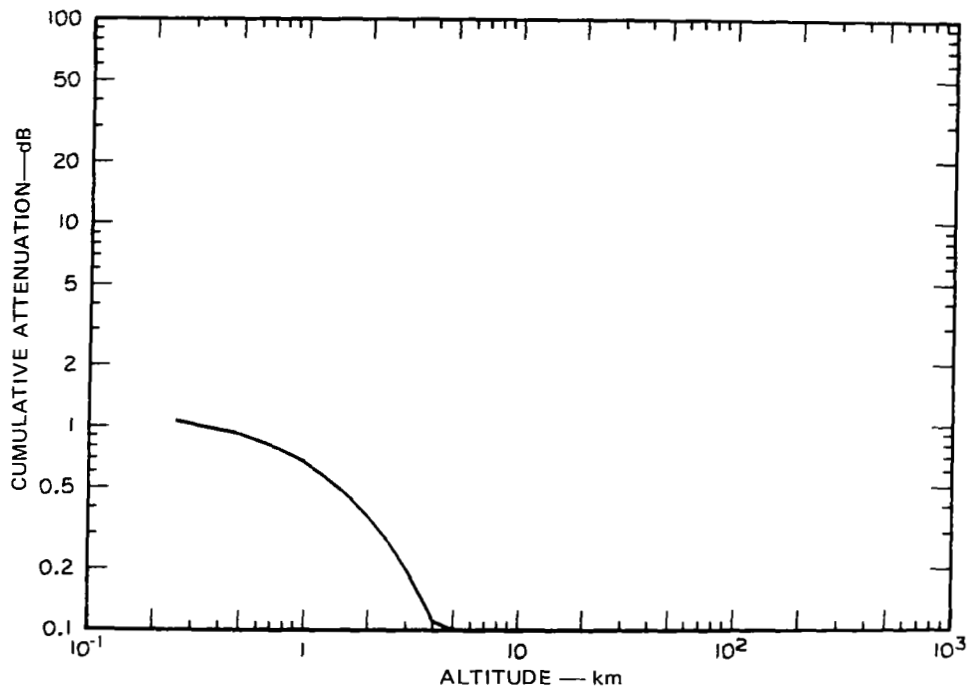FIGURE VII-28    SCATTERING RATIO AS A FUNCTION OF ALTITUDE AT 1.06 μm

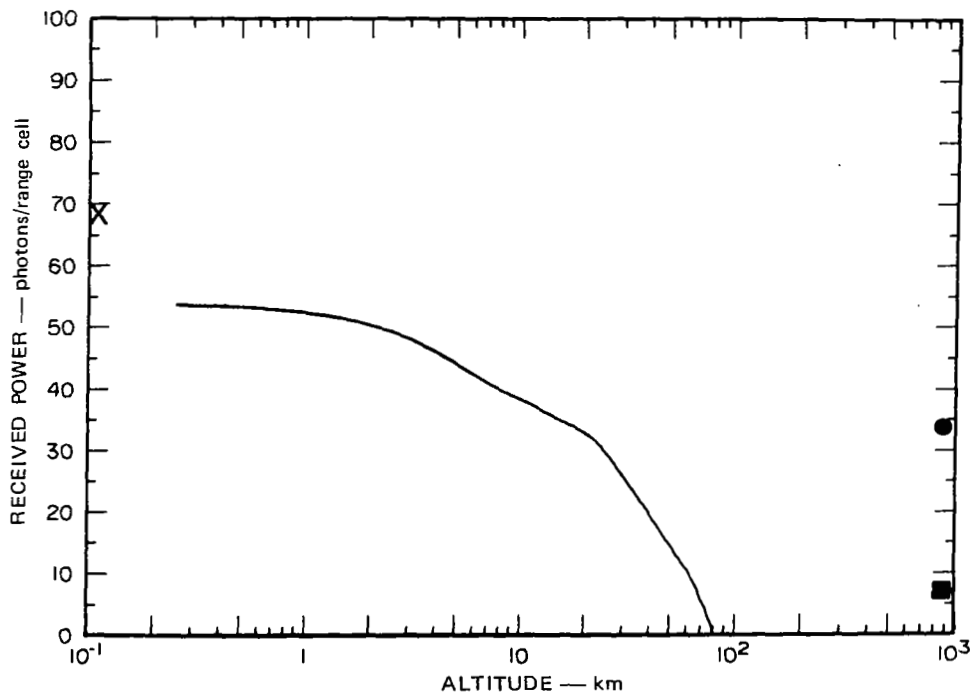FIGURE VII-29    ATTENUATION AS A FUNCTION OF ALTITUDE AT 1.06 $\mu$m



FIGURE VII-30    RECEIVED POWER AS A FUNCTION OF ALTITUDE AT 1.06 $\mu$m

232

near the ground rises to a value of about 28. The total scatter, however, has decreased, as is evident from the decreased cumulative attenuation shown in Figure VII-29. Again, this cumulative attenuation is due almost entirely to the aerosol component.

Because the backscatter contribution from the 23-km aerosol layer is 40% of the total signal, the shape of the returned-signal curve (Figure VII-30) as a function of altitude is altered, thus producing a noticeable bump at 22 km. The received signal is approximately equal to the background level at about 20 km. The decrease in signal strength relative to the values at 0.6943 $\mu$m are due primarily to the reduced backscatter at 1.06 $\mu$m and is partially offset by the larger assumed laser energy of 10 J. The background noise is too high to permit daytime measurements of the aerosol layer at 22 km. However, a 10% photon fluctuation is obtained at slightly less than 40 km and would permit marginal night measurements of the aerosol layer at the 10-J energy level.

The scattering quotient from the data for $NO_2$ monitoring at 450 nm discussed earlier has a value of approximately 0.04, which corresponds to a scattering ratio of approximately 1.04 for the 22-km aerosol layer. Thus, it would be more difficult to make accurate measurements at 450 nm than at either 1.06 $\mu$m or 0.6943 $\mu$m and would begin to impose a severe accuracy requirement because of the small contribution of aerosol scatter that must be measured accurately.

F.   Calculations for Aircraft Cases

1.   Range-Resolved Measurements for 12-km Aircraft Altitude

a.   Ozone at UV Wavelengths

There are interesting portions of the ozone profile both above and below 12 km. Here, ozone measurements both above and below the aircraft would be worthwhile.

233

A wider wavelength spacing, allowing greater attenuation and more differential absorption, is permissible from 12 km than from 166 km because the optical signal does not have to propagate through both the tropospheric and stratospheric $O_3$ layers. For the 12-km altitude, wavelengths of 298.20 nm and 310.90 nm provided the best performance. A laser energy of 0.5 J with a 0.1-$m^2$ receiver area were chosen.

Figure VII-31(b) shows that an adequate differential signal is obtained for $O_3$ both in the troposphere and the stratosphere. The sharp increase in signal level near the 12-km aircraft altitude are caused by the $1/R^2$ signal variation at short ranges.

For this calculation, compensation for the systematic errors in both the Rayleigh and the Mie components of differential scattering was assumed, which accounts for the excellent agreement between measured and modeled $O_3$ concentrations shown in Figure VII-31(c).

The limiting error in the measurement of material concentration is caused by noise at both low and high altitudes. The low-altitude error of 0.006 ppm is too small to appear on the graph in Figure VII-31(d). The minimum detectable material concentration is 0.006 ppm at ground level and decreases slowly up to the 12-km aircraft altitude.

The rapid decrease in signal level with increasing altitude above 12 km shown in Figure VII-31(b) accounts for the sudden increase in noise error shown in Figure VII-31(d). It is possible, however, to make adequate measurements of the high-altitude $O_3$ layer up to 25 km by integration of 400 pulse pairs. The 0.5-J energy level assumed for this calculation places the realizability of this system in the future (3-to-5-year) time frame. The same system with the laser energy reduced to 0.1 J is feasible with current technology, but measurement accuracy would be poor. A minimum detectable material concentration
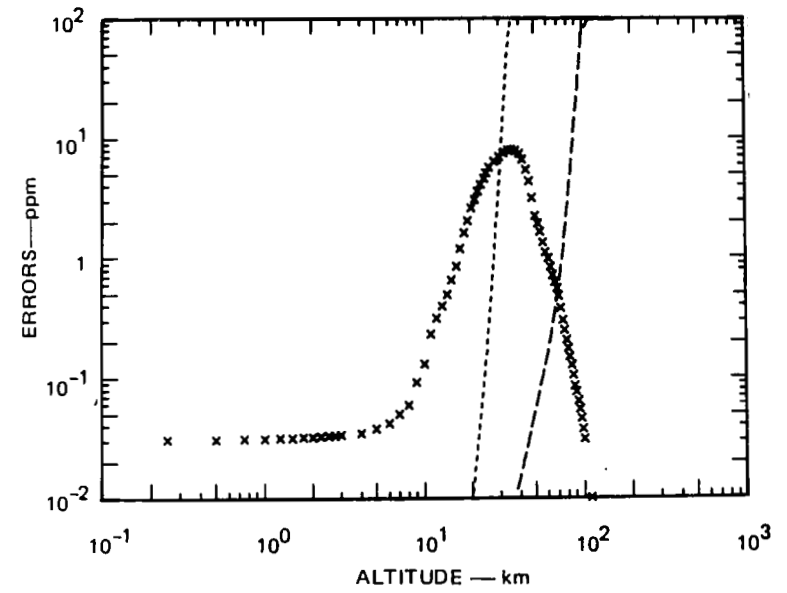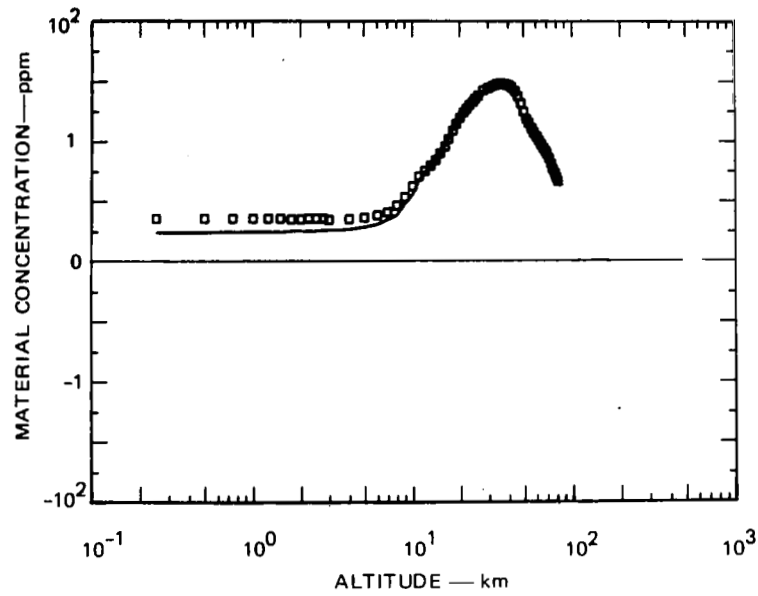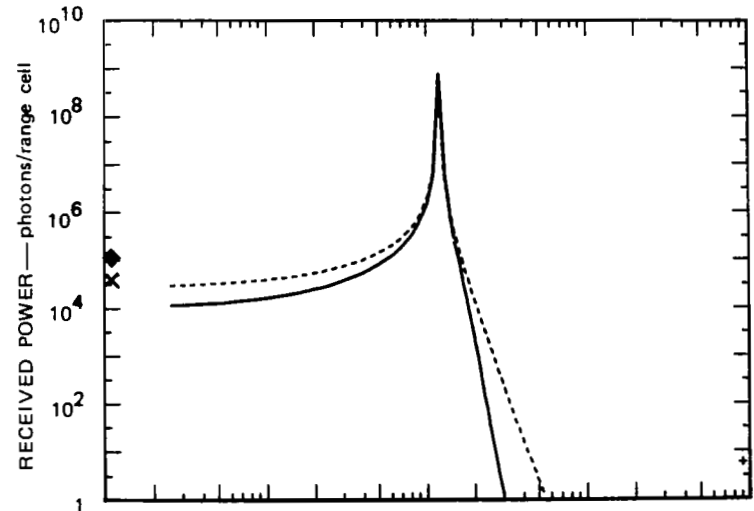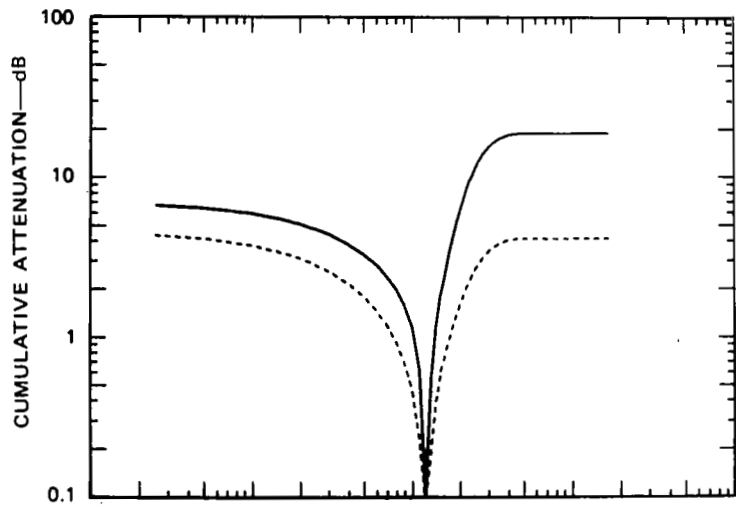
FIGURE VII-31   DETAILED PERFORMANCE SUMMARY FOR $O_3$ AT 300 nm FOR H = 12 km

slightly below the model concentration would result at all altitudes from 0 to 12 km, however, and would provide some measurement capability for low-altitude urban concentrations. Thus, for some applications, monitoring of the low-altitude urban-level concentration is within the present state of the art.

b.    Ozone at IR Wavelengths

Laser wavelengths of 1057.730 $cm^{-1}$ and 1057.950 $cm^{-1}$ were chosen for monitoring $O_3$ in the IR from the 12-km aircraft altitude. Figure VII-32(a) shows that the attenuation for this line pair is slightly low for altitudes of 0 to 12 km and somewhat higher than desired for monitoring the stratospheric $O_3$ layer. A one-way, high-altitude attenuation of almost 40 dB is indicated. This line pair thus provides a reasonable compromise between the optimum conditions for low and high altitudes.

A 1-J energy level with 0.1-$m^2$ aperture and a heterodyne detector produced the excellent signal returns below the aircraft shown in Figure VII-32(b). Integration of 100 pulse pairs produces the excellent performance shown in Figure VII-32(d). The noise-limited error in measurement of material concentration is below the bottom of the graph and is equal to 0.00025 ppm. This is slightly lower than the systematic error from interfering materials in this measurement, which is approximately 0.0003 ppm for altitudes below the aircraft. Although the interfering-material error for this line pair is fairly low and is satisfactory for the assumed conditions, another line pair could probably be found with still lower interference. In searching in this spectral region, however, many line pairs must be considered because of the large number of interfering lines from $CO_2$ and especially from $H_2O$. The excellent capabilities of the postulated system based on the modest 1-J energy requirement can be achieved with current technological capabilities.
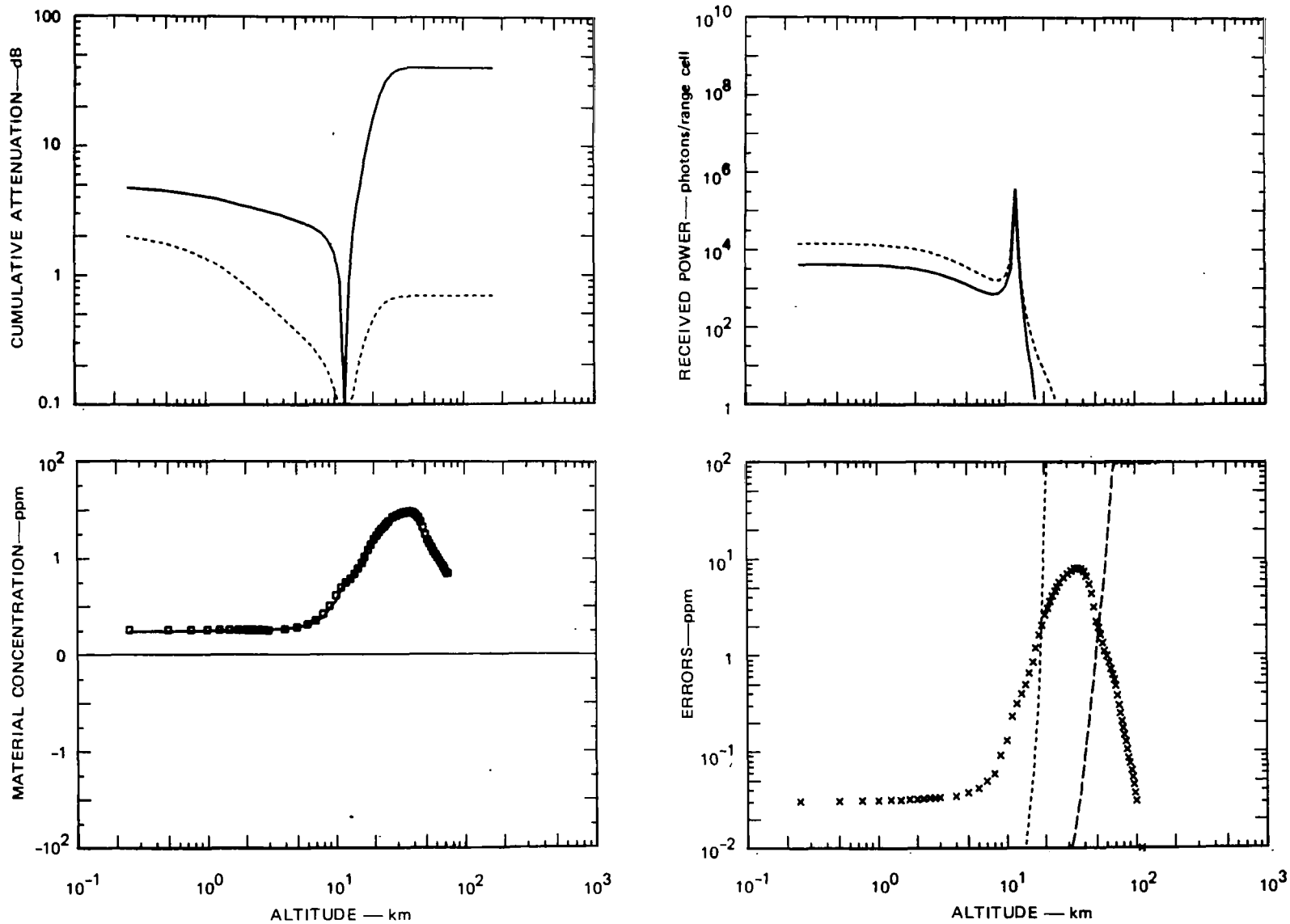
FIGURE VII-32    DETAILED PERFORMANCE SUMMARY FOR $O_3$ AT 9.5 $\mu$m FOR H = 12 km

The large cumulative attenuation above the aircraft and
the rapid decrease in backscatter with increasing altitude combine to
produce signal levels that decrease rapidly with altitude, as shown in
Figure VII-32(b). This decrease results in a rapid increase in the
error in material concentration, as shown in Figure VII-32(d). Even
with integration of 100 pulses as assumed in this example, the noise
error equals the model concentration at approximately 18 km, which is
well below the peak of the $O_3$ layer (at approximately 30 to 40 km) where
the concentration is almost an order of magnitude larger. Thus, moni-
toring of the stratospheric $O_3$ layer with the system described is not
feasible. Other systems specifically designed for monitoring strato-
spheric $O_3$ from high-flying aircraft may be better suited to the measure-
ment. However, detailed system designs and performance calculations
were not made for such systems.

A separate case, not shown in this report, was investi-
gated based on the 10-J laser energy level assumed to be possible within
the near-future time period and a conventional detector rather than a
heterodyne detector. This combination produced results similar to those
shown in Figure VII-31 except that the noise error is larger because of
the conventional detector, reaching a value at ground level of 0.0012 ppm.
This performance level is quite good, however, and indicates that measure-
ment of tropospheric $O_3$ with airborne systems based on either conventional
detectors or heterodyne detectors are feasible. Either system could be
built within the near-future time period.


c.    Sulfur Dioxide at UV Wavelengths

The line locations at 306.53 nm and 305.56 nm are good
choices but unfortunately provide a low attenuation and differential
attenuation, as seen in Figure VII-33(a), because of the small assumed
$SO_2$ concentration. Most of the attenuation at these wavelengths is due

238
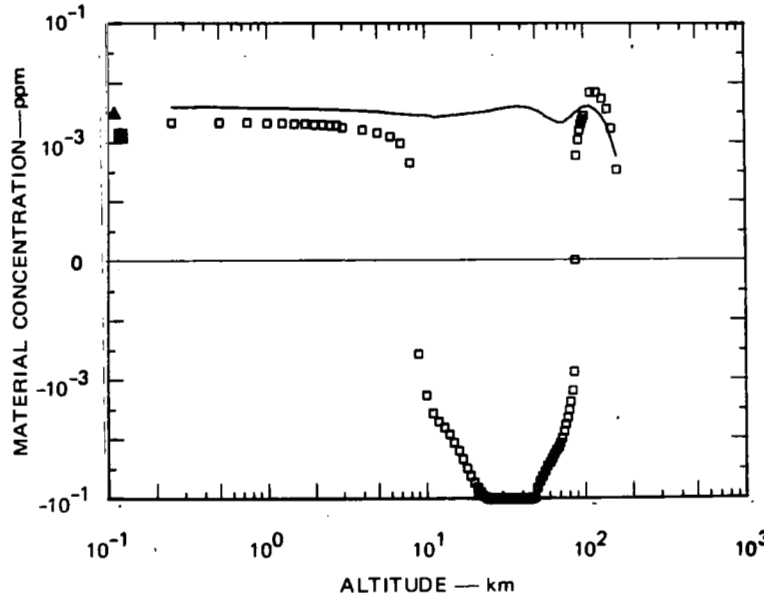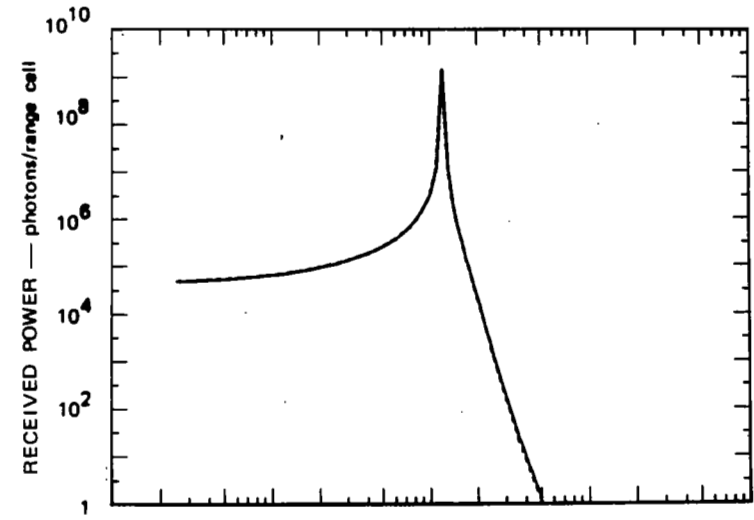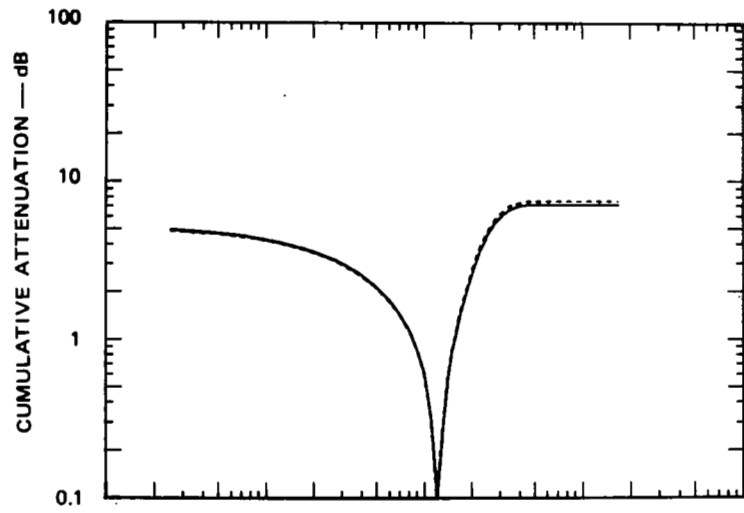
FIGURE VII-33    DETAILED PERFORMANCE SUMMARY FOR SO₂ AT 300 nm FOR H = 12 km

to Mie and Rayleigh scattering rather than attenuation by $SO_2$. $O_3$ attenuation is also significant in this region. Figure VII-33(b) shows that the SNR is large with the 1-J energy level and the $0.1\text{-m}^2$ aperture assumed for this example. The single-pulse performance level that might be expected from such SNRs is not achieved because of the small differential absorption. However, integration of 100 pulse pairs reduces the errors at altitudes below approximately 10 km to a value of about 0.0003 ppm. The primary interfering material is $O_3$. Although the interference is not substantial, it is noticeable.

The 1-J energy level assumed for this example yields good performance, but unfortunately is not achievable until the future (3-to-5-year) time period. Decreasing the laser energy to 0.2-J to achieve a capability in the near-future time frame would substantially degrade the performance, but the aperture area could be increased to $0.5 \text{ m}^2$ to compensate for the reduction in transmitted energy. Such a system would give marginal performance at rural $SO_2$ levels, but would probably provide entirely satisfactory performance levels for monitoring in urban areas where the $SO_2$ concentration is higher than is assumed in the rural model.

### d. Nitrogen Dioxide at Visible Wavelengths

The differential attenuation available for $NO_2$ is quite small because of the low absorption coefficient and the assumed low concentration of $NO_2$. Rayleigh and Mie scattering combine to produce a larger attenuation than does gaseous absorption by $NO_2$, although the total attenuation is still low. This results in the small absorption and very small differential absorption shown in Figure VII-34(a), and produces the small differential signal shown in Figure VII-34(b).
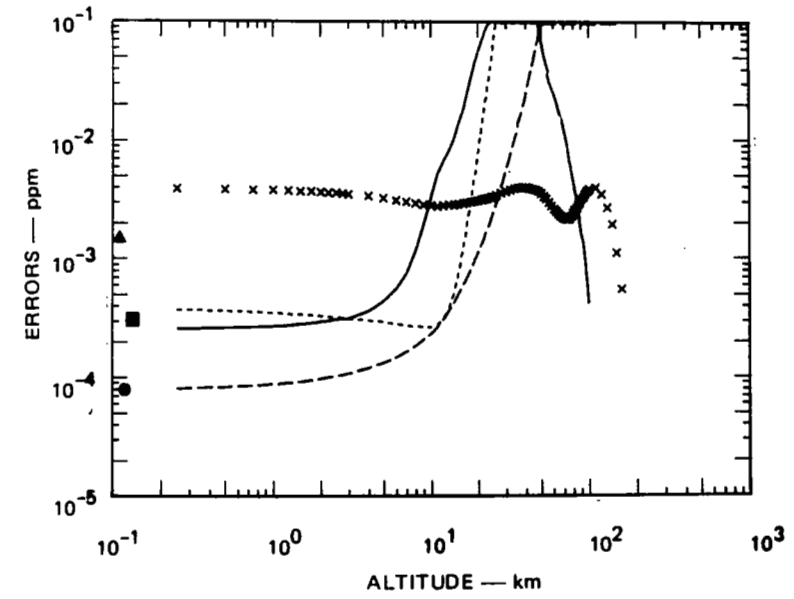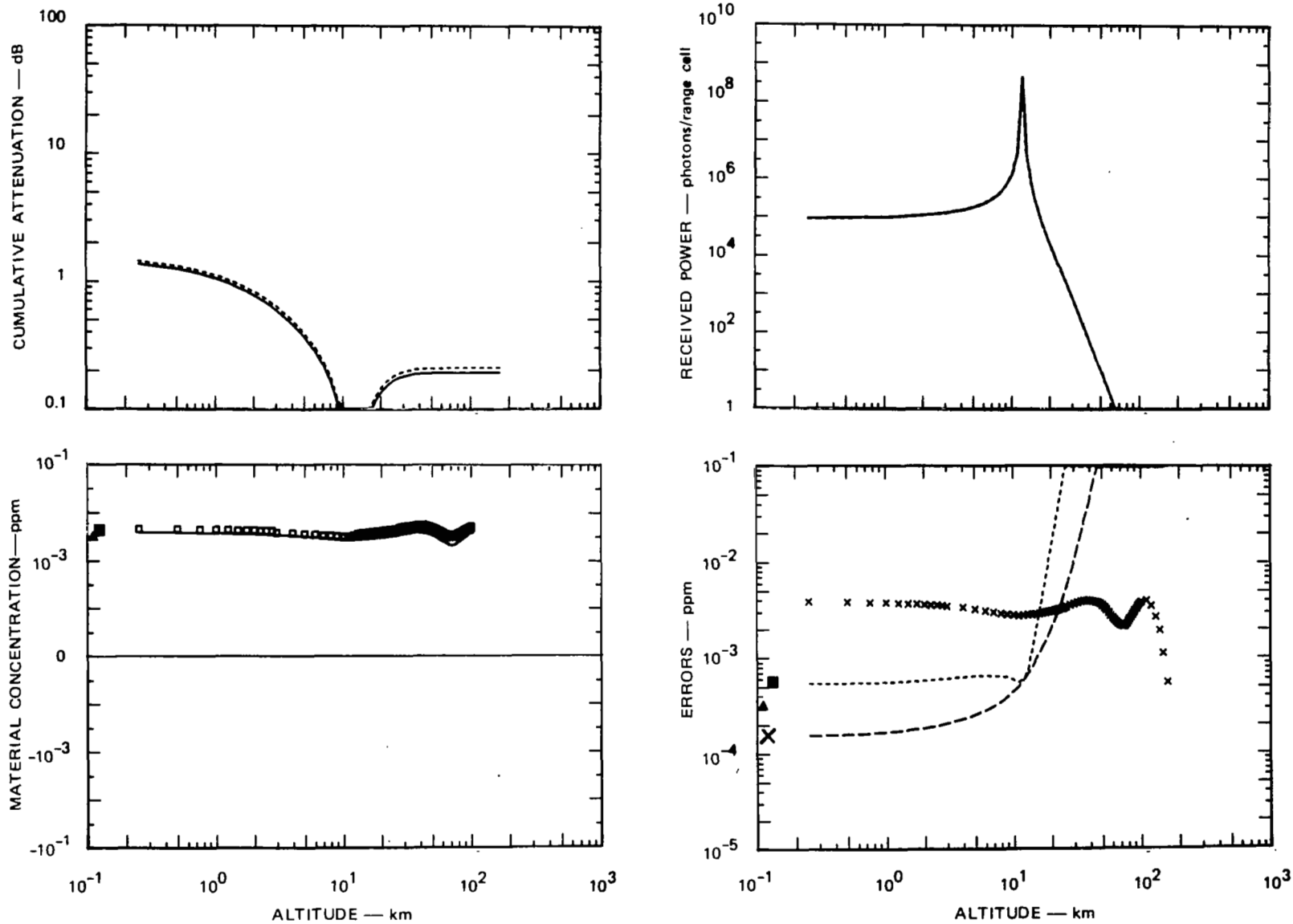
FIGURE VII-34    DETAILED PERFORMANCE SUMMARY FOR $NO_2$ AT 450 nm FOR H = 12 km

The SNR in this example is large, and, even though the differential absorption is small, a satisfactory performance level is indicated in Figure VII-34(d). There is no interfering-material error for these wavelengths. The primary limit on minimum detectable material concentration is due to noise, as shown by the dotted line in Figure VII-34(d). This error is approximately 0.0006 ppm and is adequate for monitoring both the rural $NO_2$ concentration assumed in the model and most of the background concentration range (0.5-4 ppb).

For this example the beamwidth of the transmitter and the FOV of the receiver were assumed to be 2 mrad to make the 1-J system eye-safe at ground level for a transmitter altitude of 12 km. The 1-J energy level assumed for this example can be provided by available dye lasers.

The 12-km cases were run for rural concentrations of pollutants, as were the satellite cases. A typical urban concentration of $NO_2$, which is approximately ten times the rural concentration, would give larger values of differential attenuation and differential signal, and would result in excellent performance by the postulated lidar. This case was not run because the 12-km aircraft would probably be used over large areas for which the $NO_2$ content would be closer to the rural value than the urban value. Since this premise may be wrong, usefulness of monitoring $NO_2$ in urban areas from 12 km is worthy of further investigation because an excellent operational capability is achievable with presently available system configurations.

e.  Carbon Monoxide at IR Wavelengths

Figure VII-35(a) shows that the wavenumber pair at 2147.084 cm$^{-1}$ and 2146.500 cm$^{-1}$ provides favorable attenuation and a large differential attenuation for the postulated system parameters. The SNRs shown in Figure VII-35(b) are smaller than would be desirable
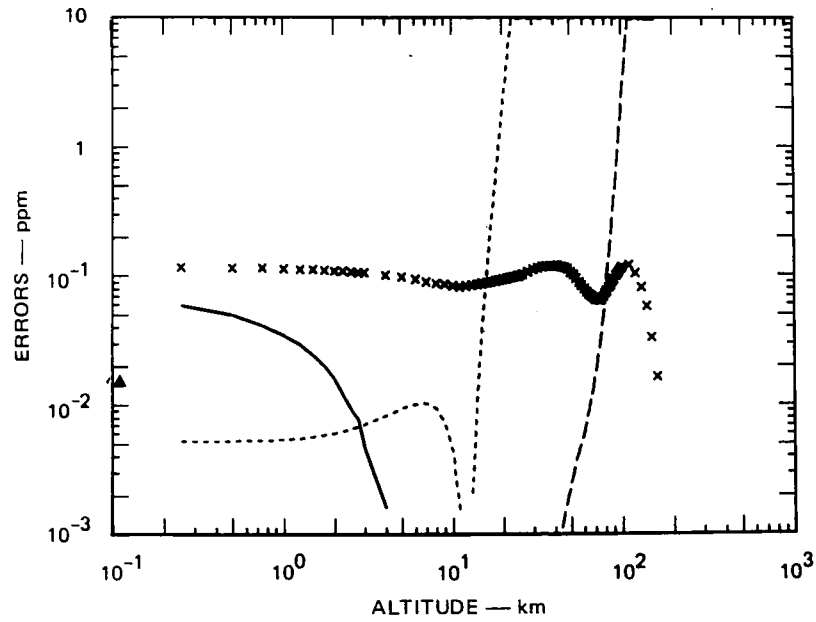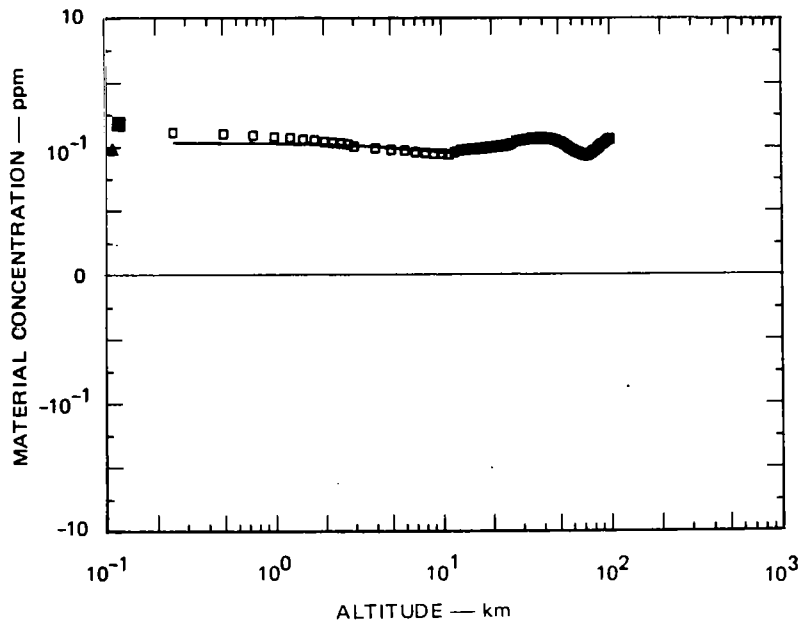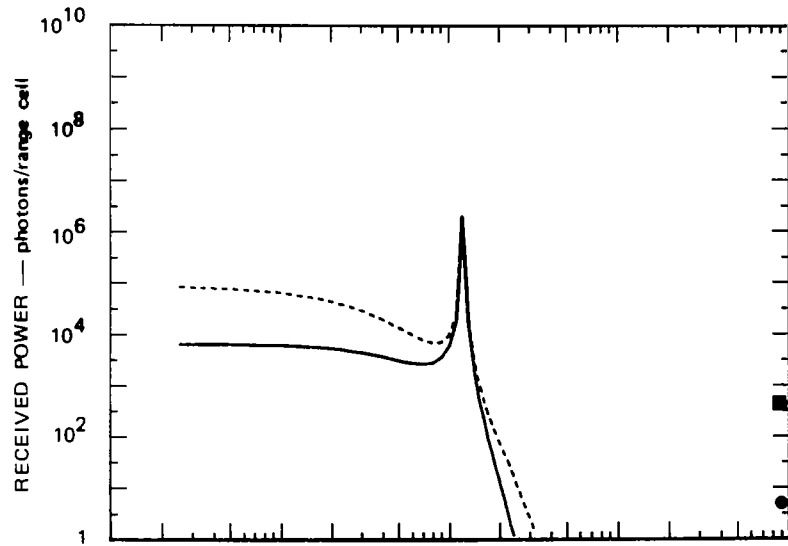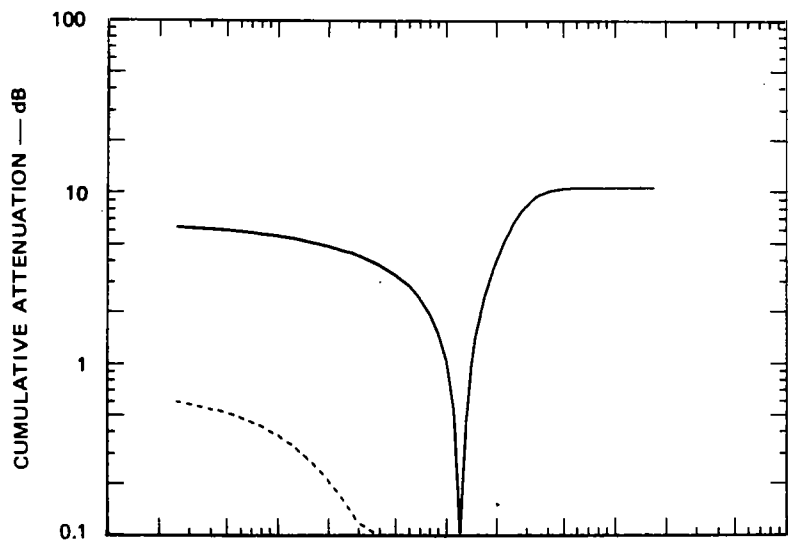
FIGURE VII-35    DETAILED PERFORMANCE SUMMARY FOR CO AT 4.5 $\mu$m FOR H = 12 km

243

because of the 1-J energy level and the $0.1\text{-m}^2$ aperture area assumed for the system. The high differential absorption, however, contributes to the excellent performance level indicated in Figure VII-35(d).

At low altitudes the limiting error, which reaches a value of 0.06 ppm ground level, is caused by interfering materials. This error is smaller than the model CO concentration, however, and would provide adequate performance even for the uncompensated measurement assumed here. Compensation for the interfering material would probably reduce the MDMC to the noise limit of approximately 0.007 ppm, which is substantially below the model concentration.

The 1-J energy level assumed for this example should be achievable within the future (3-to-5-year) time frame. Reduction of the energy level to 0.5 J to achieve a capability within the near-future time frame would have a fairly small effect on the measurement capability. The estimated noise-limited MDMC for the 0.5-J energy level is approximately one-quarter of the model concentration at ground level, which is below the uncompensated interfering-material limit and thus would not affect the performance of an uncompensated measurement.

f.   Nitrous Oxide at IR Wavelengths

The wavelengths of 2222.751 $\text{cm}^{-1}$ and 2222.460 $\text{cm}^{-1}$ provide a more favorable attenuation and differential attenuation than were obtained for the previous 12-km CO example, as can be seen in Figure VII-36(a). However, because of the 1-J energy level and the $0.1\text{-m}^2$ receiver aperture assumed, the degradation in SNR caused by the increased attenuation approximately compensates for the increased differential absorption. Thus, the major difference in the two cases is the substantially reduced interfering-material error in the $N_2O$ case.
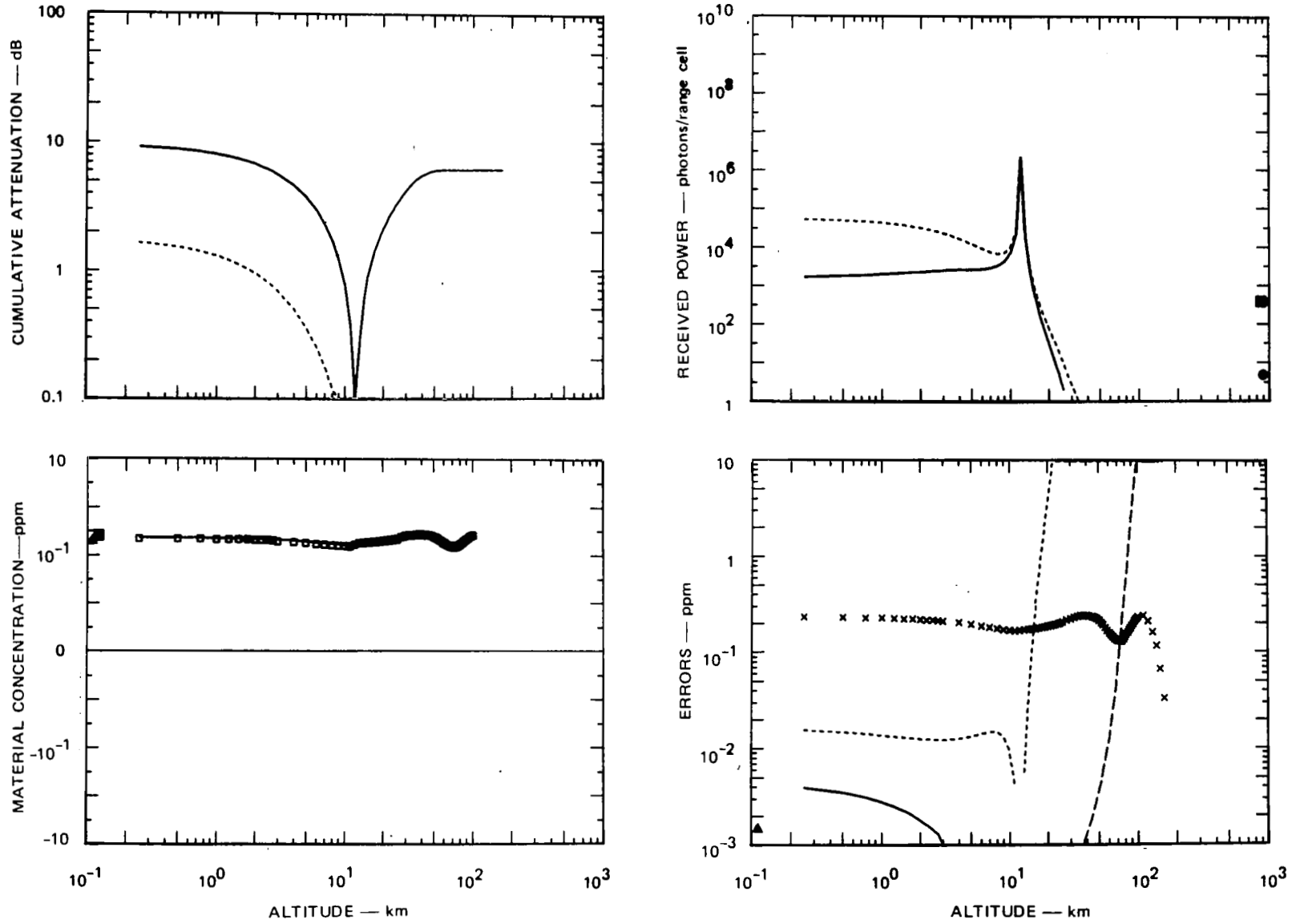
FIGURE VII-36    DETAILED PERFORMANCE SUMMARY FOR $N_2O$ AT 4.5 $\mu$m FOR H = 12 km

The accuracy of measuring material concentration is limited by noise to a value of approximately 0.017 ppm, which is more than an order of magnitude lower than the rural concentration of 0.22 ppm for $N_2O$ assumed in the model. Thus, excellent performance can be achieved with the postulated system. A reduction in laser energy from 1 J to 0.5 J to change the estimated time for achievability from the future (3-to-5-year) to the near future (1-to-5-years) would change the noise error to approximately 0.04 ppm, which is still well below the assumed concentration. Thus, satisfactory performance can be achieved even with reduced laser energy.

g.    Summary of Range-Resolved Cases from 12-km Altitude

A summary of the projected feasibility of measurements from the aircraft altitude of 12 km is given in Table VII-6.

2.    Range-Resolved Measurements for 3-km Aircraft Altitude

a.    Ozone at UV Wavelengths

From the 3-km altitudes a 100-m range resolution was assumed for the 12- and 166-km measurements. Reducing the range resolution diminishes the differential absorption per range cell, which makes the range-resolved measurements more difficult unless stronger absorption lines are available and selected. Thus, the 3-km measurements with 100-m range resolution are roughly comparable to the 12-km measurements with 1000-m range resolution.

The high-attenuation UV lines at 258.7 nm and 259.7 nm are suitable for this measurement because attenuation is not excessive. Figure VII-37(b) indicates that substantial signals are produced by the combination of a 0.2-J energy level, 0.1-$m^2$ aperture, and $3 \times 10^{-7}$-s pulse length assumed for this example. With integration of 100 pulse pairs, Figure VII-37(d) indicates that the measurement error is about

## Table VII-6

### SUMMARY OF RANGE-RESOLVED CALCULATIONS
### FOR A PLATFORM ALTITUDE OF 12 km

| Time Period for Feasibility | Material | MDMC or Altitude* Range | Assumed Laser Energy (J) |
|---|---|---|---|
| Present (0-1 year) | $O_3$(UV) | 0-12 km @ 30 ppb | 0.1 |
|  | $NO_2$ | 0.0006 ppm | 1 |
|  | $O_3$(IR) | 0-12 km | 1 |
| Near-future (1-2 years) | $N_2O$ | 0.04 ppm | 0.5 |
|  | CO | 0.014 ppm | 0.5 |
| Future (3-5 years) | $O_3$(UV) | 0-25 km | 0.5 |
|  | $SO_2$ | 0.0003 ppm | 1 |
|  | CO | 0.0007 ppm | 1 |
|  | $N_2O$ | 0.0015 ppm | 1 |

\*
Either ground-level error in material concentration (in ppm), or altitude range for satisfactory performance.

equal to the assumed model concentration at ground level and also at approximately 6 km.  Integration of 1000 pulse pairs will give approximately the same performance for the background concentration of 10 ppb. Urban or polluted atmospheres having larger concentrations of $O_3$ could be measured with a 0.1-J system achievable with present-day technology.
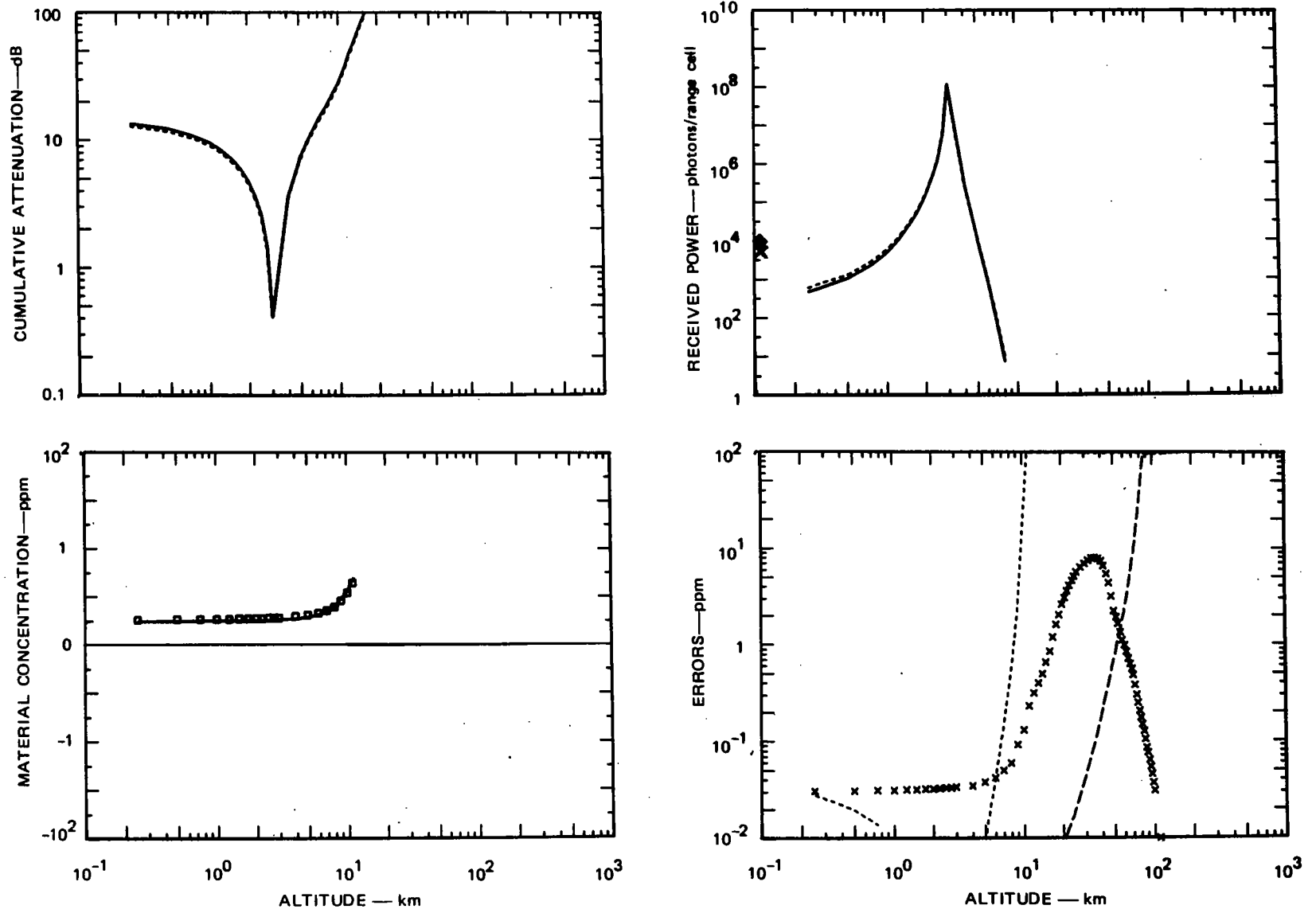
FIGURE VII-37    DETAILED PERFORMANCE SUMMARY FOR $O_3$ AT 300 nm FOR H = 3 km

b.    Ozone at IR Wavelengths

The absorption lines for monitoring $O_3$ in the IR from 3 km are the same ones used for 12 km.  Figure VII-38(a) shows that the attenuation for these lines is lower than would be desirable for monitoring from this altitude.  Also, the differential absorption is small below the aircraft.  This accounts for the small differential signal shown in Figure VII-38(b).  Figure VII-38(d) shows that the noise error is about equal to the model concentration at ground level and at approximately 4 km.  Integration of 1000 pulse pairs will give approximately the same performance for the background concentration of 10 ppb.  Thus, encouraging but inadequate performance could be obtained even with this relatively nonoptimum pair of lines.  Different lines with increased differential absorption could probably provide better performance.

c.    Sulfur Dioxide at UV Wavelengths

The attenuation values for $SO_2$ are moderately small for this case, which accounts for both the relatively large signal levels shown in Figure VII-39(b) and the small values of differential absorption and differential signal level.  Performance could be improved somewhat by using lines that provide more attenuation.  However, the results obtainable with this line pair [see Figure VII-39(d)] are encouraging though not outstanding.  Integration of 400 pulse pairs will provide comparable performance for the maximum background concentration of 2 ppb.  The dominant noise error could also be reduced to an acceptable level by enlarging the receiver aperture or increasing the transmitted energy.

d.    Nitrogen Dioxide at Visible Wavelengths

The line locations at 450 nm and 448.1 nm provide the largest attenuation and differential attenuation available for $NO_2$ in the visible-wavelength region.  Nevertheless, the cumulative attenuations are

249
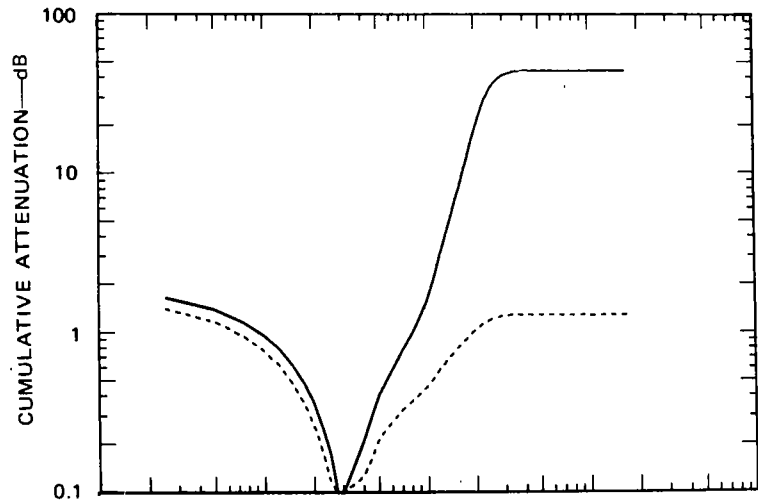
FIGURE VII-38   DETAILED PERFORMANCE SUMMARY FOR $O_3$ AT 9.5 $\mu$m FOR H = 3 km

FIGURE VII-39    DETAILED PERFORMANCE SUMMARY FOR $SO_2$ AT 300 nm FOR H = 3 km

quite small and due primarily to scattering losses rather than to absorption by $NO_2$. This results in the very small differential absorption indicated in Figure VII-40(a) and the small differential signal shown in Figure VII-40(b).

The SNRs from 3 km, even with modest systems employing 0.1 J and 0.1-$m^2$ aperture, are large, as shown in Figure VII-38(b). Note the high background-noise level shown by the symbol on the right-hand margin of the graph in Figure VII-40(b). This high level is caused by the need for a wide transmitted beam to maintain an eye-safe power level on the ground and the resulting requirement for a wide receiver field of view to encompass the entire transmitted beam. This produces a unique situation in which the performance level of the DIAL system is set by the eye-safety criterion. If the energy level is further increased, the transmitted beam and thus the received beam must be widened in order to maintain the eye-safe energy limit. This results in a constant SNR for a constant noise error in the system and thus sets the performance level independently of laser energy. However, the system performance can be improved by signal integration. For this reason, emphasis should be placed on low-power, high-PRF systems for monitoring $NO_2$ at visible wavelengths.

Even with the large SNRs shown in Figure VII-40(b), the very small differential absorption produces the relatively large noise error shown in Figure VII-40(d). In this example, integration of 1000 pulse pairs was used to achieve a noise-limited error in material concentration that is below the model concentration of $NO_2$. Integration of such a large number of pulse pairs was required because the eye-safety criterion must be met for the visible wavelengths used for $NO_2$ sensing. Even with the 0.1-J energy level assumed for the present system, the field of view had to be widened to 2 mrad in order to meet the eye-safety criterion. Thus, the system would operate at the eye-safety limit.

252
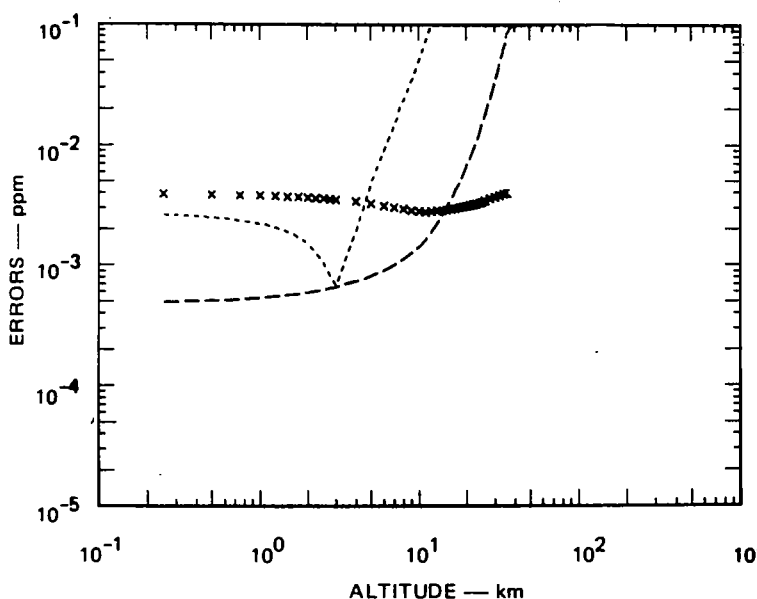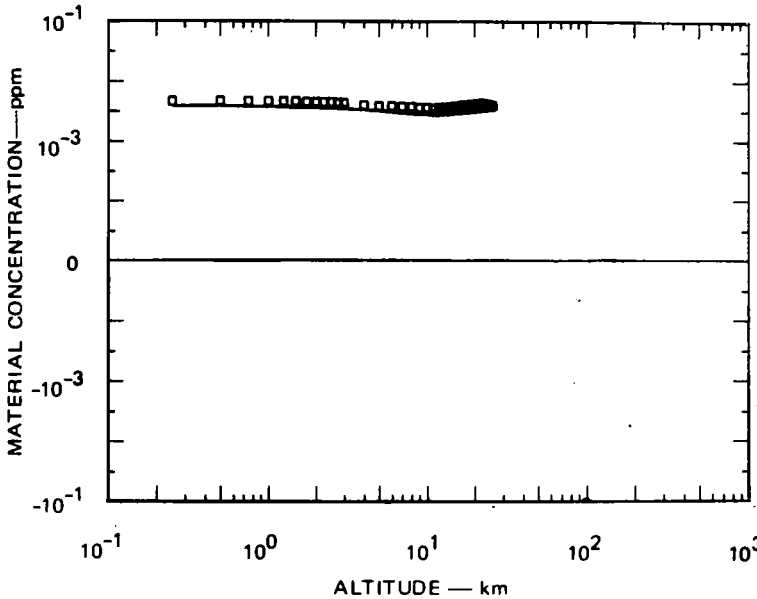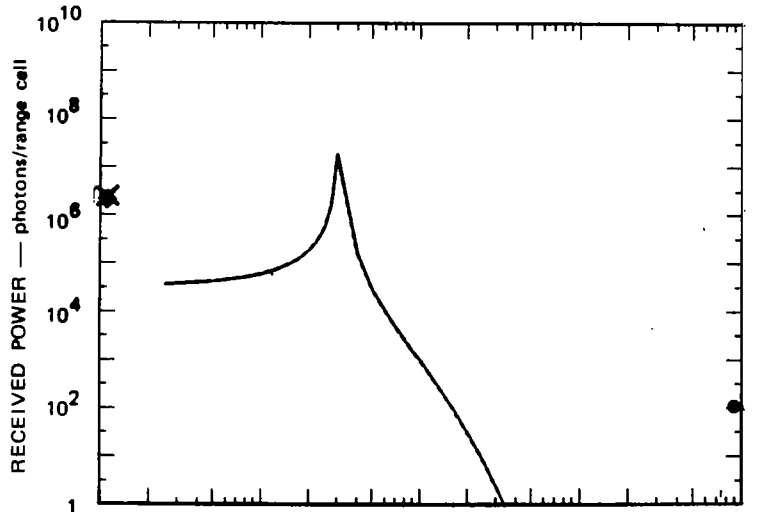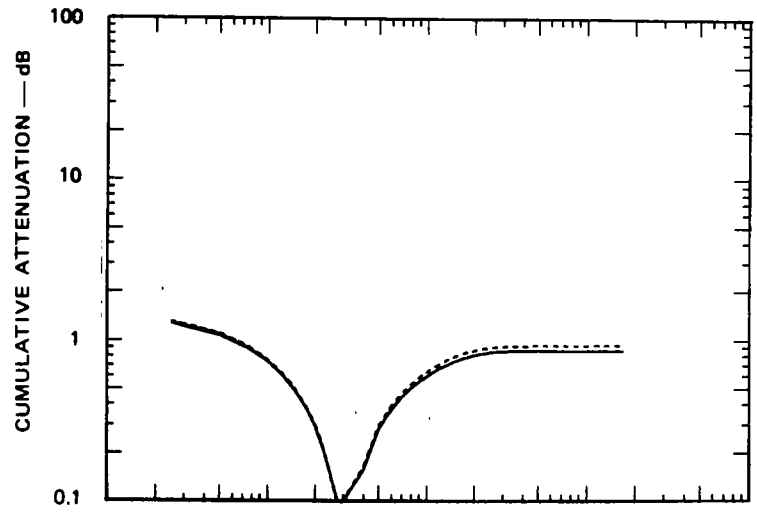
FIGURE VII-40   DETAILED PERFORMANCE SUMMARY FOR $NO_2$ AT 450 nm FOR H = 3 km

Increasing the range resolution from 100 m to 1 km would improve performance, but it was assumed that a 1-km range resolution from a 3-km altitude would not be considered adequate.

### e.   Carbon Monoxide at IR Wavelengths

As in several other 3-km cases, the attenuation shown in Figure VII-41(a) for the absorbing line is not quite as strong as would be desirable. However, this low attenuation contributes to an adequate differential signal and SNR even with the modest 0.5-J and $0.1\text{-m}^2$ aperture assumed for this system, as is evident from Figure VII-41(b). This produces the satisfactory error performance shown in Figure VII-41(d), which indicates that the primary limitation in the measurement is caused by interfering materials. This error is approximately half the assumed rural concentration at ground level and decreases with increasing altitude as is evident in Figure VII-41(d). The effect of interfering materials on the measured material concentration is fairly small, however, as is indicated in Figure VII-39(c). Thus, monitoring of CO from 3 km is feasible with good performance within the near-future time frame. With state-of-the-art systems a ground-level sensitivity about equal to typical rural concentrations would be obtained.

### f.   Nitrous Oxide at IR Wavelengths

For this example a higher attenuation line at $2229.429$ $\text{cm}^{-1}$ was chosen in conjunction with a valley wavelength of $2222.9$ $\text{cm}^{-1}$. Figure VII-42(a) shows that the attenuation for the strongly absorbing line at $2229.429$ $\text{cm}^{-1}$ is larger than would be desirable for the 1-J and $0.1\text{-m}^2$-aperture-system parameters chosen for this case. This high attenuation, in conjunction with the conventional detector, results in a relatively poor SNR for the strongly absorbed line, as indicated by the solid line in Figure VII-42(b). This low SNR results in a large noise error below
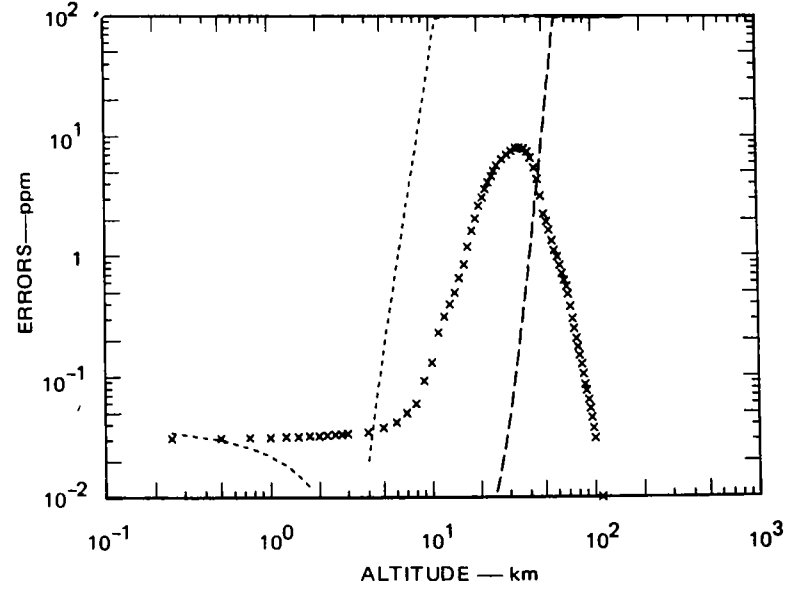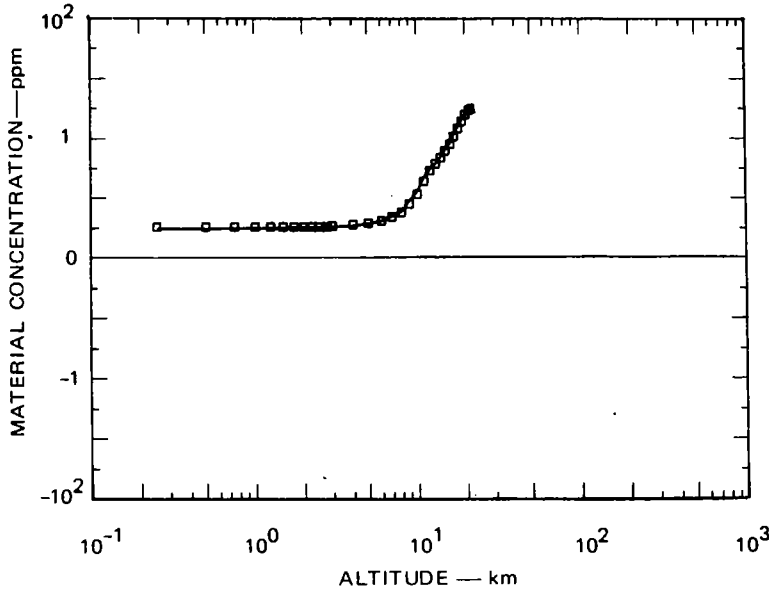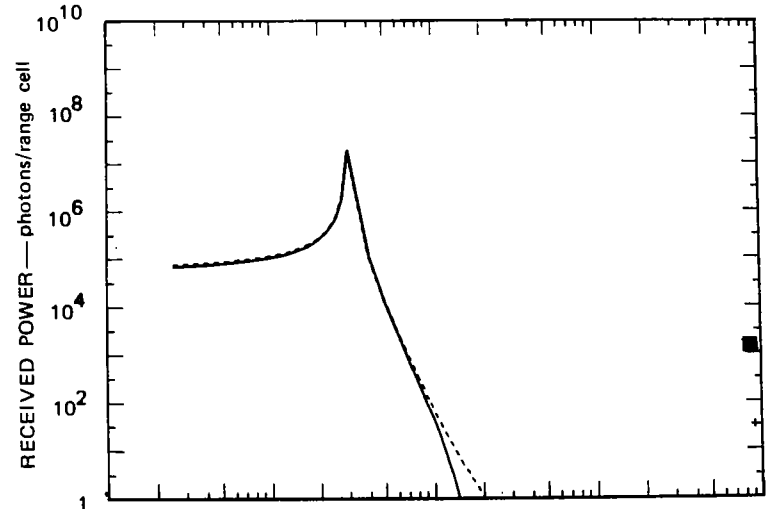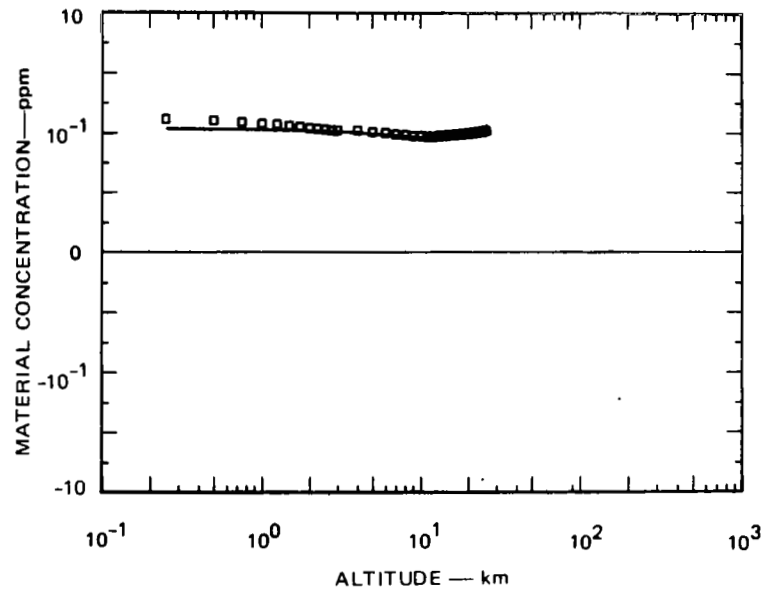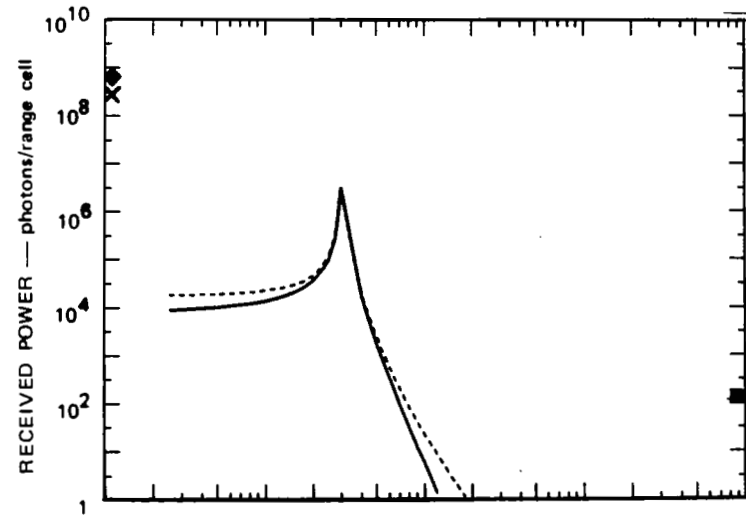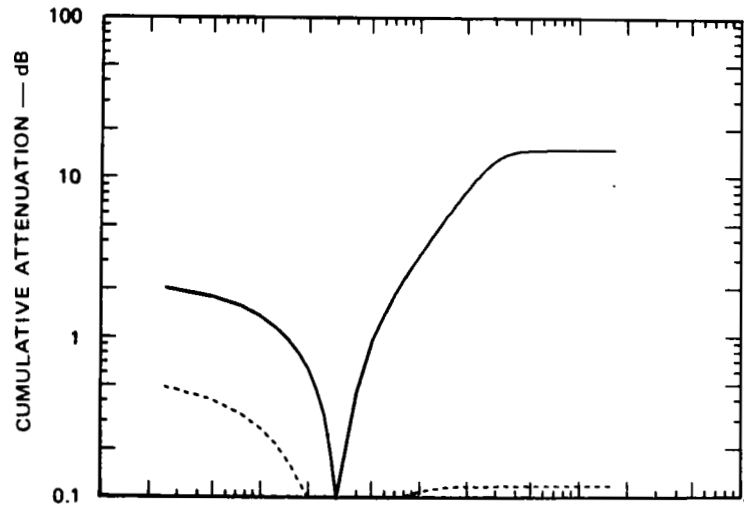
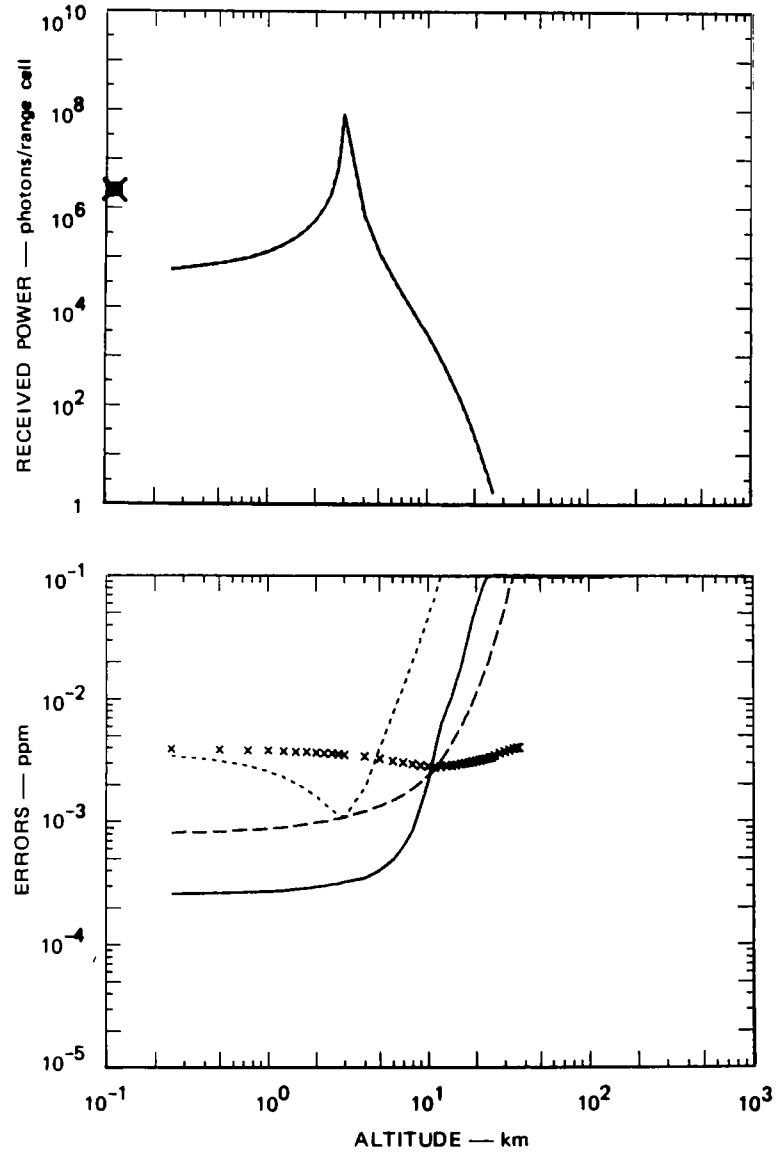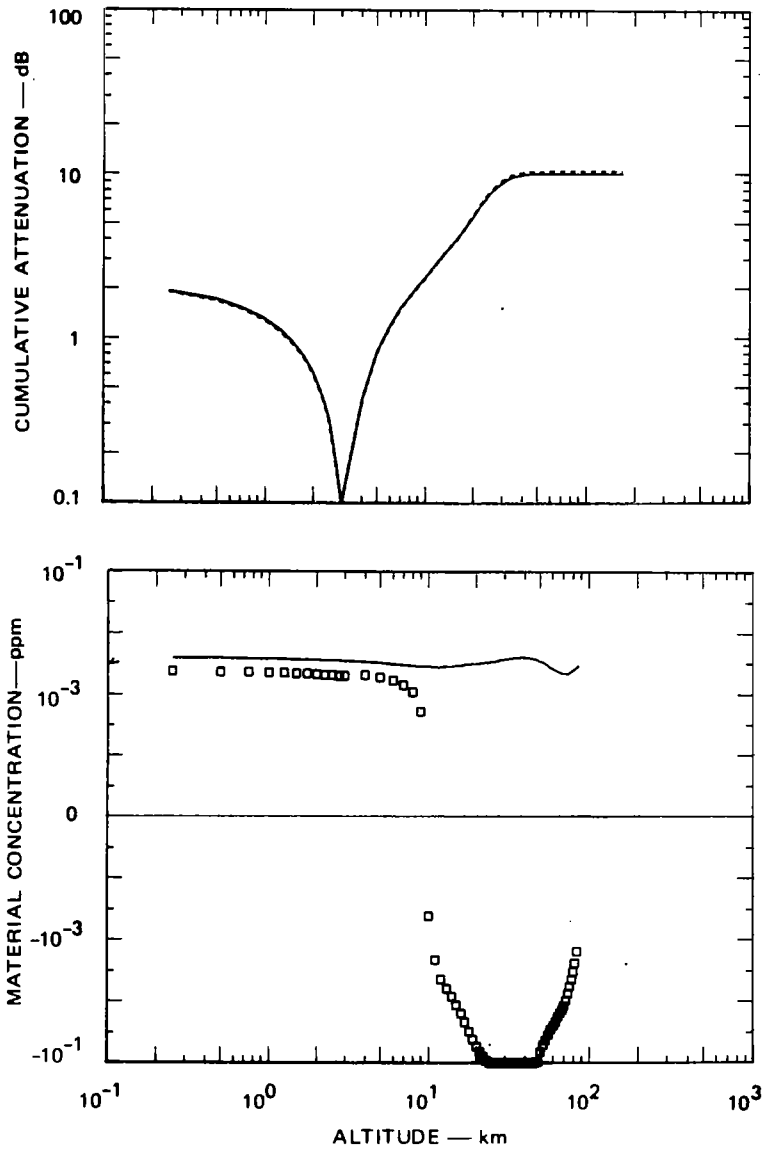FIGURE VII-41   DETAILED PERFORMANCE SUMMARY FOR CO AT 4.5 μm FOR H = 3 km

256
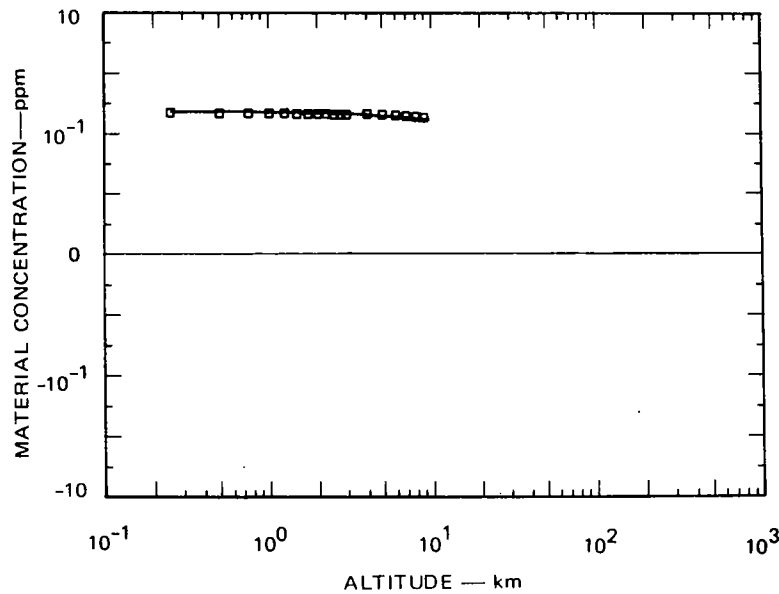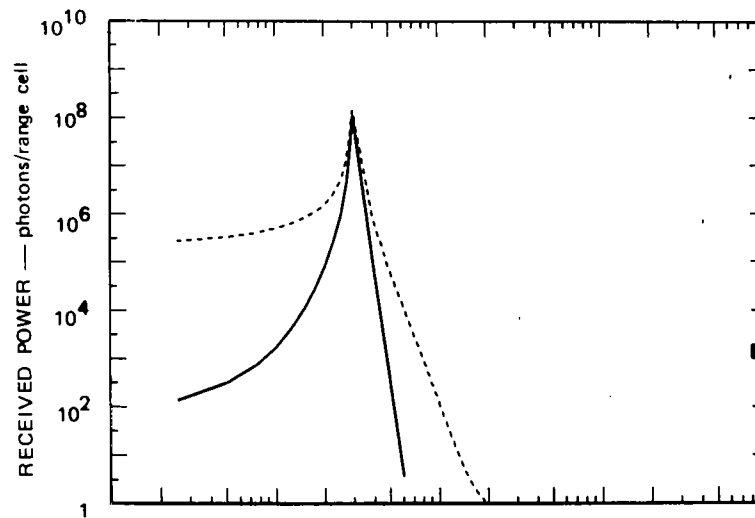
FIGURE VII-42    DETAILED PERFORMANCE SUMMARY FOR $N_2O$ AT 4.5 $\mu$m FOR H = 3 km

1 km as indicated by the dotted line in Figure VII-42(d). The large differential absorption, however, leads to a very small interfering-material error, as indicated in Figure VII-42(c).

Note that an off-the-shelf, ordinary-quality infrared detector was assumed for this system. The use of a high-quality, state-of-the-art detector would reduce the noise error to less than 0.1 ppm at ground level. Thus, the use of a high-quality conventional detector would permit $N_2O$ measurements to be made at typical rural concentrations within the near-future time period. Although under some conditions an error of 0.1 ppm may be unacceptable, use of a heterodyne detector or signal integration could produce acceptable performance even with the presently achievable 0.1-J energy level.

### g. Summary of Range-Resolved Cases for a 3-km Altitude

A summary of the projected feasibility of measurements from the aircraft altitude of 3 km is given in Table VII-7.

### G. Calculations for Ground-Based Upward-Looking Measurements

Figure VII-43 shows a performance summary for a ground-based system designed to monitor $O_3$ at both low and high altitudes in the 9.5-$\mu$m wavelength region. From Figure VII-43(a) it is apparent that most of the $O_3$ attenuation occurs in the stratospheric $O_3$ layer, as indicated by the rapid rise in attenuation of the more strongly attenuated line above 10 km. Note that with this particular choice of line pair the low-altitude differential attenuation is moderately low. This combination of small differential at low altitude and large differential at high altitude is preferable for a ground-based, upward-looking system because of the behavior of signal strength as a function of range, as indicated in Figure VII-43(b).
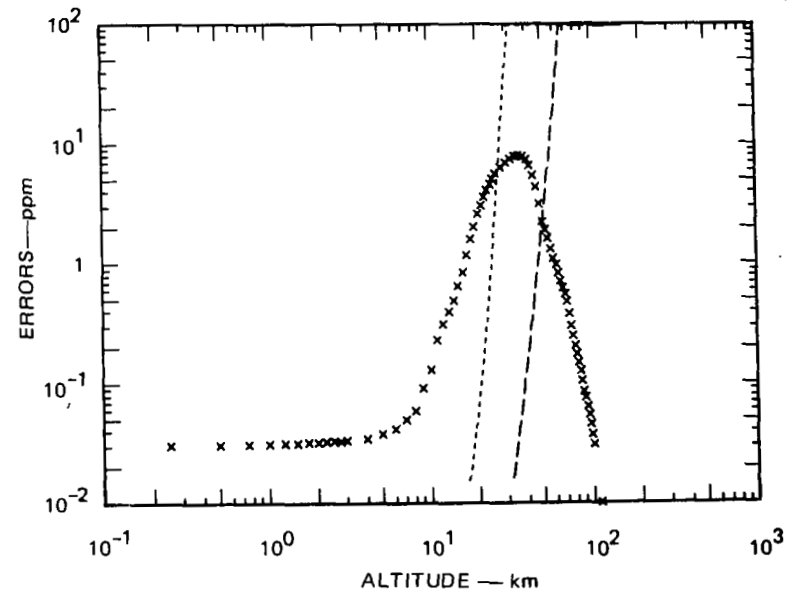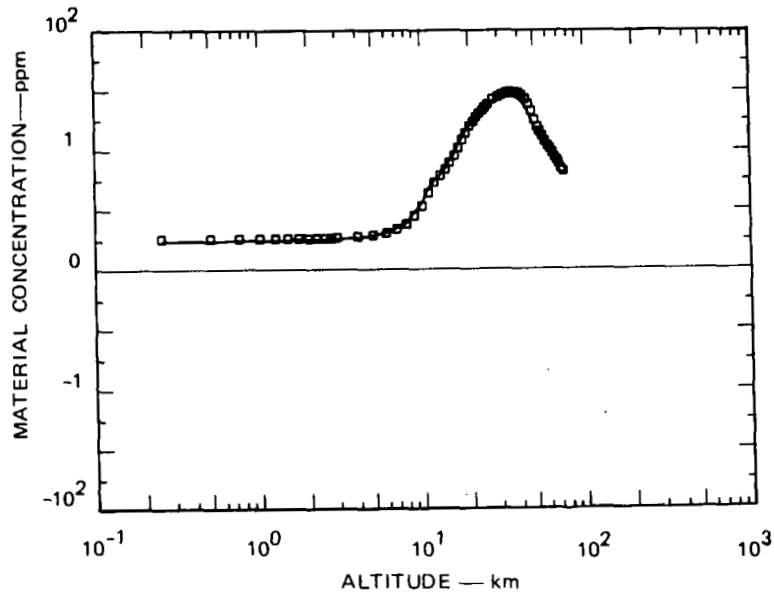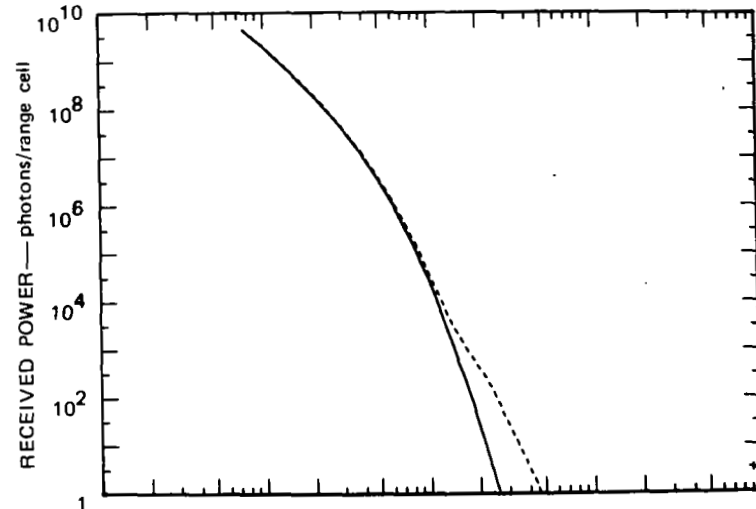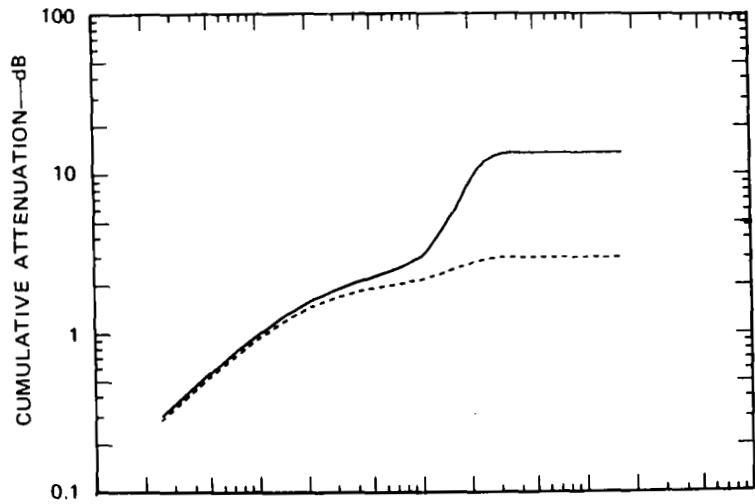
FIGURE VII-43    DETAILED PERFORMANCE SUMMARY FOR $O_3$ AT 9.5 $\mu$m FOR H = 0 km

Table VII-7

SUMMARY OF RANGE-RESOLVED CALCULATIONS
FOR A PLATFORM ALTITUDE OF 3 km

| Time Period for Feasibility | Material | MDMC or Altitude* Range | Assumed Laser Energy (J) |
|---|---|---|---|
| Present (0-1 year) | $NO_2$ | 0.0025 ppm | 0.1 |
| | $N_2O$ | < 0.1 ppm | 0.1 |
| | CO | 0.1 ppm | 0.1 |
| Near-future (1-2 years) | $O_3$(UV) | 0-6 km | 0.2 |
| | $SO_2$ | 0.004 ppm | 0.2 |
| | $N_2O$ | 0.1 ppm | 0.5 |
| | CO | 0.018 ppm | 0.5 |
| | $O_3$(IR) | 0-4 km | 10 |

*Either ground-level error in material concentration (in ppm), or altitude range for satisfactory performance.

In upward-looking systems the $1/R^2$ signal-strength variation combines with the reduction in backscatter as a function of increasing altitude to produce a rapidly decreasing received signal power for higher altitudes. The large signal strengths at short ranges partially compensate for the low differential attenuation in producing good performance. As indicated in Figure VII-43(d), a measurement capability exists up to an altitude of almost 30 km. The sharp rise in noise error beginning at approximately 20 km is caused by the onset of a rapid decrease in signal strength with

altitude above that point.  Performance below 10 km is exceptionally good, with an average error of approximately $10^{-4}$ ppm, which is more than two orders of magnitude less than the modeled rural concentration, and thus would provide for exceptionally good performance for the low-altitude $O_3$ region.  Below 15 km, all are too small to indicate on the graph of Figure VII-43(d).

The results presented here are for integration of 1000 pulse pairs. This large amount of integration was used in an attempt to increase the maximum altitude at which the stratospheric $O_3$ layer could be monitored. At altitudes below 10 km, the error in measuring material concentration is less than about 0.004 ppm for a single pulse pair.  This is approximately one order of magnitude less than the modeled concentration and thus would provide a good performance level even for a measurement using a single-pulse-pair.  At altitudes below 1 km to 2 km the primary error would be due to interfering materials, which could be reduced by compensation or perhaps by a better choice of operating lines.

Because of the rapid dropoff in signal return as a function of altitude, the additional performance obtained by integration of 1000 pulse pairs rather than a single pulse pair only increases the maximum altitude from 20 km to about 28 km.  This rapid dropoff in signal strength would probably not be significantly changed by large increases in multi-pulse integration, power output, or other system parameters.  Thus, it appears difficult to monitor the entire stratospheric $O_3$ layer with a ground-based infrared DIAL monitoring system.

The performance for a ground-based $O_3$ monitoring system operating in the UV spectral region is shown in Figure VII-44.  From this figure it is apparent that the 1-J UV system provides a performance level almost identical to that of the 100-J IR system for monitoring $O_3$ at both low and high altitudes.  As in the IR case, integration of 1000 pulse pairs provides an $O_3$ measurement capability up to approximately 30 km.
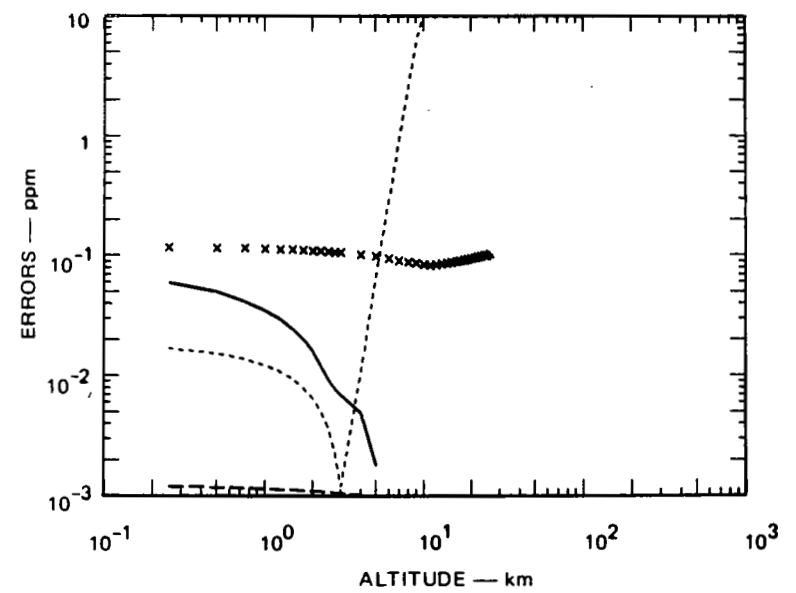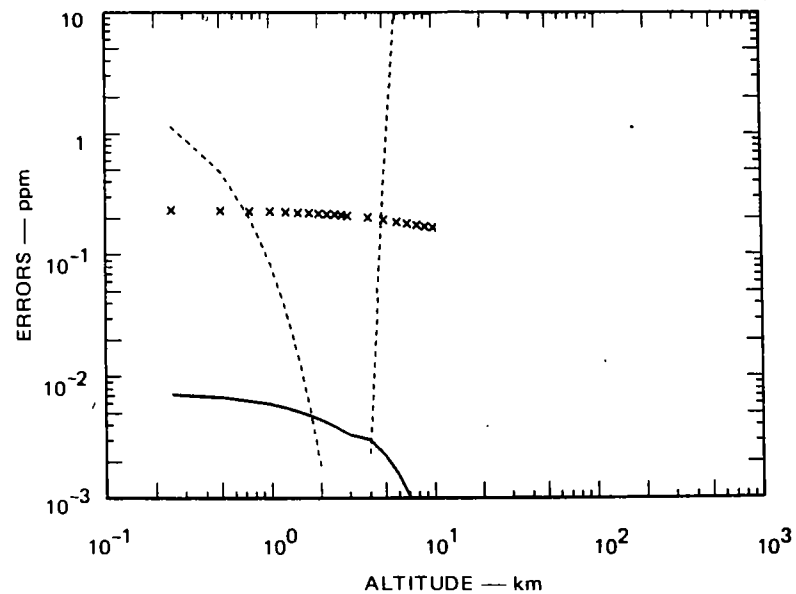
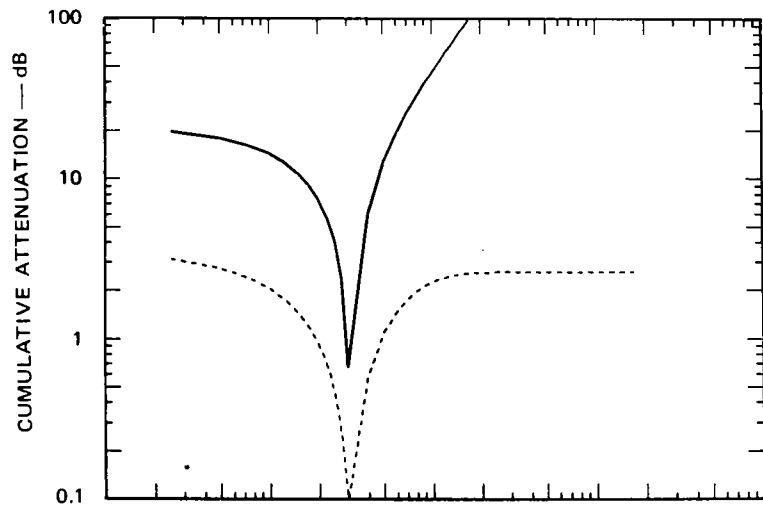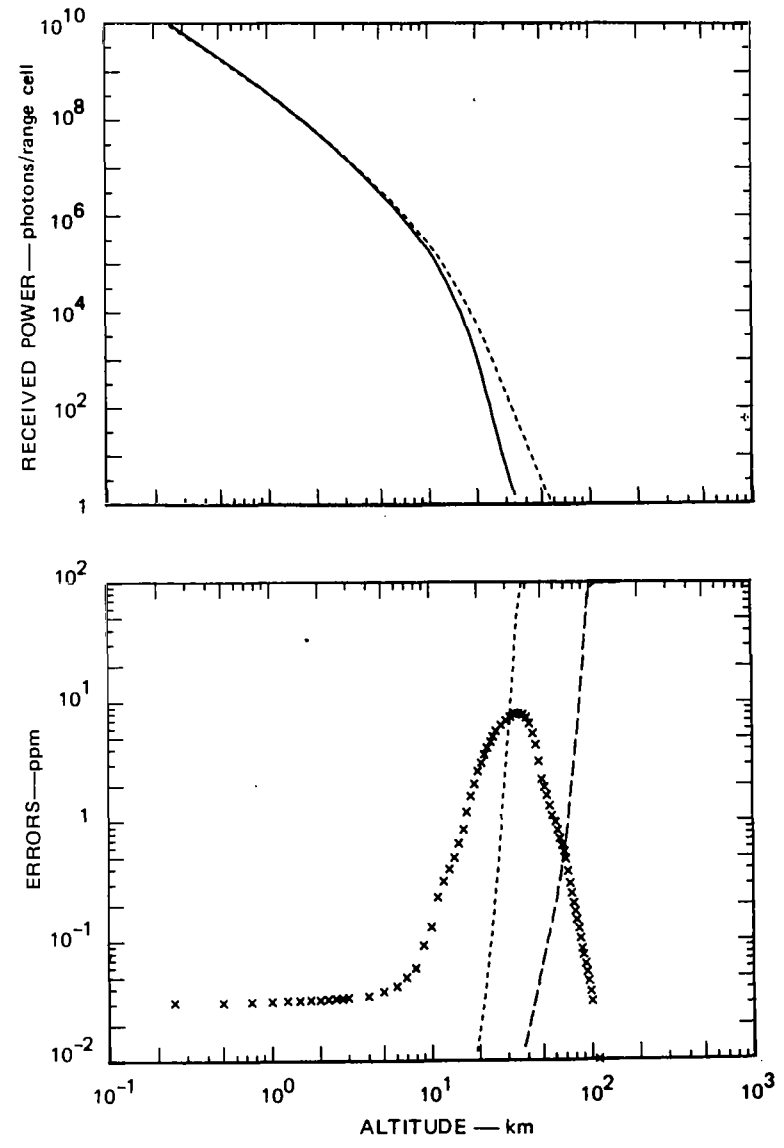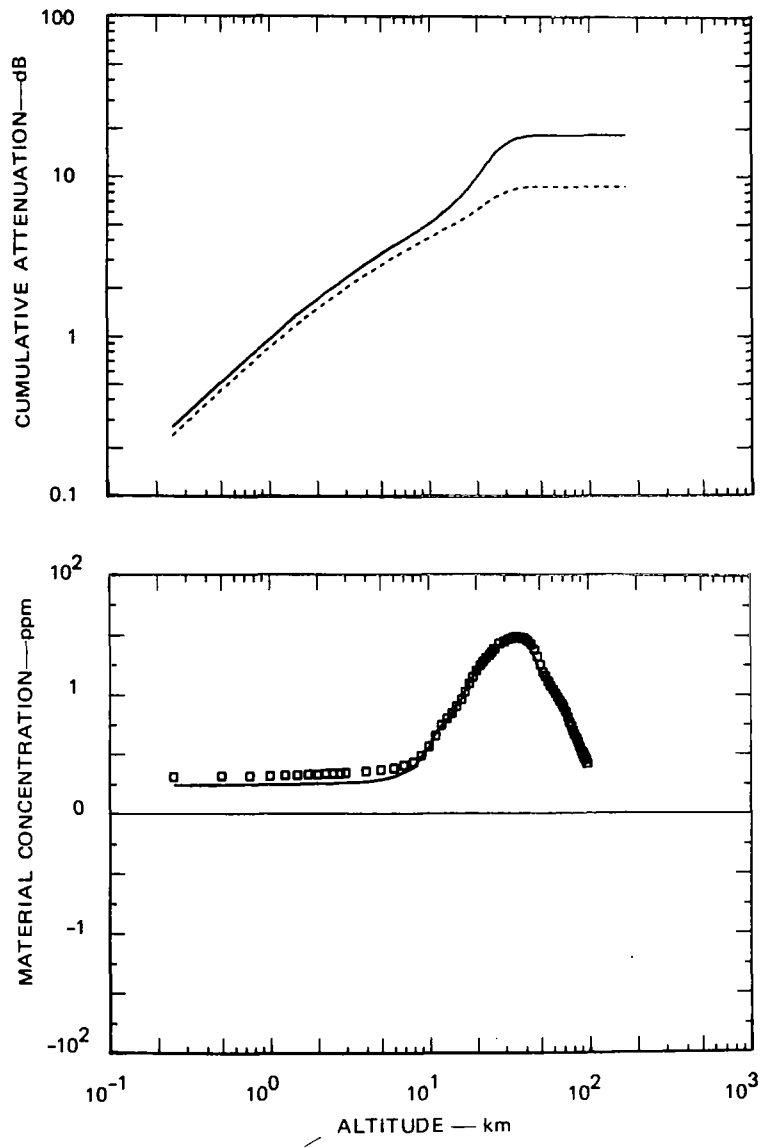FIGURE VII-44    DETAILED PERFORMANCE SUMMARY FOR $O_3$ AT 300 nm FOR H = 0 km

The sharply decreasing signal levels in the stratosphere caused by both the rapid decrease in scattering with altitude and the increasing $1/R^2$ effect makes the upper-altitude capability of the system moderately insensitive to relatively large changes in energy level of the laser for both the IR and UV systems, even with multipulse integration. For example, the altitude at which the noise error equals the model concentration is 30 km for 1000 pulse pairs and decreases to only 25 km with a single pulse pair. Thus, an improvement by a factor of 30 in system performance produces an altitude differential of only 5 km out of 30 km. This insensitivity to large changes in system parameters probably makes monitoring of the upper side of the $O_3$ layer quite difficult with any realizable system, even well into the future.

## H. Summary of Assumed System Parameters and Results of Detailed Calculations

The system characteristics assumed for the detailed performance analyses are summarized in Tables VII-8 and VII-9 for the satellite cases and for the aircraft and ground-based systems, respectively. These tables are presented as foldouts so that the system characteristics can be conveniently determined for each performance-analysis case.

A summary of the results of the analyses is shown in Table VII-10. This table indicates the estimated feasibility for both satellite and aircraft monitoring of all species studied in this project. The results are presented in terms of the time periods in which the measurements could be realized. The time periods are: present (0-1 year), near future (1-2 years), future (3-5 years), and extended (>5 years). Within each time period the results are tabulated in the order in which they appear in the report. Further ranking within time periods is not very meaningful because of the large number of system variables that could occur for a specific application. The third column in Table VII-10 indicates the

Table VII-8

SUMMARY OF SYSTEM CHARACTERISTICS FOR DETAILED PERFORMANCE ANALYSES OF SATELLITE CASES

| Type of Measurement | Material | Laser Wavelengths | Transmitted Energy (J) | Receiver Aperture (m²) | Field of View (mrad) | Optical Bandwidth | Range Resolution (m) | Detector NEP or D* | Background Light Level (W m⁻² sr⁻¹ μ⁻¹) | Eye-Safe Energy Limit (J) | Number of Pulses Integrated | See Page Numbers |
|---|---|---|---|---|---|---|---|---|---|---|---|---|
| Range-resolved, satellite at 166 km | $O_3$(UV) | 301.6 nm 310.9 nm | 10 | 1.0 | 0.1 | $7.5 \times 10^{-3}$ | 1000 | $4 \times 10^{-17}$ | $10^{-4}$ | $3 \times 10^8$ | 1000 | |
| | $O_3$(IR) | 1057.677 cm⁻¹ 1057.950 cm⁻¹ | 100 | 1.0 | 0.01 | $7.5 \times 10^{-4}$ | 1000 | Heterodyne | $1.6 \times 10^{-4}$ | $8 \times 10^4$ | 100 | |
| | $SO_2$ | 306.53 nm 305.56 nm | 100 | 1.0 | 0.1 | $7.5 \times 10^{-3}$ | 1000 | $4 \times 10^{-17}$ | $10^{-4}$ | $3 \times 10^8$ | 1000 | |
| | $NO_2$ | 450 nm 448.1 nm | 10 | 1 | 0.1 | $7.5 \times 10^{-3}$ | 1000 | $4 \times 10^{-17}$ | $2 \times 10^{-3}$ | $10^2$ | 100 | |
| | CO | 2147.084 cm⁻¹ 2146.500 cm⁻¹ | 100 | 1 | 0.01 | $7.5 \times 10^{-4}$ | 1000 | Heterodyne | $10^{-5}$ | $1 \times 10^7$ | 100 | |
| | $N_2O$ | 2219.808 cm⁻¹ 2221.06 cm⁻¹ | 1 | 0.1 | 0.01 | $7.5 \times 10^{-4}$ | 1000 | Heterodyne | $10^{-5}$ | $1 \times 10^7$ | 100 | |
| Column-content, satellite at 166 km | $O_3$(UV) | 303.6 nm 310.9 nm | 1.0 | 1.0 | 9.0 | $7.5 \times 10^{-3}$ | -- | $4 \times 10^{-17}$ | $10^{-4}$ | $3 \times 10^8$ | 100 | |
| | $O_3$(IR) | 1057.677 cm⁻¹ 1057.95 cm⁻¹ | 10 | 1.0 | 1.0 | $7.5 \times 10^{-3}$ | -- | $10^{11}$ | $1.6 \times 10^{-4}$ | $8 \times 10^4$ | 10 | |
| | $SO_2$ | 306.53 nm 305.56 nm | 0.2 | 1.0 | 1.0 | $7.5 \times 10^{-3}$ | -- | $4 \times 10^{-17}$ | $10^{-4}$ | $3 \times 10^8$ | 100 | |
| | $NO_2$ | 450 nm 448.1 nm | 1 | 1 | 0.1 | $7.5 \times 10^{-3}$ | -- | $4 \times 10^{-17}$ | $10^{-4}$ | $10^2$ | 100 | |
| | CO | 2147.084 cm⁻¹ 2146.500 cm⁻¹ | 0.5 | 0.1 | 0.01 | $7.5 \times 10^{-4}$ | -- | Heterodyne | $10^{-5}$ | $1 \times 10^7$ | 100 | |
| | $N_2O$ | 2219.808 cm⁻¹ 2221.06 cm⁻¹ | 0.1 | 1 | 0.1 | $7.5 \times 10^{-3}$ | -- | $10^{12}$ | $10^{-5}$ | $1 \times 10^7$ | 100 | |
| Cloud, satellite at 166 km | Thin cirrus | 699.3 nm | 4 | 1 | 0.1 | $7.5 \times 10^{-4}$ | 1000 | $4.1 \times 10^{-17}$ | $10^{-1}$ | $10^2$ | -- | |
| | cirrus | 694.3 nm | 4 | 1 | 0.1 | $7.5 \times 10^{-4}$ | 1000 | $4.1 \times 10^{-17}$ | $10^{-1}$ | $10^2$ | -- | |
| | Thick cirrus | 694.3 nm | 4 | 1 | 0.1 | $7.5 \times 10^{-4}$ | 1000 | $4.1 \times 10^{-17}$ | $10^{-1}$ | $10^2$ | -- | |
| | Stratus | 694.3 nm | 4 | 1 | 0.1 | $7.5 \times 10^{-4}$ | 1000 | $4.1 \times 10^{-17}$ | $10^{-1}$ | $10^2$ | -- | |
| | Cumulus | 694.3 nm | 4 | 1 | 0.1 | $7.5 \times 10^{-4}$ | 1000 | $4.1 \times 10^{-17}$ | $10^{-1}$ | $10^2$ | | |
| Aerosol, satellite at 166 km | | 694.3 nm | 4 | 1 | 1.0 | $7.5 \times 10^{-3}$ | 1000 | $4 \times 10^{-17}$ | 0.1 | $10^2$ | -- | |
| | | 1.06 μm | 10 | 1 | 0.1 | $7.5 \times 10^{-4}$ | 1000 | $1.9 \times 10^{13}$ | 0.1 | $8 \times 10^2$ | -- | |

TABLE VII-9

SUMMARY OF SYSTEM CHARACTERISTICS FOR DETAILED PERFORMANCE ANALYSES OF AIRCRAFT AND GROUND CASES

| Type of Measurement | Material | Laser Wavelengths | Transmitted Energy (J) | Receiver Aperture ($m^2$) | Field of View (mrad) | Optical Bandwidth | Range Resolution (m) | Detector NEP or $D^*$ | Background Light Level ($W\ m^{-2}\ sr^{-1}\ \mu^{-1}$) | Eye-Safe Energy Limit (J) | Number of Pulses Integrated | See Page Numbers |
|---|---|---|---|---|---|---|---|---|---|---|---|---|
| Range-resolved, aircraft at 12 km | $O_3$(UV) | 298.2 nm<br>310.9 nm | 0.5 | 0.1 | 0.1 | $7.5 \times 10^{-3}$ | 1000 | $4 \times 10^{-17}$ | $10^{-4}$ | $10^6$ | 400 | |
| | $O_3$(IR) | 1057.730 $cm^{-1}$<br>1057.950 $cm^{-1}$ | 1.0 | 0.1 | 0.01 | $7.5 \times 10^{-4}$ | 1000 | Heterodyne | $1.6 \times 10^{-4}$ | $4 \times 10^3$ | 100 | |
| | $SO_2$ | 306.53 nm<br>305.56 nm | 1.0 | 0.1 | 0.1 | $7.5 \times 10^{-3}$ | 1000 | $4 \times 10^{-17}$ | $10^{-4}$ | $10^6$ | 100 | |
| | $NO_2$ | 450 nm<br>448.1 nm | 1.0 | 1.0 | 0.1 | $7.5 \times 10^{-3}$ | 1000 | $4 \times 10^{-17}$ | $2 \times 10^{-3}$ | 0.8 | 100 | |
| | CO | 2147.084 $cm^{-1}$<br>2146.500 $cm^{-1}$ | 1.0 | 0.1 | 0.1 | $7.5 \times 10^{-3}$ | 1000 | $10^{12}$ | $10^{-5}$ | $2 \times 10^4$ | 100 | |
| | $N_2O$ | 2222.751 $cm^{-1}$<br>2222.46 $cm^{-1}$ | 1.0 | 0.1 | 0.1 | $7.5 \times 10^{-3}$ | 1000 | $10^{12}$ | $10^{-5}$ | $2 \times 10^4$ | 100 | |
| Range-resolved, aircraft at 3 km | $O_3$(UV) | 258.7 nm<br>259.7 nm | 0.2 | 0.1 | 0.1 | $7.5 \times 10^{-2}$ | 100 | $4 \times 10^{-17}$ | $10^{-4}$ | $2 \times 10^4$ | 100 | |
| | $O_3$(IR) | 1057.730 $cm^{-1}$<br>1057.950 $cm^{-1}$ | 10 | 0.1 | 0.1 | $7.5 \times 10^{-3}$ | 100 | $2 \times 10^{11}$ | $1.6 \times 10^{-4}$ | 200 | 100 | |
| | $SO_2$ | 306.53 nm<br>305.56 nm | 0.2 | 0.1 | 0.1 | $7.5 \times 10^{-2}$ | 100 | $4 \times 10^{-17}$ | $10^{-4}$ | $2 \times 10^4$ | 100 | |
| | $NO_2$ | 450 nm<br>448.1 nm | 0.1 | 0.1 | 2 | $7.5 \times 10^{-3}$ | 100 | $4 \times 10^{-17}$ | $2 \times 10^{-3}$ | 0.16 | 1000 | |
| | $N_2O$ | 2229.429 $cm^{-1}$<br>2229.100 $cm^{-1}$ | 1.0 | 0.1 | 0.1 | $7.5 \times 10^{-3}$ | 100 | $10^{11}$ | $10^{-5}$ | $4 \times 10^3$ | 100 | |
| | CO | 2147.084 $cm^{-1}$<br>2146.500 $cm^{-1}$ | 0.5 | 0.1 | 0.1 | $7.5 \times 10^{-3}$ | 100 | $10^{12}$ | $10^{-5}$ | $4 \times 10^3$ | 100 | |
| Range-resolved ground-based at 0 km | $O_3$(IR) | 1057.677 $cm^{-1}$<br>1057.950 $cm^{-1}$ | 100 | 1.0 | 0.01 | $10^{-5}$ | 1000 | Heterodyne | $1.6 \times 10^{-4}$ | -- | 1000 | |
| | $O_3$(UV) | 301.6 nm<br>310.9 nm | 1.0 | 1.0 | 0.1 | $7.5 \times 10^{-3}$ | 1000 | $4 \times 10^{-17}$ | $10^{-4}$ | -- | 1000 | |

## Table VII-10

### SUMMARY OF DETAILED PERFORMANCE-ANALYSIS RESULTS

| Time Frame | Platform Altitude (km) | Material | MDMC (ppm), Altitude Range (km), or Percent Error* | Assumed Laser Energy (J) |
|---|---|---|---|---|
| Present (0-1 year) | 166 | $NO_2$ (CC)† | 0.0003 ppm | 1 |
| | 166 | $NO_2$ | 0.004 ppm | 1-2 |
| | 166 | $N_2O$ (CC) | 0.04 ppm | 0.1 |
| | 12 | $O_3$ (IR) | 0-12 km | 1 |
| | 12 | $O_3$ (UV) | 0-12 km (30 ppb) | 0.1 |
| | 12 | $NO_2$ | 0.0006 ppm | 1 |
| | 3 | $NO_2$ | 0.0025 ppm | 0.1 |
| | 3 | CO | 0.1 ppm | 0.1 |
| | 3 | $N_2O$ | < 0.1 ppm | 0.1 |
| Near-future (1-2 years) | 166 | $NO_2$ | 0.001 ppm | 10 |
| | 166 | $N_2O$ (CC) | 0.007 ppm | 0.5 |
| | 166 | CO (CC) | 0.012 ppm | 0.5 |
| | 166 | $O_3$ (IR) | 0-2 km | 10 |
| | 166 | $SO_2$ (CC) | 0.01 ppm‡ | 0.2 |
| | 166 | $O_3$ (IR) (CC) | < 1% error | 10 |
| | 12 | $N_2O$ | 0.04 ppm | 0.5 |
| | 12 | CO | 0.014 ppm | 0.5 |
| | 3 | $O_3$ (IR) | 0-4 km | 10 |
| | 3 | $O_3$ (UV) | 0-6 km | 0.2 |
| | 3 | $SO_2$ | 0.004 ppm | 0.2 |
| | 3 | $N_2$ | 0.1 ppm | 0.5 |
| | 3 | CO | 0.018 ppm | 0.5 |
| Future (3-5 years) | 166 | $N_2O$ | 0.1 ppm | 1 |
| | 166 | CO | 0.1 ppm | 1 |
| | 166 | $O_3$ (UV) | 15-30 km | 1 |
| | 166 | $O_3$ (UV) (CC) | 1.5% | 1 |
| | 166 | $O_3$ (IR) | 0.009 ppm | 100 |
| | 12 | $O_3$ (UV) | 0-25 km | 0.5 |
| | 12 | $SO_2$ | 0.0003 ppm | 1 |
| | 12 | $N_2O$ | 0.0015 ppm | 1 |
| Extended (> 5 years) | 166 | $SO_2$ | 0.0009 | 100 |
| | 166 | CO | 0.008 ppm | 100 |
| | 166 | $O_3$ (UV) | 0.008 ppm | 10 |

*Either ground-level error in material concentration, altitude range for satisfactory performance, or percent error in column-content measurement.

†(CC) indicates a column-content measurement. All others are range-resolved.

‡An MDMC of 0.0004 ppm is obtainable with interference compensation and integration of 1000 pulses.

material that is monitored (including the wavelength range for $O_3$, in which both IR and UV calculations were made) and also whether the measurement was a range-resolved or a column-content measurement. The fourth column indicates the performance level that is achievable under the assumed conditions. Three different performance criteria are given in this column. Where the material is represented by a relatively uniformly mixed distribution with altitude, the ground-level error (in ppm), which can be interpreted as minimum detectable material concentration in ppm, is indicated as the performance parameter. For these materials the ground-level error is often the maximum error for altitudes below the platform. For $O_3$, which is assumed to be a nonuniformly mixed material, the altitude range for satisfactory measurement is given rather than a concentration because of the difficulty in interpreting the concentration number where the material varies widely in concentration as a function of altitude. For column-content measurements of $O_3$, a percentage error for the integrated column-content measurement is given. The last column gives the laser energy that was assumed for each case. This column does not necessarily indicate the minimum laser energy that would be required to achieve a particular measurement capability. Reductions in performance requirements, or increases in minimum detectable material concentrations, could significantly affect the required laser energy for realizing a particular measurement capability.

The global background concentrations of $SO_2$, NO, $NO_2$, and $NH_3$ are not accurately known. An estimated range of background concentrations is given for each of these materials in Table II-1. Most computer simulations were made using model concentration values at or near the maximum estimated background values. Many simulations produced errors or minimum detectable material concentration (MDMC) values that are substantially below the assumed model values.

268

If the desired error or MDMC value is less than those assumed for the computer model, the discussion of each case should be consulted to determine the actual values obtainable for each specific computer simulation. These calculated values can then be compared to the desired value to determine the feasibility under the conditions of the simulation.

# VIII  CONCLUSIONS

From the results of the four study tasks on this project, the following conclusions have been drawn.

(1)  At ranges in excess of a few hundred meters, the differential-absorption lidar (DIAL) technique provides better sensitivity for quantitative measurement of a wider range of gases than fluorescence, Raman scattering, or resonant Raman scattering.

(2)  The feasibility of realizing each monitoring system is largely dependent on the availability of certain laser energies at the desired wavelengths.  A detailed examination of the expected energies for present (0 to 1 year), near-future (1 to 2 years), and future (3 to 5 years) capabilities of tunable lasers leads to the following predictions for feasibility:

(a)  <u>From 166 km</u>

- Column-content measurements of $O_3$, $SO_2$, $NO_2$, CO, and $N_2O$ will be feasible within two years.  Adequate performance levels for column-content measurements of $NO_2$ and $N_2O$ can be made within the present time period.  An exceptionally good column-content measurement of $O_3$ can be made in the IR in the near future (1-2 years) with less than 1% error.  To achieve a measurement accuracy of a fraction of 1% would require a signal-processing accuracy of the order of 0.1%, compensation for spectral interference, and improved receiver sensitivity.

● Range-resolved measurements of $O_3$, $NO_2$, $N_2O$, and
possibly CO will be technologically feasible within five
years. Range-resolved measurements of $NO_2$ at the maximum
estimated background concentration of 4 ppb are possible
at present, and at lower concentration levels, in 1 to 2
years. Range-resolved measurements of $O_3$ using IR wave-
lengths will be feasible in the near future (1 to 2 years).
Measurements at both high- and low-altitude regions of $O_3$
at IR wavelengths will be feasible in the 3-to-5-year time
period. $O_3$ can also be monitored from 15 to 30 km by using
UV wavelengths; this capability can be achieved in 3 to 5
years. UV wavelengths, however, will not be useful for
vertical-profile measurements from ground level for more
than 5 years because of the increased laser energy require-
ments for monitoring at all altitudes of interest.

● Cloud-top heights can be measured for cirrus clouds,
stratus clouds, and cumulus clouds with present technology.
Cloud thickness can be measured for cirrus clouds, and
optical depth can be determined for thin cirrus and medium
cirrus, but not thick cirrus clouds with presently available
technology.

● Measurement of stratospheric aerosols (scattering
ratio) is now feasible using multiple-pulse integration.
Future technology may permit single-pulse measurements
of stratospheric-aerosol scattering ratios.

(b) From 12 km

● Range-resolved measurements of $O_3$, $SO_2$, $NO_2$, CO, and
$N_2O$ should be feasible within five years. Range-resolved
measurements of $O_3$ and $NO_2$ are possible within the

limitations of presently available equipment. IR monitoring of $N_2O$ and CO will be possible in 1 to 2 years.

(c) <u>From 3 km</u>

- Range-resolved measurements of $O_3$, $SO_2$, $NO_2$, CO, and $N_2O$ should be feasible within two years. Range-resolved measurements of $NO_2$, $N_2O$, CO, and possibly $O_3$, are feasible within the limitations of present technology. $SO_2$ measurements will be possible in 1 to 2 years. Significant increases in $O_3$ performance levels can be expected in 1 to 2 years.

(3) It is now technically feasible to meet the well recognized need for global monitoring of the distribution and variability of the stratospheric aerosol with a satellite-borne lidar operating at a fixed wavelength.

(4) The pulse-repetition rates required for a data-grid spacing of 0.1 km from aircraft operating at either 3 km or 12 km are compatible with achievable laser capabilities. Hence, aircraft are suitable vehicles for monitoring pollutants on local and regional scales.

(5) Local and regional monitoring of pollutants from a satellite would be desirable if they could be shown to be cost-effective. However, the extremely high pulse-repetition rates that would be required to obtain a data grid of useful size makes this application technically unpromising at present and for the predictable future.

(6) Among the gases ordinarily considered as pollutants, only $CO_2$, $CO$, $O_3$, and $N_2O$ have reasonably long atmospheric residence times and would be expected to have relatively smooth variations in world-wide distribution. Other gases have shorter atmospheric residence times and probably have very large variations in concentration between urban and rural areas. This large variability in concentration of shorter-lived atmospheric pollutants complicates measurements at both the high and low concentration extremes.

The study reported here required investigation of an extensive and varied range of technical topics. Because a complete analysis was not possible, this report should be considered as a preliminary document that indicates the general feasibility of measuring five of the most important pollutant gases from both satellite and aircraft altitudes.

Detailed calculations were limited to five gases ($O_3$, $SO_2$, $NO_2$, $CO$, and $N_2O$), plus clouds and aerosols. Conclusions concerning other gases must await the outcome of further analyses. In addition, many of the performance analyses for airborne measurements were carried out, for reasons of economy, at the same wavelengths selected for satellite-borne systems. These wavelengths are probably not optimum for the aircraft altitudes. Techniques utilizing CW or nontunable lasers have not been considered, although these techniques may also have applicability for gaseous monitoring.

# IX RECOMMENDATIONS FOR FURTHER STUDIES

Because of funding limitations, it was not possible to investigate
all the important ramifications of the study in adequate depth. Therefore,
the following additional research is recommended:

(1) Investigate new laser types for monitoring specific materials.
These should include the use of HBr high-pressure lasers and
$CO_2$-isotope high-pressure lasers with non-linear doublers and
mixers to achieve useful power levels in the 4.5-$\mu$ region. The
use of these lasers would enable monitoring of $N_2O$, CO, and
perhaps $O_3$. High-pressure $CO_2$ lasers, with the use of isotopes,
should also be investigated for monitoring $O_3$ in the IR at about
9.5 $\mu$. This type of laser, in conjunction with a higher-
sensitivity receiver, offers promise for range-resolved measure-
ments of $O_3$ from satellite altitudes.

(2) Investigate the potential for monitoring water vapor and $CO_2$
in addition to the materials investigated on this project.
These gases together with $O_3$ have significant impacts on the
heat-balance problem, as do high-altitude and tropospheric
aerosols. Range-resolved measurements may be of value in
determining the radiation balance. A higher accuracy level
than that assumed for the pollutant materials may be required
for these materials. For this reason, the attainment of high-
accuracy measurements should also be investigated and appropriate
system and signal-processing techniques to obtain these high
accuracies should be identified.

(3)  Investigate the performance improvement that is possible by
     compensating for measurable spectral interference.  In the
     present study, absorption-line pairs were optimized to provide
     minimum interfering-material errors as well as other errors.
     If spectral interference were compensated, a wider range of
     usable line pairs would become available and could in some
     cases provide a substantial improvement in performance level.
     The interfering-material error cannot be completely eliminated
     by this technique because of the limited accuracy in measuring
     the interfering component.  The effects of these multiple
     errors should be studied and new error limits, assuming com-
     pensation, should be determined.  This should be followed by
     a reexamination of the optimum line pairs and best system per-
     formance available, and should result in improved system
     performance.  At the same time the improvements due to better
     detectors can be incorporated in the optimization process.

(4)  Investigate modulated CW systems with range resolution as an
     alternative to the pulse techniques investigated in this project.
     This alternative has particular importance in monitoring $NO_2$ in
     the visible where, even with improved receiver sensitivity, the
     energy levels required for pulsed operation can exceed the
     eye-safety limit.

(5)  Explore the lidar performance improvement that could be achieved
     by using advanced lidar techniques in the IR.  These should
     include, as a minimum, more accurate modeling of heterodyne
     lidar systems and optical parametric upconverters.  These
     systems might be able to reduce the detector noise levels to
     the point where photon fluctuations in the received signal limit
     the performance of the system.  These improved detectors,

particularly in combination with other system improvements, show promise for providing satellite-altitude-measurement capability for several materials in the near-future time frame.

(6)   Investigate the use of optimized line pairs for aircraft altitudes. The line pairs used in this study and the associated performance levels have been determined primarily from optimizing the line pairs for operation at satellite altitudes. In most cases, this will not provide the best performance available from aircraft altitudes. This optimization procedure together with the improved detector performance levels should be re-examined for the 12- and 3-km altitudes.

(7)   Investigate $NO_2$ and $SO_2$ in the IR for potential improvements in monitoring performance. In the original investigations, only $O_3$ was investigated at both UV and IR wavelengths. The difficulties encountered in monitoring $NO_2$ in the visible and $SO_2$ in the UV suggest that both these materials should be investigated at longer wavelengths.

(8)   Investigate the use of atmospheric models, including distribution of interfering materials as a function of altitude, to improve the accuracy of the interfering-material compensation for range-resolved measurement. This would allow the use of a variable compensation factor as a function of altitude and might improve the accuracy of the interfering-material compensation in range-resolved measurements by a substantial amount. Compensation for both molecular and particulate scattering differences as a function of the wavelengths used for the measurement would be particularly affected, since this compensation is known to vary considerably as a function of altitude because of the large variation in scattering ratio with altitude. For

materials like $NO_2$ where the scattering compensation is the
primary interference, the use of a single compensation factor
is inadequate to substantially improve the interfering-material
error and, for these cases, an atmospheric model is almost
essential for effectively reducing this interference to a
low value.

(9)   Investigate further the use of multipulse integration involving
measurements made over a large geographical area. In conjunction
with improved receiver sensitivities, this technique appears to
offer a capability for range-resolved satellite measurements
for several materials. These estimates of capability need to
be further investigated because the detailed noise mechanisms
operative during multipulse integration are somewhat different
from the assumptions made in the investigation reported here.

(10)  Study the feasibility and importance of monitoring other gases
than those considered in detail in this report. The fluoro-
carbons (freons) and HCl should be prime candidates. The
chemical intermediates resulting from the interaction of
chlorine and ozone should also be considered.

(11)  Assess the effects of clouds, especially their statistical
distributions, on the ability to measure concentrations of
gases in the troposphere from aircraft and spacecraft. In
addition, assess the usefulness of clouds as reflectors for
making stratospheric column-content measurements from space-
craft.

Appendix

FLUORESCENCE, AND RAMAN AND RESONANT RAMAN SCATTERING[*]

279

## Appendix

## FLUORESCENCE, AND RAMAN AND RESONANT RAMAN SCATTERING

### 1.   Introduction

Raman scattering has recently been demonstrated to be a useful method to detect air pollutants remotely (up to a range of about 1 km) (Hirschfeld et al., 1973).  The possibility of increasing the scattering cross section by up to three orders of magnitude for molecular Raman scattering by using tunable lasers has attracted considerable attention recently.  This appendix discusses the process, reviews progress to date, and evaluates the prospects for using the phenomenon for practical purposes.

### 2.   Inelastic Light-Scattering Processes

Five inelastic light-scattering processes are shown in Figure A-1. In each case, some vibrational levels of the ground electronic state and of an excited electronic state are shown.  The initial, final, and intermediate molecular states are labeled i, f, and m, respectively. $\omega_L$ and $\omega_S$ are the energies of the incident and scattered photons.

Case (a) is ordinary Raman scattering (ORS), where the laser photon energy falls far below the excited band.  Many intermediate states are excited, but only weakly because of the large energy mismatch between the excited-state energies of the molecule and the photon energy of the laser.

Case (b) represents resonance Raman scattering (RRS), where the laser photon energy falls near the electronic absorption band.  Many
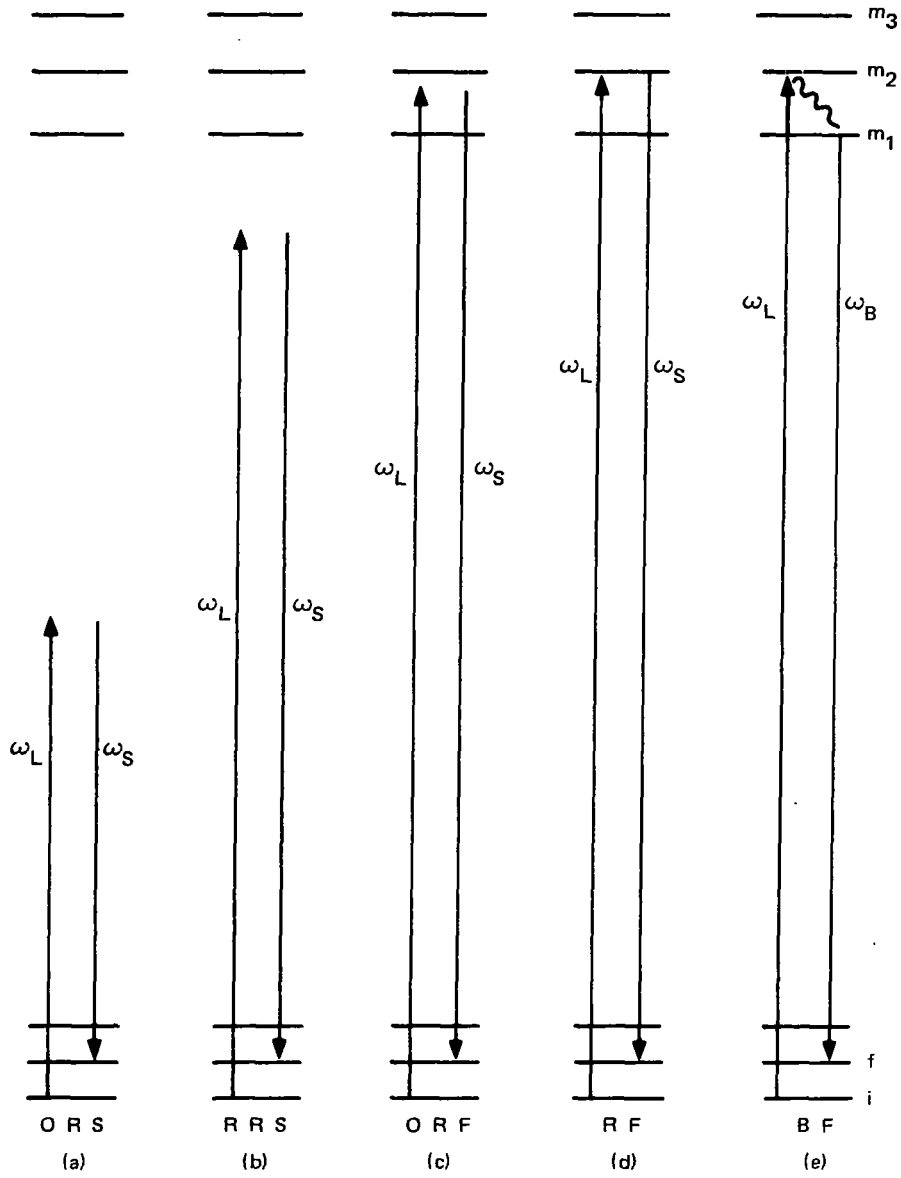
FIGURE A-1   ENERGY-LEVEL DIAGRAMS FOR INELASTIC LIGHT-SCATTERING
PROCESSES

intermediate states are again excited, but more strongly than in case (a) because of the smaller energy mismatch.

In process (c), the laser line falls within the absorption band, but outside the linewidths of all molecular levels. The contribution from the few intermediate states that are nearest to the laser photon energy dominates in the scattered intensity. This process will be called "off-resonance fluorescence" (ORF). It is often referred to as "resonance Raman scattering," however, and will be discussed in this appendix.

Case (d) is resonance fluorescence (RF), where the laser photon energy falls within the width of a molecular level. This single intermediate state will·dominate the scattered intensity.

In case (e), the laser photon energy again falls within the absorption band, but the excited molecule undergoes one or more inelastic collisions before it can reradiate. Because of the possible transfer of energy to translation and rotation, $\omega_S$ can take on a nearly continuous range of values, so that this process gives rise to a broad continuum in the scattered spectrum. Therefore, it will be called "broad fluorescence" (BF). In contrast, $\omega_S$ in processes (a), (b), (c), and (d) takes on discrete values, so that these processes yield "spikes" in the scattered spectrum.

3. Basic Equation

In processes (a) through (d) the molecule started out in a state i and ended up in a state f, and the electromagnetic field lost a photon $\omega_L$ and gained a photon $\omega_S$. These processes all may be described by a Kramers-Heisenberg-type dispersion equation:

$$\sigma = \frac{e^4 \omega_S^4}{c^4 h^2} \left| \sum_m \left( \frac{\hat{e}_S \cdot \langle f | \vec{r} | m \rangle \langle m | \vec{r} | i \rangle \cdot \hat{e}_L}{\omega_{im} - \omega_L + \frac{i}{2}\Gamma m} + \frac{\hat{e}_L \cdot \langle f | \vec{r} | m \rangle \langle m | \vec{r} | i \rangle \cdot \hat{e}_S}{\omega_{im} + \omega_L + \frac{i}{2}\Gamma m} \right) \right|^2 .$$

(A-1)

283

A derivation of this equation by perturbation theory may be found in Barnett and Albrecht (1970).

$\sigma$ is the cross section of the entire process and has units of area. It is equal to the number of photons with polarization vector $\hat{e}_S$ scattered per second divided by the number of photons with polarization vector $\hat{e}_L$ incident per second and per unit area.

$c$, $e$, $h$, $\omega_L$, and $\omega_S$ are the speed of light, the electronic charge, Planck's constant divided by $2\pi$, and the circular frequencies of the incident laser light and of the scattered light, respectively.

The sum is over all states $|m\rangle$ of the molecule except for the initial ( $|i\rangle$) and final ( $|f\rangle$) states (Tang and Albrecht, 1970), $\vec{r}$ is the sum of all electron position vectors, $h\omega_{im}$ is the energy difference between states $|i\rangle$ and $|m\rangle$, and $\Gamma_m$ is the width of the molecular state $|m\rangle$.

Equation (A-1) represents a two-photon process in the electric-dipole approximation. $\langle m|\vec{r}|i\rangle$ is the matrix element for a dipole transition from the initial state to the intermediate state, and $\langle f|\vec{r}|m\rangle$ is the matrix element for a dipole transition from the intermediate to the final state. The first term within parentheses represents the absorption of a photon $\omega_L$ followed by the emission of a photon $\omega_S$. The second term represents the emission of a photon $\omega_S$ followed by the absorption of a photon $\omega_L$. Both processes are possible, but the second is less probable than the first because of energy considerations. The denominators make this explicit: $(\omega_{im} + \omega_L)$ is bigger than $(\omega_{im} - \omega_L)$.

An important point to note about **Eq. (A-1) is that all inter**mediate states can contribute to the scattering. But the energy denominators show that the farther from the laser photon energy a state is, the less it can contribute. The difference $\Delta\omega = (\omega_{im} - \omega_L)$ is called the "energy mismatch."

The vectors and molecular states in **Eq. (A-1) are referred to** a laboratory-fixed set of axes. When one scatters light from a gas of freely orientable molecules, it is convenient to have the matrix elements referred to molecular-fixed axes. The transformation involves 3-j symbols, 6-j symbols, and generalized spherical D functions. For details, one can refer to Mortenson (1970). For our purposes, we will be concerned mainly with properties internal to the molecule and will write

$$\sigma \propto \left| \sum_m \left( \frac{\langle f \mid r \mid m \rangle \langle m \mid r \mid i \rangle}{\omega_{im} - \omega_L + \frac{i}{2}\Gamma_m} + \frac{\langle f \mid r \mid m \rangle \langle m \mid r \mid i \rangle}{\omega_{im} + \omega_L + \frac{i}{2}\Gamma_m} \right) \right|^2 \qquad . \quad \text{(A-2)}$$

$r$ is now the magnitude of the sum of the electron position vectors referred to the molecular center of mass as origin. The molecular states will be functions of only the internal electron and nuclear coordinates.

In order to simplify the following qualitative discussions, two assumptions will be made.

First, the molecular eigenstates will be taken as direct products of electronic and vibrational eigenstates (Born-Oppenheimer approximation):

$$\mid k \rangle = \mid k_{el} \rangle \mid k_v \rangle \qquad . \qquad \text{(A-3)}$$

In the matrix elements $\langle 1 \mid r \mid k \rangle$, the integral over electron coordinates will be done first. Define $r_{1k}^{el} \equiv \langle 1_{el} \mid r \mid k_{el} \rangle$. The remaining integral $\langle 1_v \mid r_{1k}^{el} \mid k_v \rangle$ must be done over the internuclear coordinate. $r_{1k}^{el}$ will usually depend only slightly on the internuclear coordinate over the ranges of molecular vibrations so that it may be treated as a constant. The result is $r_{1k}^{el} \langle 1_v \mid k_v \rangle$, and $\langle 1_v \mid k_v \rangle$ is known as a "Franck-Condon

overlap integral." To better understand the meaning of an overlap integral, refer to Figure A-2, which shows the potential curves of the ground and excited electronic state and some vibrational wave functions. R is the internuclear coordinate. $\langle 1_v \mid k_v \rangle$ is the integral over R of the product of the two vibrational wave functions. The magnitude of the overlap integral will be one factor governing the strength of a transition. For example, the states at $E = 0$ and $E = h\omega_1$ have a small overlap so that a transition between these two states has a low probability. On the other hand, the large overlap between the states at $E = 0$ and $E = h\omega_6$ makes a transition between these two states much more likely.

Second, the molecular linewidth $\Gamma_m$ will be assumed constant for all the rotational and vibrational states within a given electronic band. For simplicity, consider only the first excited electronic state so that the subscript m will refer to rotational and vibrational states only. $\Gamma_m$ is the sum of a width $\Gamma_{RAD,m}$, due to spontaneous radiative emission from the excited state, and a width due to perturbations caused by collisions with other molecules. $\Gamma_{RAD,m}$ is not quite independent of m; according to Sandorfy (1964, pp. 96 and 106).

$$\Gamma_{RAD,m} = \frac{4}{3hc^3} \sum_f \omega_S^3 \mid \langle f \mid r \mid m \rangle \mid^2 \qquad (A-4)$$

$$= \frac{4}{3hc^3} \sum_f (\omega_m - \omega_f)^3 \mid r_{fm}^{el} \mid^2 \mid \langle f_v \mid m_v \rangle \mid^2$$

where the sum is over all rotational-vibrational states of the ground electronic state. But to the extent that $\omega_s = (\omega_m - \omega_f)$ and $\mid r_{fm}^{el} \mid^2$ can be considered independent of both f and m, $\Gamma_{RAD,m}$ may be considered constant:
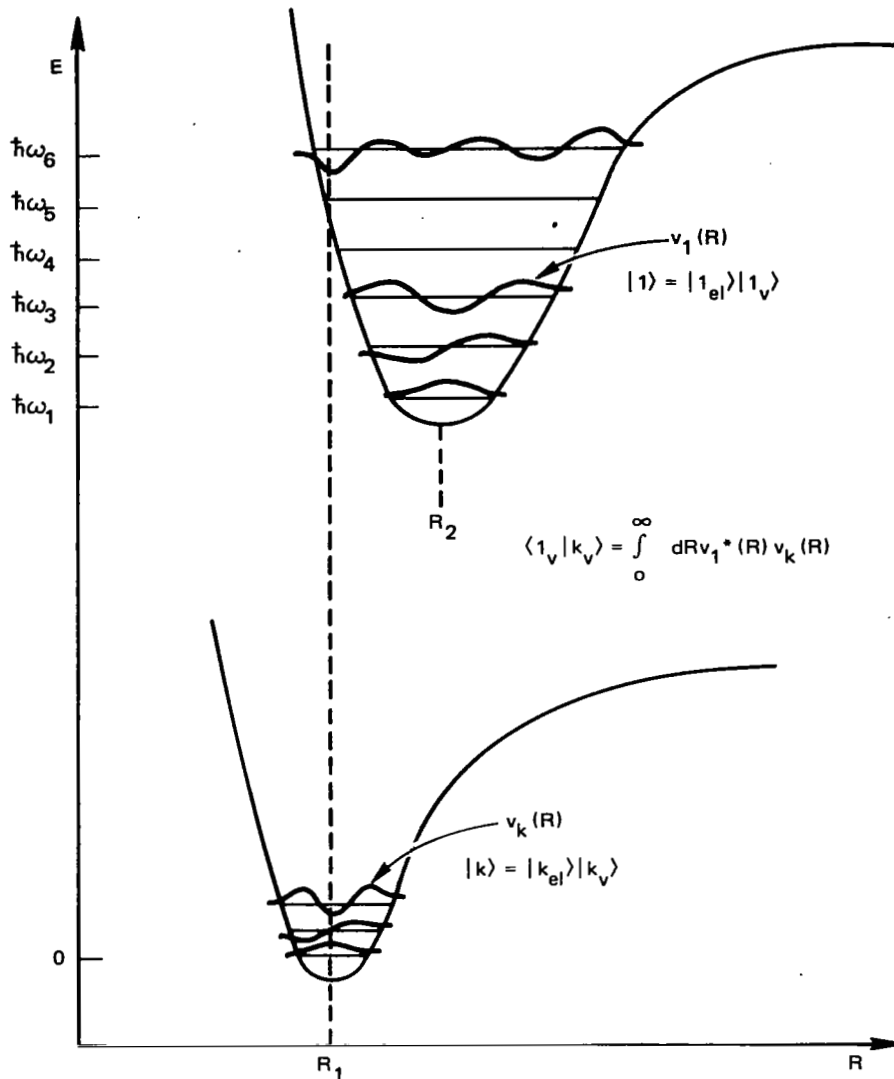
FIGURE A-2    POTENTIAL CURVES AND VIBRATIONAL WAVE FUNCTIONS

$$\Gamma_{\text{RAD},m} \approx \frac{4}{3hc^3} \overline{(\omega_m - \omega_f)^3} \, \overline{|r^{el}_{fm}|^2} \sum_f \langle m_v | f_v \rangle \langle f_v | m_v \rangle$$

$$= \frac{4}{3hc^3} \overline{(\omega_m - \omega_f)^3} \, \overline{|r^{el}_{fm}|^2} \equiv \Gamma_{\text{RAD}} \qquad . \qquad \text{(A-5)}$$

The width due to collisional perturbations will also not be the same

for all m, because some energy levels will be perturbed more than others

during collisions. Nonetheless, $\Gamma_m$ will be assumed constant, and the subscript will be dropped.

After using these two assumptions, we now have

$$\sigma \propto \left| \sum_m \left| r_{im}^{el} \right|^2 \left( \frac{\langle f_v \mid m_v \rangle \langle m_v \mid i_v \rangle}{\omega_{im} - \omega_L + \frac{i}{2}\Gamma} + \frac{\langle f_v \mid m_v \rangle \langle m_v \mid i_v \rangle}{\omega_{im} + \omega_L + \frac{i}{2}\Gamma} \right) \right|^2 . \tag{A-6}$$

### 4. Relative Sizes of Cross Sections

Now let us use Eq. (A-6) to discuss qualitatively the relative cross sections of the processes in Figure A-1.

In the ordinary Raman effect of process (a), the laser photon energy falls far below the excited states so that all of them contribute little to the scattering. Thus the cross section for ORS is small. Most air-pollutant molecules have their first electronic absorption band in the UV, so that ORS results when a visible laser line is used. The cross section for this process increases approximately as $\omega_L^4$, as can be seen from Eq. (A-1). Because $\omega_{im} \gg \omega_L$, changes in $\omega_L$ do not affect the energy denominators. However, $\omega_S^4 = (\omega_L - \omega_{if})^4$, and since molecular vibrational frequencies $\omega_{if}$ are on the order of 1000 cm$^{-1}$, whereas $\omega_L$ is on the order of 20,000 cm$^{-1}$, we have $\sigma \propto \omega_s^4 \approx \omega_L^4$.

As $\omega_L$ is increased closer to the absorption band, $(\omega_{im} - \omega_L)$ decreases rapidly for intermediate states near the bottom of the excited band, so that an increase in $\omega_L$ causes a much faster rise in the cross section than $\omega_L^4$. The "resonance" Raman effect of process (b) is dominant.

Once in the band, the cross section will undergo rapid fluctuations as the laser photon energy is continually increased (assuming $\Gamma$ is much less than the molecular line spacing). This fluctuation arises from

288

the changes in the various $(\omega_L - \omega_{im})$. For example, consider the case where the laser line is close to one absorption line only. The contribution from this intermediate state will so dominate in the sum that the other terms may be neglected. Approximately, then,

$$\sigma \propto \left| \; | r_{im}^{el} |^2 \; \frac{\langle f_v | m_v \rangle \langle m_v | i_v \rangle}{\omega_{im} - \omega_L + \frac{i}{2}\Gamma} \; \right|^2$$

$$\propto \frac{\Gamma_{RAD}^2 \, | \langle f_v | m_v \rangle |^2 \, | \langle m_v | i_v \rangle |^2}{(\omega_{im} - \omega_L)^2 + \frac{1}{4}\Gamma^2} \quad . \tag{A-7}$$

The cross section is a Lorentzian function of $\omega_L$ and will attain its peak value at $\omega_L = \omega_{im}$. This corresponds to the RF process of Figure A-1(d). When $\omega_L$ is tuned off of $\omega_{im}$, corresponding to ORF, the cross section decreases.

Because of the magnitude of the energy denominators alone, then, in general, $\sigma_{ORS} < \sigma_{RRS} < \sigma_{ORF} < \sigma_{RF}$. But the magnitude of the matrix elements must also be taken into account. For example, if $\langle m | r | i \rangle$ is very small, the cross section $\sigma_{RF}$ when $\omega_L = \omega_{im}$ may also be small. Furthermore, not only the magnitudes, but also the phases of the matrix elements and denominators must be accounted for--i.e., **there may be** values of $\omega_L$ where positive and negative contributions to the sum approximately cancel, yielding a small cross section.

To get a feeling for the size of the broad fluorescence cross section, assume that $\omega_L$ is close to resonance with a single molecular state m so that Eq. (A-7) may be used. Subscripting $\sigma$ with an F (fluorescence), we can group Eq. (A-7) into two parts:

$$\sigma_F \propto \frac{|\langle m_v \mid i_v \rangle|^2 \, \Gamma_{RAD} \, \Gamma}{(\omega_{im} - \omega_L)^2 + \frac{1}{4}\Gamma^2} \cdot \frac{\Gamma_{RAD} \, |\langle f_v \mid m_v \rangle|^2}{\Gamma} \qquad . \qquad \text{(A-8)}$$

The first factor of Eq. (A-8), apart from some constants, is the cross section for an absorption of a photon $\omega_L$ (Merzbacher, 1961, p. 458). The significance of the second factor becomes clear when it is noted that $\Gamma$ is the total transition rate out of the $m^{th}$ state. $\Gamma$ is equal to $\Gamma_{RAD} + \Gamma_C + \Gamma_Q$, $\Gamma_{RAD}$ is the transition rate for spontaneous radiative emission from the upper to the lower state, $\Gamma_C$ is the rate of collisions that transfers the molecule into a different vibrational level of the same excited electronic state, and $\Gamma_Q$ is the rate of collisions that transfers the molecule all the way down to the ground electronic state. Thus $\Gamma_{RAD}/\Gamma$ is the probability that the excited molecule will de-excite from level m via a radiative transition. Also,

$$\sum_{f_v} |\langle f_v \mid m_v \rangle|^2 = \sum_{f_v} \langle m_v \mid f_v \rangle \langle f_v \mid m_v \rangle = 1 \qquad \text{(A-9)}$$

since the final vibrational states form a complete set. Thus, $|\langle f_v \mid m_v \rangle|^2$ represents the probability that the radiative transition will go to a particular final vibrational state $| f_v \rangle$. The second factor of Eq. (A-8) is, therefore, the probability that the excited molecule will undergo a radiative transition from state m to state f.

Hence, when the laser is close enough to resonance that only one term involving intermediate state m is important, the cross section automatically factors into two independent parts--namely, the cross section for an absorption to state $| m \rangle$ times the probability of a re-emission from state $| m \rangle$ to state $| f \rangle$. The method of decay of the excited state is independent of the absorption process because the laser photon

is producing only one quantum state of the molecule, and the properties of a quantum state are independent of the way it is produced (Friedman and Weisskopf, 1955, p. 140). The independence of the two processes would break down if more than one term of Equation (A-6) contributed to the cross section, for the method of decay depends on the relative phases of the various excited intermediate states, and the relative phases depend on the nature of the excitation (Friedman and Weisskopf, 1955, p. 140).

Armed with the property of independence, one can readily compute the cross section for background fluorescence (Fouche, Herzenberg, and Chang, 1972). The cross section for the absorption of a photon $\omega_L$ followed by a collision leading to some other level m' in the excited electronic state is proportional to

$$\frac{|\langle m_v | i_v \rangle|^2 \Gamma_{RAD} \Gamma}{(\omega_{im} - \omega_L)^2 + \frac{1}{4}\Gamma^2} \cdot \frac{\Gamma_C}{\Gamma} \quad . \tag{A-10}$$

After the collision, the probability that the molecule will reradiate to a final state f' is $\Gamma_{RAD} |\langle m' | f' \rangle|^2/\Gamma$. The total probability for re-emission is $\sum_{f'} \Gamma_{RAD} |\langle m' | f' \rangle|^2/\Gamma = \frac{\Gamma_{RAD}}{\Gamma}$. Therefore, the cross section for the emission of a photon after a single molecular collision is

$$\frac{|\langle m_v | i_v \rangle|^2 \Gamma_{RAD} \Gamma}{(\omega_{im} - \omega_L)^2 + \frac{1}{4}\Gamma^2} \cdot \frac{\Gamma_C}{\Gamma} \cdot \frac{\Gamma_{RAD}}{\Gamma} \quad . \tag{A-11}$$

The cross section for the emission of a photon after another intermediate collision contains a second factor $\Gamma_C/\Gamma$, and so forth. Therefore, the

cross section for the emission of a photon after one, two, three, or more collisions is obtained by replacing the factor $\Gamma_C/\Gamma$ in Eq. (A-11) by

$$\sum_{n=1}^{\infty}\left(\frac{\Gamma_C}{\Gamma}\right)^n = \frac{\Gamma_C}{\Gamma - \Gamma_C} = \frac{\Gamma_C}{\Gamma_Q + \Gamma_{RAD}} \quad . \qquad \text{(A-12)}$$

Thus the cross section for broad fluorescence into all wavelengths is

$$\sigma_{BF} \propto \frac{|\langle m_v | i_v \rangle|^2 \Gamma_{RAD}^2}{(\omega_{im} - \omega_L)^2 + \frac{1}{4}\Gamma^2} \cdot \frac{\Gamma_C}{\Gamma_Q + \Gamma_{RAD}} \quad . \qquad \text{(A-13)}$$

$\Gamma_C$ occurs in the numerator because it represents the rate of collisions that throw the excited molecule into various levels of the upper electronic state, and it is precisely collisions of this kind that give rise to broad fluorescence. $\Gamma_Q$ occurs in the denominator because it represents the rate of collisions that transfers the molecule all the way down to the ground electronic state, without re-emission. A comparison of Eqs. (A-8) and (A-13) shows that

$$\frac{\sigma_{BF}}{\sigma_F} = \frac{\Gamma_C}{\Gamma_Q + \Gamma_{RAD}} \cdot \frac{1}{|\langle f_v | m_v \rangle|^2} \quad . \qquad \text{(A-14)}$$

From this last equation, it is evident that a broad background (due to the BF process) will accompany the spikes (due to the RF or ORF processes) in the scattered spectrum. As the laser line is tuned toward and away from an absorption line, this background will rise and fall in direct proportion as the spikes rise and fall.

292

The following arguments may be made to show that $\sigma_{BF}$ will in general be greater than $\sigma_F$.

First, Eq. (A-9) shows that $|\langle f_v | m_v \rangle|^2$ is less than 1. How much less than 1 depends on the molecule and the particular final state that is observed. As an example. **Fouche and Chang (1972)** have observed significant intensity in more than 40 overtones, so that on the average $|\langle f_v | m_v \rangle|^2$ was less than 1/40.

Second, $\Gamma_C/(\Gamma_Q + \Gamma_{RAD})$ will generally be greater than 1. $\Gamma_{RAD}$ will be less than $10^9$ per second because fluorescence lifetimes are no faster than about $10^{-9}$ s. And $\Gamma_C + \Gamma_Q$ will be on the order of $10^{10}$ per second, which is the collision rate in a gas at atmospheric pressure. Also, the rate for collisions into other vibrational levels of the excited electronic state ($\Gamma_C$) will in general be higher than the rate for collisions that return the molecule to its ground electronic state ($\Gamma_Q$), because the energy differences are less in the former case. For iodine vapor mixed with various gases, Kurzel and Steinfeld (1970) have shown $\Gamma_C \approx 5\Gamma_Q$. Thus, in general, $\Gamma_{RAD}$ can be neglected in comparison with $\Gamma_Q$, and $\Gamma_C/\Gamma_Q$ will be greater than 1.

The processes of Figure A-1 are ordered from left to right in terms of increasing cross sections.

It should be mentioned here that the transition from RRS to RF is a gradual one that is often hard to distinguish experimentally. In ordinary situations, the total emission from both Raman scattering and fluorescence should increase as the center of the absorption line is approached. Fluorescence increases the time delay of the emission; however, in air at atmospheric pressure, the collision rate is $\Gamma \sim 10^{10}$ s$^{-1}$, and the efficiency for collision-induced quenching may be as high as $\Phi = 0.3$ (Penney and Silverstein, 1972). The fluorescence will be reduced by $\gamma/\Gamma\Phi$, where $\lambda$ is the radiative decay rate for the transition.

Thus, the signal will be significantly reduced from the values obtained at low pressures. Those molecules that do fluoresce will do so in a time of $(\Gamma\Phi)^{-1}$, or about $0.3 \times 10^{-9}$ s, at atmospheric pressure. Therefore, there will be no emissions at times longer than a nanosecond after excitation and no significant loss of range information.

5. <u>Effect of the Laser Spectral Distribution</u>

The treatment thus far has assumed that the incident laser beam is monochromatic. However, when the laser energy falls near discrete molecular levels, as in processes (c), (d), and (e), its spectral distribution must be included in the treatment.

With monochromatic light $\omega$ and a molecule with resonant frequency $\omega'$,

$$\sigma \propto \frac{1}{(\omega' - \omega)^2 + \frac{1}{4}\Gamma^2} \qquad (A-15)$$

To get the scattered intensity from the molecule, Eq. (A-15) must be integrated over the laser spectral distribution:

$$I'_F(\omega') = \int d\omega \, f(\omega) \propto \int d\omega \, f(\omega) \frac{1}{(\omega' - \omega)^2 + \frac{1}{4}\Gamma^2} \qquad (A-16)$$

Furthermore, the molecules in a gas move with a gaussian distribution of speeds so that the laser beam sees a gaussian distribution of Doppler-shifted resonant frequencies, $e^{-(\omega' - \omega_{im})^2/2\Delta_D^2}$, where $\omega_{im}$ is the resonant frequency of a molecule at rest, and $\Delta_D$ is the Doppler width of the gas. Thus, the scattered intensity from all the molecules is

$$I_F \propto \int d\omega' \; I_F' \; (\omega') e^{-(\omega' - \omega_{im})^2/2\Delta_D^2} = \iint d\omega' \; d\omega \; \frac{f(\omega) e^{-(\omega' - \omega_{im})^2/2\Delta_D^2}}{(\omega' - \omega)^2 + \frac{1}{4}\Gamma^2}$$

$$(A-17)$$

Two possible laser distributions are the Lorentzian and the gaussian. If the laser distribution is a normalized Lorentzian,

$$f(\omega) = \frac{\Gamma_L}{2\pi} \cdot \frac{1}{(\omega - \omega_L)^2 + \frac{1}{4}\Gamma_L^2} \qquad (A-18)$$

then Eq. (A-17) can be reduced to

$$I_F = k \; \frac{\Gamma_L + \Gamma}{\Gamma} \int_{-\infty}^{\infty} d\omega' \; \frac{e^{-(\omega' - \omega_L)^2/\Delta_D^2}}{(\omega' - \omega_{im})^2 + \frac{1}{4}(\Gamma + \Gamma_L)^2} \qquad (A-19)$$

If the laser distribution is a normalized gaussian,

$$f(\omega) = \frac{1}{\sqrt{2\pi} \; \Delta_L} \; e^{-(\omega - \omega_L)^2/2\Delta_L^2} \qquad (A-20)$$

then Eq. (A-17) can be reduced to

$$I_F = k \sqrt{\frac{\Delta_D^2}{\Delta_L^2 + \Delta_D^2}} \int_{-\infty}^{\infty} d\omega \; \frac{e^{-(\omega - \omega_L)^2/2(\Delta_D^2 + \Delta_L^2)}}{(\omega - \omega_{im})^2 + \frac{1}{4}\Gamma^2} \qquad (A-21)$$

where k represents the same constant in both Eq. (A-19) and Eq. (A-21). The integrand in both Eq. (A-19) and Eq. (A-21) is a Lorentzian times

a gaussian, and the integral can be converted to a form tabulated by Faddeyeva and Terent'ev (1961).

The point to note is that when the laser line falls near discrete molecular levels, its exact frequency and spectral width may have to be accurately known in order to get correct quantitative results. Equations (A-19) and (A-21) show that the scattered intensity depends on the laser width if it is comparable to or larger than the molecular line width or the Doppler width. For the atmosphere at 25°C, both $\Gamma$ and $\Delta_D$ are on the order of $10^9 - 10^{10}$ s$^{-1}$, and many laser lines are broader than this. These equations also show that the scattered intensity may vary considerably if the laser frequency is shifted with respect to the molecular resonances by as little as $\Gamma$ or $\Delta_D$, whichever is larger. Correct quantitative measurements cannot be made in the field unless the laser used in the field has the same bandwidth and frequency, both to within the larger of $\Gamma$ and $\Delta_D$, as the laser that was used in the laboratory to determine the scattered intensity per molecule.


6. Disadvantages

In Section 1 it was pointed out that the Raman technique of detecting air pollutants has only one major disadvantage--that of poor sensitivity. It was also conjectured that the advantage of the Raman technique could be retained because its disadvantage was overcome by approaching resonance. We are now in a position to discuss this possibility.

As a preliminary remark, the Raman and resonance fluorescence techniques both involve light backscattering and are very much related. The former can be changed into the latter in a continuous fashion by tuning the laser wavelength. But then there is a distinct break in a switchover to the absorption technique. As the laser is tuned toward resonance,

the advantages and disadvantages will lie somewhere between those of ORS and RF, and will not reach the extremes of the IR absorption technique.

The first advantage of the Raman technique, single-endedness, will not degrade at all in going to resonance. The second advantage--good depth resolution--in a ranging experiment could be degraded as resonance because of the long decay times ($10^{-9}$ s to $10^{-5}$ s) for fluorescence. However in normal atmospheric conditions, collisions with air molecules will quench any molecules that have not radiated in less than a nanosecond, so that no more than 1 ft of distance resolution will be lost.

As for the third advantage--the ability to monitor all pollutants simultaneously with a single laser wavelength--suppose one is using the Raman technique to do this and he decides to increase the sensitivity for detecting pollutant X by tuning the laser line toward one of its resonances. Again, as resonance is approached, the probability of absorption increases, thereby increasing the amount of delayed scattering. The delayed part is subject to collisions before re-emission, and collisions cause background fluorescence to arise in the spectrum. This BF will extend over a large spectral range $\Delta\nu_B$ and may be so strong that it will mask out the Raman signals from the other pollutants. Of course, when the spectrometer slit width is closed to a given Raman linewidth $\Delta\nu_R$, only a fraction $\Delta\nu_R/\Delta\nu_B$ of the BF can interfere with the Raman line. However, the Raman signal can still be lost in the BF because the cross section for BF can be several orders of magnitude greater than the cross section for Raman scattering. Thus we see that by increasing the sensitivity for detecting X by approaching resonance, one may correspondingly decrease the sensitivity for detecting the other pollutants. A further lessening of this advantage is that one cannot approach the resonances of all the pollutants with a single laser wavelength, because the absorption bands are not the same. Thus, a principal advantage of the

297

Raman method--the ability to measure all pollutants with a single non-tunable illuminating wavelength--is lost.

The fourth advantage of arbitrary wavelength also disappears. The more resonant enhancement that is desired, the more the laser wavelength is restricted to lie close to an absorption line. Furthermore, as noted in the last section, whenever the laser line falls within an absorption band, its exact frequency and bandwidth must be accurately known (to within $\Gamma$ or $\Delta_D$) in order to get correct quantitative results.

7.   Experimental Results

Observations of resonance Raman scattering in gases have been very few. Observations of ORF, RF, and BF that are applicable to the discussion of this appendix are reported here.

Fouche and Chang (1972) claimed to have measured an $8 \times 10^5$ enhancement of Raman scattering in $I_2$ by tuning through an $I_2$ absorption line. This has been disputed by St. Peters et al. (1973), who repeated the experiment under different conditions. They added $N_2$ at various vapor pressures to the $I_2$ sample and observed that the signal was not only strongly decreased (quenched) but also redistributed, both of which are characteristic of fluorescence and not of Raman scattering.

Fouche, Herzenberg, and Chang (1972) used an argon-ion laser to measure RF and BF from $NO_2$. With the $NO_2$ molecule mixed with air at atmospheric pressure, the cross section of a single overtone was measured to be about 100 times $\sigma_{N_2}$. The BF per angstrom was smaller by a factor of 10. In this case also, the BF could mask out the Raman signals from other gases.

Holzer, Murphy, and Bernstein (1970) observed RRS from various halogen vapors at low pressures using various argon-ion laser lines. In this case the laser line falls above the dissociation limit of the

upper electronic state so that an integral over continuum states must be included in Equation (A-1). The cross section of a single overtone of $I_2$ using 4880 Å (15 Å above the dissociation limit) was measured to be 800 times $\sigma_{N_2}$. The amount of BF was not given.

Berjot, Jacon, and Bernard (1972) observed a continuous change from RF to RRS by increasing the gas pressure to broaden the molecular lines. The 5017 Å line of the argon-ion laser was used to excite $I_2$. The amount of light scattered from $I_2$ was not compared to that from any other gas.

Berjot, Jacon, and Bernard (1971) measured the relative intensities from the fundamental of $I_2$ vapor at low pressures using seven argon-ion laser lines between 4545 Å and 4965 Å (and thus above the dissociation limit). The relative cross sections varied from an $\omega_L^4$ law by a factor of 4.

Unfortunately, no one has yet tuned a laser line from a point well below the absorption band of a molecule up to the absorption band while checking the deviations from the $\omega_L^4$ law and for the amount of background.

Bernstein (1973) measured resonant Raman enhancements in gaseous $Cl_2$, $Br_2$, and $I_2$. He obtained intensities of 10 to 1000 times stronger than the normal Raman effect.

Williams et al. (1974) and Robrish et al. (1975) have recently reported experiments on resonance Raman scattering and fluorescence from $I_2$, and have concluded that there is a continuous transition from one to the other. The Heisenberg uncertainty principle was used to show that for laser excitations very near the absorption line center the time spent by the molecule in the intermediate state is limited by the frequency difference. At greater separations, the influence of collisions in affecting lifetime becomes more important, and the scattering cross section decreases.

Penney et al. (1973) made some scattering and fluorescence measurements at visible wavelengths of $NO_2$ and $O_3$, and $SO_2$ for excitation near 300 nm. They discussed the possibility of using Raman scattering for remote atmospheric probing.

Rosen et al. (1975) estimated the feasibility of using resonance Raman scattering for the remote detection of pollutants. They were optimistic about the prospects of using the technique, and estimated that for $10^4$ pulses of 0.05 mJ each, $10^2$ ppm $NO_2$ and 10 ppm of $SO_2$ could be detected at 1 km at night, and $10^2$ ppm of NO could be detected during daytime. These are for an SNR of 10. No comparison was made with the sensitivity of the DIAL technique operating at the same wavelengths.

Marsden and Bird (1973) have reported a portion of the $NO_2$ resonance Raman spectrum, for excitation at 514.5 nm.

8. Potential Wavelengths

The principal pollutants that have absorption bands in the UV are $O_3$, $NO_2$, and $SO_2$. $O_3$ has an absorption peak at 253 nm, with a line-width of about 45 nm. $SO_2$ has broad absorption bands, one centered at 148.5 nm with a 16-nm width, one at 191.5 nm with about a 27-nm width, and one at about 290 nm with a 60-nm width. $NO_2$ has broad absorption from at least 130 to 270 nm. These broad peaks limit the possibility for observing RRS from these molecules. Inspection of the resonance denominator $[(\omega_1 - \omega_e) - i\Gamma]^2$, shows that the linewidth, $\Gamma$, will limit the amount of enhancement obtainable. Enhancements greater than a factor of 5 or 10 over ORS would not be expected. Furthermore, absorption would be very pronounced, and one would have a large amount of broadband fluorescence.

Since ordinary Raman scattering is proportional to $\lambda^{-4}$, resonant Raman scattering should be less by about $10^4$ for IR wavelengths than for

300

UV or visible wavelengths. Furthermore, detectors in this spectral region tend to be two to three orders of magnitude less sensitive than for the visible region.

# BIBLIOGRAPHY ON SPECTRAL INFORMATION

The prime bibliographic reference is:

Nels Laulainen, "Minor Gases in the Earth's Atmosphere:
A Review and Bibliography of their Spectra," Project
ASTRA Publication No. 18, September 1972, University of
Washington, Seattle, Washington.

This document contains 1214 references that are cross-indexed. A
second general reference is:

Philip L. Hanst, "Spectroscopic Methods for Air Pollu-
tion Measurement," a chapter in Advances in Environ-
mental Science and Technology, Vol. 2, edited by J. N.
Pitts, Jr. and R. L. Metcalf, Wiley-Interscience, 1971.

General references on ultraviolet spectra are:

Hudson, R. D., "Critical Review of Ultraviolet Photoabsorp-
tion Cross Sections for Molecules of Astrophysical and
Aeronomic Interest," Reviews of Geophysics and Space
Physics, Vol. 9, No. 2, p. 305 (May, 1971).

Watanabe, K., M. Zelikoff, and E.C.Y. Inn, "Absorption
Coefficients of Several Atmospheric Gases" [$O_2$, $O_3$, CO,
$CO_2$, NO, $N_2O$, $N_2$, $H_2O$, $H_2$, $CH_4$, $NH_3$], Geophysical Re-
search Paper No. 21, Air Force Cambridge Research
Center Technical Report 52-53, June 1953 (AD 19700).

Thompson, B. A., P. Harteck, and R. R. Reeves, Jr.,
"Ultraviolet Absorption Coefficient of $CO_2$, CO, $O_2$,
$H_2O$, $N_2O$, $NH_3$, NO, $SO_2$, and $CH_4$ between 1850 and
4000 Å," J. Geo. Res., Vol. 68, No. 24, pp. 6431-6436   (1963).

The prime reference to the infrared spectra of the normal atmosphere

is:

McClatchey, R. A., et al., "AFCRL Atmospheric Absorption
Line Parameter Compilation," Air Force Cambridge Research

Laboratory Report No. TR-73-0096, 26 January 1973 (Environmental Research Paper No. 434).

The following references are those that are not included in the above documents:

- <u>CO</u>

    Locke, J. L., and L. Herzberg, "The Absorption Due to Carbon Monoxide in the Infrared Solar Spectrum," <u>Can. J. Phys.</u>, Vol. 31, pp. 504-516 (1953).

- $SO_2$

    Burch, D. E., J. D. Pembrook, D. A. Gryvnak, "Absorption and Emission by $SO_2$ between 1050 and 1400 cm$^{-1}$ (9.5-7.1 μm," Philco-Ford Corporation, July 1972 (PB 203 523).

    Calawa, A. R., E. D. Hinkley, S. A. Clough, and P. L. Kelley, "Determination of the $v_1$-Band of $SO_2$ by Tunable Laser Spectroscopy," Lincoln Laboratories (MIT), <u>Solid State Research</u>, 1971, No. 4, pp. 25-27.

    Corice, R. J., K. Fox, and G.D.T. Tejwani, "$v_1 + v_3$ Combination Band of $SO_2$," UTPA-ERAL-03, December 1972, University of Tennessee, Knoxville, Tenn. (to be published in <u>J. Chem. Phys.</u>).

    _____, "Experimental and Theoretical Studies of the Fundamental Bands of Sulfur Dioxide," <u>J. Chem. Phys.</u>, Vol. 58, No. 1, pp. 265-270 (1973).

    Fox, K., G.D.T. Tejwani, and R. J. Corice, Jr., "Fundamental Bands of $^{32}S^{16}O_2$," UTPA-ERAL-01, September 1972, University of Tennessee, Knoxville, Tenn.

    Hinkley, E. D., A. R. Calawa, S. A. Clough, and P. L. Kelley, "Determination of Total Band Intensity and Transition Moment for the $v_1$-Band of $SO_2$," Lincoln Laboratories (MIT), <u>Solid State Research</u>, 1972, No. 1, pp. 16-17.

    Hinkley, E. D., A. R. Calawa, and P. L. Kelley, "Tunable Laser Spectroscopy of the $v_1$ Band of $SO_2$," <u>J. Appl. Phys.</u>, Vol. 43, No. 7, pp. 322-3224 (1972).

_____, "Computed Linewidths of $SO_2$," UTPA-ERAL-02, November 1972, University of Tennessee, Knoxville, Tenn.

Tejwani, G.D.T., K. Fox, and R. J. Corice, Jr., "Dipole Moment Derivations for $SO_2$," Chem. Phys. Letters, Vol. 18, No. 3, pp. 365-368 (1973).

Warneck, P., F. F. Marmo, and J. O. Sullivan, "Ultra-Violet Absorption of $SO_2$: Dissociation Energies of $SO_2$ and SO," J. Chem. Phys., Vol. 40, No. 4, pp, 1132-1136 (1964).

• **NO**

Blum, F. A., A. R. Calawa, K. W. Nill, and T. C. Harman, "Resolved Q-Branch Absorption in Nitric Oxide: Nuclear Hyperfine Splitting," Lincoln Laboratories (MIT), Solid State Research, 1972, No. 1., pp. 35-37.

Keck, D. B., "High Resolution Absorption, Zeeman and Magnetic Rotation Spectra of the Fundamental and Satellite Bands of Nitric Oxide in the Near Infrared," Michigan State University, University Microfilms No. 68-7914 (1968).

• **$NO_2$**

Hurlock, S. C., "High Resolution Absorption Spectra of the Isotopic Modifications of Nitrogen Dioxide and Other Small Molecules," Diss. Abst., Vol. 31, No. 4, 2195-B, October 1970 (Order No. 70-19322).

Nakayama, T., M. Y. Kitamura, K. Watanabe, "Ionization Potential and Absorption Coefficient of Nitrogen Dioxide," J. Chem. Phys., Vol. 30, No. 5, pp. 1180-1186 (1959) [Ultraviolet].

Tejwani, G.D.T., "Calculation of Pressure-Broadened Line-widths of $SO_2$ and $NO_2$," J. Chem. Phys., Vol. 57, No. 11, pp. 4676-4681 (1972).

Wilkerson, T. D., B. Ercoli and F. S. Tomkins, "Absorption Spectra of Atmospheric Gases," Institute for Fluid Dynamics and Applied Mathematics, University of Maryland, College Park, Tech. Note BN-784, February 1974.

- HNO$_3$

    Murcray, D. G., T. G. Kyle, F. H. Murcray, and W. J. Williams, "Presence of HNO$_3$ in the Upper Atmosphere," J. Opt. Soc. Am., Vol. 59, No. 9, pp. 1131-1134 (1969).

- Hydrocarbons

    Jaynes, D. N. and B. H. Beam, "Hydrocarbon Gas Absorption by an HeNe Laser Beam at 3.39 μ Wavelength," Appl. Optics, Vol. 8, No. 8, pp. 1741-1742 (1969).

    Toth, R. A., "High Resolution Measurements of the Line Positions and Strengths of the $2\nu_2$ Band of H$_2$CO$^*$," accepted for publication, J. Mol. Spect.

- H$_2$O

    Blum, F. A., K. W. Nill, P. L. Kelley, A. R. Calawa, and T. C. Harman, "Tunable Infrared Laser Spectroscopy of Atmospheric Water Lines," Science, Vol. 177, pp. 694-695 (1972).

    Newman, E. H. and G. L. Trusty, "Absorption of Five to Six Micron Carbon Monoxide Laser Radiation by Water Vapor," Technical Report 2819-1, Air Force Avionics Laboratory, Wright-Patterson Air Force Base, Ohio (August 1971).

    Nill, K. W., F. A. Blum, P. L. Kelley, A. R. Calawa, and T. C. Harman, "High Resolution Spectroscopy of Atmospheric Water Vapor," Lincoln Laboratories (MIT), Solid State Research (1), pp. 15-17 (1972).

    Rusk, A. N. and D. Williams, "Optical Constants of Water in the Infrared," J. Opt. Soc. Am., Vol. 61, No. 7, pp. 895-903 (1971).

- HCl

    Rank, D. H., W. B. Birtley, D. P. Eastman, B. S. Rao, and T. A. Wiggens, "Precise Measurement of Some Infrared Bands of Hydrogen Chloride," J. Opt. Soc. Am., Vol. 50, Vol. 12, pp. 1275-1279 (1960).

# REFERENCES

Anderson, L. K., and B. J. McMurty, 1966. "High Speed Photodetectors,"
Proc. IEEE, Vol. 54, pp. 1335-1349, October.

Anderson, L. K., et al., 1965. "Microwave Photodiodes Exhibiting
Microplasma Free Carrier Multiplication," Appl. Phys. Lett.,
Vol. 6, pp. 62-64, February.

Barnett, G. P., and A. C. Albrecht, 1970. "Comments on the Derivations
of the Dispersion Equation for Molecules," Raman Spectroscopy,
H. A. Szymanski, ed., Vol. II, Appendix, Plenum Press, New York.

Barth, C. A., 1966. "Nitric Oxide in the Upper Atmosphere," Ann. de
Géophys, Vol. 22, p. 198.

Bartlett, B. E., et al., 1969. "Background Limited Photoconductive
HgCdTe Detectors for Use in the 8-14 Micron Atmospheric Window,"
Infr. Phys. Vol. 9, p. 35.

Berjot, M., M. Jacon, and L. Bernard, 1971. "Effet Raman de Résonance
par Excitation dans le Continuum d'Absorption: Sections Efficaces
Relatives de Diffusion," Opt. Comm., Vol. 4, p. 117.

_____, 1972. "Passage Continu de la Fluroescence de Resonance
a l'Effet Raman de Resonance," Can. J. Spectroscopy, Vol. 17, p. 60.

Bernstein, H. J., 1973. Paper presented at the 1973 Spring Meeting of
the Optical Society of America, New York, N.Y., 11-13 April.

Bradley, Prof. D. J., 1972. School of Physics and Applied Mathematics,
The Queen's University of Belfast, Northern Ireland. Seminar at
Stanford University, Palo Alto, California, Summer.

Braslau, N., and J. V. Dave, 1973. Effect of Aerosols on the Transfer
of Solar Energy Through Realistic Model Atmospheres (to be published).

Bullrich, K., 1963. "Mie Scattering of an Atmospheric Air Volume," in
Electromagnetic Scattering, p. 191 et seq., Pergamon Press, New
York.

Byer, R. L., and M. Garbuny, 1973. "Pollutant Detection by Absorption Using Mie Scattering and Topographic Targets as Retroreflectors," Appl. Optics, Vol. 12, No. 7, pp. 1496-1505, July.

Byer, R. L., 1975a. "Remote Air Pollution Measurements," to be published in Opto-electronics.

Byer, R. L., 1975b. "Optical Parametric Oscillators," to be published in Treatise on Quantum Electronics, H. Rabin and C. L. Tang, eds. Academic Press, New York, N.Y.

Cadle, R. D., 1972. "Composition of the Stratospheric 'Sulfate Layer," Proc. of CIAP Survey Conference, February 15-16, NTIS No. DOT-TSC-OST-72-13. Also in Trans. of Amer. Geophysical Union, Vol. 53, No. 9, pp. 812-820, September.

Chang, T. Y., and O. R. Wood II, 1972a. "Optically Pumped Atmospheric-Pressure $CO_2$ Laser," Appl. Phys. Lett., Vol. 21, No. 1, p. 19, July.

_____, 1972b. "A Simple Self-Mode-Locked Atmospheric Pressure $CO_2$ Laser," IEEE J. of Quantum Electronics, p. 721, August.

_____, 1973. "Optically Pumped $NO_2$ Laser," Appl. Phys. Lett., Vol. 22, No. 3, 1 February.

Charlson, R., 1973. Stockholm Tropospheric Aerosol Seminar. Drafted by R. Charlson. Institute of Meteor. U. of Stockholm. Report AP-14, August.

Cicerone, R. J., et al., 1974. "Stratospheric Ozone Destruction by Man-Made Chlorofluoromethanes," Science, Vol. 185, p. 1165, September.

Collis, R.T.H., 1970. "Lidar," Appl. Optics, Vol. 9, p. 1782, August.

Collis, R.T.H., and E. E. Uthe, 1972. "Mie Scattering Techniques for Air Pollution Measurement with Lasers," Opto-electronics, Vol. 4, No. 2, pp. 87-99, May.

Collis, R.T.H., et al., 1973. "Lidar Observations of Atmospheric Particulate Content," paper presented at the UCLA International Conference on Radiation and Remote Probing of the Atmosphere, Los Angeles, 28-30 August.

Corice, R. J. Jr., K. Fox, and G.D.T. Tejwani, 1972. "$\nu_1 + \nu_3$ Combination Band of $SO_2$," Research Report No. UTPA-ERAL-03, Department of Physics and Astronomy, The University of Tennessee, Knoxville, Tenn.

Danilychev, V., 1973, of the Lebedev Institute, Moscow, USSR. Paper presented at the Conference on Laser Engineering and Applications, Washington, D.C., May.

Dave, J. V., 1969. "Scattering of Visible Light by Large Water Spheres," Appl. Optics, Vol. 8, No. 1, pp. 156-164, January.

Deirmendjian, D., 1964. "Scattering and Polarization Properties of Water Clouds and Hazes in the Visible and Infrared," Appl. Optics, Vol. 3, No. 2, pp. 187-196, February.

_____, 1969. "Electromagnetic Scattering on Spherical Polydispersions, American Elsevier Publishing Co., Inc., New York.

Deirmendjian, D., R. Clausen, and W. Viezee, 1961. "Mie Scattering with Complex Index of Refraction," J. Optical Society of America, Vol. 51, No. 6, pp. 620-633, June.

Dimmock, J. O., 1971. Infrared Detectors and Applications, Lincoln Laboratory, Massachusetts Institute of Technology, Lexington, Mass.

Dynatrend, 1973. "Laramie Comparative Experiment, Data Report and Preliminary Report of Conclusions." Report CIAP. DOT. edited by Dynatrend Inc., March 15.

Eckstrom, D. J., et al., 1973. "Studies of E-Beam Pumped Molecular Lasers," Semiannual Technical Report No. 2 on SRI Project PYU-1925, Stanford Research Institute, Menlo Park, California, July 31.

Elterman, L., R. B. Toolin, and J.D. Essex, 1973. "Stratospheric Aerosol Measurements with Implications for Global Climate," Appl. Optics, Vol. 12, pp. 330-337.

Evans, W. E., 1973. Private Communication.

Evans, W. E., et al., 1966. "Performance Specifications for a Meteorological Satellite Lidar," Final Report, Contract NASR-49 (22), SRI Project 5373, Stanford Research Institute, Menlo Park, California, June.

Faddeyeva, V. N., and N. M. Terent'ev, 1961. <u>Tables of the Value of</u>
<u>the Function</u>

$$w(Z) = e^{-t^2} \left( 1 + \frac{2i}{\sqrt{\pi}} \int_0^Z e^{t^2} \, dt \right)$$

<u>for Complex Argument</u>, Pergamon Press, New York.

Fiocco, G., and G. Grams, 1964. "Observation of the Aerosol Layer at
20 km by Optical Radar," <u>J. Atmos. Sci.</u>, Vol. 21, pp. 323-324.

Fouche, D. G., and R. K. Chang, 1972. "Observation of Resonance Raman
Scattering Below the Dissociation Limit in $I_2$ Vapor," <u>Phys. Rev.</u>
<u>Lett.</u>, Vol. 29, No. 9, pp. 536-539, August 28.

Fouche, D. G., A. Herzenberg, and R. K. Chang, 1972. "Inelastic Photon
Scattering by a Polyatomic Molecule: $NO_2$," <u>J. Appl. Phys</u>. Vol. 43,
p. 3846.

Fox, K., G.D.T. Tejwani and R. J. Corice, Jr., 1970. "Fundamental Bands
of $32_S16_{O_2}$," Research Report No. UTPA-ERAL-01, Department of Physics
and Astronomy, The University of Tennessee, Knoxville, Tenn.

Foyt, A. G., W. T. Lindley, and J. P. Donnelly, 1970. "n-p Junction
Photodetectors in InSb Fabricated by Proton Bombardment," <u>Appl.</u>
<u>Phys. Lett.</u> Vol. 7, No. 9, pp. 536-539, August 28.

Franken, P. A., et al., 1961. "Generation of Optical Harmonics,"
<u>Phys. Rev. Lett.</u>, Vol. 7, p. 118.

Friedman, F. L., and V. F. Weisskopf, 1955. "The Compound Nucleus,"
in <u>Niels Bohr and the Development of Physics</u>, E. Pauli, ed.,
Pergamon Press, New York.

Gambling, D. J., and K. Bartusek, 1972. "Lidar Observations of Tropo-
spheric Aerosols," <u>Atmos. Environ.</u>, Vol. 6, pp. 181-190, and Vol. 6,
pp. 869-870.

Giordmaine, J. A., and R. C. Miller, 1965. "Tunable Coherent Parametric
Oscillation in $LiNbO_3$ at Optical Frequencies," <u>Phys. Rev. Lett.</u>,
Vol. 14, p. 973.

Grams, G., and G. Fiocco, 1967. "Stratospheric Aerosol Layer During 1964 and 1965," J. Geophys. Res., Vol. 72, pp. 3523-3542.

Grams, G. W., et al., 1973. "Complex Index of Refraction of Airborne Soil Particles and Implications for Climatic Change," to be published.

Grant, W. B., R. D. Hake, Jr., E. M. Liston, R. C. Robbins, and E. K. Proctor, Jr., 1974. Appl. Phys. Lett., Vol. 24, No. 11, pp. 550-552 June.

Grant W. B. and R. D. Hake, Jr., 1975. "Calibrated Remote Measurements of $SO_2$ and $O_3$ Using Atmospheric Backscatter," to be published in J. Applied Physics, July.

Grobecker, A. J., S. C. Coronoti, and R. H. Cannon, Jr., 1974. "The Effects of Stratospheric Pollution by Aircraft," Climatic Impact Assessment Program, Department of Transportation, Washington, D.C., Report No. DOT-TST-75-50, December.

Hake, R. D., E. K. Proctor, and R. A. Long, 1971. "Tunable Dye Lidar Techniques for Measurement of Atmospheric Constituents," Proceedings of the SPIE Seminar on Remote Sensing of Earth Resources and the Environment, Palo Alto, California, November.

Hanst, P. L., 1971a. "Spectroscopic Methods for Air Pollution Measurement," Advances in Environmental Science and Technology, James N. Pitts, Jr. and Robert L. Metcalf, ed., pp. 91-213, Wiley-Interscience, New York.

_____ 1971b. "Infrared Spectroscopy and Infrared Lasers in Air Pollution Research and Monitoring," Appl. Spectroscopy, Vol. 24, pp. 161-174.

Harris, S. E., 1969. "Tunable Optical Parametric Oscillators," Proc. IEEE, Vol. 57, p. 2096.

Heitler, W., 1960. The Quantum Theory of Radiation, 3rd. ed., Clarendon Press, Oxford.

Hinkley, E. D., and P. L. Kelley, 1971. "Detection of Air Pollutants with Tunable Diode Lasers," Science, Vol. 171, No. 3972, pp. 635-639, 19 February.

Hirono, M., et al., 1972. "Observations of Aerosol Layers in the Upper Atmosphere by Laser Radar," Report of Ionospheric and Space Research in Japan, Vol. 26, pp. 237-244.

Hirschfeld, T., et al., 1973. "Remote Spectroscopic Analysis of PPM Air Pollutants by Raman Spectroscopy," Appl. Phys. Lett., Vol. 22, No. 1, 1 January.

Holland, A. C., and J. S. Draper, 1967. "Analytical and Experimental Investigation of Light Scattering from Polydispersion of Mie Particles," Appl. Optics, Vol. 6, No. 3, pp. 511-518, March.

Holland, A. C., and G. Gagne, 1970. "The Scattering of Polarized Light by Polydisperse Systems of Irregular Particles," Appl. Optics, Vol. 9, No. 5, pp. 1113-1121, May.

Holzer, W., W. F. Murphy, and H. J. Bernstein, 1970. "Resonance Raman Effect and Resonance Fluorescence In Halogen Gases," J. Chem. Phys., Vol. 52, p. 399.

Jacobs, G. B., and L. R. Snowman, 1967. "Laser Techniques for Air Pollution Measurement," IEEE J. of Quantum Electronics, Vol. QE-3, No. 11, November.

Jaynes, D. N., and B. H. Beam, 1969. "Hydrocarbon Gas Absorption by a HeNe Laser Beam at 3.39 $\mu$ Wavelength," Appl. Optics, Vol. 8, pp. 1741-1742.

Johnson, K. M., 1965. "High-Speed Photodiode Signal Enhancement of Avalanche Breakdown Voltage," IEEE Trans. Electron Devices, Vol. 1D-12, pp. 55-63, February.

Kent, G. S., and R. W. Wright, 1970. "A review of laser radar measurements of atmospheric properties," J. Atmos. Terrest. Phys., Vol. 32, pp. 917-943.

Kerker, M., 1969. The Scattering of Light and Other Electromagnetic Radiation, Academic Press, New York.

Keyes, R. J., and T. M. Quist, 1970. "Low-Level Coherent and Incoherent Detection in the Infrared," in Semiconductors and Semimetals, Vol. 5 - Infrared Detectors, R. K. Willardson and A. C. Beer, eds., p. 321, Academic Press, New York.

Kildal, H., and R. L. Byer, 1971. "Comparison of Laser Methods for the Remote Detection of Atmospheric Pollutants," Proc. IEEE, Vol. 59, No. 12, pp. 1644-1663, December.

Koehler, H. A., et al., 1972. "Stimulated VUV Emission in High Pressure Xenon Excited by High-Current Relativistic Electron Beams," Appl. Phys. Lett., Vol. 21, p. 198.

Kruse, P. W., L. D. McGlauchin, and R. B. McQuistan, 1962. Elements of Infrared Technology, New York.

Kurzel, R. B., and J. I. Steinfield, 1970. "Energy-Transfer Processes in Monochromatically Excited Iodine Molecules. III Quenching and Momentum Transfer from v' = 43," J. Chem. Phys., Vol. 53, pp. 3293.

Lawrence, R. S., and J. W. Strohbehn, 1970. "A Survey of Clear-Air Propagation Effects Relevant to Optical Communications, Proc. IEEE Vol. 58, No. 10, October.

Logan, N. A., 1965. "Survey of Some Early Studies of the Scattering of Plane Waves by a Sphere." Proc. IEEE, Vol. 53, pp. 773-785, August.

Long, R. K., 1966. "Atmospheric Absorption and Laser Radiation," Bulletin 199, Engineering Experiment Station, Ohio State University, Columbus, Ohio.

Lorents, D. C., and R. E. Olson, 1972. "Excimer Formation and Decay Processes in Rare Gases," Semiannual Technical Report No. 1 on SRI Project PYU-2018. Stanford Research Institute, Menlo Park, California, 27 December.

Lucovsky, G., and R. B. Emmons, 1965. "High Frequency Photodiodes," Appl. Optics, Vol. 4, pp. 697-702, June.

Ludwig, C. B., et al., 1969. "Study of Air Pollutant Detection by Remote Sensors," NASA CR-1380, July.

Mack, M. E., 1973. Post-deadline paper presented at the 1973 IEEE/OSA Conference on Laser Engineering and Applications, Washington, D.C., May 30-June 1.

Marsden, M. J. and G. R. Bird. "Resonance Raman Spectrum of Gaseous Nitrogen Dioxide ($NO_2$)," 1973, J. Chem. Physics, Vol. 59, p. 2766.

Mathur, D. P., R. J. McIntyre, and P. P. Webb, 1968. "A New Germanium Photodiode with Extended Long-Wavelength Response," presented at the Int. Electron Device Meet., Washington, D.C., October.

McClatchey et al., 1973. "AFCRL Atmospheric Absorption Line Parameter Compilation," AFCRL-TR-73-0096, Environmental Research Papers No. 434, Air Force Cambridge Research Laboratory, Bedford, Mass., 26 January.

McCormick, M. P., et al., 1968. "Mie Total and Differential Back-scattering Cross Sections at Laser Wavelengths for Junge Aerosol Models," Appl. Optics, Vol. 7, No. 12, pp. 2424-2425, December.

Measures, R. M., and G. Pilon, 1972. "A Study of Tunable Laser Techniques for Remote Mapping of Specific Gaseous Constituents of the Atmosphere," Opto-Electronics, Vol. 4, pp. 141-153.

Melchior, H., and W. T. Lynch, 1966. "Signal and Noise Response of High Speed Germanium Avalanche Photodiodes," IEEE Trans Electron Devices, Vol. ED-13, pp. 829-838, December.

Melchior, H., et al., 1970. "Photodetectors for Optical Communication Systems," Proc. IEEE, Vol. 58, No. 10, pp. 1466-1483, October.

Melfi, S. H., G. B. Northam, and M. P. McCormick, 1973. "Comparison of Lidar and In-Situ Measurements of Stratospheric Aerosols," presented at 5th Conference on Laser Radar Studies of the Atmosphere, Williamsburg, Virginia.

Melingallis, I., 1973. Paper presented at the First Laser Spectroscopy Conference, Vail, Colorado, July.

Menzies, R. T., N. George, and M. L. Bhaumik, 1970. "Spectral Coincidences Between Emission Lines of the CO Laser and Absorption Lines of Nitrogen Oxides," IEEE J. of Quantum Electronics, Vol. QE-6, No. 12, December.

Merzbacher, E., 1961. Quantum Mechanics, John Wiley and Sons, Inc., New York, N.Y.

Mie, G., 1908. Ann. d. Physik, Vol. 25, pp. 377-422.

Molina, M. J., and F. S. Rowland, 1974. "Stratospheric Sink for Chlorofluoromethanes: Chlorine Atom-Catalysed Destruction of Ozone," Nature, Vol. 249, p. 810, June 28.

Mortenson, O. S., 1970. "Depolarization Ratios in Resonance Raman Scattering," Chem. Phys. Lett., Vol. 5, p. 515.

NASA, 1969. "Atmospheric Exploration by Remote Probes," Vol. I and II. Final Report, Panel on Remote Atmospheric Probing to Committee on Atmospheric Sciences, National Academy of Sciences, National Research Committee.

NASA, 1971. NASA Langley Research Center, "Remote Measurement of Pollution," SP-285.

Neuman, J., 1973. "Radiation Absorption by Droplets of Sulfuric Acid Water Solutions and by Ammonium Sulphate Particles," J. Atmos. Sci. Vol. 30, pp. 95-100.

Newman, E. H., and Gary L. Trusty, 1971. "Absorption of Five to Six Micron Carbon Monoxide Laser Radiation by Water Vapor," Tech. Report. 2819-1, Air Force Avionics Laboratory, W-PAFB, August.

Niki, H., and B. Weinstock, 1972. "Carbon Monoxide Balance in Nature," Science, Vol. 176, p. 390.

Pagel, B. R., and R. L. Petritz, 1961. "Noise in InSb photodiodes," J. Appl. Phys., Vol. 32, pp. 1901-1904, October.

Pal, S. R., and A. I. Carswell, 1973, "Polarization Properties of Lidar Backscattering from Clouds," Appl. Optics, Vol. 12, pp. 1530-1535.

Patel, C.K.N., 1973. "Tunable Raman Lasers," to be published in Coherence and Quantum Optics, L. Mandel and E. Wolf, eds., Plenum Publishing Corp., New York, N.Y.

Penney, C. M., 1973. "Resonant Raman Scattering or Resonance Fluorescence in $I_2$ Vapor," Appl. Phys. Lett., Vol. 30, No. 6, 5 February.

Penney, C. M., and S. D. Silverstein, 1972. "Near-Resonance Raman Scattering and Fluorescence, Report No. 72CRD150, General Electric Co., Schenectady, N.Y., May.

Penney, C. M., W. W. Morey, R. L. St. Peters, S. D. Silverstein, M. Lapp, and R. D. White, 1973. "Study of Resonance Light Scattering for Remote Optical Probing," NASA CR-132363, General Electric Corp., Research and Development, P.O. Box 8, Schenectady, New York, September.

Plass, G. N., 1966. "Mie Scattering and Absorption Cross Sections for Absorbing Particles," Appl. Optics, Vol. 5, No. 2, pp. 279-285, February.

Robrish, P., H. J. Rosen, and O. Chamberlain, 1975. "Observation of a Continuous Transition from Resonance Raman Scattering to Fluorescence," Lawrence Berkeley Lab., Energy & Environment Div., U.C. Berkeley, California, submitted for publication.

Rosen, H., P. Robrish, and O. Chamberlain, 1975. "Feasibility of the Remote Detection of Pollutants Using Resonance Raman Scattering," Lawrence Berkeley Lab., Energy & Environment Div., U.C. Berkeley, California, submitted for publication.

Rusk, A. N., D. Williams, and M. R. Querry, 1971. "Optical Constants of Water in the Infrared," J. Optical Society of America, Vol. 61, No. 7, pp. 895-903, July.

Russell, P. B., W. Viezee, and R. D. Hake, 1973a. "Lidar Measurements of the Variability of Stratospheric Particulates," SRI Report CIAP DOT Contract NAS2-7261, July.

_____, 1973b. "Lidar Measurements of the Variability of Stratospheric Particulates," SRI Report CIAP DOT Contract NAS2-7261, October.

Russell, P. B., et al., "Results of Stratospheric Lidar Observations," 1975. Fourth Conference on the CIAP, DOT Transportation Center, Cambridge, Mass., February 4-7.

Sandorfy, C., 1964. Electronic Spectra and Quantum Chemistry, Prentice Hall, Inc., New York, N.Y.

SCEP, 1970. Man's Impact on the Global Environment - Study of Critical Environmental Problems, Cambridge, Mass., MIT Press.

Schotland, R. M., 1974. "Errors in the Lidar Measurement of Atmospheric Gases by Differential Absorption," J. Appl. Meteorol., Vol. 13, No. 1, pp. 71-77, February.

Schotland, R. M., 1964. "The Determination of the Verbal Profile of Atmospheric Gases by Means of a Ground-Based Optical Radar," Proceedings of Third Symposium on Remote Sensing of the Environment, pp. 215-224, University of Michigan, Ann Arbor, Michigan, October 14-16.

Schotland, R. M., et al., 1962. "Optical Sounding," Technical Report 2, Contract DA-36-039-SC-87299, Dept. of Meteorology and Oceanography, New York University, New York, N.Y.

Schotland, R. M., E. E. Chermack, and D. T. Chang, 1964. "The Measurement of the Vertical Distribution of Water Vapor by the Differential Absorption of Scattered Energy from a Searchlight Beam," Proc. First International Symp. of Humidity and Moisture, pp. 569-582, Reinhold Book Division, New York, N.Y.

Schuster, B. G., F. G. Fernald, and C. L. Frush, 1973. "Global Reconnaissance of Stratospheric Aerosols by Aircraft Radar," Fifth Conference on Laser Radar Studies of the Atmosphere, 4-6 June, Williamsburg, Virginia, Conference Abstracts, 34.

Slanger, T. G., and G. Black, 1969. "Resonance Fluorescence and Xenon Sensitization of the $CO(A^1\pi \rightarrow X^1\Sigma^+)$ System," J. Chem. Phys., Vol. 51, p. 4534.

SMIC, 1971. Inadvertent Climate Modification - Study of Man's Impact on Climate, Cambridge, Mass., MIT Press.

Smith, J. H., 1973. Unpublished data, SRI.

Snowman, L. R., 1972. "Laser Coincidence Absorption Measurements," General Electric Technical Information Series, No. R72ELS-15. March.

Sommers, H. S., Jr., 1970. "Microwave-Biased Photoconductive Detector," Chap. 11 of Semiconductors and Semimetals, Vol. 5 - Infrared Detectors, R. K. Willardson and A. C. Beer, eds., p. 436, Academic Press, New York, N.Y.

St. Peters et al., 1973. "Resonant Raman Scattering or Resonance Fluorescence in $I_2$ Vapor?" Phys. Rev. Lett., Vol. 30, No. 6, pp. 191-192.

Tang, J., and A. C. Albrecht, 1970. "Developments in the Theories of Vibrational Raman Intensities," Raman Spectroscopy, Vol. II, Ch. 2, H. A. Szymanski, ed., Plenum Press, New York, N.Y.

Tatarski, V. I., 1960. Wave Propagation in a Turbulent Medium, R. A. Silverman, trans., McGraw Hill Book Company, New York, N.Y.

Tejwani, G.D.T., 1972. "Computed Linewidths of $SO_2$," Research Report No. UTPA-ERAL-02, Department of Physics and Astronomy, The University of Tennessee, Knoxville, Tenn.

TRW Space Data, 1967. Third Edition, J. B. Kendrick, ed., TRW Systems, Redondo Beach, California.

317

United Detector Technology Manufacturers data.

Uthe, E. E., and P. B. Russell, 1973. "Experimental Study of the Urban
    Aerosol Structure and its relation to Urban Climate Modification,"
    Submitted to Bull. Am. Meteorol. Soc.

Valley, S. L., 1965. Scientific Editor, Handbook of Geophysics and
    Space Environments, Air Force Cambridge Research Laboratories,
    Office of Aerospace Research, United States Air Force.

Van de Hulst, H. C., 1957. Light Scattering by Small Particles, John
    Wiley & Sons, Inc., New York, N.Y.

Vassiliadis, A., and R. B. Battelle, 1965. "Study of the Applicability
    of Laser Radars to Probe Nuclear Weapon Effects and Natural Upper-
    Atmosphere Phenomena (U)," Final Report, Contract DA-49-146-XZ-324,
    SRI Project 5080, Stanford Research Institute, Menlo Park, California,
    January.

Verie, C., and J. Ayas, 1967. "$Cd_X Hg_{1-X} Te$ Infrared Photovoltaic
    Detectors," Appl. Phys. Lett., Vol. 10, pp. 241-243, May.

Viezee, W., R. D. Hake, and P. B. Russell, 1973. "Lidar Measurements
    of Stratospheric Constituents," SRI Report CIAP DOT Contract
    NAS2-7261, March.

Williams, P. F., D. L. Rousseau, and S. M. Dworetsky, 1974. "Resonance
    Fluorescence and Resonance Raman Scattering: Lifetimes in Molecular
    Iodine," Phys. Rev. Lett., Vol. 32, pp. 196-199, February.

Wofsy, S. C., et al., 1975. "Freon Consumption: Implications for
    Atmospheric Ozone," Science, Vol. 187, p. 535, February 14.

Wolfe, W. L., 1965. Editor, Handbook of Military Infrared Technology,
    Office of Naval Research, Department of the Navy, Washington, D.C.

Wright, L. M., and K. S. Krishnan, 1973. "Feasibility Study of In-Situ
    Source Monitoring of Particulate Composition by Raman or Fluorescence
    Scatter," Contract No. 68-02-0594, National Environmental Res.
    Center, Research Triangle Park, North Carolina, June.

Yamamoto, G., and M. Tanaka, 1969. "Determination of Aerosol Size
    Distribution from Spectral Attenuation Measurements," Appl. Optics
    Vol. 8, No. 2 pp. 447-453, February.

Yang, Lien C., 1973. "A Compact Glass Pulser," Laser Focus, Vol. 9, No. 7, pp. 37-39.

Zaromb, S., 1969. "Remote Sensing of Invisible Air Pollutants by Lidar Absorption Spectroscopy," Proceedings of Electro-Optical Systems Design Conference.